

**Developing Atom Probe Tomography
For Unique Nanoscale Insights
Into Biomaterials**



Yanru Ren
St. Edmund Hall
University of Oxford

A thesis submitted for the degree of
Doctor of Philosophy
Michaelmas Term 2022

Abstract

Bone provides structure and support for vertebrates, and it is the largest ion exchanger in the body to maintain homeostasis. Bone is a complex and heterogeneous composite material mainly composed of inorganic phases (mineral), organic phases (collagen, non-collagenous proteins), and water. Understanding the spatial structure and chemical composition of bone across different length scales is of great significance for elucidating its biomineralization mechanism, mechanical support, bone pathological treatment, and bone scaffold development. However, the simultaneous characterization of structure and chemical information of bone at the nanoscale presents many limitations, especially the exploration of 3D spatial structure and the mapping of low atomic mass elements.

Among the many synthetic bone substitutes, bioactive glasses (BG) are an attractive candidate with applications in critical bone damage repair, as they stimulate biological responses that favor bone formation and angiogenesis. However, previously it has been difficult to develop an amorphous BG that combines a 3D porous structure with a strong biological activity because conventional BG easily crystallizes during processing. The crystallization of bioactive glass limits the dissolution rate of the material and therefore slows down the surface reactivity, leading to a decrease in scaffold bioactivity and bone regeneration capabilities. In recent years, a new amorphous 3D strontium-containing BG (pSrBG) scaffold was developed by adding strontium to increase the bioactivity of BG. Prior characterization of this material showed a scaffold with a near-perfect bone contact without fibrous tissue coverage, and that it supports nearly exclusively lamellar bone repair, similar to normal and functional bone. Besides, strontium was detected in new formed bone and plasma after 21 days of transplantation *in vivo*, indicating that strontium successfully diffused as the material dissolved. However, due to the detection limits of conventional characterization techniques, it was not possible to specify the precise locality of released ions, and hence, it is not clear whether the locally achievable strontium concentration at the interface exceeds the medically acceptable range. Furthermore, the mechanism of Sr uptake into the bone and bone repair remains inconclusive.

Atom probe tomography (APT) is a 3D microscopy characterization technique with a unique combination of high spatial and chemical resolution, which can be used to characterize this new type of biomaterial, animal bone, and the interface between material and bone.

The work in this thesis presents the enabling preliminary development of APT techniques prior to this interface analysis. The synthetic bone material and porcine trabecular bone were investigated and characterized using APT. The challenges and corresponding countermeasures of biomaterials for APT sample preparation and experiments are outlined. The influence of various experimental parameters such as temperature, detection rate, laser pulse energy, and pulse frequency on the data quality by the LEAP-5000XR is explored and discussed. To this end, optimal operating conditions of APT were investigated and selected for two strontium-containing bioactive glass particles, the pSrBG scaffold, and porcine trabecular bone. The structure, including the

spatial distribution of collagen and mineral phases, and their chemical composition were analyzed at the atomic level within the porcine trabecular bone. The challenges and limitations of APT in reconstruction analysis and quantitative chemical composition measurements of biomaterials are addressed. This study demonstrates that APT has the unique capacity to identify and characterize significant compositional variations in nanoscale volumes within individual bone phases that may provide new insights into the further development and demonstration of the potential of APT in exploring the spatial structure and chemical composition of bones. It also provides the basis for advancing knowledge in APT research at the interface of pSrBG and bone.

Preface

The work presented in this doctoral thesis has been carried out at the Department of Materials, University of Oxford from October 2018 to October 2022, under the supervision of Prof. Michael P. Moody, Dr. Paul A. J. Bagot, and Prof. Molly M. Stevens. All of the research carried out for this thesis is original and where the work of others has been included it has been clearly referenced and acknowledged. No part of this thesis has been submitted for a degree at this, or any other university. Some of this work has been published in peer-reviewed journals and presented at conferences as detailed below:

Publications:

- Yanru Ren, H el ene Autefage, Julian R. Jones, Molly M. Stevens, Paul AJ Bagot, and Michael P. Moody. "Developing Atom Probe Tomography to Characterize Sr-Loaded Bioactive Glass for Bone Scaffolding." *Microscopy and Microanalysis* 28, no. 4 (2022): 1310-1320.
- Yanru Ren, Martina Cihova, Axel C. Moore, Molly M. Stevens, Paul AJ Bagot, and Michael P. Moody. "Nanoscale Spatial and Chemical Exploration of Porcine Trabeculae Bone using Atom Probe Tomography." *Microscopy and Microanalysis* 28, no. S1 (2022): 738-740.

Poster Presentations:

- Yanru Ren, Molly M Stevens, Paul AJ Bagot, Michael P Moody. Developing Atom Probe Tomography to Characterise Sr Containing Bioactive Glass for Bone Scaffolding. The European Atom Probe Workshop, Rouen, France, 2019.

Conference Presentations:

- Yanru Ren, Molly M Stevens, Paul AJ Bagot, Michael P Moody. Application of 3D Atom Probe Tomography in Biomaterial Research. The 10th Atom Probe Tomography (APT) Technology User Workshop, Shanghai, China, 2020.
- Yanru Ren, Molly M Stevens, Paul AJ Bagot, Michael P Moody. Developing Atom Probe Tomography to Characterise Sr-Loaded Bioactive Glass for Bone Scaffolding. The Microscience Microscopy Congress, 2021.
- Yanru Ren, Hok M. Tang, Helene Autefage, Julian R. Jones, Molly M. Stevens, Paul A. J. Bagot, Michael P. Moody. Developing Atom Probe Tomography to Characterise Sr-Loaded Bioactive Glass for Bone Scaffolding. The North-Rhine Westphalia (NRW) APT Virtual Meeting, 2021.
- Yanru Ren, Martina Cihova, Axel C. Moore, Molly M Stevens, Paul AJ Bagot, Michael P Moody. Nanoscale Spatial and Chemical Exploration of Porcine Trabecular Bone using Atom Probe Tomography. The Microscopy & Microanalysis, Portland, USA, 2022.

Acknowledgments

I would like to begin by thanking Prof. Michael P. Moody, Dr. Paul A. J. Bagot, and Prof. Molly M Stevens for providing me with the opportunity to undertake this DPhil project. The work in this thesis would not have been possible without their support and guidance. Thanks to the Stevens Group for providing experimental biomaterials to support me to complete this work. Huge thanks to Michael and Paul for their selfless sharing and careful teaching of their deep understanding and prodigious knowledge of Atom Probe Tomography. I would also like to thank Michael and Paul for their care in my life. They gave me great confidence, and because of them, my life and study at Oxford are full of optimism and warmth.

Thank you to everyone on the Oxford Atom Probe team for their help and valuable discussions over the years. I would like to especially thank Michael and Errin for fostering such a positive environment by sharing their passion for life and organizing various holiday parties within the group. I am grateful to be a part of such an enjoyable, collaborative, and friendly team, and thanks all for mutual encouragement and companionship during the COVID-19 pandemic.

I am also grateful to Dr. James O. Douglas for his patient training in SEM/FIB techniques, Dr. Shen Zhao for providing his unique insights after I experienced countless failures in needle preparation of biomaterials, and for his help and company on countless nights in the windowless FIB room. Thanks to Dr. Andrew J. London for providing access to the indispensable MATLAB scripts for APT data analysis. Thanks to Dr. Benjamin M. Jenkins for always being open to questions and for his valuable insights on a variety of issues. Special thanks to Dr. Martina Cihova for her helpful discussion throughout the exploration of animal bones, and thanks to her for giving me many new insights and inspirations on the interpretation of APT of animal bones. Thanks to the many members of the Department of Materials Oxford who have assisted me.

I would like to thank my family and friends who have provided support, great memories, and laughter throughout. I wish to thank my mother and father for their financial support for my study and life in Oxford, and for everything they have done for me over the years. None of this would be possible without them. Thanks to Minyi Zhang, Xinya Niu, Yi Liang, and Yumeng Yin for their companionship, and a lot of wonderful time had been spent with them in my life at Oxford. Special thanks to Minyi Zhang who brought me so much joy and support, I feel very lucky to have met such a good friend in Oxford.

Finally, I would like to thank my husband and best friend, Jiawei Shen. Thank you for everything! I also want to thank my soon-to-be-born daughter for enriching my life with your presence.

Acronyms

ACP Amorphous calcium phosphate

APT Atom probe tomography

AP suite Atom probe's toolkit for data analysis workstations

BGs Bioactive glasses

BG-Sr10 Bioactive glass particle which replacing 10 mol% Ca with Sr

BG-Sr100 Bioactive glass particle which replacing 100 mol% Ca with Sr

BMPs Bone morphogenetic proteins

CPC Calcium phosphate cement

Cys Cysteine

EBSD Electron backscatter diffraction

EDX Energy dispersive x-ray analysis

EPMA Electron probe microanalysis

FIB Focused ion beam

FTIRI Fourier transform infrared imaging

HAp Hydroxyapatite

HCA Hydroxycarbonate apatite

Hyp Hydroxyl-proline, hydroxylysine

IVAS Imago visualization and analysis software

LEAP Local electrode atom probe

Lys Lysine

Met Methionine

Pro Proline

PSD Position sensitive detector

pSrBG Strontium-releasing bioactive glass-based scaffold

SAXS Small angle x-ray scattering

SBF Simulated body fluid

SEM Scanning electron microscopy

STEM Scanning transmission electron microscopy

TEM Transmission electron microscopy

XRF X-ray fluorescence

Contents

Chapter 1. Introduction.....	1
Chapter 2. Literature Review.....	5
2.1. Introduction	5
2.2. Biology of Bone, Bone Fracture and Bone Regeneration	5
2.3. Grafts and Bone Substitutes	7
2.3.1. Auto/Allo Bone Grafts.....	8
2.3.2. Synthetic Bone Graft Substitutes.....	9
2.4. 3D Sr-releasing Bioactive Glass-Based (pSrBG) Scaffold for Bone	14
2.5. Methods to Characterize Biomaterials and Organic-Inorganic Interface.....	19
2.5.1. Histological and Histomorphometry	20
2.5.2. Scanning Electron Microscopy (SEM), Focused Ion Beam (FIB), and Energy Dispersive X-ray Analysis (EDX).....	21
2.5.3. Transmission Electron Microscopy (TEM).....	25
2.5.4. Raman Spectroscopy and Fourier Transform Infrared Imaging (FTIRI). 27	
2.5.5. X-ray Fluorescence (XRF) and Small Angle X-ray Scattering (SAXS). . 28	
2.6. Limitation of Biomaterials Analysis and Developing Atom Probe Tomography (APT) for Biomaterials.....	30
2.7. Summary.....	37
Chapter 3. Experimental Procedures	38
3.1. Introduction	38

3.2. Materials	38
3.2.1. 10% and 100% Sr Containing Bioactive Glass Particles (BG-Sr10 and BG-Sr100)	38
3.2.2. Sr-releasing Bioactive Glass-Based (pSrBG) Scaffold	40
3.2.3. Porcine Trabecular Bone.....	41
3.3. Electron Microscopy.....	43
3.3.1. Scanning Electron Microscopy (SEM)	43
3.3.2. Electron Probe Micro Analyzer (EPMA).....	44
3.4. Atom Probe Tomography (APT)	45
3.4.1. Basic Principles	45
3.4.2. Specimen Preparation.....	48
3.4.3. Limitations and Challenges	51
3.4.4. Atom Probe Analysis Optimization for Biomaterials	54
3.4.5. Interpretation of the Mass Spectra.....	55
3.4.6. Peak Overlaps	57
3.4.7. Analysis Techniques and Tools to Interpret Reconstructions	59
3.4.7.1 Iso-concentrations/ Iso-density Surfaces and Volume Render	60
3.4.7.2 Concentration Profiles and Proxigrams	61
3.4.8. Compositional Measurements	62
3.5. Summary.....	63

Chapter 4. Strategies to Overcome Sample Preparation Challenges for Biological

Specimens.....	64
4.1. Introduction	64
4.2. Challenges I: Sample Damage and Cantilever Loss of Brittle/Surface Sensitive Materials	65
4.3. Challenges II: Needle Bending and Contamination during APT Tips Sharpening for Biological Materials.....	69
4.4. Challenges III: Complex Topography and Pores in Animal Trabecular Bone	74
4.5. Summary.....	77
Chapter 5. Atom Probe Analyses of Synthetic Bone Substitutes	80
5.1. Introduction	80
5.2. Sr-Containing Bioactive Glass Particles (BG-Sr10 and BG-Sr100)	81
5.2.1. APT Operating Conditions Optimization	82
5.2.2. Mass Spectra and Reconstruction Interpretation	91
5.2.3. Composition Analysis.....	93
5.2.4. Comparison of BG-Sr10 with BG-Sr100	96
5.3. Sr-Releasing Bioactive Glass-based (pSrBG) Scaffold.....	100
5.3.1. APT Operating Conditions Optimization	100
5.3.1.1. Operating Temperature and Detection Rate.	101
5.3.1.2. Pulse Frequency.....	104
5.3.1.3. Pulse Energy	106
5.3.2. Mass Spectra and Reconstruction Interpretation.....	107

5.3.3. Composition Analysis.....	109
5.4. Summary.....	111
Chapter 6. Atom Probe Analyses of Porcine Trabecular Bone.....	113
6.1. Introduction	113
6.2. APT Operating Conditions Optimization	115
6.3. Mass Spectra Interpretation.....	120
6.3.1. Main Structural Components of Bone	120
6.3.2. Mass Spectrum and Critical Overlaps	122
6.4. Interpretation of the Spatial Reconstruction.....	126
6.4.1. Horizontal Sampling.....	126
6.4.1.1. Specimen 1: R5083_12600.....	127
6.4.1.2. Specimen 2: R5083_22723.....	132
6.4.1.3. Specimen 3: R5083_22923.....	138
6.4.2. Vertical Sampling	141
6.4.2.1. Specimen 4: R5083_23568.....	142
6.4.2.2. Specimen 5: R5083_23632.....	144
6.4.3. Collagen Phase and Mineral Phase Exploration and Comparison	149
6.4.4. Distribution of Other Essential and Trace Elements	155
6.5. Composition Investigation.....	162
6.6. Further Features of APT Analysis of Porcine Trabecular Bone	169
6.6.1. Reconstruction Observed to Incorporate A “Hole” Area?.....	170

6.6.2. Are the Observed Organic Regions Collagenous Fibrils or Non-Collagenous Proteins?	176
6.7. Summary.....	180
Chapter 7. Conclusions.....	184
Chapter 8. Future Work	193
Chapter 9. Bibliography	197
Chapter 10. Appendix	212

Chapter 1

Introduction

With the increasing demand for medical procedures requiring bone grafts, the development of synthetic bone substitutes has rapidly increased over the past few decades, to the extent that bone graft substitutes now represent one of the most promising markets in the orthopedic industry [1]. Among most synthetic bone substitutes such as calcium sulfate and calcium phosphate ceramics/cement, bioactive glasses (BGs) are particularly attractive candidates because of their excellent osteoconductive and osteoinductive properties [2]. Studies have shown that bioactive glass can directly bind to bones, transfer active ions during material degradation, and stimulate biological responses that are conducive to osteogenesis and blood vessel formation [3-5]. Furthermore, many studies have shown that strontium is one of the key active ingredients in the anti-osteoporosis drug strontium ranelate (SrRan) [6-8]. Combining the advantages of BGs and strontium, strontium-substituted BG has been studied for bone repair, and has been shown to increase the activity of osteoblasts and inhibited activities of osteoclasts in vitro [9-11], and enhance bone formation and osseointegration in vivo [12-14]. However, the application of BGs has thus far been limited due to the manufacturing challenges associated with the amorphous porous bioactive glass scaffolds, which crystallize during sintering, leading to a decrease in the scaffold's bioactivity and bone regeneration capabilities [15-18]. Although such crystallization cannot completely inhibit biological activity, the presence of a large number of crystals leads to a slowed glass reaction rate and uncontrolled release of ions. For example, there have been reports that due to the non-congruent dissolution

of silicate glass, these materials have been shown to remain within the surgical site even 14 years postoperatively [19]. Furthermore, the crystallization of bioactive glasses slows down their surface reactivity. Studies have shown that the ratio of proteins and their functional groups adsorbed to amorphous bioactive glass is greater than that adsorbed to crystalline bioactive glass [20].

In recent years, a porous, strontium-releasing bioactive glass-based scaffold (pSrBG) has been designed, by tailoring and optimizing the composition of pSrBG. It has been previously demonstrated that this scaffold both achieved stable delivery of strontium and retained the amorphous phase, which can induce tissue infiltration and promote bone formation [15]. Preliminary tests have shown that the scaffold exhibits good performance, which can achieve almost perfect bone contact without fibrous tissue coverage. *Vivo* testing detected strontium in new form bone and plasma after 21 days of transplantation [15], indicating that strontium successfully diffused as the material dissolved. However, due to detection limits of conventional characterization techniques, it was impossible to specify the precise locality of released ions, and hence it is not clear whether the achievable strontium concentration locally at the interface exceeds the medically acceptable range, and the mechanism of Sr uptake into the bone and bone repair remains inconclusive.

Although the recent developments in Scanning Transmission Electron Microscopy (STEM) have made progress in atomic resolution element mapping, the spatial resolution and chemical sensitivity in the analysis of biominerals are still greatly limited due to the fact that these materials are sensitive to damage by the applied electron beam [21]. Furthermore, the resolution of Raman spectroscopy and Fourier transform infrared spectroscopy which is commonly used in the characterization of biological materials are usually limited to the molecular level [22]. The low detection limit of Atom

Probe Tomography (APT) opens up new areas for the characterization of biological materials. APT is a technique for a highly magnified analysis of chemical identities and 3D positions of atoms within an extremely small volume of material [23, 24]. APT is based on the phenomenon of field evaporation, in which ions successively desorb from a micro-tip surface in the presence of an intense electric field. The development of laser pulsing technology has expanded the applicability of APT to almost all dielectric materials, including a limited range of biological and geological minerals such as bone-type material [21, 25], chiton tooth [26], rodent tooth enamel [27, 28], and dentin and implants interface [29]. Combining APT with other microscopy techniques has the potential to better understand the complex processes that occur at the smallest-scale implant interface, leading to the development of improved biomaterials.

However, APT analyses of biomaterials can present significant challenges such as specimen preparation of non-conductive biological composite materials, identifying atom probe experimental parameters to simultaneously optimize specimen viability and accuracy of compositional measurements, interpretation of complex mass spectra, and understanding the reproducibility and precision of the 3D spatial reconstructions. This research aims to develop APT specimen preparation, experimental protocols, 3D reconstruction, and data interpretation specifically for biomaterials characterization. In addition, this project will apply those techniques to explore synthetic bone scaffolds and animal bones using Atom Probe Tomography.

The thesis is divided into eight chapters, with Chapter 2 providing a brief introduction to bone biology, bone fractures and regeneration, bone grafts, and bone substitutes. Furthermore, current methods for characterizing biomaterials and organic-inorganic interfaces are reviewed. A critical review and discussion of the current literature associated with Atom Probe Tomography of biomaterials are presented in Chapter 2.

Chapter 3 provides information on the materials, instruments and methods used in this project. Chapter 4 discusses difficulties encountered in APT sample preparation of biological specimens, and develops corresponding strategies to overcome those challenges. To this end, effective approaches for APT specimen preparation methods for biological materials are presented in detail in Chapter 4.

Atom probe analysis of synthetic bone substitutes are presented in Chapter 5. This chapter investigates how experimental conditions can affect the analysis of different synthetic bone materials, and investigates the influence of various parameters such as temperature, detection rate, laser pulse energy, and pulse frequency on the data quality using LEAP-5000XR. Comparative analysis of the mass spectra interpretation, composition calculations, and reconstruction of three synthetic bone materials are also shown in Chapter 5.

Atom probe analyses of porcine trabecular bone are investigated in Chapter 6. Theoretical background on porcine trabecular bone are provided. Optimal APT operating conditions are identified for the analysis of porcine trabecular bone using the LEAP-5000XR. Complex mass spectra of porcine trabecular bone are ranged and interpreted. Chapter 6 presents different sampling orientations of porcine trabecular bone tips and corresponding 3D reconstructions of tips containing collagen fibrils in different orientations. Further, Chapter 6 also investigates the spatial distributions of organic and inorganic phases in porcine trabecular bone. The components of each phase of porcine trabecular bone are studied and compared. The limitations and challenges of APT in trabecular bone research are also discussed in Chapter 6. A brief summary of the key findings from this research is presented in Chapter 7, whereas Chapter 8 discusses potential future research.

Chapter 2

Literature Review

2.1. Introduction

This chapter provides background knowledge on bone biology, fractures, bone regeneration, bone grafting, and bone substitutes. Various characterization methods currently used to characterize biomaterials and organic-inorganic interfaces will be reviewed and compared. Besides, relevant research on Atom Probe Tomography of biomaterials so far will be summarized.

2.2. Biology of Bone, Bone Fracture and Bone Regeneration

With improved living conditions, the average life expectancy has increased significantly and the world's population is gradually aging. As a consequence, medical care and costs associated with bone-related issues are increasing as a result of the rising morbidity of musculoskeletal disorders, bone fracture, osteoporosis, and bone metastases [30]. For example, the economic impact of musculoskeletal disease in the United States is approximately \$126 billion, and around 6.8 million people are treated per year in the United States [31]. In addition, more than 1 million total hip and knee replacement operations are undertaken, which cost more than \$25 billion each year in the United States alone [32].

Bone provides structure and support for the body, it is a heterogeneous composite containing mineral phase (hydroxyapatite, $\text{Ca}_{10}(\text{PO}_4)_6(\text{OH})_2$), organic phase (collagen, non-collagen proteins, and lipids), and water [33]. A bone fracture is a medical condition

in which the continuity of the bone is partially or completely broken by high impact or stress, and can be exacerbated even for small trauma due to some diseases that weaken bones such as osteoporosis, osteopenia, bone cancer, or osteogenesis imperfections [34]. There are two main types of fracture healing, primary bone healing and secondary bone healing. Primary healing (direct healing) only requires the regeneration of lamellar bone and blood vessels without the formation of callus. This healing needs a correct anatomical reduction, stable with no gap formation [35]. Secondary fracture healing (indirect fracture healing) which is more common represents spontaneous fracture healing without rigid fixation of the fracture site. Fracture healing can be simply divided into three phases which have different cellular characteristics and extracellular matrix components. These are the inflammatory phase, the reparative phase (including intramembranous ossification), and cartilage formation (including endochondral ossification and remodeling) [36, 37]. Figure 1 is a schematic interpreting three continuous stages of secondary bone fracture healing [31]. Osteoblasts and osteoclasts are the two main cells involved in bone remodelling. Osteoblasts are connective tissue cells on the bone surface, which can be stimulated to proliferate and differentiate into bone cells. On the other hand, osteoclasts are bone tissue resorption cells [38, 39]. For common bone fractures, the bone tissue normally heals itself. However, for complex fractures and diseases, external intervention or applicable replacement is required for full recovery [30]. By further investigating the biology of bone fracture and regeneration, the mechanisms of healing could be understood better, and more techniques and biomaterials can be developed to promote treatment.

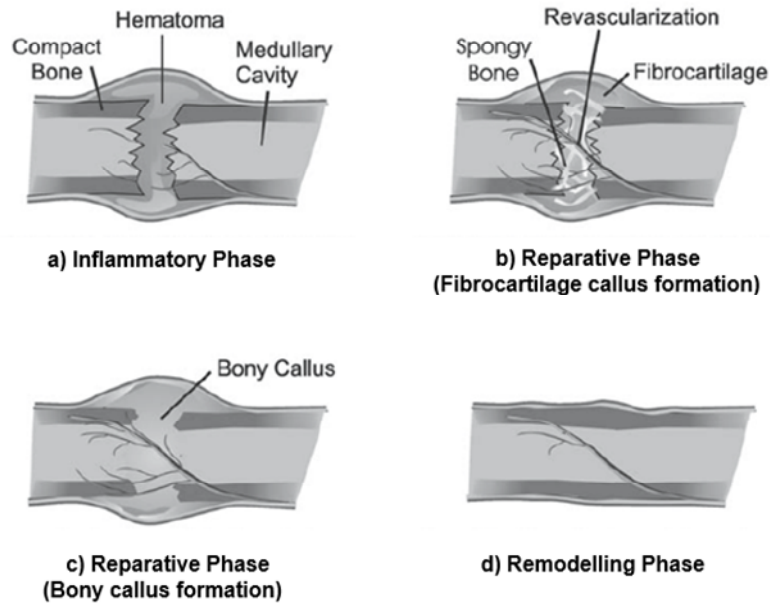


Figure 1. The illustration of continuous healing stages of secondary bone fracture. a) Hematoma formation after a bone fracture, cells including such as lymphocytes, platelets, blood monocytes, macrophages, neutrophils, and osteoclasts accumulate on this site. b) With the expression of macrophage, chondrocyte, osteoclast, fibroblast, and endothelial cell, the fibrous tissue and new cartilage begin to form, and revascularization takes place. c) Intramembranous and endochondral ossification begins for the laying of new woven bone. d) Lamellar bone replaces the woven bone and excess callus resorption takes place, returning to normal bone structure [31].

2.3. Grafts and Bone Substitutes

Bone grafting is one of the most common surgeries in orthopedic surgery procedures, and it is the second most common tissue transplant procedure after blood transfusion. More than 2 million bone grafts are performed each year around the world, the operation frequency is at least 10 times higher than the number of other transplantable organ procedure [31, 40, 41]. The history of bone grafting can be traced back to more than 300 years ago when Job van Meekeren first applied a canine xenograft to repair a skull defect [42]. In the past, a successful transplant was considered to be achieved if the graft was able to support the forces exerted by the individual. Today, bone grafts aim to have not only good mechanical properties, but also to stimulate and promote bone

formation and vascularization, and they can be modified into specific shapes to tackle various defects [31]. An ideal bone graft or bone graft substitute should incorporate three basic factors: osteoconduction, osteoinduction, and osteogenesis [43]. Osteoconduction represents the ability to support the attachment of osteoblasts and osteoprogenitor cells on the surface, allowing these cells to migrate and in grow within specific graft structures (for example, 3D porous graft). Osteoinduction refers to the graft stimulating the host tissue to induce primitive, undifferentiated and pluripotent cells to differentiate into osteogenic cells (mediated by many growth factors such as bone morphogenetic proteins (BMPs)). Osteogenesis describes the osteo-differentiation and the formation of new bone in later stage from host or graft donor cells [43-45].

2.3.1. Auto/Allo Bone Grafts

There are two main types of bone grafting: auto/allografts, and synthetic bone substitutes. Auto/allografts are natural resources from one same individual or two genetically different individuals respectively. Among all available clinical bone grafts, autogenetic bone grafts are the ‘gold standard’ as they perfectly meet all the basic factors as mentioned before, along with having histocompatibility, not spreading disease, and retaining active osteoblasts involved in bone formation [1, 30, 31, 46]. However, autologous transplantation has obvious shortcomings, such as multiple surgical procedures and pain, potential complications and infections, limited donor material, etc [30, 45, 47, 48]. The second-highest choice for surgeons is allogeneic bone grafts, which are reported to account for nearly one-third of all bone grafts used in North America [49].

2.3.2. Synthetic Bone Graft Substitutes

With the increasing demand for bone grafts, the development of synthetic bone substitutes has greatly increased over the past few decades to solve the limitations mentioned above, enabling bone grafts substitutes to obtain the most promising market in the orthopedic industry [50]. The most commonly used synthetic bone substitutes today are calcium sulfate, calcium phosphate ceramics, calcium phosphate cement, bioactive glass, or combinations thereof [51]. Osseointegration is an important criterion when we evaluate the bone healing outcomes of synthetic bone graft substitutes, which is defined as the ability to form a direct interface between an implant and bone without forming fibrous tissue at the bone-implant interface [43].

Calcium sulfate (plaster of paris), is an osteoconductive and biodegradable ceramic composed of CaSO_4 , which has been used to fill void defects in bone since 1892 [52]. Calcium sulfate can be prepared in different forms by heating gypsum with a patented alpha hemihydrate crystal structure, for example, hard particles or viscous liquids that can be injected (hardened in vivo) [47]. Calcium sulfate has the characteristics of a fast absorption rate even without macroporous structure, and weak internal strength. It is normally only applied for filling small bone defects with a rigid internal fixation [53]. For larger bone defects, for example, as Niu has reported, calcium sulfate cannot obtain the optimal fusion rate in spinal arthrodesis due to the faster degradation rate relative to the deposition rate of bone in the early stage of bone regeneration [54].

Calcium phosphate ceramics are composed of calcium hydroxyapatites which have similar chemical composition to the calcified tissue mineral phase [51]. As a bioabsorbable ceramic with good osteoconductivity, bioceramics have obtained extensive attention and has been widely experimented with in clinical research [47, 55, 56]. One typical bioceramic available in the market is hydroxyapatite (HAp), one of the most stable

and least soluble calcium phosphate bioceramics with a Ca/P ratio of 1.67 [57, 58]. HAp ($\text{Ca}_{10}(\text{PO}_4)_6(\text{OH})_2$) is a naturally occurring mineral form, which structure is similar to the bone apatite (one of the inorganic components of bone) [55-58], is used as a bone substitute alternative to auto-grafts. The osteoconduction and osteoinductive properties of the HAp scaffolds are well known, and studies have shown that HA has the ability to directly bond to the bone [58]. For example, osteoinductive mechanisms have been seen in different host studies with goats, baboons and dogs, and spontaneous bone formation in non-bone sites has been shown [59-61]. For calcium phosphate ceramics, the crystal and porous structures are significant factors. For example, the porous structures will affect osteoprogenitor cells adhesion, proliferation, and differentiation, as well as angiogenesis, followed by new bone ingrowth [55, 56]. Besides, high Ca/P ratio and crystallinity will affect the resorption rate by giant cells and macrophages and lower the bioactivity [62]. Typically, non-porous dense implants and porous granular particles are a common commercially available form of HAp. HAp is also commonly used as a coating on implants to increase the implants' lifetime by improving the osseointegration of implants [30, 58]. However, studies have also shown that long-term HA-coated implants are not stable, and infections and complications can be caused by exfoliation of the HA coating (formation of fibrous tissue) around the implant [63].

Calcium phosphate cement (CPC) is a bioactive cement that acts as a HA when wet. The first calcium phosphate cement was created by Brown and Chow in the 1980s [64]. Since then, many CPCs with different compositions have been studied and are commercially available. CPC is produced by a chemical reaction between two phases, solid and liquid. When the two phases are mixed, a paste is formed that can gradually solidify and hardens into a solid matter; similar to the cement used in civil engineering [63]. At present, although there are many CPC recipes, there are only two possible end

products for CPC reactions: brushite (dicalcium phosphate dihydrate, DCPD) or apatites, such as hydroxyapatite or calcium-deficient hydroxyapatite (CDHA) [65]. The main advantage of CPC is that they can be injected and have the ability to harden in vivo at body temperature. The CPC forms a viscous paste that can be easily handled and shaped. In some cases, it is convenient to inject to treat defects of various shapes and could avoid invasive surgery, unlike calcium phosphate ceramics which are difficult to process and shape [63, 65]. The main shortcoming of CPC is its poor mechanical properties. More specifically, toughness, brittleness, and reliability all limit the application of CPC. Also, CPC pastes tend to disintegrate when exposed to blood or biological fluids at an early stage due to their weak cohesion [63-65]. Therefore, current clinical applications are limited to craniofacial operation [1].

Bioactive glass (bioglass, BG), a group of silicate-based ceramics with an amorphous structure, was first developed in the 1970s based on an initial composition of silicon dioxide (SiO_2), sodium oxide (Na_2O), calcium oxide (CaO) and phosphorus pentoxide (P_2O_5) [66]. The original Bioglass[®] 45S5 (BG45S5), made by Larry Hench at the University of Florida, was the first artificial material that formed a chemical bond with bones [67]. BG45S5 (46.1% SiO_2 , 24.4% Na_2O , 26.9 % CaO and 2.6% P_2O_5 , from NovaBone Products LLC, US) and S53P4 (53.8% SiO_2 , 22.7% Na_2O , 21.8 % CaO , and 1.7% P_2O_5 , from BonAlive Biomaterials, Finland) are currently the two commercially bioglasses that have been most accepted for bone graft replacement on the market [1]. Studies have shown that bioactive glass has good osteoconductive and osteoinductive, it supports new bone growth, both at the bone-implant interface and away from the interface. Bioactive glass binds bone faster and stimulates more bone regeneration than other bio-ceramics such as hydroxyapatite [16, 48]. In vivo studies in the rabbit and rat femur showed that BG45S5 bioactive glass particles can promote bone proliferation faster than

(synthetic) HA [4]. Furthermore, BG can provide reactive ions to alter cellular responses and stimulate bone regeneration. Chemical degradation begins on the surface of bioactive glass, and biological reactions begin with the release of ions (e.g. sodium, calcium, phosphate, and soluble silica ions), those ions can participate in ion exchange and stimulate cellular responses such as new bone formation and vascularization [73]. In vitro research has shown that the degradation rate of BG45S5 is faster than HAp, which is attributed to solution-mediated dissolution rather than cell/enzyme action [48]. Further studies indicated that bioglass fiber scaffolds can be completely absorbed within six months in vivo with almost no inflammatory response [68].

Generally, a biologically active material refers to a substance which is designed to induce specific biological activity [69]. In other words, a HAp-like layer (e.g. hydroxycarbonate apatite (HCA)) can be formed to create a strong bond to hard/soft tissue when a material undergoes some specific surface reactions after implantation [16]. It has been proposed that the ability of a material to form a HAp-like surface layer when immersed in simulated body fluid (SBF) in vitro represents its biological activity, and is an important indicator to estimate its biological activity potential in vivo [70]. Bioactive glass is a bioactive material, and its osseointegration mechanism is attributed to the formation of HCA layers on the glass surface [66, 71, 72]. HCA is similar to bone minerals and is believed to interact with collagen fibrils to form a strong bond with the host bone [48]. Figure 2 shows the surface reaction after implantation on BG45S5. When the bioactive glass contact with interstitial fluid, ion exchange occurs between doped ions and protons in solution, forming hydroxyl groups. The process then continues to release silicon in the form of silanols, and a silica gel layer is formed. With continued ion exchange of calcium and phosphate groups, an amorphous calcium phosphate layer gradually forms on top of the silica layer. The continued association of hydroxyl and

carbonate groups leads to the formation of the HCA layer. With the formation of the HCA layer, growth factors are adsorbed on the surface and followed by the attachment, proliferation, and differentiation of osteoprogenitor cells [73]. Next, osteogenesis cells produce an extracellular matrix where mineralization occurs to form nanocrystalline minerals and collagen on the interface of bone-implant, meanwhile, the degradation and conversion of the glass continue [74]. More details of HCA reaction are provided in the publications of Hench et al. [66, 67, 73]. Although this mechanism is generally accepted, some details of its chemical and structural changes are still unclear. It has been pointed out that the properties of glass such as the dissolution rate and the rate of formation of HCA layers on the bioactive glass are a direct result of atomic structures, which may require advanced characterization techniques to understand their complex amorphous structures and any structural changes [48].

Bioglass with its many advantages would appear to be a better regenerative bone substitute than bioceramics, however, this is not reflected in its current market share. Current applications are mainly limited to ear cartilage, small teeth, and facial and bone defect repair [15, 48]. The main reason for this is caused by the challenge of making a bioglass scaffold. It is difficult to produce an amorphous porous bioactive glass scaffold because it crystallizes during sintering, leading to a decrease in the scaffold's bioactivity, bone regeneration, and degradation rate [1, 15, 16, 48]. In addition, bioglass mechanical properties are reported to be brittle and weak, similar to other ceramics [75].

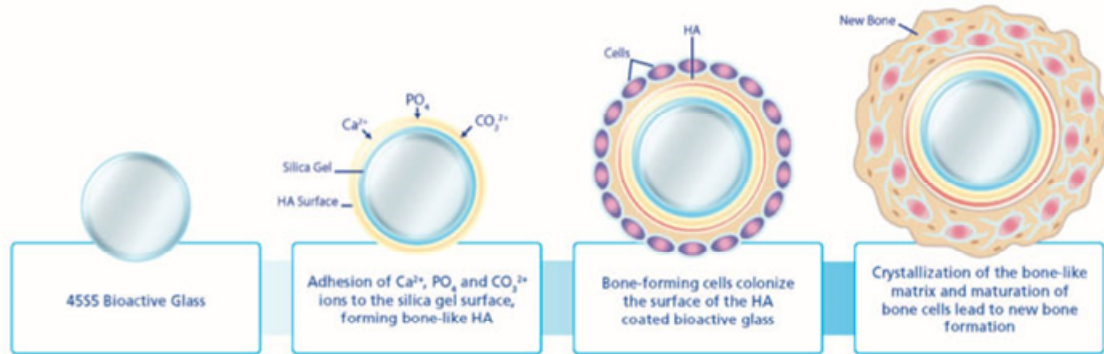


Figure 2. The illustration of surface reaction steps of BG45S5.

2.4. 3D Sr-releasing Bioactive Glass-Based (pSrBG) Scaffold for Bone

The incorporation and/or local delivery of bioinorganic ions has long been used in various therapies, even though there is little known about their underlying mechanisms [76]. The amorphous property of BG enables it to deliver bioinorganic ions at a sustained rate [15]. Bioactive glass can be doped with microelements such as Cu, Zn, and Sr, which are known to be beneficial for healthy bone growth [16]. Strontium is a bone-seeking element, 98% of which in the human body can be found in the skeleton. It accounts for 0.035 wt% of the mineral content of the skeleton [77]. From a chemical point of view, the size and behavior of Sr and Ca are similar (charge and ionic radius), and they come from the same IIA group of the periodic table. Although Sr is not an essential microelement, due to this chemical similarity to Ca, significant research has been carried out on its properties and effects [16]. Strontium ranelate (SrRan) has been clinically used as a prescription for postmenopausal women with osteoporosis in Europe [6, 77], and although the mechanism of action of SrRan is not fully understood, it is reported that the Sr ion is the active ingredient of the drug [78]. Research has indicated that Sr promotes the bone formation of osteoblasts including osteoblast proliferation, differentiation and viability. It also inhibits osteoclast activity and induces osteoclast apoptosis, which in turn

inhibits osteoclastic bone resorption, leading to reduced bone resorption [10, 15, 48], as shown in Figure 3. In addition, experiments with bone cells (OPC1) showed both increased adhesion and proliferation of bone cells in HA containing 20 mol% Sr compared to HA without Sr [16].

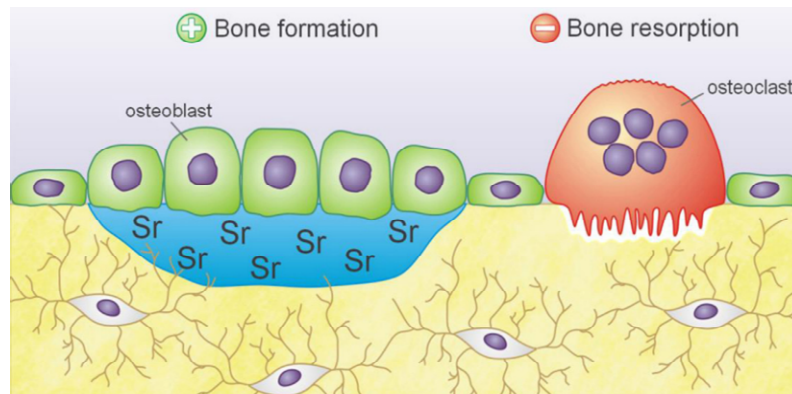


Figure 3. Effects of Sr on bone. Sr promotes bone formation by osteoblasts, inhibits bone resorption by osteoclasts, and leads to the incorporation of Sr into the mineralized matrix formed during treatment [78].

In order to increase the bioactivity of BG, Sr can be doped into the glass by replacing some calcium in BG to form new materials for bone regeneration [15]. Yann et al. have researched the effect of Sr on the glass properties and osteoblasts and osteoclasts response by replacing 0-100% Ca with Sr in the Bioglass 45S5 composition [10, 79], and research has shown that the metabolic activity of osteoclast activity is inhibited and the alkaline phosphatase activity of osteoblasts is increased with the increase of Sr content [10]. Sr-releasing bioactive glass can be used in a wide range of orthopedic applications, such as bone void fillers, and porous stents or metal implant coatings for tissue engineering applications [79]. Some researchers also indicate that Sr in bioactive glass can be used as a probe for the HCA formation process to help us understand the process of HCA formation as Sr forms a complete and continuous solid solution series with Ca in

apatite [80].

From a material science perspective, bone is a nanocomposite of collagen and bone minerals with a hierarchical structure. Cancellous bone has an open interconnected porous network with pores over 500 μm and with large interconnects between the pores [48]. The ideal synthetic bone graft should be a porous material that acts as a temporary scaffold for three-dimensional bone growth [81]. Various factors for a synthetic bone graft such as micro-porosity, surface area, geometry, and topography are important for bone regeneration, for example, micro-porosity has a positive effect on increasing bone formation [31, 82]. Porosity regulates the biological activity of the graft substitute and controls the rate of bone repair, the local environment, and the new bone balance at the repair site. The extent and interconnection of the pores also affect bone ingrowth and blood vessel formation. The appropriate 3D structure provides mechanical support and space for cell infiltration and neovascularization before the new bone formation [83]. As mentioned, bioactive glasses are attractive candidates in bone regeneration, however, it is hard to make an amorphous porous bioactive glass scaffold from Bioglass 45S5 as it has a very narrow sintering window [84]. The first melt-derived bioactive glass scaffold with a pore structure was developed by Fu et al. [85], using a polymer foam replication technique. The sintering window was expanded by adjusting the glass composition, allowing the glass to be sintered without crystallization. Although the glass scaffolds sintered well with approximately 85% porosity, later experiments show that after 7 days of immersion in simulated body fluid (SBF), the scaffold only nucleated apatite, which indicates it is impossible to form a rapid bond in vivo [84, 85]. In 2011, an amorphous porous melt-derived bioactive glass scaffold with interconnected pore networks was developed by Wu et al., which can form amorphous calcium phosphate within 8 hours and HCA within 3 days in SBF [84], which shows the potential of fast binding to host

bone and stimulates bone growth well for this scaffolds.

A strontium-releasing bioactive glass-based (pSrBG) scaffold with porous structure (Patent No.: WO2007/144662) was developed by the Stevens Group, which shows a near-perfect (near 100%) bone-to-material contact (without forming fiber tissues) and excellent formation of new well-organized lamellar bone (similar to normal functional bone tissue) in a large animal model [15]. The pSrBG scaffold with properties of non-toxic, amorphous, and highly porous is made by the melt-quenching route, and the composition of pSrBG is designed and optimized so that the glass can release strontium at a sustained rate in the treatment range. Furthermore, it also allows a wider sintering window to be achieved [15]. Table 1 shows the composition of pSrBG measured by X-ray fluorescence (XRF). Figure 4 compared BG45S5 and pSrBG by XRD, showing that pSrBG retains an amorphous phase. In addition to strontium addition, Figure 5 shows that the pSrBG scaffold has highly interconnected holes, and a genuine 3D porous structure to provide sufficient mechanical support and space for cell infiltration and neovascularization, followed by new bone formation [15]. The pSrBG scaffold consists of a 3D porous scaffold that retains the amorphous phase, which is a feature that cannot be achieved using a conventional BG such as the BG45S5 [83]. Further characterizations of this 3D-pSrBG scaffold which has been previously undertaken will be presented in Section 2.5.

Table 1. Composition of pSrBG as measured by XRF. Table shows mol% of each oxide from the nominal composition and the composition obtained from the glass powder and scaffolds [15].

	SiO ₂	Na ₂ O	CaO	SrO	K ₂ O	MgO	P ₂ O ₅
Nominal composition (mol %)	44.5	4.0	17.8	17.8	4.0	7.5	4.5
XRF glass powder (mol %)	44.7	4.0	18.0	17.5	4.1	7.2	4.5
XRF pSrBG scaffold (mol %)	44.8	4.0	18.0	17.4	4.1	7.2	4.5

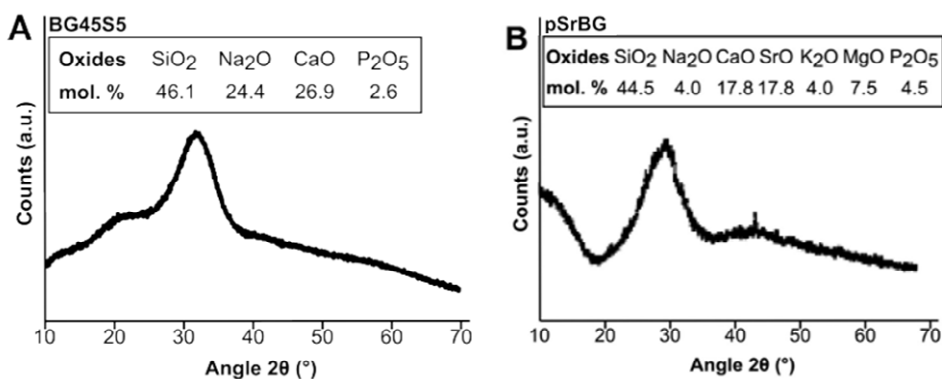


Figure 4. Material characterization. (A) XRD pattern of BG45S5. (B) XRD pattern of pSrBG, showing that pSrBG retains an amorphous phase and pSrBG composition [15].

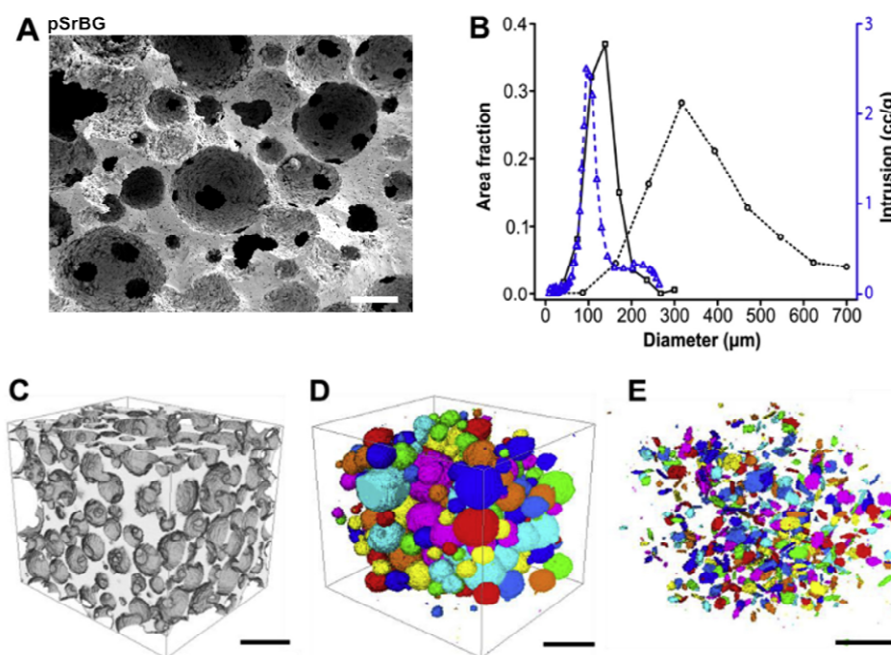


Figure 5. 3D pSrBG scaffold shows highly interconnected pores. (A) Representative SEM image of pSrBG scaffold cross-section that shows the presence of pores and interconnects (scale bar: 200 μm). (B) Interconnect (solid black line) and pore (dotted black line) diameter distribution (measured by X-ray micro-computed tomography (μCT)), and interconnect diameter distribution measured by mercury porosity (dashed blue line). (C–E) μCT reconstruction of pSrBG scaffold showing (C) the whole scaffold, (D) the pores and (E) interconnects within the scaffold (scale bar: 500 μm) [15].

2.5. Methods to Characterize Biomaterials and Organic-Inorganic Interface

Characterization of material microstructure for the understanding of material properties and insights into the underpinning mechanism is critical for their further development. In the case of biomaterial, the characteristic of the surface or interface has a significant impact on the success or failure of biomaterial devices [86]. Surfaces and interfaces play a particularly important role in biological materials because they affect early biologic activities in the material biology system [87]. The surface of biological materials can alter or affect proteins and cells, and this interaction determines the biocompatibility and blood compatibility of materials. For example, certain species (e.g., Sr, F) accumulating at the interface of bone and implant can change the mineral solubility and crystallite size, interfere with collagen-mineral bonding, and also affect bone cells [88]. Investigating the interface could help gain an in-depth understanding of the nature of biological reactions within materials such as marginal bone loss, ion release, and material degradation. A deeper understanding of the complex processes that take place at the surface of an implant at the smallest scale is of interest for the development of improved biomaterials [89]. In addition to conventional histological and histomorphometric for biological tissues, characteristics of interest in the surface and interface features of biomaterials include chemical structure, whether they are hydrophilic or hydrophobic, the presence of ionic groups and the morphology (porosity, surface roughness, flatness, and feature size) [90, 91]. Different types of information about these properties can be obtained using different analytical methods, for example, Scanning Electron Microscope (SEM); Energy Dispersive X-ray Detector (EDX); Transmission Electron Microscopy (TEM); X-ray Diffraction; Raman Spectroscopy and Fourier Transform Infrared Imaging (FTIRI) [86].

2.5.1. Histological and Histomorphometry

Histology, also known as microanatomy, is a branch of biology that studies the microanatomy of animals and plant tissues [92]. Histology is a microscopic counterpart of gross anatomy that observes larger structures that are not visible to the microscope. Histomorphometry is broadly defined as a measure of the shape or form of tissue. Quantitative analysis of bone structure is achieved by using bone histomorphometry, which provides valuable information about bone mass and its cellular activity [93]. Usually, researchers will start to study the region of interest by analyzing the histological and histomorphological cross-section as shown in Figure 6, which shows the histological section of an empty defect control sample from experiments of pSrBG scaffolds in large animal models. A further example is shown in Figure 7 (E-H), highlighting a histological examination after 6 weeks of implantation of BG45S5 and pSrBG in the animal models. In the macroscopic view, histological analyses show that there is new bone in the defects of pSrBG and BG45S5 treatment, which are characterized by the presence of bone cells, voids, bone marrow, and blood vessels [15]. The differences between pSrBG and BG45S5 can be seen in Figure 7, pSrBG performed 100% bone-to-material contact (without fibrous tissue coverage) and good formation of organized lamellar bone [15].

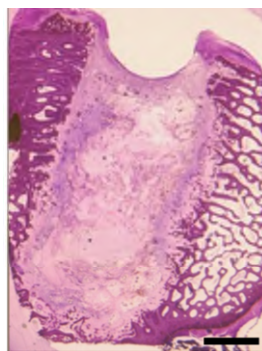


Figure 6. Histological section of an empty defect control from experiments of pSrBG scaffolds in large animal models, scale bar is 3 mm [15].

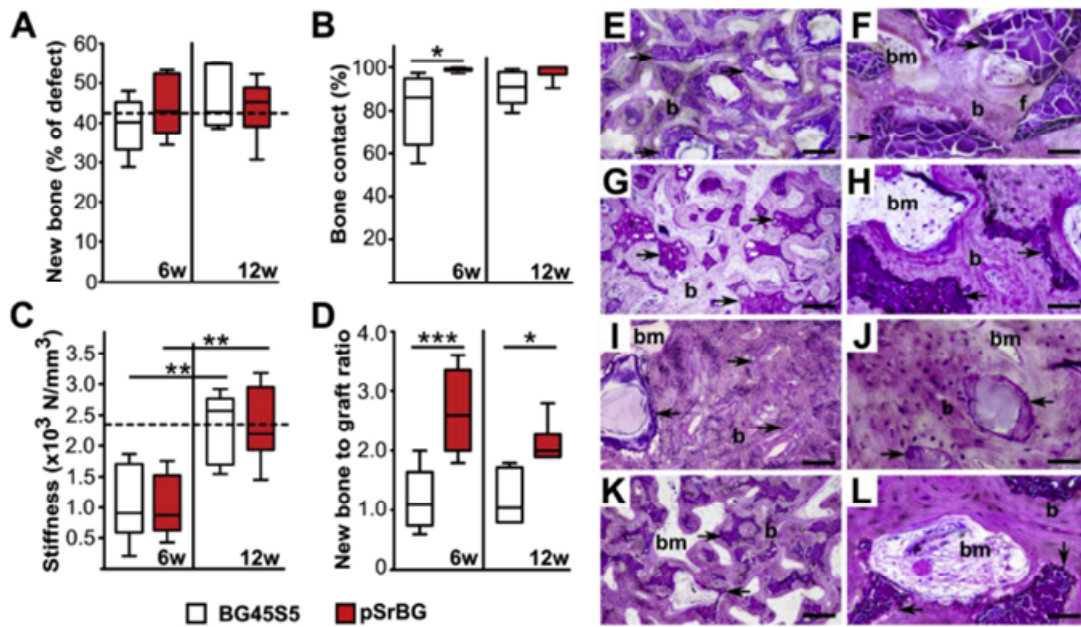


Figure 7. pSrBG exhibits enhanced osteoconductive properties and induces the formation of well-localized localized layered bone tissue. (A) Percentage of newly formed bone in defects treated with BG45S5 particles or pSrBG granules for 6 weeks and 12 weeks. The dashed line represents the median of the percentage of bone in non-defect areas ($n=19$). (B) Percentage of bone that contacts the remaining scaffold. (C) Local mechanical assessment of the defect sites performed by indentation testing. The dashed line represents the stiffness median of the control trabecular bone in BG45S5-treated animals at 12 weeks ($n=5$). (D) The ratio of newly formed bone to the remaining scaffold. The box plots represent the 5th to 95th percentiles. Asterisks denote statistically significant differences between indicated groups ($*p < 0.05$, $**p < 0.01$, $***p < 0.001$). In (A, B and D), at 6 weeks $n=5$ and at 12 weeks $n=6$, in (C) $n=6$ for both time points. (E–H) Histological examination after 6 weeks of implantation of BG45S5 (E, F) and pSrBG (G, H). (I–L) Histological examination after 12 weeks of implantation of BG45S5 (I, J) and pSrBG (K, L). Histology sections were stained with Toluidine Blue and Paragon. Arrows point at the remaining synthetic materials; b represents newly formed bone; bm represents bone marrow; f represents fibrous tissue. Scale bars in E, G, I, K are 300 μm ; scale bars in F, H, J, L are 60 μm [15].

2.5.2. Scanning Electron Microscopy (SEM), Focused Ion Beam (FIB), and Energy Dispersive X-ray Analysis (EDX).

SEM is commonly used for studying both the surface morphology and the cellular response to biomaterial [94, 95]. These techniques utilize a primary electron beam that interacts with a sample of interest in a vacuum environment, resulting in the emission of

different types of electrons and electromagnetic waves [86], such as secondary electrons ejected from the surface of the sample are collected and interpreted to provide a high-resolution photomicrograph. SEM imaging in Figure 8 indicates the cell attachment on the pSrBG scaffold after 7 days, showing good biocompatibility. In addition, backscattered electron SEM images of BG45S5 and pSrBG after 12 weeks of implantation (Figure 9), and focused ion beam milling and scanning electron microscopy (FIB-SEM) images of the interface between the scaffold and the newly formed tissue (Figure 10), suggest that there may be differences in the mechanism of bone formation or remodeling between BG45S5 and pSrBG and further confirm the finding of histological and histomorphometric measurements.[15]

EDX is an analytical tool for elemental analysis and chemical characterization. The analysis is performed by collecting X-rays emitted by the sample interaction with the SEM electron beam. Different elements emit different emission spectra, hence, it is possible to distinguish the different components contained in the sample by analyzing the X-ray spectrum [96]. EDX can give information on the bulk material and determine elemental distribution. Figure 11 (a) (b) shows the SEM images of an Sr50 disc samples with specific composition (SiO₂:49.47 mol%; P₂O₅: 1.07 mol%; CaO: 11.54 mol%; SrO: 11.54 mol%; Na₂O: 26.38 mol%) of Sr-substitute bioactive glass after SBF immersion from the research of Yann et al. [10]. In Yann's study, zone 1 indicates that the phase is rich in alkaline earth ions (Sr and Ca) and phosphorus, showing that it is a surface layer of apatite. Besides, the concentration of Sr and Ca in zone 1 is similar, which could indicate that the formation of HCA is formed by Ca and Sr from the original glass instead of SBF. Although the mechanism of HCA is still not clear, the occurrence of ion release and the existence of HAC layer formation can be confirmed by SEM/EDX.

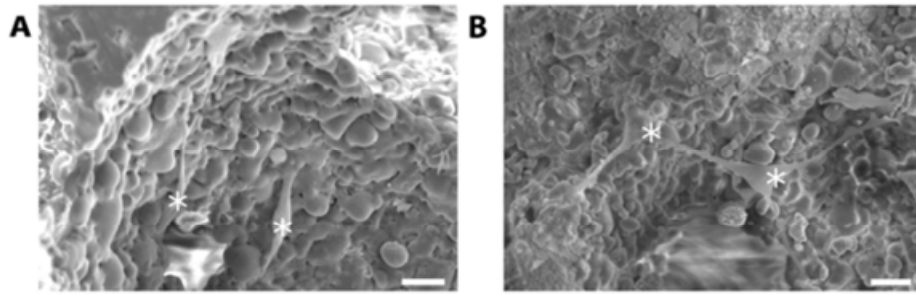


Figure 8. A & B, Cross-section SEM images of Human Mesenchymal Stem Cells (hMSC) onto pSrBG scaffold after 7 days. Asterisks: hMSC. Scale bars are 20 μm . [15].

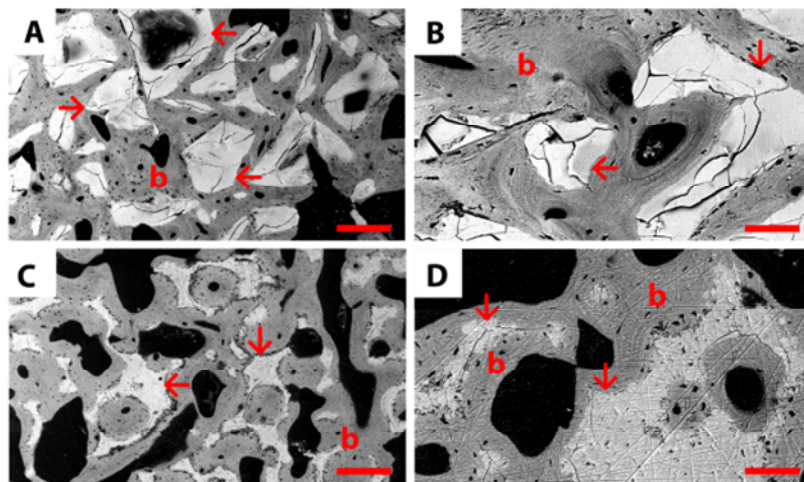


Figure 9. pSrBG induces the formation of well-organized lamellar bone tissue. Backscattered SEM images after week 12 of implantation of BG45S5 (A, B) and pSrBG (C, D). Arrows point at the remaining grafts; b represents new-formed bone. Scale bars in A, C are 270 μm ; scale bars in B, D are 80 μm [15].

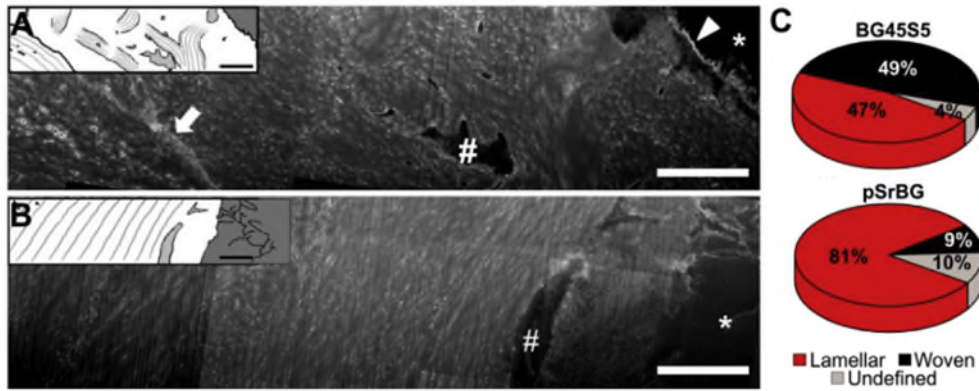


Figure 10. FIB-SEM investigations reveal that pSrBG promotes lamellar neo-bone at the bone/material interface at 12 weeks. (A-B) Broad cross-sections (compound images) through the interface between the implant particle on the right hand side and the newly deposited bone. (A) BG45S5 sample cross-section shows a broad intensively stained scalloped boundary (arrowhead) that separates the particles from bone containing chaotically oriented bundles. An irregularly shaped osteocyte lacuna can be observed in this region (#). Another interface (arrow) separates this presumably woven bone from parallel arrays of collagen, characteristic of lamellar bone. In pSrBG (B), collagen fibrils are deposited directly on the granule surface with no obvious non-collagenous interface. To the left of the osteocyte lacuna (#) bone matrix is organized in lamellar layers. Asterisks represent remaining inorganic materials. (C) Percentage of woven and lamellar bone at the material interface in ion-milled cross-sections from three pSrBG- and BG45S5-treated defect samples (2 or 3 cross-sections per sample). Scale bars are 5 μm [15].

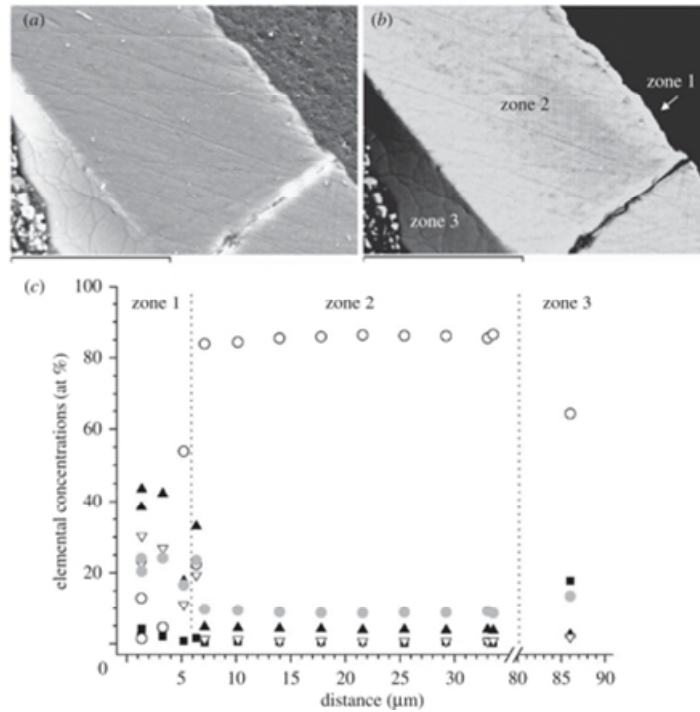


Figure 11. SEM–EDX analysis of a cross-section of Sr50 disc after 1 week in SBF: (a) secondary electron; (b) back-scattered electron images (scale bars: 60 mm); (c) atomic composition on a straight line from zone 1 (i.e. the glass/SBF interface) to zone 3 (i.e. the unreacted glass; filled squares, Na; open circles, Si; filled triangles, P; open inverted triangles, Ca; filled grey circles, Sr) [10].

2.5.3. Transmission Electron Microscopy (TEM)

Transmission electron microscopy (TEM) is a microscopy technique in which a beam of electrons is transmitted through a thin specimen to form an image [97]. The development of electron microscopy technology has enabled the detection of relatively high bone-implant interface resolutions, revealing some new details about these interfaces [89, 98]. TEM provides a suitable method for nanoscale imaging and chemical analysis with the possibility of electron tomography in both 2D and 3D. For example in Figure 12, TEM imaging showed that mineralized bone tissue was in direct contact with the laser-modified titanium-based implant surface [88]. In addition, high-resolution TEM images show lattice fringes in bone tissue near the surface of the titanium-based implant, indicating crystalline minerals, as shown in Figure 13 [89]. However, due to the

limitations of TEM for the determination of low Z elements, providing more detailed and reliable data of biomaterials rich in a bunch of low atomic mass elements (P, C, N, Cl, Mg, Ca, etc.) is still a challenge.

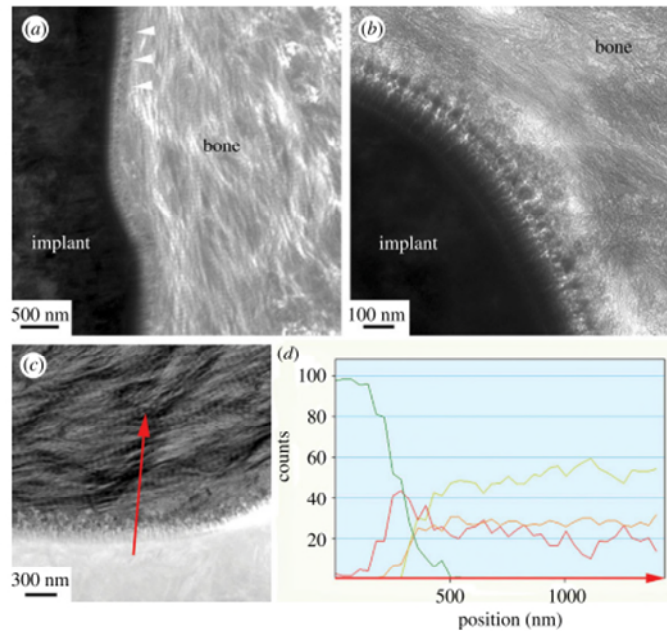


Figure 12. TEM of the laser-modified titanium-based implant surface and bone. Bone tissue was observed in intimate contact with the implant surface. (a) Characteristic collagen banding was observed close to the implant (white arrowheads). (b) Higher magnification of the interface shows the surface oxide and bone tissue. (c) HAADF-STEM micrograph with a corresponding EDS line scan (red arrow). (d) Element distribution where an overlap zone was observed with calcium (yellow) and phosphorus (orange) increasing simultaneously as titanium (green) decreased and oxygen (red line) peaked, indicating osseointegration on the nanoscale [88].

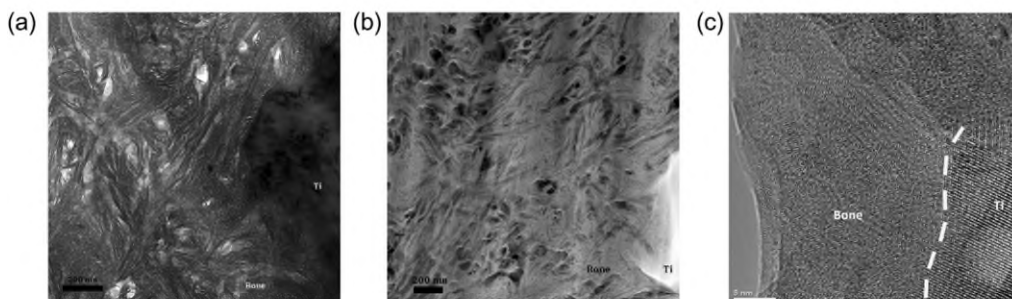


Figure 13. (a) High-angle annular dark field scanning transmission electron (HAADF-STEM) micrograph of the bone-titanium-based implant interface region. (b) Bright-field TEM image of the interface. (c) A high-resolution TEM image of (b) [89].

2.5.4. Raman Spectroscopy and Fourier Transform Infrared Imaging (FTIRI).

Raman Spectroscopy is a non-destructive chemical analysis technique that provides detailed information about chemical structure, phase and polymorph, crystallinity, and molecular interactions [99]. It is based on the interaction of light with the chemical bonds within a material. Typically a Raman spectrum is a distinct chemical fingerprint for a particular molecule or material, and can be used to very quickly identify the material, or distinguish it from others [99]. The use of Raman spectroscopy in biological research has several advantages [100]. Raman microscopy can detect samples in micrometers with little interference from water. Since the acquisition is obtained using reflective optics, there is no limit to the transparency or thickness of the sample. The main bands observed correspond to mineral and organic components in the tissue spectrum, respectively, and are clearly separated so that the two phases can be studied simultaneously in a non-destructive manner.

Raman spectroscopy and Fourier Transform Infrared Imaging (FTIRI) can be applied to see changes in phosphate distribution [46]. The Fourier transform infrared imaging (FTIRI) method is mainly used to obtain information on mineral maturity and the organic composition of mineralized tissues [101]. FTIRI determines is sensitive to several absorption bands of bone tissue, enabling: (i) estimating the relative amounts of minerals and organics; (ii) the stoichiometry of apatite minerals used to characterize mineral maturity; (iii) the relative carbonate content of hydroxyapatite - the second indicator of mineral maturity; (iv) the ratio of cross-linking to non-reducible/reducible collagen in the bone, and thus the maturity of the collagen [101]. Wu et al. also found the deposition of calcium phosphate and the formation of HCA by combining FTIR and XRD as shown in Figure 14 [84]. From Figure 14 (a), calcium phosphate deposition occurred

after 8 hours of immersion in SBF as the P-O bending zone first occurred. XRD results confirmed the P-O peak corresponds to HCA.

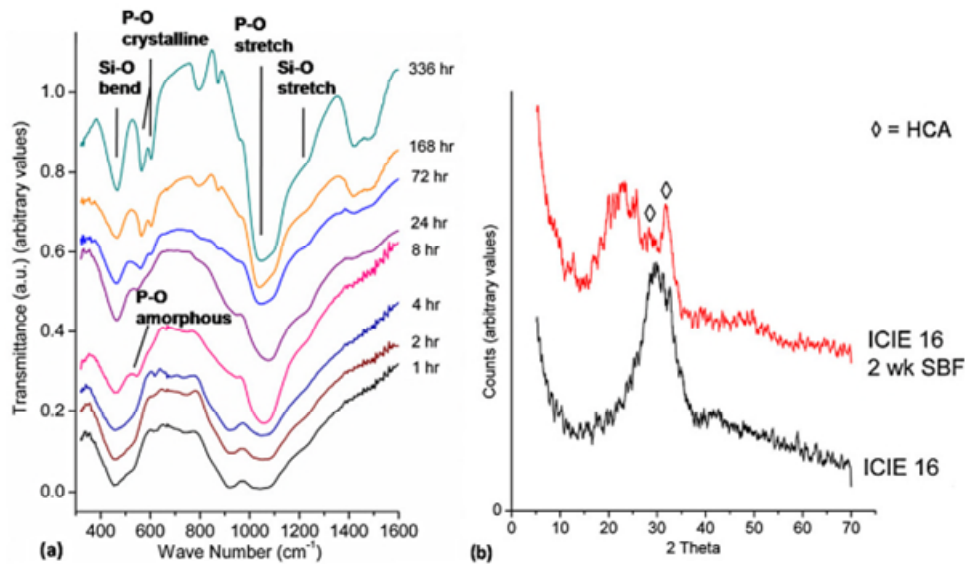


Figure 14. FTIR of the scaffolds immersed in SBF for up to 2 weeks, (b) XRD of the bioactive glass powder (<math><38\ \mu\text{m}</math>) before process and after immersion of the scaffold in SBF for 2 weeks [84].

2.5.5. X-ray Fluorescence (XRF) and Small Angle X-ray Scattering (SAXS).

XRF is a non-destructive analytical technique used to determine the elemental composition of a material. The XRF analyzer determines the chemical composition of a sample by measuring the fluorescent (or secondary) X-rays emitted by the sample as it is excited by the primary X-ray source. SAXS is an analytical technique that measures the intensity of X-rays scattered by a sample as a function of the scattering angle. Measurements are made at very small angles, typically in the range of 0.1 to 5 degrees. For example, Autefage et al. investigated the Sr release from a 3D strontium-containing BG (pSrBG) scaffold after 12 weeks of implantation using SAXS and XRF [15]. The changing concentration of Ca and Sr can be seen in Figure 15. SAXS results show that

the Sr in the pSrBG scaffold does not seem to affect the nanoscale characteristics of the bone apatite crystal. Results from XRF indicated the presence of Sr in both newly formed bone and residual material, but not in the trabecular bone near the defect, which may reflect that Sr is incorporated into bone apatite by replacing Ca ions with Sr ions in the bone formation process. Although the research confirmed the ion release from the implant materials and the existence of Sr in new-formed bone, it is unable to specify the locality of released ions and the mechanism of Sr uptake into the bone and bone repair.

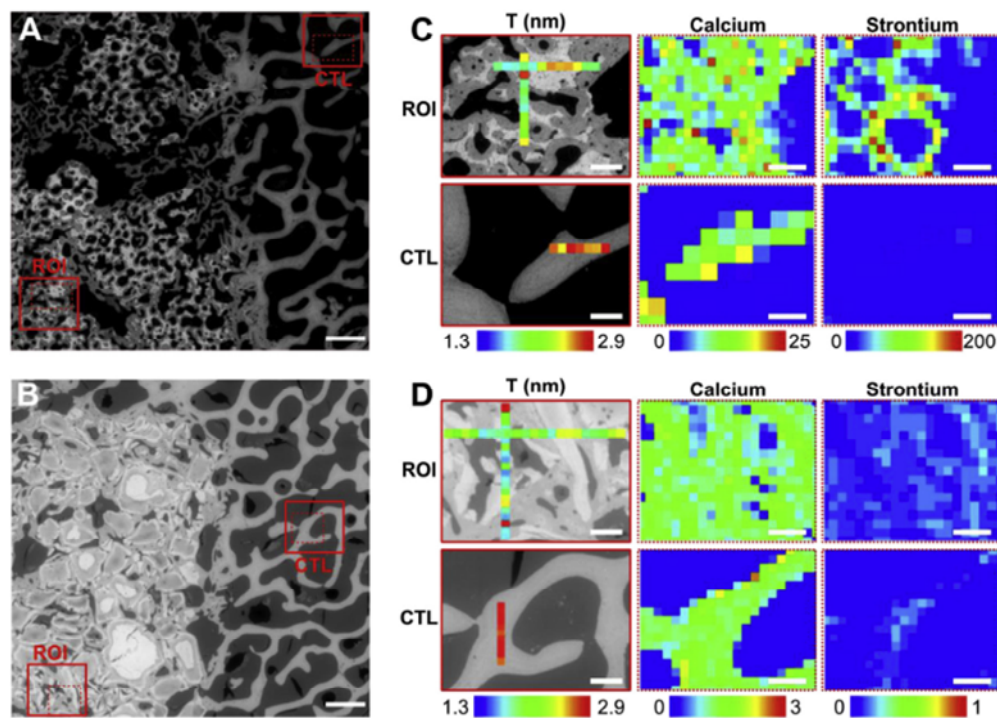


Figure 15. The pSrBG-released strontium incorporates into the neo-bone exclusively and promotes native-like bone mineral crystal thickness. (A–B) Environmental scanning electron microscope (ESEM) image of (A) pSrBG- and (B) BG45S5- treated defect at 12 weeks showing the regions of interest (ROI) and control (CTL). (C–D) SAXS measurement of T-parameter (average thickness of the mineral crystals) (left) and XRF reading (right), showing the localization of strontium and calcium ions, in the defects treated with (C) pSrBG and (D) BG45S5. Scale bars in (A, B) are 1 mm; scale bars in (C, D) are 250 μm for T-parameter (left) and 200 μm for XRF reading (right) [15].

2.6. Limitation of Biomaterials Analysis and Developing Atom Probe Tomography (APT) for Biomaterials

Although the new generation of biomaterials is becoming more and more complex, their development is still largely based on empirical methodologies [102]. The subtle interactions between materials and biology at the atomic level are unclear. For example, the understanding of interface structure, chemical composition, and bonding is very limited [26]. The common use of Raman spectroscopy and Fourier transform infrared spectroscopy for biomaterials are normally limited at the molecular level [103]. Some researchers have shown that Focused Ion Beam (FIB) continuous sectioning represents another potential 3D imaging of bone structure, however current studies have reported demineralized bone tissue, and this method is limited to the resolution of SEM [103, 104]. Although the recent development of STEM or EDX has made progress in atomic resolution element mapping, the spatial resolution and chemical sensitivity in the analysis of biominerals are still greatly limited due to the fact that these materials are sensitive and easy to damage by the applied electron beam [21]. In addition, conventional electron probe microanalysis techniques have limitations in the determination of low-Z elements such as C and N [105], which are abundant in biological materials. As previously mentioned, testing of the new 3D strontium-containing BG (pSrBG) scaffold shows a near-perfect bone contact can be achieved [15]. However, it is unable to specify the locality of released ions, and the mechanism of Sr uptake into bone and bone repair remains inconclusive. Also, in other research such as the *in vitro* study by Gentleman et al. [79], Sr released from bioactive glasses can be observed, but it is unclear what the total percentage of Sr is released from the glass. To specify and analyze individual elements from "structural" compositions such as ceramics is difficult.

Atom Probe Tomography (APT) underpins the research and development of a

wide range of materials and devices [106]. APT is a technique for a highly magnified analysis of chemical identities and 3D positions of atoms within an extremely small volume of material [23]. APT has a higher spatial resolution than SIMS and other technologies and is equally sensitive to the detection of all elements [107]. APT is based on the phenomenon of field evaporation, in which ions successively desorb from a micro-tip surface in the presence of an intense electric field. These ions are then collected by a lateral (x, y) position-sensitive detector. The z-coordinates of the ions can be determined by the sequence of ion arrivals at the detector, while measurement of the ion flight times enables them to be determined using time-of-flight mass spectrometry, enabling chemical identification [108, 109]. The results can be reconstructed to provide a 3D model of the analyzed volume with sub-0.3nm spatial resolution and parts-per-million (ppm) chemical sensitivity [110]. Figure 16 shows the analytical sensitivity and analytical volume of APT compared to other characterization techniques [111].

Traditionally, field evaporation in APT was triggered by a pulsed electric field which required the sample to have good electrical conductivity and reasonable ductility (e.g. metal alloys), limiting its application [110]. However, the development of laser pulsing technology has expanded the applicability of APT to almost all dielectric materials, including a limited range of biological minerals such as bone-type material [21, 25, 112, 113], chiton tooth [26], rodent tooth enamel [27, 98, 114], dentin and Ti-based implants interface [89, 115], and individual proteins [116]. The first detailed APT research of apatites and biominerals was pioneered by the Joester Group at Northwestern University. Research developing APT for analysis of hydroxyapatite, elephant dentin, rat femur cortical bone, and dental enamel have reported by them [21, 26, 27, 98], demonstrating APT as a potentially powerful characterization technique for bone-like materials and biominerals. For example, Figure 17 shows the 3D reconstructions and

proximity histograms of the fiber–the mineral interface of the chiton tooth generated by APT [26]. The unique APT mass spectral fingerprints of different synthetic and geological apatites are shown in Figure 18 [21], and the mass spectra of biomaterials are complicated and hard to identify. Compared to other materials like metal, existing studies have underlined the complexity of accurately identifying the multiple peaks present in the mass spectrum, which currently causes issues for fully quantitative analyses for biomaterial.

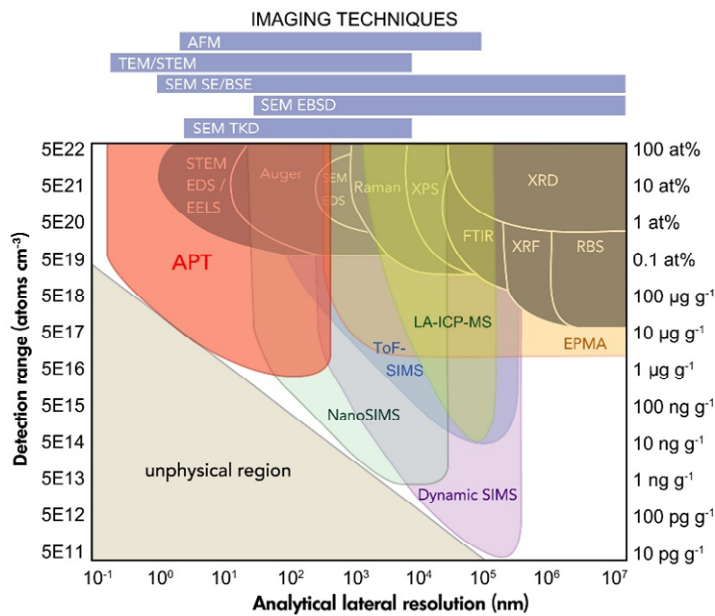


Figure 16. Analytical sensitivity versus analytical volume for APT compared with other characterization techniques [111].

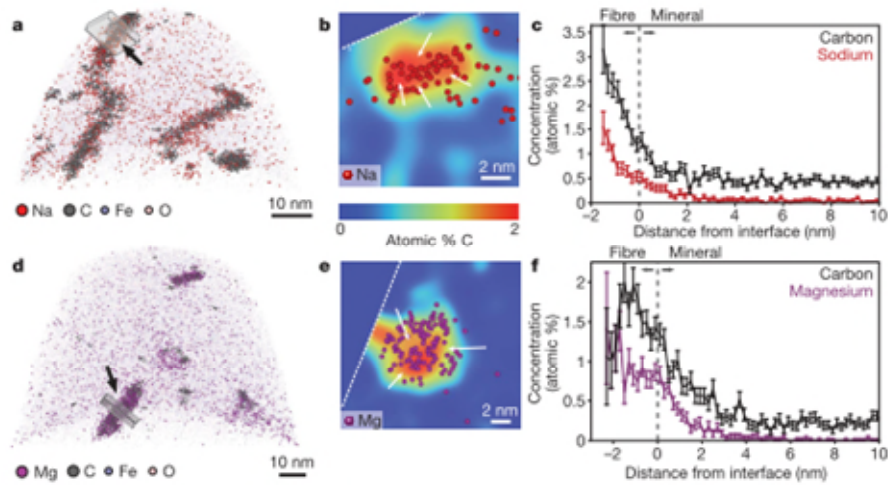


Figure 17, APT 3D reconstructions and proximity histograms of chiton tooth. (a), (d), Two representative samples containing organic fibers that exclusively bind Na^+ (a-c) or Mg^{2+} (d-f). For clarity, only about 5% of the Fe/O ions are rendered; the edge of the field-of-view is marked (dashed line in b). (b), (e), Overlay of Na^+ (b, red spheres) and Mg^{2+} (e, magenta) ion positions on carbon concentration maps integrated over the boxed regions indicated in (a) and (d). Some regions of the fibers appear devoid of Na or Mg (arrows). (c), (f), Proximity histograms (error bars, $\pm 1\sigma$) of Na/C (c) and Mg/C (f) across the organic–inorganic interface of fibers indicated by arrows in (a) and (d). Interfaces appear graded over 2–4 nm [26].

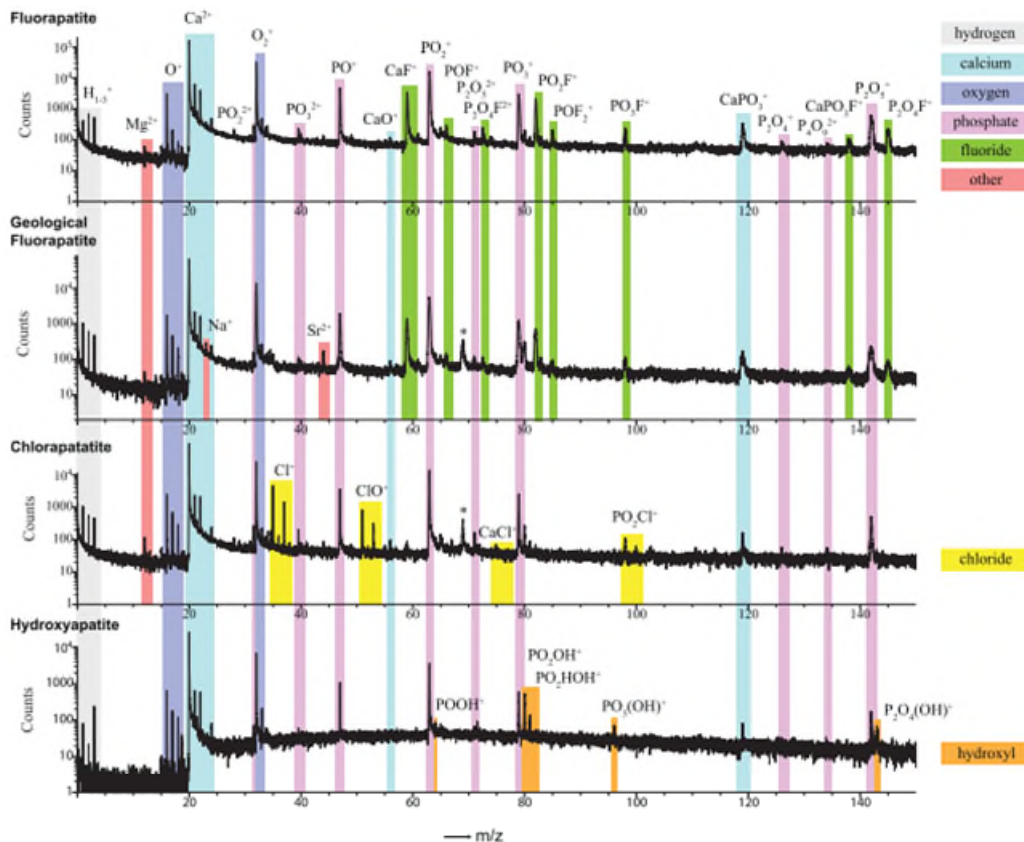


Figure 18. APT mass spectrums of synthetic and geological apatites [21].

APT applied to research of the bone-implant interface can provide an unprecedented resolution into implant interfaces, and provide important insight into the mechanisms behind osseointegration. By combining the structure and topographical information provided by electron microscopy with atomic resolution 3D chemical analysis by APT, a higher level understanding and characterization of the organic-inorganic interface of the implants can be revealed [117]. For example, Johan and Gustav's research of the bone-implant interface of dental titanium-based implants in humans on the atomic scale by APT shows the distribution of different atoms at the interface between implants and living tissue [89, 115], which both indicate there is a direct contact between the titanium oxide surface of the implant and Ca of bone minerals (Figure 19). Figure 20 shows the SEM images of the *in vivo* healing and of the tip geometry together with the APT analysis, the contact of minerals and titanium oxide is evident at the atomic scale, and the bone near the implant has a higher Ca / P ratio than a few hundred nanometers into the tissue [89].

The low detection limit of APT opens up new areas of characterization possibilities for biomaterials [118]. However, the development and application of APT in the biological field are still in their infancy. The application of APT to the analysis of biomaterials and the study of the organic-inorganic interface is considerably complicated. There are significant challenges to not only undertaking successful experiments but also maximizing the quantity and accuracy of the information that can be extracted from the data. For example, the APT specimen preparation for a biomaterial is a big challenge [119]. The specimen for APT requires a very sharp needle shape, with a hemispherical apex of radius less than 100 nm [106]. An APT experiment only runs the first 50-200 nm below the apex instead of the entire specimen length, so a feature of interest must be precisely located at the tip of the specimen for the characterization [106]. However, the

complex hierarchical microstructure of many biomaterials complicates the identification, and isolation of nanoscale regions of interest for incorporation into the specimen. Furthermore, a biomaterial specimen is often brittle [120], and given a huge electrostatic pressure when APT applies a high voltage to a very-fine specimen. It is easy to fail under the electric field (fails early before yielding information). In addition, other challenges such as parameterizing the APT experiments, interpreting the complexity of biomaterial mass spectra including peak overlaps, and understanding the reproducibility and accuracy of the 3D atomistic reconstructions, limit the current growth of the application of APT to biomaterials.

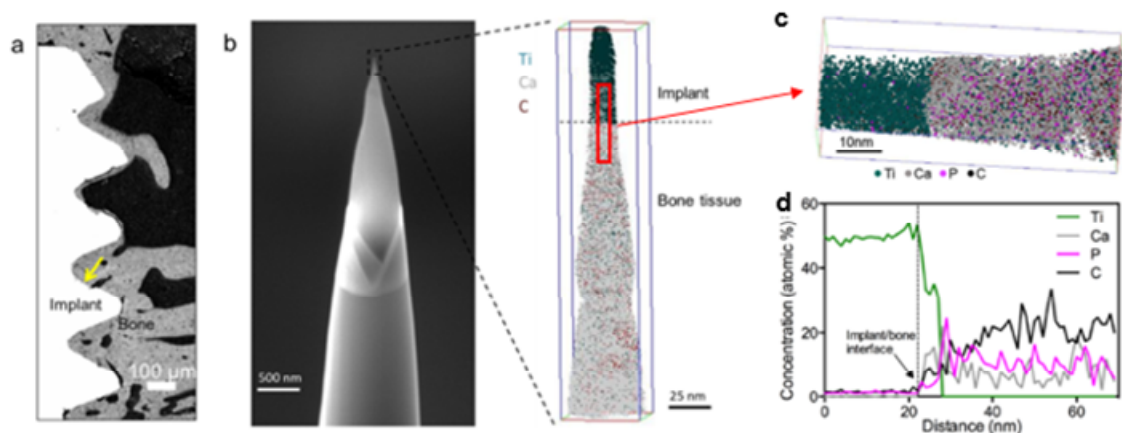


Figure 19. SEM images of the in vivo healing and of the tip geometry together with the APT analysis, the implant is a mesoporous titanium oxide-coated implant. (a) Backscattered SEM image of the implant in bone retrieved after 4 weeks of healing. The arrow indicates the interface between the implant and the surrounding bone tissue from where the liftout was extracted. (b) SEM image of the sharpened tip, together with the APT reconstruction, in which the Ti-containing ions are displayed in dark green, Ca-containing ions are gray, and C-containing ions are brown. (c)-(d) 3D reconstruction of the implant–tissue interface and 1D concentration profiles. (c) APT image displaying the direct contact between Ca of the bone mineral and Ti of the coating surface. (d) 1D concentration profiles of Ti, C, Ca, and P from the coating and across the interface into the bone tissue, were obtained from the reconstruction in (c) [115].

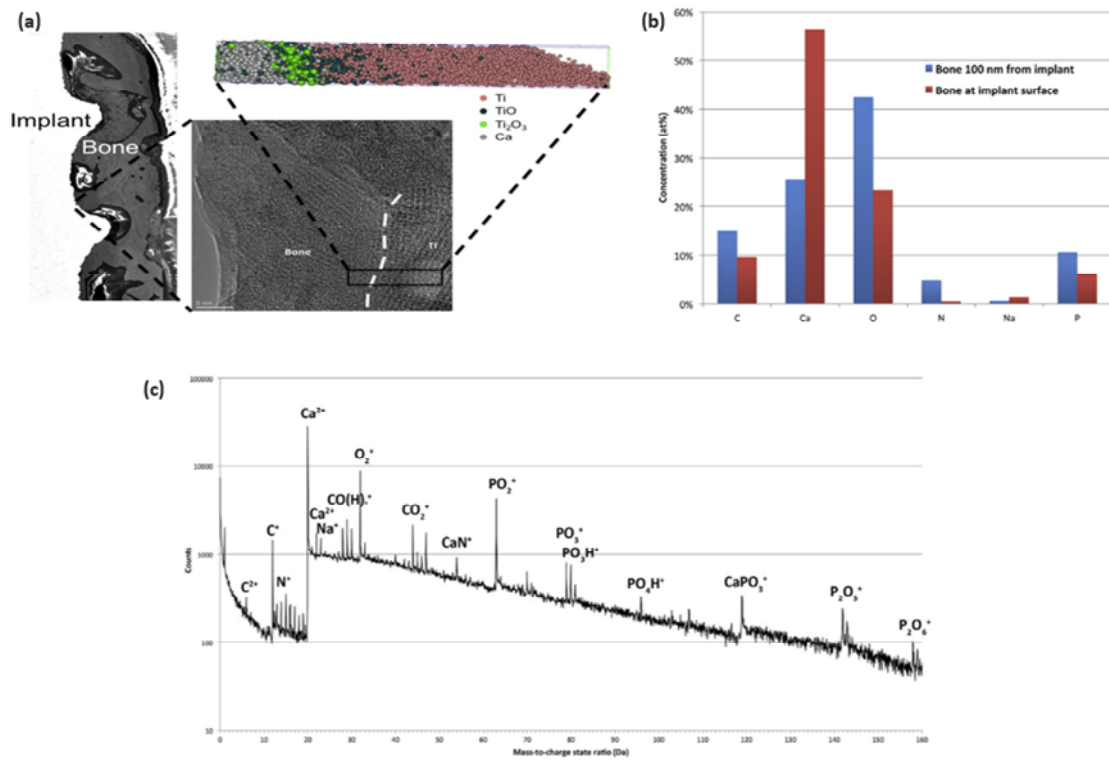


Figure 20. (a) SEM images of the in vivo healing and TEM of the interface together with the APT analysis. (b) Comparison of the composition in the bone tissue 100 nm from the implant and the bone tissue directly at the implant surface. (c) Atom probe mass spectrum retrieved from bone analysis approximately 100 nm from the implant surface. Major peaks in the spectrum are labelled [89].

As discussed before, the new bone formed with the new 3D strontium-containing BG (pSrBG) scaffold was analyzed using conventional histological analyses, in addition to Raman spectroscopy, X-ray crystallographic analyses, and FIB-SEM [15]. Despite these exciting data, more atomistic analyses using APT of Sr ion distribution in newly formed bone and its influence on material properties would be greatly informative to evaluate this new biomaterial candidate and would provide a step-change in the way bone-biomaterial interfaces can be evaluated. These new data can inform on the kinetics of material degradation/dissolution and release of Sr (and other) ions and subsequently influence the effect on neo-bone. By combining APT with other techniques, there is the potential to better understand the complex processes that occur at the smallest-scale

implant interfaces, leading to an increasingly comprehensive understanding of materials across multiple length scales.

2.7. Summary

This chapter summarized the background knowledge of bone biology, bone fracture, bone regeneration, bone grafting, and bone substitutes. This chapter reviewed current methods for characterizing biomaterials and organic-inorganic interfaces and discussed recent research on Atom Probe Tomography of biomaterials. The feasibility of using APT to characterize the novel biomaterials of pSrBG, animal bones, and organic-inorganic interfaces was proposed. This chapter provides a theoretical basis for the follow-up experiments of this project.

Chapter 3

Experimental Procedures

3.1. Introduction

The purpose of this chapter is to introduce the materials, techniques, and methods used in this project. The basics and details of 10% and 100% strontium-containing bioactive glass particles, strontium-releasing bioactive glass-based (pSrBG) scaffolds, and porcine trabecular bone are summarized. The basics of used EM techniques and APT are introduced. Sample preparation methods for biological materials for APT are outlined, and the APT data analysis methods used in this project are summarized.

3.2. Materials

3.2.1. 10% and 100% Sr Containing Bioactive Glass Particles (BG-Sr10 and BG-Sr100)

Glasses (BG45S5) were made via the melt-quenching route [15]. To produce these, silica (99.8%, Tarmac Ltd. or High Purity, Prince Minerals, Stoke-on-Trent), calcium carbonate (all $\geq 98\%$, Sigma Aldrich, UK), magnesium oxide, sodium carbonate, calcium phosphate, strontium carbonate, and potassium carbonate were mixed according to their molar percentage, melted (1200–1400 °C) and quenched in deionized water to produce a frit. The frit was dried at >100 °C then ground with a Jet Mill (Hosokawa Micron Ltd

Runcorn, UK). Particles were sized by sieving. This BG45S5 glass without Sr addition is labelled as Sr0, which composition is 46.1 mol% SiO₂, 24.4 mol% Na₂O, 2.6 mol% P₂O₅ and 26.9 mol% CaO.

The Sr-containing bioactive glass particles of BG-Sr10 (Figure 21) and Sr100 were produced by replacing 10 mol% or 100 mol% of the calcium ions within the original BG45S5 composition with strontium BG-Sr0 (

Table 2). BG-Sr10 (46.1 mol% SiO₂, 24.4 mol% Na₂O, 2.6 mol% P₂O₅, 24.2 mol% CaO, 2.7 mol% SrO), and BG-Sr100 (46.1 mol% SiO₂, 24.4 mol% Na₂O, 2.6 mol% P₂O₅, 26.9 mol% SrO) were prepared using SiO₂ (99.8%; Tarmac Ltd), Na₂CO₃, Na₃P₄O₁₄, CaCO₃, and SrCO₃ (all >99%; Sigma-Aldrich) as precursor materials. Precursor materials were mixed, melted at 1,400 °C for 90 min, and cast into distilled water allowing the formation of a frit. The frit was collected in a sieve and allowed to dry at 150 °C for 1 h before milling. Glass particles of 0.1–1.0 mm were selected. The composition (at %) of BG-Sr10 and BG-Sr100 bioactive glass particles that were investigated in this thesis are shown in Table 3.

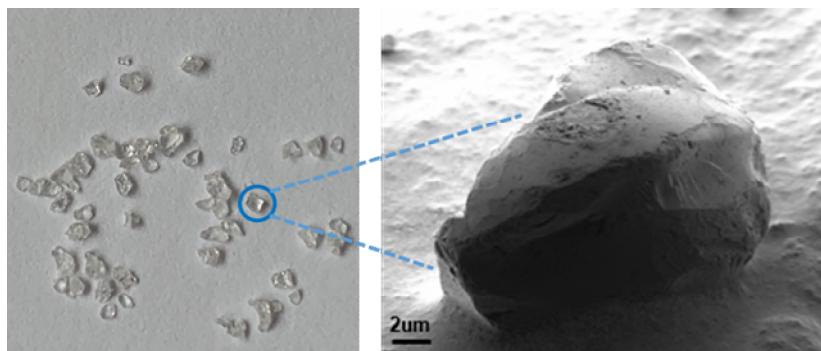


Figure 21. BG-Sr10 and its SEM image.

Table 2. Compositional comparison of BG-Sr10 and commercial bioactive glass 45S5.

Oxide	BG-Sr10	BG (45S5)
Na₂O	21.83	24.50
SiO₂	48.53	45.00
CaO	21.70	24.50
SrO	3.75	0
P₂O₅	6.05	6.00

Table 3. BG-Sr10, BG-Sr100 and pSrBG sample compositions in at%. Nominal compositions were provided by The Stevens Group from Imperial College London.

Atomic%	O	Si	Na	Ca	P	Sr	K	Mg
Sr10	55.203	16.261	17.213	8.540	1.834	0.949	0	0
Sr100	55.203	16.261	17.213	0	1.834	9.490	0	0
pSrBG	59.084	16.170	2.907	6.468	3.270	6.468	2.907	2.725

3.2.2. Sr-releasing Bioactive Glass-Based (pSrBG) Scaffold

For pSrBG processing, a glass composition of 44.5 mol% SiO₂, 4 mol% Na₂O, 4 mol% K₂O, 4.5 mol% P₂O₅, 17.8 mol% CaO, 17.8 mol% SrO, 7.5 mol% MgO was used and porous scaffolds were made by a gel-cast foaming technique, with a glass slurry produced (using particles < 38 μm), foamed with a surfactant and gelled by in situ polymerization [84]. The polymer was then removed by thermal decomposition immediately prior to sintering. More preparation details can be found in Zoe's research [84]. These scaffolds were characterized by X-Ray Diffraction, X-Ray Fluorescence (XRF), Mercury Intrusion Porosimetry and X-Ray Microtomography (μCT) Analyses. In

vitro and in vivo studies were conducted on the material whose production was up-scaled at a ratio 1:5 [15]. The resulting up-scaled sintered pSrBG scaffolds were then ground using a Kek cone mixer (Kemutec, USA) to give granules of sizes 1–3 mm. The SEM image and composition (at %) of pSrBG scaffold that is investigated in this thesis can be found in Figure 22 and Table 3.

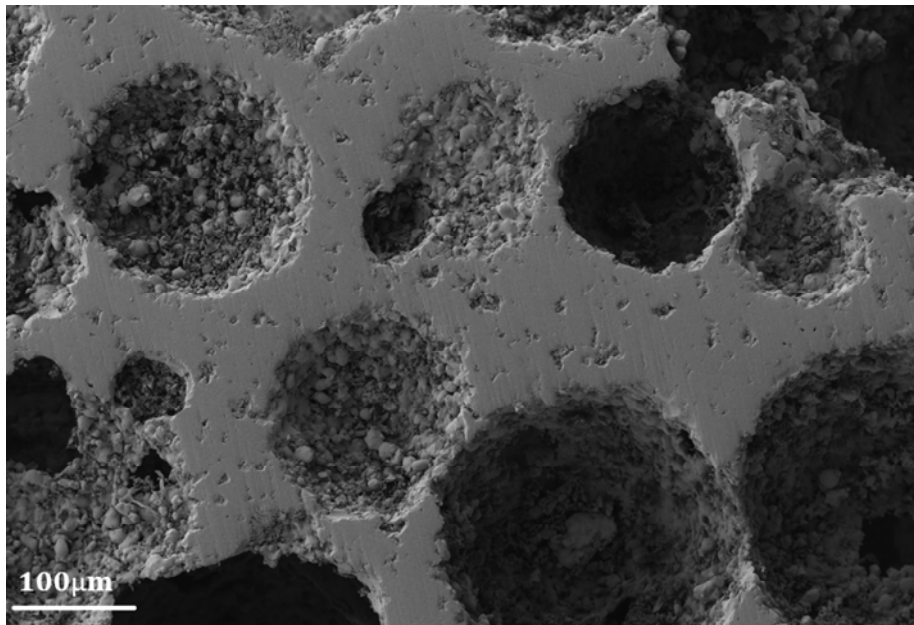


Figure 22. SEM image of pSrBG scaffold.

3.2.3. Porcine Trabecular Bone

Trabecular bone, also called spongy bone, is highly vascularized and characterized by a largely porous structure. Compared to cortical bone, trabecular bone is lighter, less dense, and more elastic, but cannot support large compressive stresses [121], and the schematic of different hierarchies of cortical and trabecular bone is shown in Figure 23.

The porcine donor bone employed in this thesis was received from the Department of Biomaterials, Imperial College London. This porcine bone donor is around 6 months of age without gender characteristics. Trabeculae bone is extracted from whole bone, fixed in 4% paraformaldehyde (PFA), dehydrated in a graded series of ethanol, defatted and dried. Figure 24 shows SEM images of the porcine trabecular bone sample.

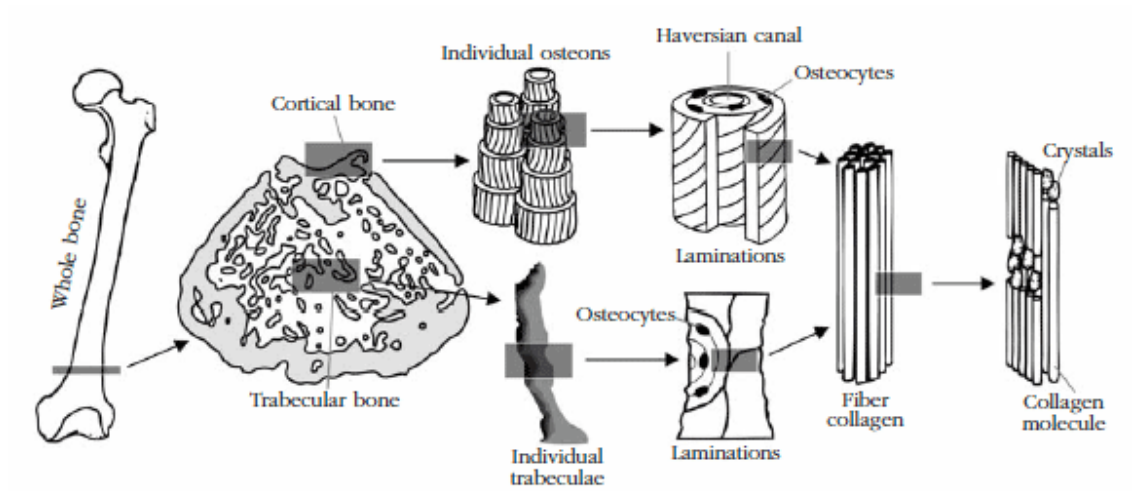


Figure 23. Schematic of different hierarchies of cortical and trabecular bone [122].

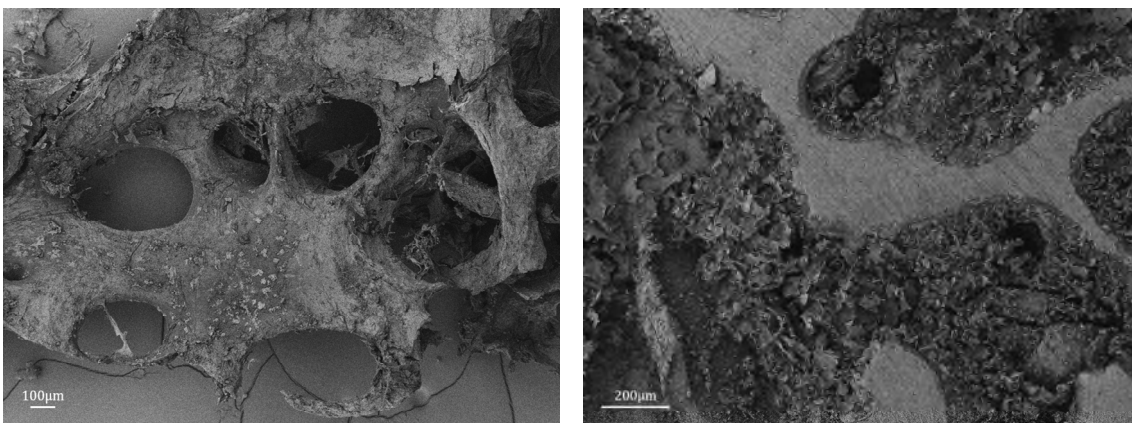


Figure 24. SEM images of the porcine trabeculae bone.

3.3. Electron Microscopy

Conventional Light Microscopy (LM) has many advantages in studying cellular structure and function, and specimen preparation are relatively simple and inexpensive. However, due to the limited resolution of LMs, Electron Microscopy (EM) is an irreplaceable option for investigating the ultrastructure of samples of interest [123].

Sample Coating. Before Scanning Electron Microscope (SEM) imaging or other Electron Microscopy, samples were secured to a silicon stub with silver conductive paint, coated with 15 nm of Pt in a sputter deposition system (Leica ACE600 Coater), with the coating layer in contact with both the sample and silicon stub.

3.3.1. Scanning Electron Microscopy (SEM)

Scanning Electron Microscopy (SEM) can study the surface or near-surface structure of bulk samples and is often used to study the surface morphology of biological materials and the response of cells to biological materials[95]. These techniques use a primary electron beam to interact with a sample of interest in a vacuum environment, emitting different types of electrons and electromagnetic waves [86]. The two most common electronic signals are secondary electrons and backscattered electrons. Secondary electrons are generated as a result of the electrons in the atoms being excited by the collision of the primary electron beam with the atoms in the sample [124]. These low-energy secondary electrons can provide high spatial resolution, and topographic information, and are often used as imaging signals [125]. Backscattered electrons originate from the primary electron beam electrons and are a fraction of the incident electrons bounced back by nuclei in the sample, electrons scattered back into the direction

of the incident beam at large angles, and losing energy with each scattering [124]. Backscatter analysis imaging has low resolution but the range produced in the sample is large, which can provide crystallographic and some compositional information [125]. Figure 21, Figure 22, and Figure 24 show the basic topography of different biological samples. Since biological samples are electron beam sensitive, the SEM images in this thesis were taken using a working distance of 5 mm and low voltages (≤ 3 kV) and currents (≤ 500 pA), unless otherwise stated.

3.3.2. Electron Probe Micro Analyzer (EPMA)

The Electron Probe Microanalyzer (EPMA) was conceived by Raymond Castaing in France in the late 1940s. EPMA is an instrument that analyses the elements that make up a substance by shining an electron beam onto the surface of the substance and measuring the characteristic X-rays produced [126]. Electrons emitted from the electron source are accelerated at a certain accelerating voltage and collimated by an electron lens, and when this electron beam hit the sample, the sample produces X-rays. By dispersing this X-ray using a dispersive element, the composition of the micro-area sample can be examined. This type of spectrometer is called a wavelength-dispersive X-ray spectrometer (WDS) [127]. EPMA enables on-site analysis, which is possible to directly analyse small areas in a large sample without removing the analyte from the sample. EPMA combines electron microscopy with electron probes, combining observation of microstructure and analysis of elemental composition. This technology is widely used in basic research in various fields such as steel, minerals, semiconductors, ceramics, textiles, medical and dental materials, medicine and biology, as well as product research and quality management [126]. In this thesis, Sr10 was analysed by EPMA to preliminarily

determine its composition, and compared it with the nominal composition from the supplier.

3.4. Atom Probe Tomography (APT)

Atom probe tomography (APT) is an analytical technique that enables simultaneous nanoscale chemical analysis and spatial mapping of individual atoms. [106]. The spatial resolution of APT is highly anisotropic, with resolutions up to about 0.1-0.3 nm in depth and about 0.3-0.5 nm in lateral [128]. Different from conventional techniques like TEM, APT is able to provide quantitative chemical compositions and 3D space imaging across the entire periodic table (same sensitivity independent of atomic mass).

3.4.1. Basic Principles

APT is based on the phenomenon of field evaporation, in which ions successively desorb from a needle-shaped specimen surface in the presence of an intense electric field [129]. The formula for surface electric field estimation (F) is:

$$F = \frac{V}{k_f R}$$

Where V is the applied voltage, k_f is the geometric field factor specifying the shape of the tip, and R is the radius of curvature of the sample [106]. The schematic illustration of APT is shown in Figure 25. A very sharp (tip radius less than 50 nm) needle-like sample is placed in an ultra-high vacuum chamber (10^{-8} Pa - 10^{-9} Pa) with cryogenic temperature (20 K - 80 K) [106, 130]. The specimen is fixed in front of the counter electrode, a DC voltage (1 kV - 10 kV) is connected to the specimen to generate the desired electrostatic

field, and ion evaporation is induced by superimposing a voltage pulse or laser pulse on the specimen [106, 111, 130]. It is generally believed that only atoms at the surface of the tip are affected by the field evaporation process, which occurs almost atom by atom and layer by layer [106]. The tip radius is gradually increased as the experiment progresses, and the magnitude of the voltage is continuously increased to maintain the electric field required to evaporate ions [131, 132]. The evaporated ions are collected by a Position Sensitive Detector (PSD), which records the time and location their hit the detector [133]. From the recorded information, the m/q ratio (mass-to-charge ratio) can be determined by measuring the time-of-flight of the ions and allowing the chemical identification of each atom. The original position of the atoms on the tip can be reconstructed by measuring the X-Y position and the order of arrival of the ions at the detector [134]. After data collection, the Integrated Visualization and Analysis Software (IVAS 3.8.8) or Atom Prober's Toolkit (AP suite 6.1) are applied to reconstruct the data by using a reverse-projection algorithm. Based on the point projection model [131], IVAS uses a more advanced derivation algorithm without making a small angle approximation [135]. By combining the chemical and positional information of ions, a three-dimensional positional map of contained atoms in the specimen is obtained.

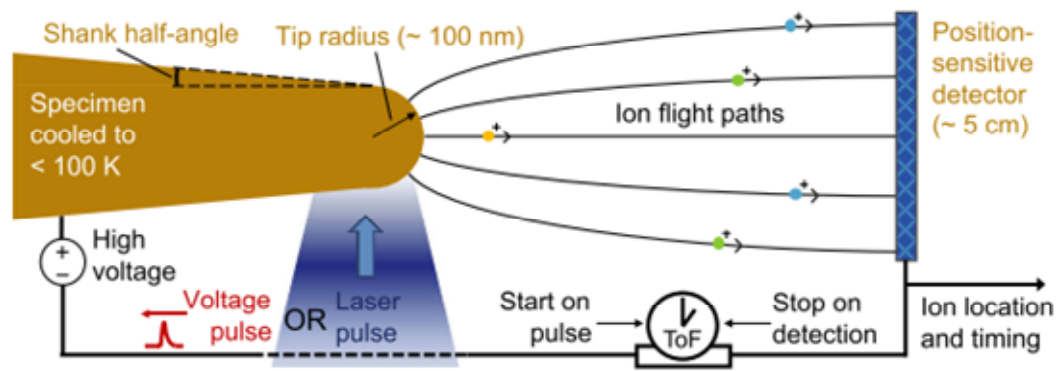


Figure 25. The schematic illustration of APT, including two operating modes of the voltage pulse and laser pulse [111].

The main models of the field evaporation process were originally developed for metals, and the APT of high-voltage pulses is usually unable to provide adequate experimental conditions for non-conductive materials [130]. With the addition and development of laser pulse functions, APT can be applied to almost all materials, including biological and geological materials that are gaining increasing attention. The physical mechanism of field evaporation in pulsed laser atom probes has been controversial. The widely accepted explanation today is that field evaporation is thermally activated, where the light of the laser pulse is absorbed by the sample, causing an increase in its surface temperature, and triggering the field evaporation [106]. In contrast to metal materials, low/non-conductive materials have a high proportion of multiple hits, which means the detection of more than one ion following a single high voltage or laser pulse [130, 136]. These multiple events may have two origins. First, after surface ions evaporated, the charges on the surface rearrange to keep the screening of the electrostatic field, which leads to rapid field evaporation of neighbouring atoms, which occurs more in samples with poor conductance, and differences in carrier density and mobility may

explain this difference [130]. Second, the high proportion of molecular ions in low/non-conductive materials also increases the likelihood of dissociation, contributing to multiple events [130]. In addition, a high proportion of complex molecular ions can lead to complex mass spectra containing many overlapping peaks. Therefore, more careful consideration should be given to mass spectral interpretation and overlapping peak analysis of low/non-conductive materials.

3.4.2. Specimen Preparation

All needle-shaped atom probe tips with a radius of <100 nm were prepared by using a gallium source FIB/SEM liftout method which is largely based upon established procedures [137, 138], and made some small improvements which will be described in detail in Chapter 4. Two dual-beam SEM/ FIB instruments of Zeiss NVision 40 and Zeiss Crossbeam 540 were used. The samples were all sputtered with 15 nm of platinum as a surface coating prior to SEM/FIB procedures. The key steps and parameters used to prepare specimens in this thesis are summarized in Figure 26 and described below.

As biomaterials are beam sensitive, 2-3kV accelerating voltage was used for sample imaging by SEM. A protective strip of tungsten/ platinum layer was deposited on the region of the interest ($2 \times 22 \mu\text{m}$) before milling using the FIB ion beam (30 kV, 80 - 100 pA) as seen in a). A cantilever was produced with a square cross-section below the tungsten rectangle and was cut free on three sides (30 kV, from 3 nA to 700 pA as the protective strip approaches, and 700 pA for undercut milling) as shown in b) and c). During the liftout, an in situ nano-manipulator was used to approach one side of the cantilever, then adhering by depositing tungsten between the mini gap of the cantilever

3: Experimental Procedures

and nano-manipulator (30 kV, 80 -100 pA) as seen in d). The cantilever was cut free from the opposing edge (30 kV, 700 pA) and liftout from the bulk sample. 1-2 μm wide segments were subsequently mounted and then detached from this wedge onto a standard Si post microarray (Cameca Instruments) as shown in e) and f). Each segment was individually shaped and sharpened into a needle using annular milling patterns of decreasing inner diameter. This was commenced from 30 kV, 700 pA until the needle diameter was around 1 μm , then changed to 30 kV, 300 pA to sharpen the needle to around 200-300 nm, before 30 kV, 50-100 pA was used to further sharpen to <100 nm in diameter. Finally, by reducing the accelerating voltage to 2 kV, 200 pA, the remainder of the tungsten protection layer and any potentially damaged material at the tip surface was carefully polished away as the resulting needle shown in h).

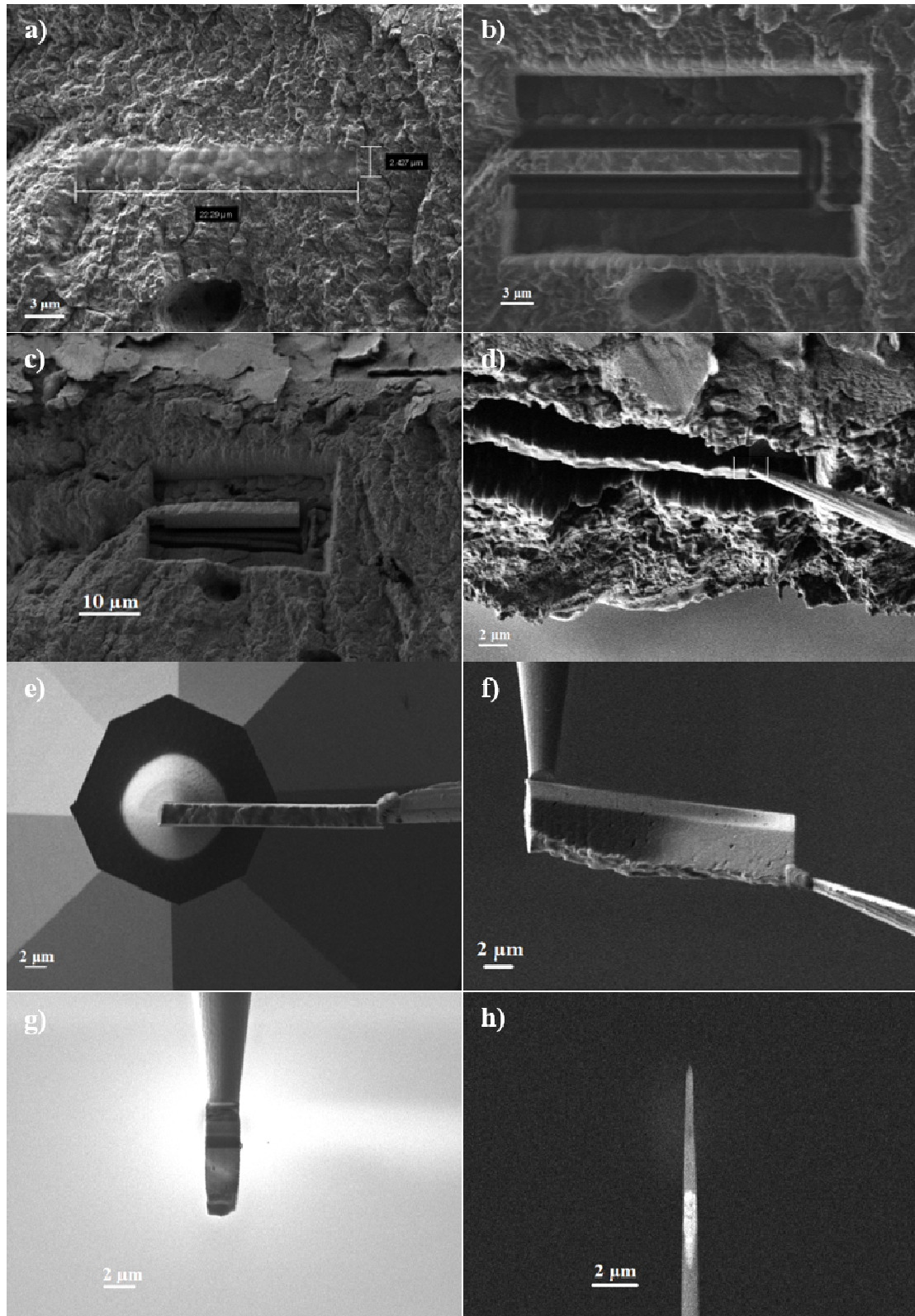


Figure 26. SEM and FIB APT specimen preparation of porcine bone.

3.4.3. Limitations and Challenges

Every powerful technology has certain limitations. When developing APT for extremely challenging biological materials, the limitations and challenges that may face must be considered. First, trajectory distortion changes the relative positions of atoms and reduces the spatial resolution of APT data, especially for complex materials and inhomogeneous samples containing multiple phases [139]. As shown in Figure 27, compared with the smooth tip surface, due to the difference in the local electric field on the sample surface with multiple phases, the low-field component evaporates preferentially relative to the high-field component, and creates unevenness shape on the sample surface, resulting in the undesired displacement of ions in the first instant of their time of flight, which appears as significant differences in local atomic density in map [111, 140, 141]. For example in bone specimens of APT, Ca (evaporation field: 18 V/nm) and C (103 V/nm) have obvious differences in evaporation field, in addition to considering the fundamental concentrations differences of Ca and C, trajectory distortion is also a factor that should be considered to compare the difference measured densities of different phases. Although methods have been developed to partially compensate for some surface-induced distortions [142, 143], this phenomenon still cannot be fully corrected, therefore some spatial inaccuracies are inevitable in reconstructions that contain multiphase, or significant chemical inhomogeneities.

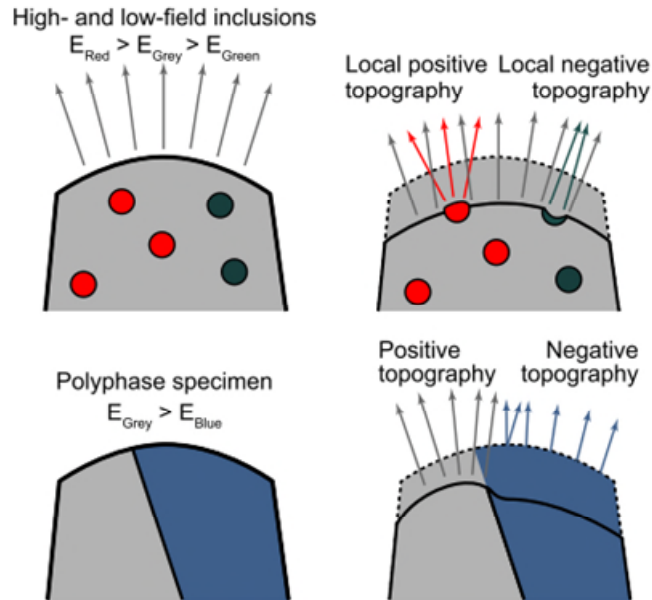


Figure 27. Local magnification effects associated with clusters and interfaces. Figures on the left show the initial geometry. Figures on the right indicate trajectory aberrations associated with high- and low-field materials [111].

Surface diffusion is also a common problem, usually more obvious in metallic material with laser mode APT. Surface scattering refers that atoms adsorbed on a surface that can randomly walk through a thermal activation process [144, 145], whereby atoms jump from one location across the sample surface to another. In fact, if enough thermal energy is provided, atoms belonging to the material can be migrated [106]. This effect can be minimized by optimizing APT experimental conditions, normally by minimizing the thermal energy of the surface.

As mentioned in the Section 3.4.1, multiple events are a potential source of quantification error in APT, and biological materials have more molecular ions and a high frequency of multiple events relative to other materials. Some elements, such as C, prefer to evaporate as composite ions. These ions are composed of multiple atoms that may dissociate after field evaporation and can contribute to an increase in multiple events

detected during the experiment [146, 147]. Multiple events cannot be completely avoided, but a high proportion of multiple ion events will result in data loss. It is also by optimizing the experimental parameters to minimize its impact.

For samples with poor electrical or thermal conductivity, such as biological and certain mineral samples, the influence of background also needs to be considered. By comparing existing biological APT studies [21, 25, 27, 112, 114, 148, 149], mass spectra with high background noise and obvious tail extension after main peaks are common issues. For poorly conductive materials, the sample tends to retain thermal energy between pulses, resulting in delayed evaporation which appears as a thermal tail in the mass spectrum. Large thermal tails can enhance the local background of other peaks of interest, or even hide them. Peak tails and overall background can be improved by optimization of experimental parameters such as laser pulse energy and evaporation rate.

There are several other limitations and challenges to biomaterial APT research including:

- For non-conductive and beam-sensitive biological samples, specimens preparation are hard and take a lot of time as the requirement of extremely small sample size and specific tip shape [150].
- The analysis volume is limited (approximately 60 nm-200 nm). Unlike metallic material, which can be known in advance whether the sample contains grain boundaries by using techniques such as Transmission Kikuchi Diffraction (TKD). For biological samples such as bone, hard to know in advance whether an area of interest (e.g. collagen fibril) is covered in the needle [151].
- Specimen failure rate is high as the strong electric fields and associated

mechanical stresses are required for field evaporation. Analysis often ends prematurely due to sample fracture during collection [152, 153].

- For LEAP-5000XR, the detection efficiency of atoms within the specimen is about 52% [154].

3.4.4. Atom Probe Analysis Optimization for Biomaterials

As mentioned earlier, many of the limitations can be reduced by optimizing the experimental parameters. An optimal balance of different experimental parameters should be found in the APT analysis of any new materials. Many atom probe studies on biological materials (e.g. tooth, apatites, enamel, bone, nacre) have used an analysis temperature of 35 K - 60 K, a pulse fractions of 16 % - 25 %, and a laser pulse of 50 -500 pJ [21, 25-27, 112, 114, 115, 148, 149]. The use of lower operating temperatures or higher pulse fractions is believed to increase the chance of sample fracture in steels [155], while for non-conductive samples, the use of higher operating temperatures is considered to increase irrelevant evaporation of ions, which results in an increase in the background [21]. Using a lower pulse fraction may also be detrimental, where preferential evaporation of species could occur between pulses. This occurs when the electric field at the surface of the sample is large enough to cause ions of certain species to evaporate between applied voltages or laser pulses [106]. Since the evaporation times of these ions are not known, their time-of-flight cannot be calculated, and their chemical properties cannot be determined, leading to the underestimation of their concentrations. In laser mode APT, high pulse energy can provide sufficient thermal energy for ion evaporation with low electric field strength, reducing the possibility of evaporation between laser pulses and

thus reducing background levels [21], while excessive laser energy may also cause overheating of non-conductive samples. Therefore, it is necessary to extensively explore the influence of experimental parameters on data quality to optimize the analysis conditions. More discussions will be in Chapter 5.

3.4.5. Interpretation of the Mass Spectra

Labelling of mass spectra, as in any spectrogram, requires the assignment of detected events to specific atomic species, and this step is called "ranging" in APT. Common mass spectrometry techniques typically utilize "fingerprint" database techniques to identify molecules based on models of large-strand breakage behaviour to identify their highly complex mass spectra [156, 157], but those methods are not applicable in the atom probe environment as relatively small molecular chains present in atom probe mass spectrometry [158]. In atom probe mass spectrometry identification, the analyst identifies possible elements at a given mass-to-charge ratio. The identification of peaks remains as unique as possible and is normally based on the background of the material being analysed, such as from the expected elements the material contains. For the complex mass spectra containing many complex unknown peaks, some tools can be used to help with interpretation. For example, the weights program [159] is used in this study to calculate possible atomic combinations based on a certain mass-to-charge ratio. After calculating possible combinations, by combining their positions in the mass spectrum and their isotopic distributions, peaks were further identified. However, it is important to note that peaks associated with minor isotopes are sometimes hidden by tails of lower mass isotope peaks or by high background levels [106]. Since both the identification of peaks and the lateral extent of peaks in the database are a manual process,

ranged data often varies between users, which can be subject to subjectivity and some error [158]. Hudson et al. analyzed different ranging techniques and provided strategies for reducing errors caused by manual ranging data or lower true solute concentration [160]. There are still no existing uniform rules to define ranging, and it is difficult to determine the accuracy of different ranging techniques without knowing the "true" composition of a real dataset. Therefore, it is important to maintain consistent ranging techniques for all datasets to ensure comparability between each data. The method used in this thesis is based on the study by Haley et al. [158], and the range is defined using the full width at nine-tenths maximum (FW9 /10M), a typical mass spectrum generated during the APT analysis of a BG 10 specimen after ranged is shown in Figure 28.

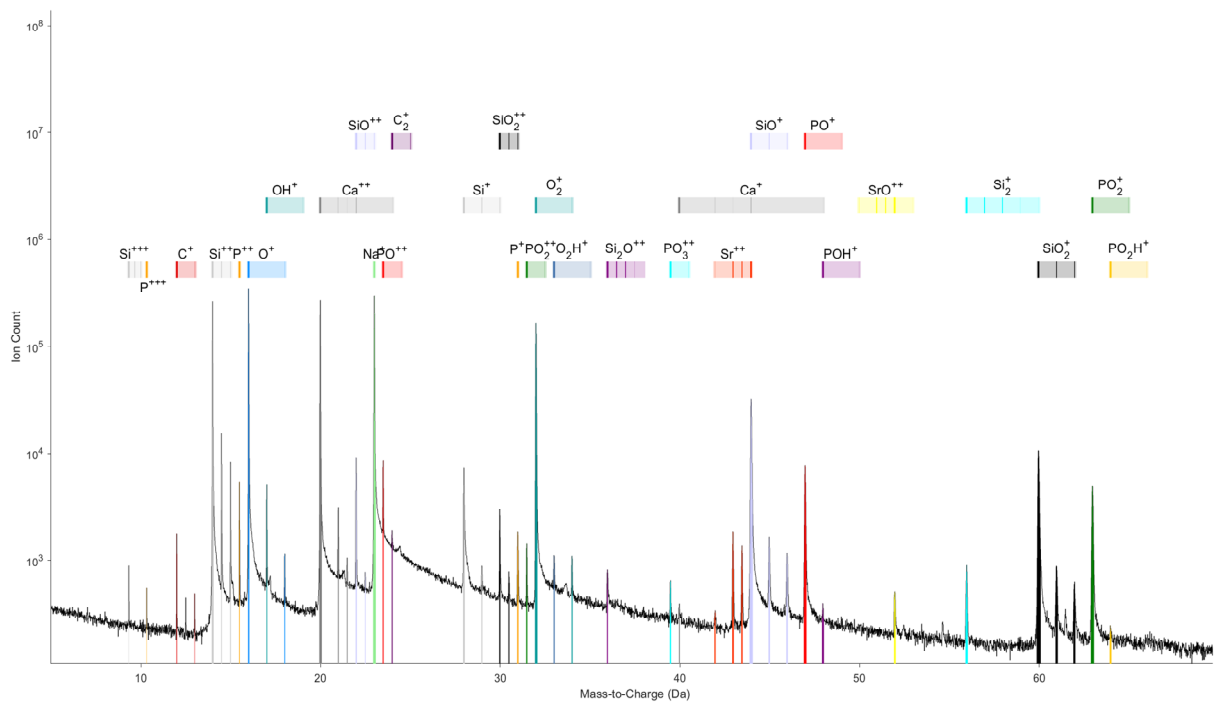


Figure 28. Typical mass spectrum generated during the APT analysis of a BG-Sr10 after ranging. The color bars above the mass spectrum show the mass-to-charge ratio of each isotope for the different ions, and the thickness of the bars represents the natural isotopic abundance (thicker bars mean higher natural abundance). Plot created using AtomProbeLab-v0.2.4.

3.4.6. Peak Overlaps

Peaks in the m/z spectrum may appear as direct overlap or tail overlap. Direct overlap means that two or more ions of different charge states or masses can have the same mass-to-charge ratio and contain two or more theoretical mass peak positions in the same m/z range. For example, the overlap of $^{88}\text{Sr}^{2+}$ and $^{28}\text{Si}^{16}\text{O}^+$ at the peak of 44 Da in the mass spectrum shown in Figure 28 and the relative schematic shown in Figure 29, in which ellipses indicate ion types, marker lines indicate overlapping locations and connected ions form "overlapping groups", line thickness represents the product of the isotopic abundances of overlapping peaks, indicating the difficulty of overlapping. Tail overlap means that a small peak may overlap with the tail of the previous peak due to the thermal transport from the tip [161], usually observed in laser pulsed mode. Direct overlap can lead to erroneous measurements of components, while tail overlap can reduce the resolution of peaks [162]. There may be multiple sets of overlaps within the same mass spectrum, but these overlaps can be resolved as separate problems. There is no unique solution if the abundance matrix for a particular overlap problem contains more ions than peaks [163]. Resolving overlap can be considered an optimization process. Tail overlap can be mitigated by optimizing experimental conditions to reduce background effects. Direct overlap can be analysed by calculating the relative amplitudes of ion mass peaks based on natural isotopic abundances. The "Decomposition of Peaks" function in the IVAS 3.8.8 and AP suite 6.1 reconstruction software can calculate the contribution of each overlapping ion type to a single total peak based on the size of neighbor non-overlapping peaks and the relative abundance of the corresponding isotopes. In order to correctly calculate the contribution of each ion in the overlapping peak, this deconvolution calculation can be performed to the mass spectrum as long as at least one isotope does

not overlap with any other isotope [106]. All overlapping peak analyses in this thesis were using the method proposed in [162, 163], and performed with AtomProbeLab v2.1.4. For example, Figure 30 shows an ion count histogram and the approximate contribution of each ion type to the different m/z peaks, where 45 Da and 46 Da do NOT overlap and were used to calculate the deconvolution. The overlapping peak at 44 Da contains 32.7% Sr^{2+} and 67.3% SiO^+ .

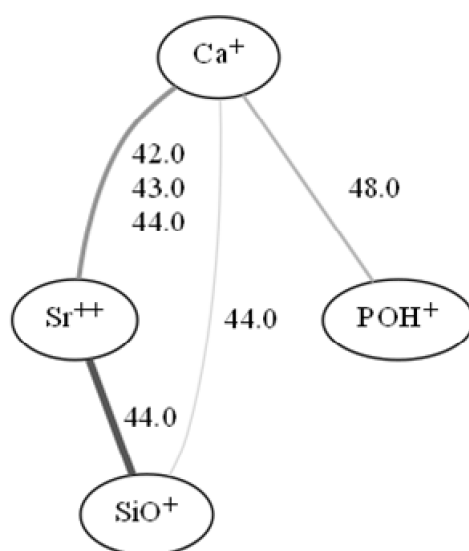


Figure 29. The schematic shows an example of ion overlap and in which mass-charge state positions. Ellipses indicate ion types, marker lines indicate overlapping locations, and connected ions form "overlapping groups". Line thickness represents the product of the isotopic abundances of overlapping peaks, indicating the difficulty of overlapping. Plot created using AtomProbeLab-v0.2.4.

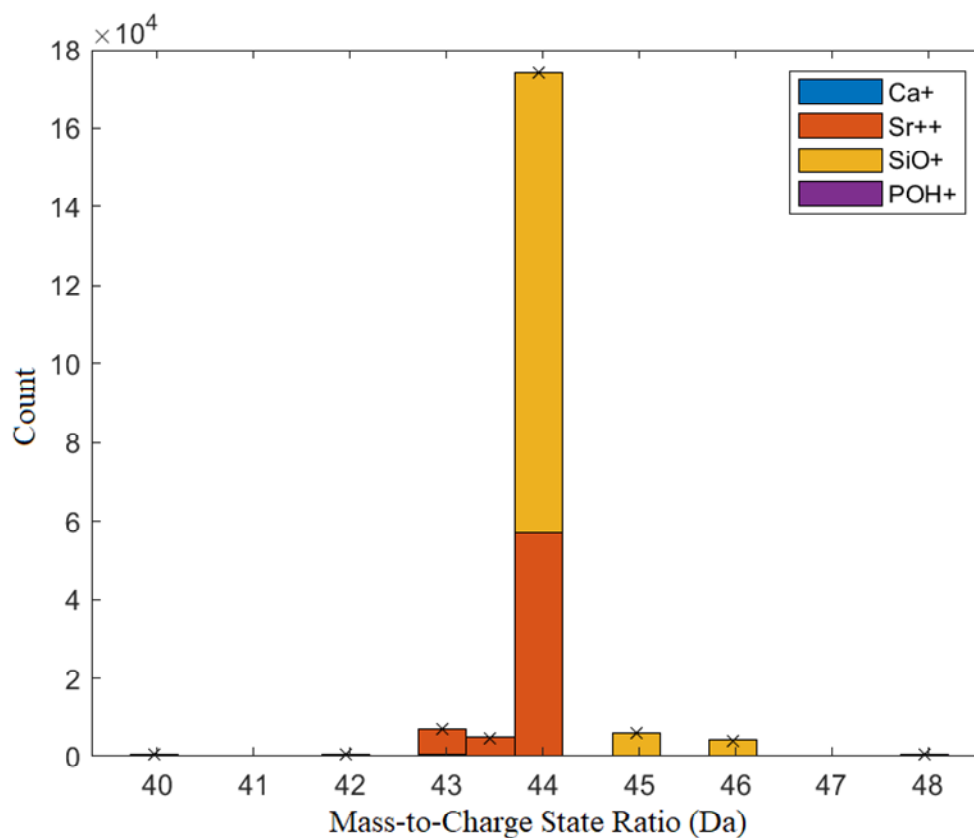


Figure 30. Ion count histogram showing the approximate contribution of each ion type to the different m/z peaks, where 44 Da contains 32.7% Sr^{2+} and 67.3% SiO^+ .

3.4.7. Analysis Techniques and Tools to Interpret Reconstructions

APT provides a powerful ability to map the positions of individual atoms in three dimensions to reveal the structural arrangement of atoms inside a material, building reconstructions atom by atom by reverse-projecting the detected positions onto the surface of a virtual sample. This thesis uses the following techniques and tools to mine the information within the reconstruction, interpret and analyse the resulting reconstruction.

3.4.7.1 Iso-concentrations/ Iso-density Surfaces and Volume Render

Visualization is the first step in interpreting atom probe data. Voxelization involves partitioning 3D data into a grid of discrete rectangular blocks or voxels, the most common way of partitioning data is by keeping the size of the blocks constant according to one of these definitions [106]. The atomic content of each voxel is then characterized. Collecting this information from all voxels allows the creation of frequency distributions and other relevant statistics that describe the arrangement of atoms throughout the dataset in terms of key physical properties such as density, concentration, and co-segregation or anti-segregation [106]. In addition to simply representing each atom as coloured dots or spheres in 3D space, applying iso-concentrations or iso-density analysis can provide a clearer picture of elemental distribution or density. Iso-concentration analysis separates blocks within a specific composition range, and iso-density analysis isolates blocks containing a specific range of atomic density for a given element or group of elements [106]. These blocks are displayed as they appear in the dataset, creating a 3D visualization of compositional fluctuations through reconstruction. A set of adjacent blocks with densities within defined concentrations or density ranges are grouped together to create an iso-surface [106]. The applied isosurface appears as a prominent blocky area in the reconstruction. They can be used to identify the presence of different phases, grain boundaries, and/or precipitates in the analysed sample. IVAS 3.8.8 or AP Suite 6.1 is used in this thesis to create and analyse iso-concentrations or iso-density surfaces.

After creating the iso-concentration/iso-density surfaces, volume renderings of concentration or density can be formed by IVAS 3.8.8 or AP Suite 6.1, and visual analysis of concentration or density fluctuations across the sample from a 3-dimensional perspective. Each block of different concentration gradients in the sample can be assigned

a normalized color value to create a 3D heat map of local concentration or density [164], and the opacity of blocks can be changed to make the visualization even clearer.

3.4.7.2 Concentration Profiles and Proxigrams

Concentration profiles can be used to measure relative changes in the spatial composition of microstructural features of interest in 3D point clouds. A one-dimensional (1D) profile is a map of local composition or density drawn along the length of a cylinder or cuboid, a rectangular or cylindrical ROI is created that defines the region of interest in the sample in more details. 1D concentration profiles originally developed for traditional 1D atom probes, algorithms adapted for 3D can provide useful information on compositional fluctuations, especially near interfaces [106]. A composite map is a two-dimensional (2D) cross-section corresponding to the one-dimensional cross-section described above. The map is computed by dividing the region of interest into a two-dimensional grid of blocks in the lateral (x-y) plane. Each point on the map represents one of these blocks, and its color represents the atomic density value measured at that x-y coordinate [106]. The thickness of the cross-section of interest needs to be adjusted to optimize the contrast of each analysis to emphasize specific features.

The development of proximity histograms or proxigram algorithms allows the compositional profiles to be measured in 3D. They facilitate more complex microstructural and interface characterization by utilising the 3D data available in APT reconstructions [165]. Proxigrams can generate concentration profiles of any constituent element to characterize the properties of an interface and its local environment. Compared to simple combinations of 1D concentration profiles, the proxigram is more complex and

computationally expensive. However, proxigram is a better solution to complex interface analysis, as the results of 1D composition profiles will be inaccurate if the interface is not flat and/or directly perpendicular to the direction of the taken composition profile, whereas the proxigram calculates atomic positions perpendicular to all points on a defined three-dimensional isosurface, regardless of the shape of interfaces [166]. For example, Figure 75 shows the 1D concentration profile of a cuboid along the length of the z-axis, and comparable, Figure 76 shows the proxigram of the isolated collagen fibril. All concentration profiles and proxigrams in this thesis were implemented by IVAS 3.8.8 or AP Suite 6.1 software.

3.4.8. Compositional Measurements

All compositional measurements in this thesis were reported using the MATLAB package of AtomProbeLab-v0.2.4. When quantifying the chemical composition of a specimen by APT, even for compositional measurements of different regions within the same specimen, there are many factors that need to be considered. These factors that may affect the measurement of components include: high levels of background noise for non-conductive specimens, incorrect identification of mass spectral peaks, selection of peak ranges, peak overlaps, multiple events, etc. As mentioned in Section 3.4.5 and Section 3.4.6, the unification of peak ranges between specimens, and consideration and interpretation of overlapping peaks are necessary. Besides, main peaks and confident peaks should be prioritized and considered in the composition analysis. Experimental parameters optimization of specimens can reduce the effects of background noise and multiple events effects, more details will be mentioned in Chapter 5.

3.5. Summary

This chapter introduced the details of specimens used in this project, such as composition and appearance. The working principles and methods of electron microscopy used in this project are summarized. The principle of APT, the method of sample preparation of APT for biomaterials, limitations and challenges of biomaterial characterization by APT, and techniques of APT biomaterial data analysis are summarised. This chapter shows the basic experimental information of APT biomaterial research, which has great reference value for future APT research on similar materials.

Chapter 4

Strategies to Overcome Sample Preparation Challenges for Biological Specimens

4.1. Introduction

APT is based upon controlled field evaporation of individual atoms from the surface of a material. Every specimen must take the same geometrical form: a very sharp needle, with a hemispherical apex of radius <100 nm. An APT experiment does not run through the entire specimen length, typically only the first 50-200 nm below the apex. Hence, a feature of interest must be precisely located at the tip of the specimen if it is to be characterized. Techniques such as Electron Backscatter Diffraction (EBSD) to isolate aspects of microstructure are well-established for alloys and semiconductors, e.g. grain boundaries, and precipitates. However, the complex hierarchical microstructure of many biomaterials [120] complicates the identification, and isolation of nanoscale regions of interest for incorporation into-the specimen. There are generally two methods to prepare needle shape samples for APT, electropolishing and FIB liftout. Electropolishing is the more conventional method for materials with good electrical conductivity [106], but is not feasible for non-conductive materials such as semiconductors, ceramics/glasses, and biological materials. Instead, the FIB liftout method offers the ability to prepare a sharp needle for non-conductive materials. However, preparing extremely small tip samples of biomaterials for APT can be very challenging. In particular, the characterization and preparation of biological materials using SEM/FIB have some limitations because biological materials are often brittle and electron and ion beam sensitive. Many studies

have addressed damage to biological samples in SEM/FIB analysis [167-176], but some damage mechanisms induced by electron/ion beams are not yet well understood. This chapter lists various difficulties encountered in sample preparation of bioactive glass, pSrBG scaffolds, and animal trabecular bones, discusses possible causes and provides some corresponding solutions.

4.2. Challenges I: Sample Damage and Cantilever Loss of Brittle/Surface Sensitive Materials

During the process of FIB-liftout of bioactive glass specimens (BG-Sr10), most of the cantilevers that were lost during the process were due to cracks, which were created by contact with the micromanipulator. An example of crack and subsequent cantilever loss can be seen in Figure 31 a) and b). The indicated crack was created after the micromanipulator contacted the surface of the cantilever. Once the crack is formed, even if tungsten deposition is performed after that on the surface for adhesion and filling, loss of the cantilever during the subsequent liftout (transfer) process cannot be avoided. This may be a result of applying an external force when using the micromanipulator in the conventional way to make contact with the top surface of the sample. It is hard to control the magnitude of any applied external force during the conventional liftout method. Furthermore, compared to other materials commonly prepared for APT by this method, such as alloys, bioactive glasses are much more brittle, which makes it easier to cause cracks or surface damage, leading to sample loss during the following transfer process.

To improve the survival rate of cantilevers during APT sample preparation, it was found that by approaching the micromanipulator on the side of a cantilever (Figure 31 c)), and leaving a gap for tungsten deposition (Figure 31 d)) was more successful. This

approach avoids direct touching of the sample with the micromanipulator. This method effectively avoids the occurrence of cracks and thus cantilever loss. A more detailed comparison of the side touching micromanipulator to the BG-Sr100 cantilever before and after tungsten deposition was shown in Figure 32, where the red arrow points to the small gap left between the cantilever and the micromanipulator, and the blue arrow shows the connection after tungsten deposition. This liftout method is optimal, not only for brittle samples, but also suitable for samples with sensitive surfaces or interest in surfaces.

Another problem that can lead to cantilever loss is sample re-adhesion with bulk, which is caused by re-deposition introduced during milling with the ion beam. Re-deposition is caused by sputtered material deposited onto the surface of the sample, usually near or on top of the cross-section [174]. Examples of re-deposition can be found as * marked in Figure 32, a).

Ensuring that there is enough space around the cantilever is a very effective way to prevent re-sticking during the liftout process. In this work, an approach is developed whereby before the undercut and the sides are cut free from the bulk of the cantilever, a square space is milled in advance at the final remaining side cut region, as shown in Figure 33 a), where blue arrows point to the pre-milled region in the pSrBG cantilever. Furthermore, during the undercutting, it is ensured that the size of the undercut area is at least 1.5 μm wide. These strategies were found to be effective in improving the survival rate of cantilevers during the sample preparation process of such relatively tricky materials and reducing the specimen's damage and loss. A typical pSrBG needle specimen for APT is shown in Figure 33, b).

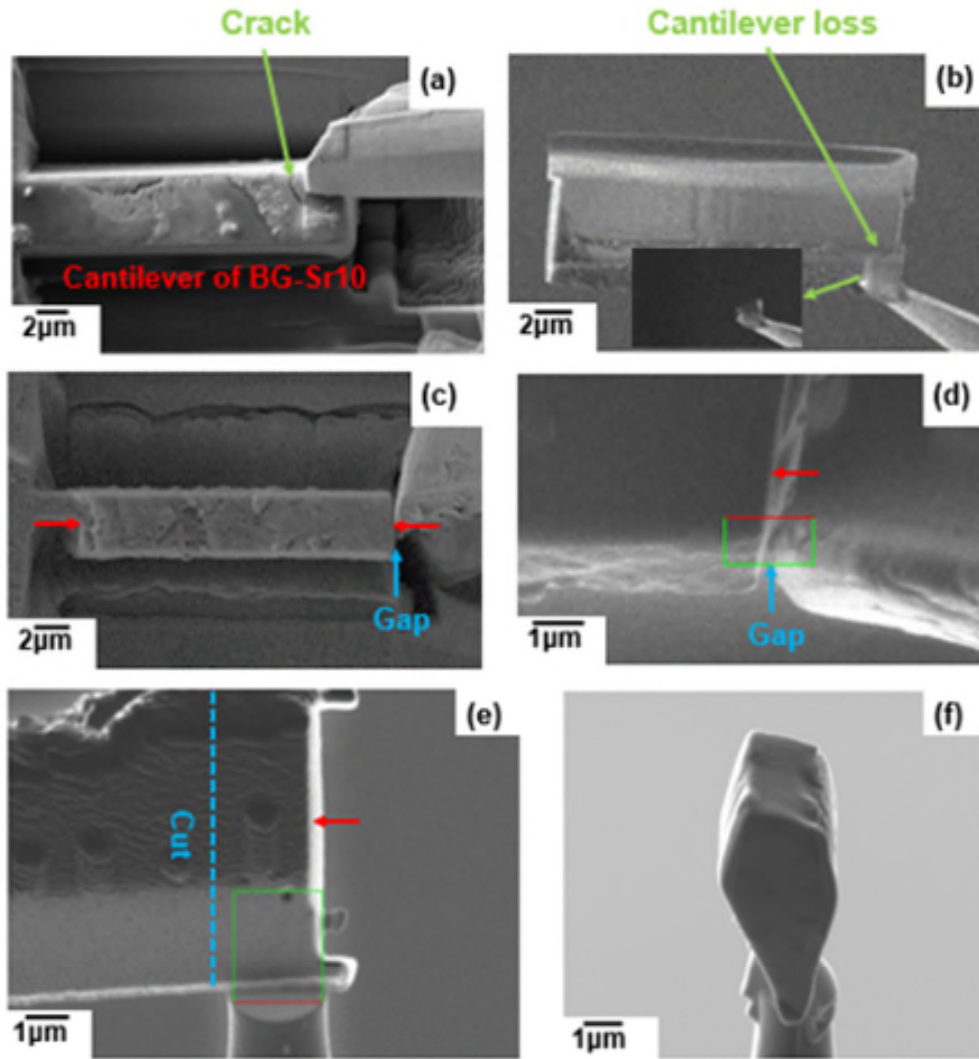


Figure 31. SEM and FIB images of BG-Sr10 liftout process, with resulting crack and cantilever loss. Experiments have shown that when the micromanipulator makes excessive contact with the top of the cantilever, (a) cracks were routinely observed. (b) Eventually leading to the loss of the cantilever during the liftout process. (c) - (d) micromanipulator approaching the side of a cantilever, leaving a gap for tungsten deposition to prevent sample loss. (e) - (f) 1-2 μm wide segments were cut off from the cantilever and adhered to a standard Si micro-tip post.

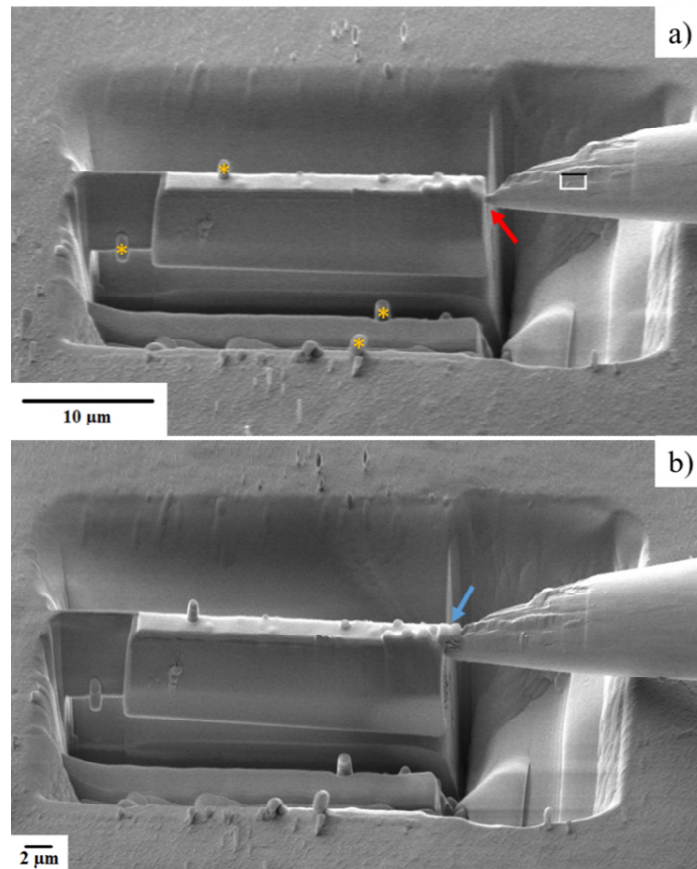


Figure 32. SEM images of the BG-Sr100 liftout process, with the micromanipulator approaching the side of the cantilever, a) the red arrow points where the gap for tungsten to deposit, and b) the blue arrow shows the connection after tungsten deposition. The * marks as re-deposition regions.

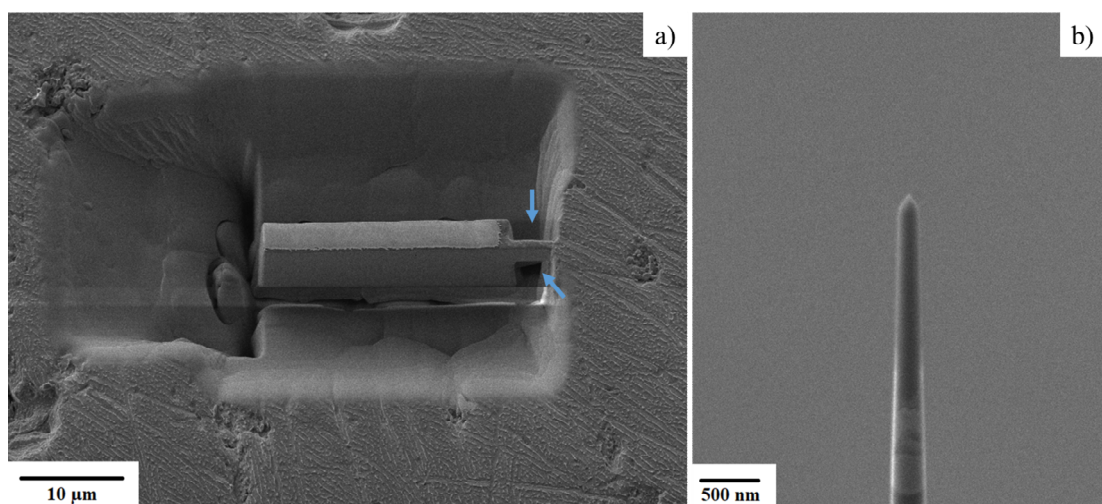


Figure 33. The pSrBG cantilever, with a resulting good tip. Blue arrows in a) point to the pre-milled region before the cantilever is cut free from the bulk, and b) present a typical pSrBG needle specimen for APT.

4.3. Challenges II: Needle Bending and Contamination during APT Tips Sharpening for Biological Materials

Another significant sample preparation challenge for biological materials is the fact that during annular milling, bending of the tips frequently occurred as shown in Figure 34, a) – c). The direction of bending of the tips was always the same (to the right side in SEM view), an effect which has also been reported by Eder et al. [149] during specimen preparation of nacre for APT analysis. In that study, the bending of the nacre tip occurred at an ion beam acceleration of 10 kV. For BG-Sr10 and pSrBG, bending begins to appear for tip diameters less than 300 nm, and when imaging with an electron beam acceleration of 5 kV, and as the magnification of SEM is raised, the bending becomes more obvious. We have not seen a significant effect of the influence of the ion beam conditions on the extent of tip bending. However, under the same Ga beam conditions it was observed that when the magnification of the SEM image was increased, the severity of bending became more pronounced. Combined with Figure 36, which shows the schematic of viewing direction in SEM and milling direction of FIB, We suspect that such bending is the result of the combined action of electrons and ions, but where the electron beam plays a dominant role. More specifically, since the ion beam direction (FIB) originates from above the apex of the tip, a protective layer of Pt or W (by ion-beam only) on top of the tip can initially protect the sample from ion beam damage. However, the relative direction of the electron beam (SEM) incident on the side of the needle, causes damage as there is no protection for the specimen in this orientation during the milling process. After the needle has been affected by the electron beam and formed into a bend, subsequent milling begins to act directly on the side of the tip (can be found in Figure 35), further accelerating the bending of the tip. So, what are the possible causes of the damage to the sample?

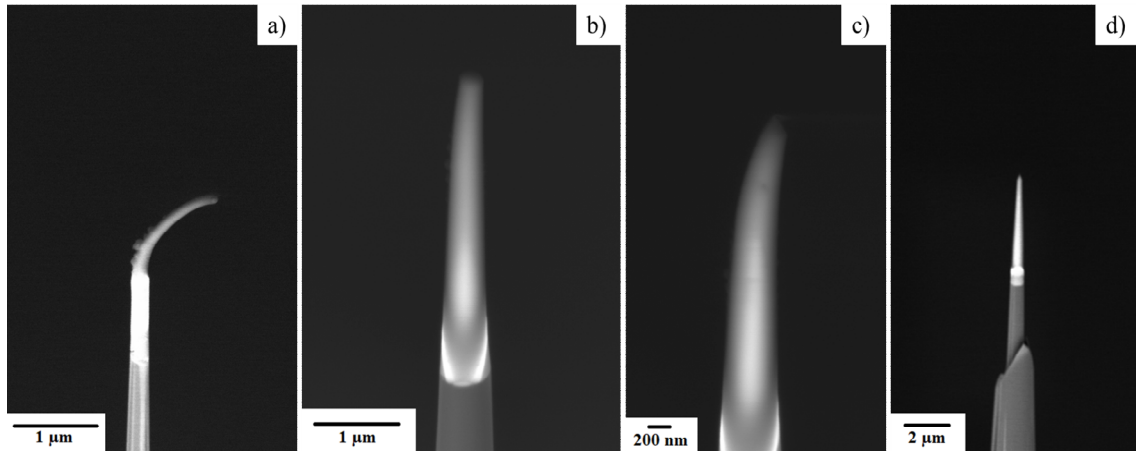


Figure 34. SEM images of tips bending during annular milling of BG-Sr10. a) – c) damaged tips caused by the electron beam, d) an example of suitable atom probe tip after optimising SEM-FIB accelerating voltage and ion beam current.

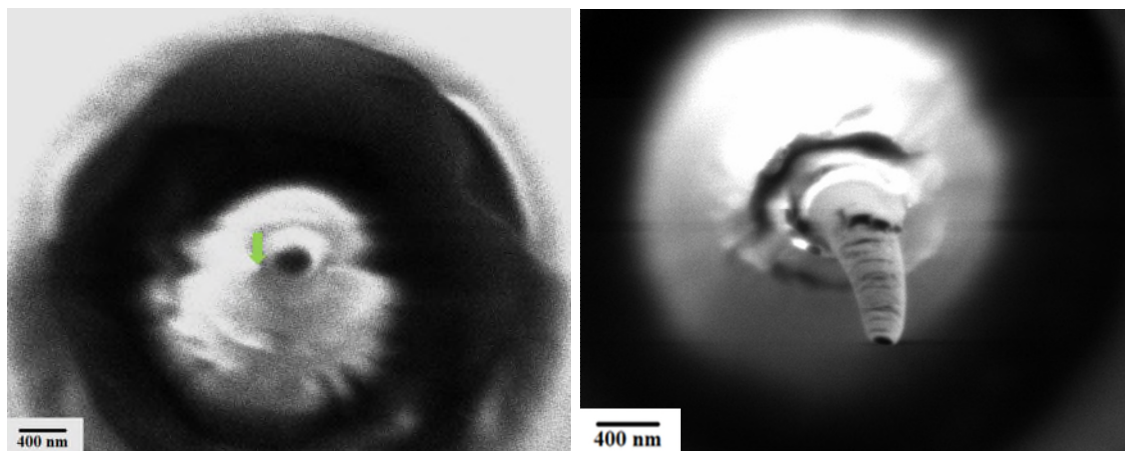


Figure 35. FIB images of tips bending during annular milling of pSrBG (left) and porcine trabeculae bone (right), green arrow shows the bending direction of the tip. Compared to pSrBG, porcine trabeculae bone tip damage is more serious.

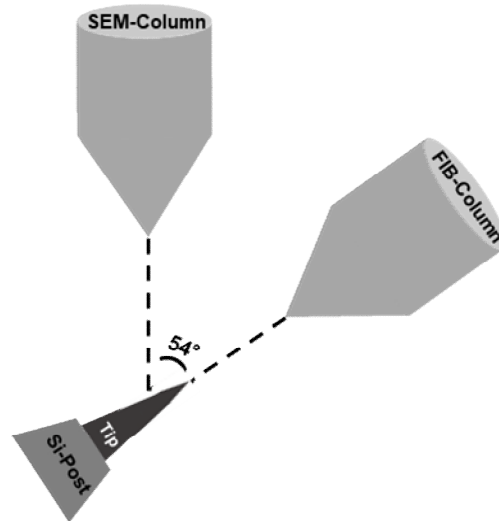


Figure 36. Schematic of viewing direction in SEM and milling direction of FIB of the APT needle annular milling.

There are mainly three types of damage caused by the FIB-SEM system, beam-induced heating damage, knock-on damage, and electron radiolysis damage [169, 172, 177]. The degree of each damage mechanism varies in different materials. Compared to metals or semiconductors, the poorer thermal conductivity and weaker bonding of biological materials make them more sensitive to damage from heating and radiolysis. The radiolysis damage mainly comes from the irradiation of SEM during sample preparation, such as Bassim et al. reported that the chemical spectrum of polyacrylamide (PAAm) changed significantly with and without electron beam irradiation [172]. In my research, the bending becomes more serious as the magnification of the SEM increases. Higher magnification means higher resolution images can be obtained, and also means the required electron exposure increases with the square of the magnification [171]. As electrons traverse the specimen, in addition to elastic scattering events which are the main contributors to useful image information, many inelastic events also occur. Some of the energy transferred from the electrons to the sample can cause radiolysis damage, which causes changes in the chemical compositions or microstructure of the specimen. In

Zhang's research of electron/ion beam damage on soft materials [168], it is observed that the electron dose level/rate was positively correlated with the degree of beam-induced damage, and the effects of beam voltage need to consider the actual interaction volume of electron beams and the thickness of the electron beam with the sample. This may explain why the bending phenomenon always starts to appear after the tip is smaller than 300 nm. Although radiation damage is always present as it is part of the electron beam/specimen interaction that produces the image, damage to biological materials can be mitigated by lowering the voltage and current of the electron beam.

In addition, there are numerous papers that discuss the potential role of beam-induced heating damage in soft materials and biological samples [172, 176, 178-183]. Bassim et al. suggest that the beam-induced heating can be attributed to the generation of phonons in the specimen during cascade collisions [184]. Wolff et al. simulate the heating damage to the pepsin-soluble porcine collagen around the ion track by using the COMSOL simulations [173]. For materials with low thermal conductivity such as soft materials and biological materials the induced change in sample temperature can be excessive, which results in significant heating damage when using conventional milling parameters of ion beams. The thermal change in most metal or semiconductor materials applying the same milling parameters is negligible. In my research, I propose that the most likely contributor to the subsequent bending of the tip is due to heat generated from the beam. The bending occurs once the heat inside the tip exceeds a certain threshold.

Hence it was necessary to develop a strategy so as to prevent/minimize damage as much as possible. Various approaches proposed in the literature are based on experience, such as using cryogenic stages, reducing beams voltage and current, and lowering beam overlap. It is important to balance the effective tip milling/imaging and specimen damage. In my experiments, when processing bioactive glass-based specimens,

it was found that the bending of the specimen was eliminated by applying a combination of low imaging voltages (≤ 3 kV) and currents (≤ 500 pA) with regards to the electron beam. Both low ion accelerating voltage (≤ 2 kV) and current (≤ 200 pA) are key factors for the successful preparation of suitable APT tips in the final stages of tip sharpening. Additionally, avoiding excessive magnification (in my case, ≤ 3.5 K X) and prolonged imaging is also a useful strategy to minimize damage. One example of an atom probe tip of BG-Sr10 after optimising SEM-FIB processing parameters is shown in Figure 34, d). When processing materials of animal bones like porcine trabeculae bone, even lower voltage/current parameters were required due to its more sensitive behavior as shown in Figure 35. A recommended set of parameters used in this research is: applying electron beam voltages of ≤ 2 kV and currents of ≤ 200 pA for imaging and using ion beam accelerating voltages of ≤ 2 kV and currents of ≤ 200 pA for the tip final sharpening.

Gallium contamination is another factor that needs to be considered during tip preparation. Some degree of surface damage to the sample induced by Ga⁺ irradiation is unavoidable, even for hard materials [185]. A large number of gallium ions may introduce high internal stress, leading to sample failure during APT analysis. Gallium ion implantation may also change or damage the microstructure of the tip [186, 187]. To reduce the amount of implantation of Ga ions, as mentioned in Section 3.3, a protective layer of W or Pt was applied to the sample prior to imaging and processing with Ga ions. Furthermore, after the annular milling stage had created a tip suitable for APT (normally with a tip diameter less than 120 nm) low energy Ga ions (< 2 kV/ ≤ 200 pA) are used to remove 0.5-1 μ m top materials from the tip, then obtain the final tip.

4.4. Challenges III: Complex Topography and Pores in Animal Trabecular Bone

Non-embedded biological samples are used in this thesis instead of embedded in resin which avoids unwanted artifacts of resin cross-sections and shrinkage in all dimensions. Since the trabecular bone fragments are small and brittle, not much polishing of the non-embedded sample was performed. The porcine trabecular bone retains the original appearance after undergoing dehydration and degreasing as shown in the top graph in Figure 37. The topography of the porcine trabecular sample is very rough, the locations that can be selected for cantilever fabrication are limited, i.e. restricted to regions that are relatively flat and avoid pores, and the production process is difficult with a high loss rate. The bottom graph in Figure 37 presents a good quality cantilever produced in the cross-section of a trabecular rod.

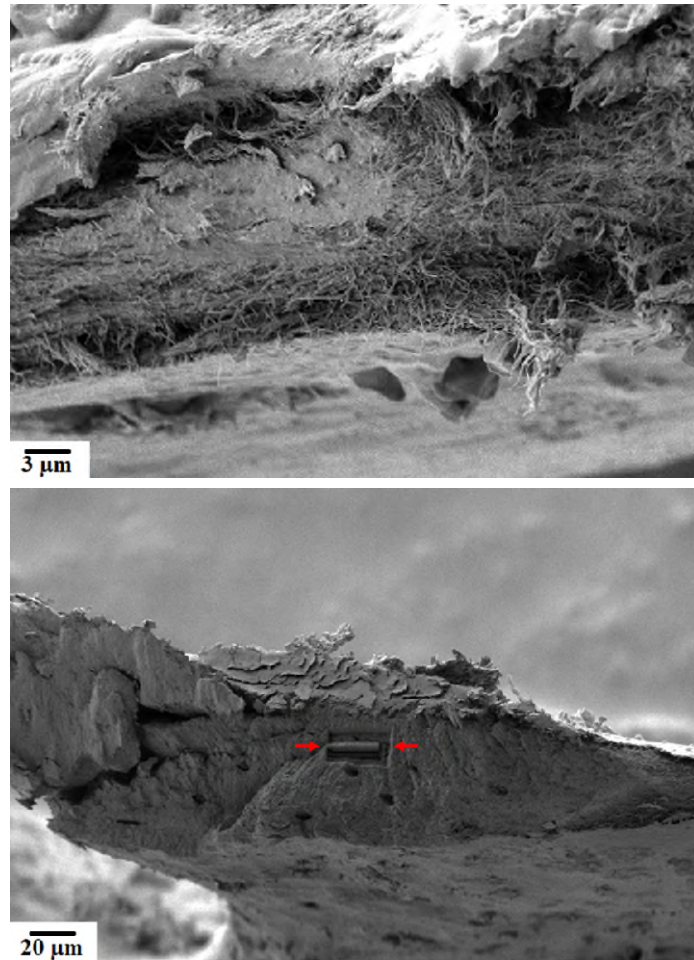


Figure 37. SEM images show the porcine trabecular bone's complex topography, with a cantilever created (red arrows pointed) in the limited terrain.

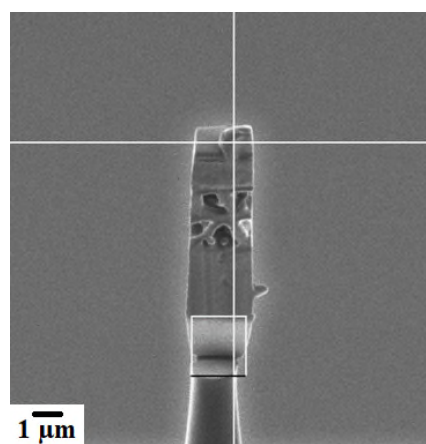


Figure 38. FIB image of a porcine trabecular bone segment, containing internal pore structure.

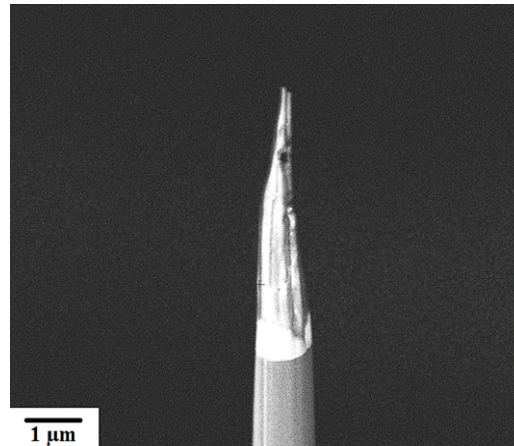


Figure 39. A damaged porcine trabecular bone tip during the final sharpening process, uneven sharpening due to the unforeseen internal pores, the tip eventually presents an irretrievable 'sailfish' shape.

Trabecular bone contains many pores, and the location and density of the pores beneath the surface cannot be predicted. Hence, the loss of specimens caused by pores is inevitable during the sample preparation process. For example, a trabecular bone segment contains a large number of internal pores, as shown in Figure 38, which can be found before the final sharpening step. Figure 39 shows a damaged tip during final sharpening, holes only appear during milling, which then leads to further uneven milling in specimens, and eventually results in needles with multiple tips or other odd shapes.

Currently, there are no routine and effective methods to avoid this specimen loss in non-embedded porosity samples. However, strategies for this based on my experience are, first to make as many potential samples as possible, such as making longer cantilevers in the liftout step. Additionally, in the process of annular milling, after the observation of pores, the position of the milling pattern should be adjusted appropriately to remove the areas containing pores as much as possible in the following sharpening process. However, this method does not rescue all of the pore-containing tips, and the survival of the needle depends on the size and depth of the pore, as the two tips are compared in Figure 40.

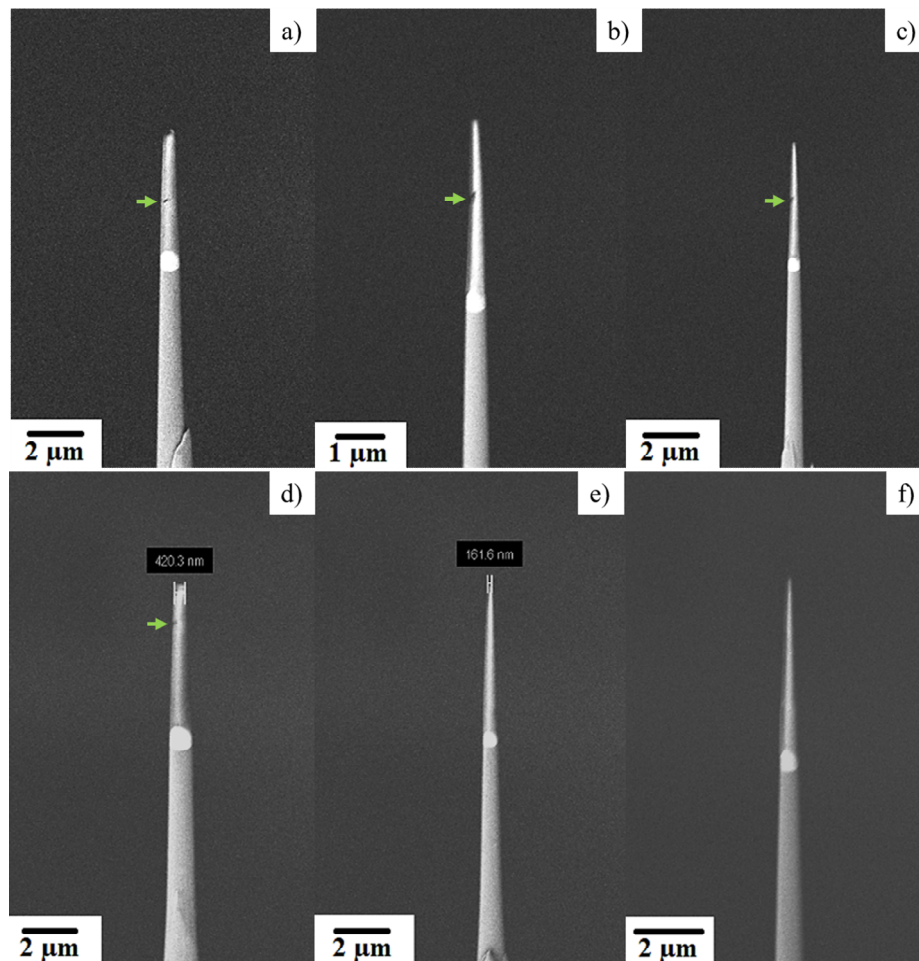


Figure 40. The final sharpening process of porcine trabecular bone tips with pores (green arrow pointed), from left to right indicates gradual sharpening. a) – c) a bad tip still contains the pore after sharpening, which eventually leads to a rapid fracture in APT analysis. d) – f) a surviving good tip, which removes the pore after final sharpening.

4.5. Summary

In this chapter, challenges encountered in APT sample preparation for biological materials (bioactive glass, pSrBG scaffold, and animal trabecular bone) were studied and discussed, and some corresponding solutions were provided. Before using improved sample preparation methods and optimized parameters, the sample preparation success rate was extremely low. And even if one or two thick needles were luckily produced, their performance in APT experiments is poor (fast fracture). After using corresponding

strategies to optimize the sample preparation process for different problems, the success rate can be increased to 80%, and the prepared needle is thin. The author hopes to provide some strategies and help for those engaged in SEM/FIB research and APT/TEM sample preparation of related biological materials in the future.

Biological materials are brittle and beam sensitive, and the traditional liftout method can readily easily cause sample damage and the loss of the cantilever. The occurrence of cracks and cantilever loss can be effectively avoided by approaching the micromanipulator on one side of the cantilever, avoiding direct contact between the micromanipulator and the cantilever, and leaving a gap for tungsten deposition. This liftout method is not only suitable for brittle materials, but also for those surface-sensitive samples or that research target is on the material surfaces. Besides, care should be taken to prevent the re-deposition of the cantilever to the block. Creating sufficient space around the cantilever is an effective method to prevent re-adhesion during the milling process.

During needle annular milling of biological materials, tips are often bent and deformed. The bending is the result of a combination of electrons and ions, but the electron beam dominates. The poor thermal conductivity and weak binding force of biomaterials make them more sensitive to damage from heating and radiolysis. Although the damage caused by the electron beam cannot be completely avoided, the influence of various factors on the biological material can be balanced by reducing the voltage and current of the electron beam. Such as for bioactive glass and pSrBG scaffold, the combination of low imaging voltage (≤ 3 kV) and beam current (≤ 500 pA) can eliminate the bending of the sample. For pig trabecular bones which are more sensitive material, the application of electron beam voltages ≤ 2 kV and currents ≤ 200 pA for imaging is critical. Besides, low ion acceleration voltage (≤ 2 kV) and current (≤ 200 pA) are both key factors for the successful preparation of suitable APT tips in the final stages of tip

sharpening. And avoiding excessive magnification ($\leq 3.5 \text{ K X}$) and imaging for extended periods of time are also useful strategies to reduce damage.

In addition, the non-embedded porcine bone trabecular samples are rough as no fine polish is applied, and places available for cantilever production are limited. Thus, the production process is difficult and the loss rate is high. Trabecular bone contains many pores, which inevitably lead to tip loss during sample preparation. In order to produce as many successfully analyzable bone tips as possible, make more samples in each cantilever such as retaining longer cantilevers during trench milling. Furthermore, unpredicted pores in the needle can be removed as much as possible by appropriately adjusting the position of the milling pattern during the annular milling.

Chapter 5

Atom Probe Analyses of Synthetic Bone Substitutes

5.1. Introduction

Due to the well-known artifacts associated with Atom Probe Tomography (APT) [106], the effects of operating conditions on data quality must first be assessed and optimized for the specific material. Existing published research on the application of APT to biomaterials is not abundant, and hence there are even fewer published studies investigating the influence of APT experimental parameters. However, it is essential to understand the role of these, and to find the optimal balance of different experimental parameters in the APT analysis of these (and any new) materials.

This chapter discusses the effect of specimen temperature, detection rate, laser pulse, and pulse frequency, respectively, on the data quality of the Sr-containing bioactive glass particles and the pSrBG Scaffold analyzed using the LEAP-5000XR. The goal was to determine the optimal operating conditions for the analysis of those materials with the LEAP-5000XR. The mass spectra generated during each experiment are ranged by either IVAS 3.8.8 or AP suite 6.1. Overlapping peaks in the mass spectrum of each experiment and the compositions for each tip are analyzed and calculated using the AtomProbeLab v2.1.4 Bulk Decomposition Tool. The 3D reconstructions of each material are presented.

5.2. Sr-Containing Bioactive Glass Particles (BG-Sr10 and BG-Sr100)

As discussed in Chapter 3, the difference between Sr-containing bioactive glass particles of BG-Sr10 and BG-Sr100 is the calcium and strontium contents. The BG-Sr10 and BG-Sr100 were produced by replacing 10 mol% or 100 mol% of the calcium ions within the original BG45S5 which contains 0 mol% of strontium.

Table 2 compares the compositional differences between the BG-Sr10 and commercial bioactive glass 45S5. Table 3 shows the BG-Sr10 and BG-Sr100 compositions in at%. Due to the similarity between BG-Sr10 and BG-Sr100, BG-Sr10 alone was used as a representative material for investigating the effects of running conditions on data quality and ultimately for the selection of optimal parameters for these type of biomaterials with LEAP-5000XR. The BG-Sr10 particle is shown in Figure 41, and its composition was measured using Electron Probe Microanalysis (EPMA) is presented in Table 4. The results of this measurement are broadly consistent with the nominal composition of this material provided by the supplier.

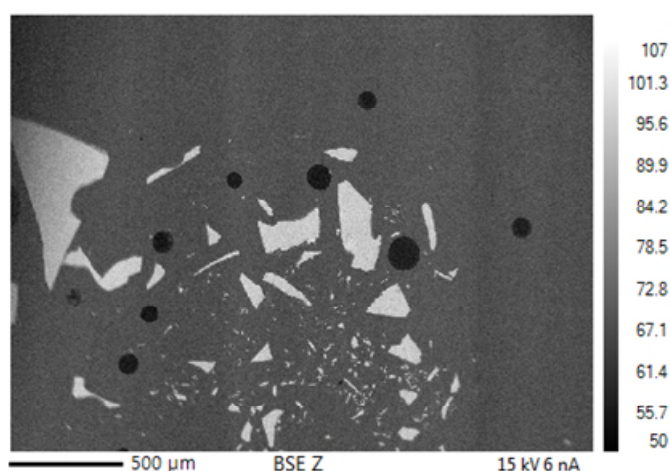


Figure 41. Electron Probe Microanalysis (EPMA) image of BG-Sr10

Table 4. Composition analysis of BG-Sr10 as measured by EPMA

Ion Type	O	Ca	Si	Na	P	Sr
EPMA (atomic %)	56.310	8.360	17.450	15.210	1.840	0.780
Nominal (atomic %)	55.203	8.540	16.261	17.231	1.834	0.949

5.2.1. APT Operating Conditions Optimization

In the first step, with the goal of accurate mass spectrum interpretation, a range of relevant operating conditions was down-selected based on a literature review of similar glass-based materials. Then the influence of different experimental parameters on the data quality within this space was systematically investigated. Table 5 displays different experimental conditions for individual atom probe analyses of BG-Sr10.

When evaluating data quality and optimizing analysis conditions, it is important to consider as many relevant factors as possible, such as the number of collected ions/yield, mass resolution, charge state ratios, and multiple hits [106]. Conversely, if the data quality is evaluated based on only one parameter, results can actually be subject to multiple other biases. Therefore, when exploring the optimal laser pulses for bioactive glass, the authors considered four specific factors: total detected hits, multiple hits, background level, and charge-state-ratio.

For the case of specimen temperature, as bioactive glasses are non-thermally conductive, the cooling rate after heating from each laser pulse is relatively slow, meaning that during the APT experiment delayed evaporation effects could to be expected. This would reduce the mass resolution of the measurement by broadening ('thermal') tails of

all mass spectra peaks, increasing the background and hiding smaller adjacent peaks. APT experiments of BG-Sr10 at 40-50 K or at low laser energies of 20-30 pJ all ended in quick fractures of the specimen (after acquiring less than 500,000 ions).

As shown in Table 5, comparing samples of BG-Sr10-03, BG-Sr10-04, and BG-Sr10-05, it was found that the likelihood of producing viable datasets was improved at 30K, 200 kHz, and 0.3% detection rate, however, a large number of multiple hit events were also detected (38.2-46.1%). This refers to when several atoms hit the detector that are correlated to a single pulse [106]. Due to detector performance limitations, multiple hit events can potentially cause data loss and decrease the overall quality of analysis. If two ions arrive detector very close (time and space), the signal will overlap/lost as there is a dead time of the detector. Besides, the high proportion of molecular ions in biomaterials also increases the probability of dissociation during the flight, leading to multiple events. The author attempted to use the method of Saxey et al. [136], expecting to obtain evidence for complex ions dissociated during the flight using correlation histograms of dissociation trajectories, but unfortunately, no useful results were obtained. Figure 42 shows how the proportion of such multiple hits varies with laser pulse energy. It was observed that with higher energy laser pulses (increasing from 50 to 250 pJ), a lower proportion of multiple hits can be obtained (37% to 24%). This may be due to the increase in laser energy leading to an associated reduction in the applied electric field, to maintain a constant detection rate, which results in less decomposition of complex ions as they travel toward the detector, and thus showing up as fewer multiple hits. After setting the stage temperature at 30 K, 0.3 % detection rate, and 200 kHz pulse frequency for these bioactive glasses, the effect of laser pulse energies was further investigated. In comparison, field evaporation of tips at laser energies higher than 100 pJ tends to be more stable and all yielded data sets of more than 11 million detector hits.

Table 5. List of experiment conditions for different atom probe probe runs of BG-Sr10

Specimen No.	Temperature (K)	Detection Rate (%)	Laser Pulse (pJ)	Pulse Frequency (KHz)	Spectrum Counts	Multiple Hits (%)	Stopping Voltage (V)	End State
BG-Sr10-01	50	0.2	100	200	<180 K	/	/	Fractured
BG-Sr10-02	40	0.2	30	125	<100 K	/	/	Fractured
BG-Sr10-03	30	0.2	20	125	<500 K	/	/	Fractured
BG-Sr10-04	30	0.2	30	200	2.04 M	32.6	4800	Fractured
BG-Sr10-05	30	0.3	30	200	5.84 M	38.2	4700	Fractured
BG-Sr10-06	30	0.3	30	200	6.22 M	46.1	4650	Fractured
BG-Sr10-07	30	0.3	40	200	7.45 M	35.1	4500	Fractured
BG-Sr10-08	30	0.3	40	200	11.0 M	36.5	4680	Good
BG-Sr10-09	30	0.3	50	200	10.5 M	37.1	4700	Good
BG-Sr10-10	30	0.3	80	200	7.34 M	33.9	4032	Fractured
BG-Sr10-11	30	0.3	100	200	15.7 M	31.6	5000	Fractured
BG-Sr10-12	30	0.3	150	200	11.4 M	30.3	4480	Good
BG-Sr10-13	30	0.3	200	200	20.0 M	25.9	4500	Good
BG-Sr10-14	30	0.3	250	200	29.0 M	23.8	5500	Good

Figure 43 displays the evolution of the applied voltage across the course of

analysis for three different APT data sets acquired using 50, 150, and 250 pJ laser pulse energy, respectively. These voltage curves show the change of the applied voltage during the experiment, which needs to maintain the critical field required to induce the field evaporation at the set detection rate (ions per pulse). Usually, as the experiment progresses, the needle tip becomes gradually blunt, therefore the applied voltage gradually increases to maintain a constant field, and as such the observed gradual voltage increase over time is typical. In this experiment, pure biological glass BG-Sr10 was used. This is a relatively homogeneous sample without distinct organic and inorganic regions that would behave differently under the applied field evaporation conditions. Hence, a relatively smooth voltage curve would be expected. However, there are obvious differences in the smoothness of the different voltage curves under changing laser pulse powers in Figure 43. In the case of poorly conducting materials, the observed field evaporation can be significantly more uneven, with evaporation often occurring in bursts of ions, i.e. large multiple detection events, when compared to the more highly uniform and controlled evaporation demonstrated by most metals. This leads the applied voltage to fluctuate to maintain a constant detection rate. Compared with higher laser pulses (Figure 43, c), the voltage curve appears to fluctuate most at low laser energies such as 50 pJ (Figure 43, a). A potential problem reflected by such large fluctuations is a ‘mini-fracture’, whereby a large amount of material is instantly removed from the specimen, which often appears as a sudden voltage dip and then subsequent voltage rise in the voltage history curve. Mini-fractures often correlate with a decrease in specimen survival likelihood, and the instability of evaporation leads to spatial inaccuracies in the reconstruction. This instability is potentially caused by the mini-fractures altering the shape of the specimen away from the assumed model of a hemispherical tip, thus leading to aberrations in the reconstruction. But if the mini fracture is not too extreme, the tip may be able to reform its steady-state shape and the experiment can be continued.

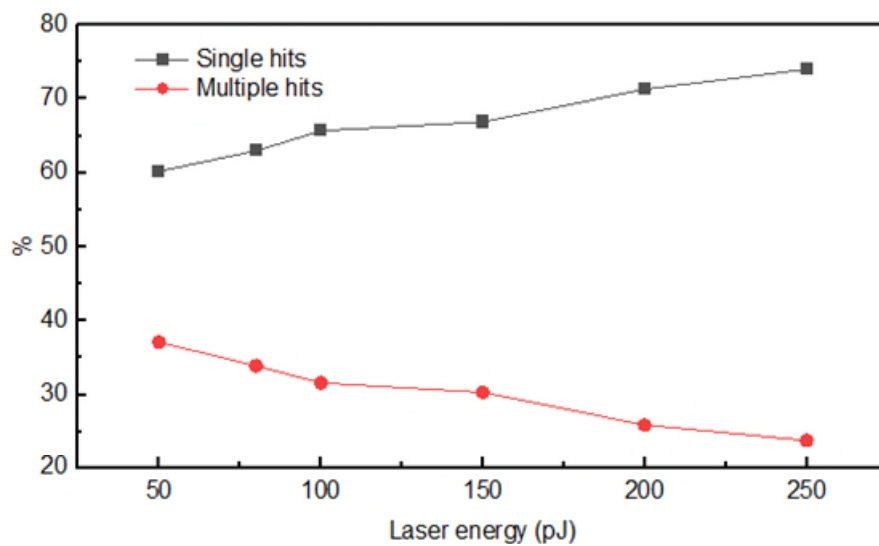


Figure 42. Detection events under different laser pulses of BG-Sr10. Samples were evaporated at a fixed laser pulse frequency (200 kHz), and $10\text{-}20 \times 10^6$ ions were collected at each condition. Square and circular symbols represent single hits and multiple hits respectively.

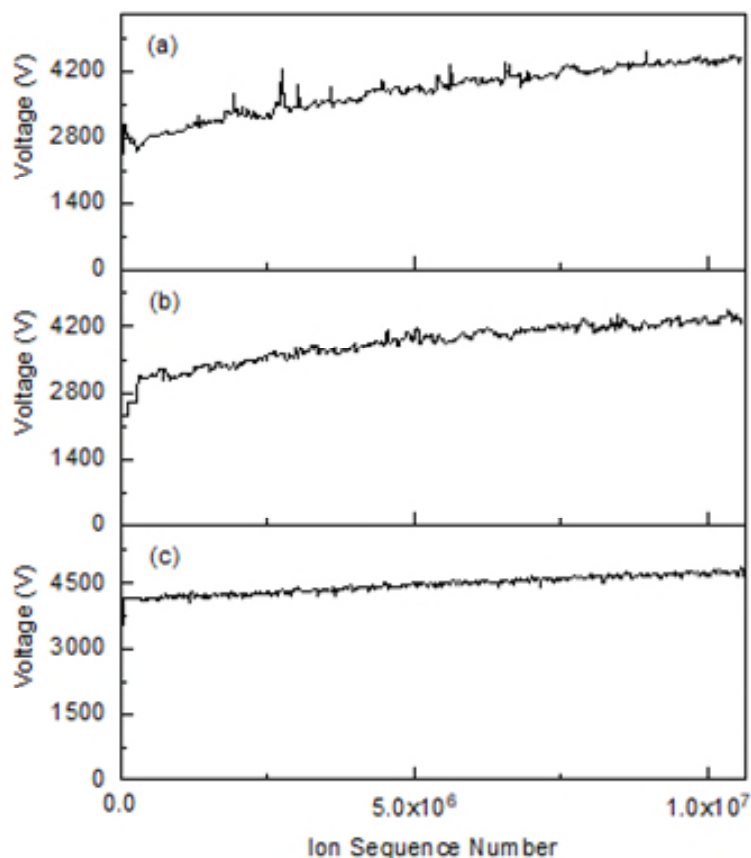


Figure 43. The instantaneous value of applied voltage as a function of ion detection sequence number for the study of BG-Sr10 with laser pulse energies of (a) 50, (b) 150, and (c) 250 pJ.

Figure 44 a) examines the extent of background noise as a function of laser pulse energy. Experimental background levels vary significantly with material type and acquisition conditions. From this, it is apparent that the background noise level is much reduced when running at higher laser powers. Higher laser powers deliver more thermal energy to the tip, enabling the atoms to more readily overcome the barrier to ionization at lower electric field strengths. This can reduce the probability of uncorrelated evaporation between laser pulses, resulting in a decreased background level and improved mass spectra resolution [188]. However, the background level appears to increase again at a laser pulse energy of 250 pJ. At this threshold, it is feasible that the high laser energy induces excess heating in the tip, meaning the specimen retains thermal energy between

pulses, which can lead to uncorrelated evaporation manifesting as ‘thermal’ tails in the mass spectrum. Cooling after the laser pulse is mediated by heat conduction through the specimen shank [189], for samples with poor conductivity such as biomaterials, the thermal tail effect is particularly obvious. This phenomenon has also been proposed by Gordon et al. to affect the APT analysis of apatite [21], and more information on laser-induced thermal tails can be explored in the paper of Joseph et al. [190]. Overall underlines the need to broadly explore the influence of laser pulse energies to optimize analysis conditions.

Figure 44 b) shows the charge-state ratios of strontium and silicon oxide as a function of laser pulse energy. For this, the charge state ratio is the ratio of the detected number of hits for one specific ion type, but from two different charge states. This parameter is typically used to monitor the applied electric field strength in operation throughout a run, such as the application of the classic Kingham Curve [191], which shows the evolution of the charge state ratio as a function of the amplitude of the electric field. And some studies used the relative charge state ratio to measure sample temperature irradiated by nanosecond laser pulses [192, 193]. In this study, the authors examine the charge-state ratio to set the laser energy at suitable values for bioactive glass to obtain high quality data. Particular focus is given to strontium, given applications as bone scaffolds where characterizing the distribution of strontium atoms in the strontium-containing bioactive glass is key. Strontium ions are mainly detected in two forms in the APT mass spectrum as shown in Figure 45: Sr^+ at a single peak of 88 Da and Sr^{2+} at a peak of 44 Da, which overlaps with $^{28}\text{Si}^{16}\text{O}^+$. The relative contribution to the peak overlap of $\text{Sr}^{2+}/\text{SiO}^+$ can be deconvolved by software such as Atom Probe Lab v2.1.4 [194], taking into account the abundance of the corresponding observable and non-overlapping isotope peaks of each contributing ion as a reference to obtain the corresponding

proportion of each ion in the overlapping peak. By comparing the charge state ratios of $\text{Sr}^+/\text{Sr}^{2+}$ and $\text{SiO}^+/\text{SiO}^{2+}$ for different laser pulse energies, it is seen that higher laser pulse energies, and corresponding relatively low electric field, reduce the content of Sr^{2+} in the overlapping peak, transferring more ions into the non-overlapped Sr^+ peak at 88 Da. The ratio of $\text{Sr}^{2+}/\text{SiO}^+$ in the peak of 44 Da thus decreases with increasing laser pulse energy. The change in mass-to-charge-state ratio is more sensitive to the laser pulse energy for greater than 150 pJ. All of the collected APT data slightly overestimates the Sr content compared to its nominal value (more details can be found in Section 5.2.3). However, the measured value of Sr gets closer to the nominal value as the laser pulse energy increases (accuracy increased as more Sr at 88 Da without overlap). Hence, combining consideration of the respective effects of the laser energy on background level and mass-to-charge-state ratios in the mass spectrum, it is suggested that laser energy suitable for bioactive glasses BG-Sr10 should be around 200-250 pJ.

Figure 44 c) shows the measured concentration ratios of Ca/P by APT for different laser energies. In order to further confirm the applicability of the chosen laser pulse energy range, the concentration ratios of Ca and P under different laser energies were compared as an indicator of the data quality. The nominal ratio of Ca/P in Sr-10 is 4.656. The measured concentration is affected by many factors in the resulting mass spectra such as signal-to-background ratio, non-uniform evaporation behavior, incorrect peak identification (due to a wide variety of complex ions that can potentially be detected), and peak-width definitions. However, given the focus of this study on Sr, the effect of the Ca/P ratio was used as a secondary reference point in the overall selection of optimal laser energy for bioactive glass. By combining all such factors, the optimal operational laser pulse energy in our experiments was confirmed as between 200-250 pJ for bioactive glass.

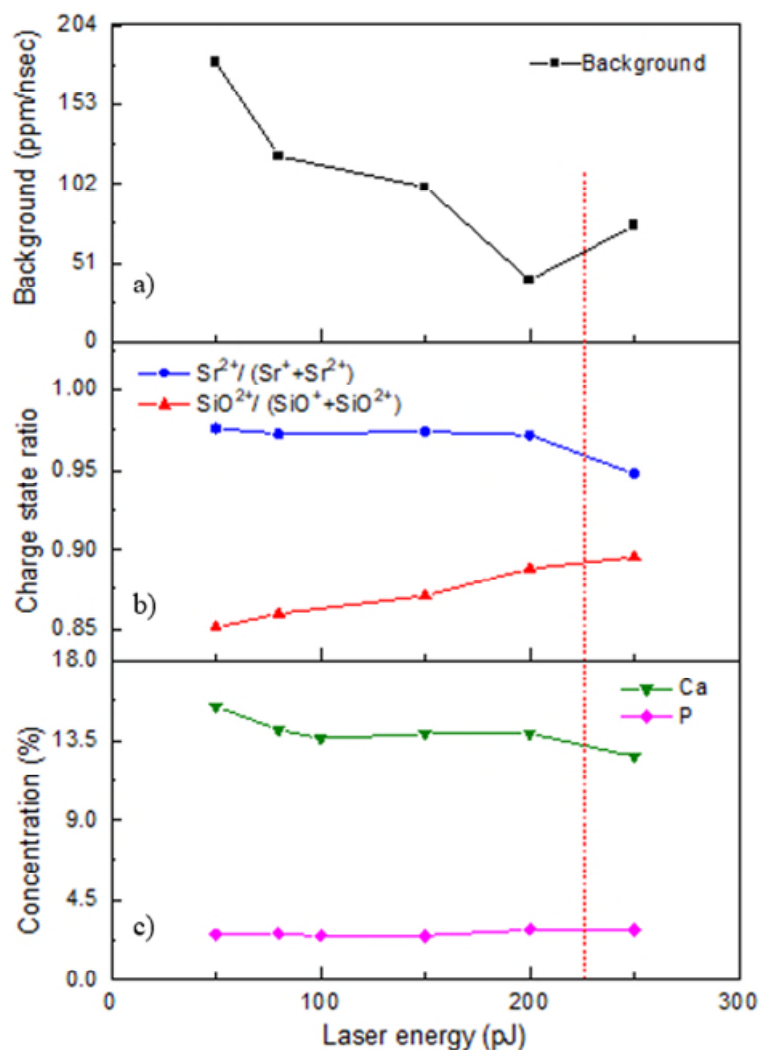


Figure 44. Effect of APT experimental parameters on data quality of BG-Sr10. a) Background mass spectra levels for different laser pulse energies, showing that increased laser pulse reduces the background. b) Charge state ratios of Sr and SiO ions, respectively, as a function of laser pulse energy, showing higher energies reduce Sr^{2+} contributions in the overlapping peak at 44 Da, with more Sr^+ present at 88 Da. c) Variation in the concentration ratio of Ca and P was analysed as a reference indicator of data quality. The nominal ratio of Ca/P is 4.656, as marked by the vertical red dotted line. The identified optimal operational laser energy was between 200-250 pJ.

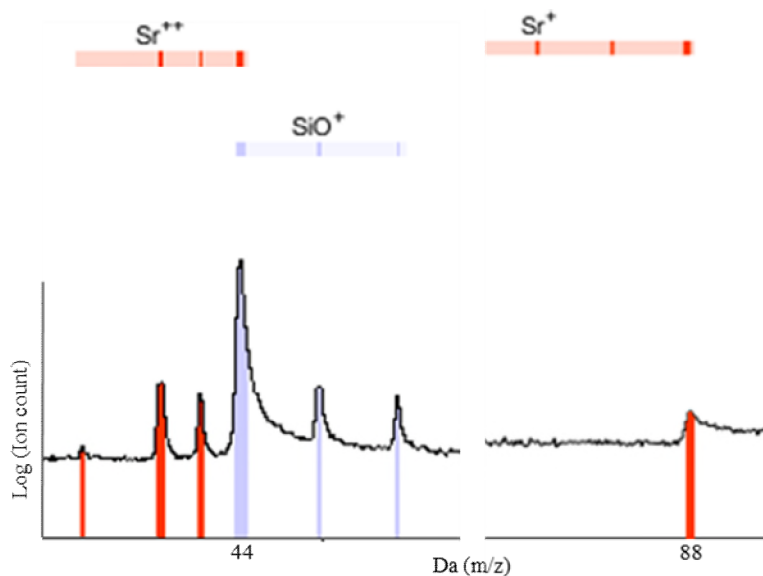


Figure 45. Close-up of the region around Sr²⁺ in the mass spectrum, highlighting the major overlap of Sr and SiO.

5.2.2. Mass Spectra and Reconstruction Interpretation

A typical BG-Sr10 mass spectrum is presented in Figure 46, in which 20 million hits were detected using conditions of 30 K stage temperature, 0.3 % detection rate, 200 kHz pulse frequency, and a pulse energy of 200 pJ. Main peaks in the mass spectrum have been labelled such as Si²⁺ at 14 Da, Ca²⁺ at 20 Da, Na⁺ at 23 Da, and PO⁺/ PO₂⁺/ PO₃⁺ at 47/63/79 respectively. However, there were also few peaks, such as at 56, 72, and 82 Da which were not able to be confidently identified despite the use of auxiliary calculation program such as ‘AtomProbeLab’ [194] and ‘Weights’ [159]. The author suspects that the composition of these peaks may be some complex ions that have been difficult to determine so far. Since these unknown peaks contribute a negligible proportion to the mass spectrum, they have little effect on the bulk composition measurements reported. From the mass spectrum, all expected elements can be observed. Na, Ca and Sr mostly appear as single peaks, while P and Si are mostly detected in the form of molecular ions such as PO_x, SiO_x, and Si_xO_y (x,y ≥ 1). A small amount of C was detected in the mass

spectrum, however, since the material does not contain C, it is likely due to the SEM-FIB sample preparation process and environmental contamination, which can be neglected for the purposes of these samples. However, in the future application of APT to the analysis of animal bones, it will be necessary to solve the overlapping problem of Mg and C at 12 Da, as also highlighted by other researchers [27, 148]. The atom probe reconstruction corresponding to the mass spectrum data in Figure 46 is shown in Figure 47. As the spatial distributions of all elements are expected to be homogenous in this selected section, the corresponding reconstruction of each isolated species looks similar. The ion distribution of BG-Sr10 is uniform in the APT analysis range, which also indicates that its analysis process is stable throughout the duration of the experiment.

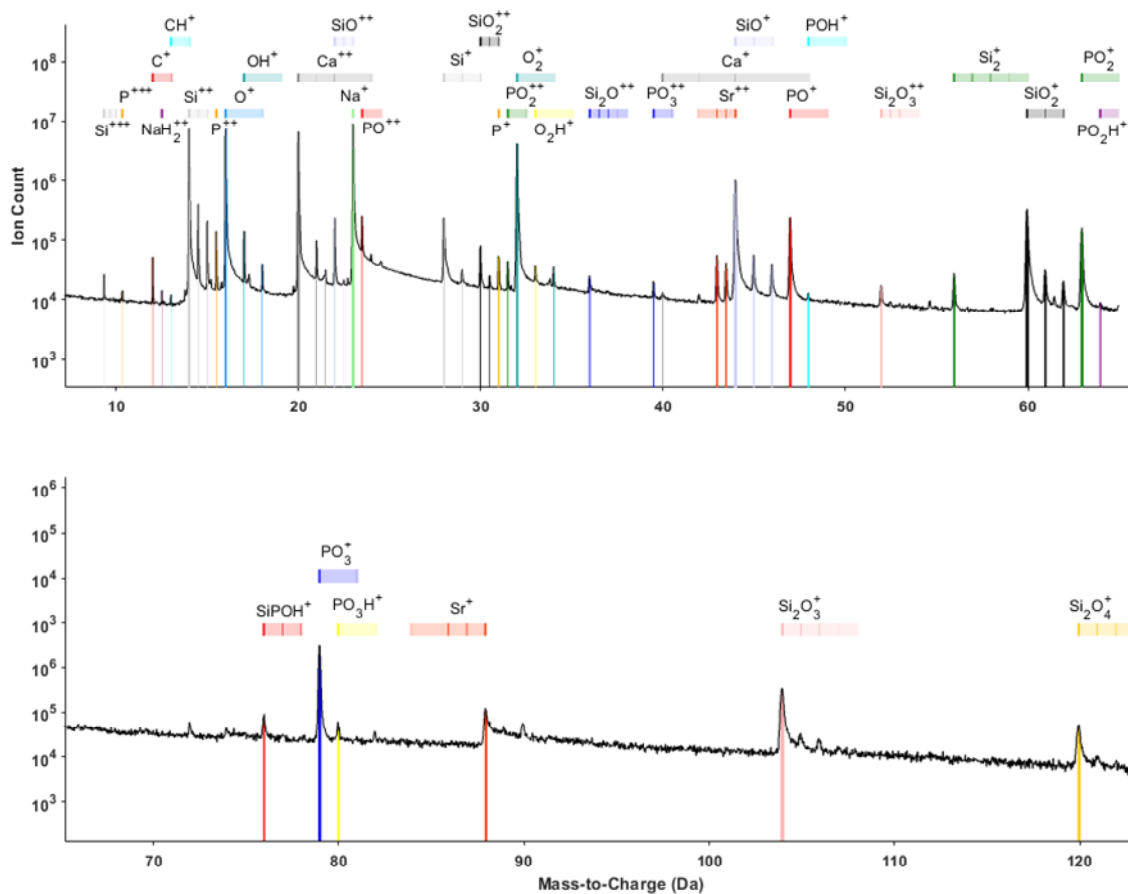


Figure 46. The mass spectrum of the BG-Sr10 (5-120 Da).

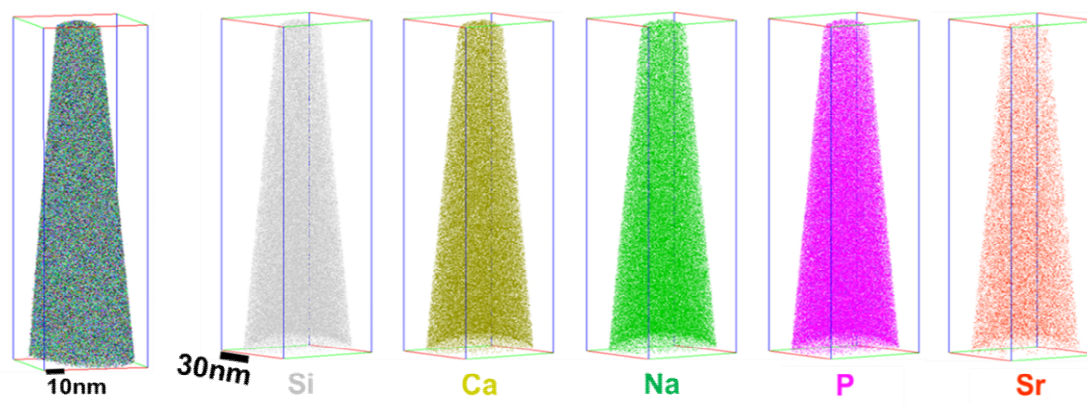


Figure 47. Atom maps for all ions and separately for silicon, calcium, sodium, phosphorus, and strontium of the BG-Sr10.

5.2.3. Composition Analysis

Peak overlaps contributions of BG-Sr10 were deconvoluted by using the Atom Probe Lab v2.1.4 Overlap Group Tool. Table 6 indicates which ions potentially overlap and the corresponding mass-to-charge-state ratio values positions. These overlaps can be resolved by calculating contributions using the relative amplitudes of associated neighboring isotope mass peaks based on their natural abundances. More specifically, most of these overlaps can be deconvoluted by calculating the contribution of each ion to a single total peak based on the size of each corresponding relative abundance of non-overlapping isotope peaks. The ratio of valuable data in BG-Sr10 is 6/14. Some tips were broken before enough ion counts were obtained, and some tips had poor data quality due to factors such as high background, those all resulted in data with low value. The average bulk composition from 6 data sets of BG-Sr10 is shown in Table 7. Apart from the good agreement of Si and Na, there are some differences between the bulk composition measured by APT and the nominal composition, with overestimation of Ca, P, Sr and a

deficit of O. The issue of deficient oxygen in APT measurements is a well-documented problem in the analysis of a variety of materials [195-201]. The origins of this issue are not fully resolved. The most accepted current explanation is underpinned by the known process of decomposition of complex molecular ions into charged or neutral fragments en route to the detector by the electric field. If neutral O species are formed, it is likely that they will not be detected as they are no longer sufficiently accelerated by the electric field to be registered by the detector [202], this leads to the systematic underestimation of O concentration. The atomic percentage value is used when calculating the bulk concentration of the specimen by APT, if the percentage value of O is underestimation, it will cause the ratio of other components to increase, thus making the final result overestimate the content of other components. The over-measurement of Ca and P is prevalent in APT of biomaterials, while similar discrepancies have also been reported in other studies of hydroxyapatite and nacre [113, 149]. It is suspected that the origins of these can be ascribed to limitations within the atom probe measurement, as there are also many factors that can potentially affect the accuracy of concentration measurements. For example, the non-conductive nature of these samples can cause high levels of background noise in the mass spectra. Furthermore, due to the complex composition of biological materials and the existence of a large variety of complex molecular ions, the distribution of which can change significantly from experiment to experiment, it is possible that not all peaks in the mass spectra are correctly identified. Furthermore, there are no universally agreed upon ranging standards applicable to APT data analysis, and the definition of peak widths when ranging can affect the measured composition (range widths and peak maxima location may vary slightly across different datasets). For example, too narrow range may result in data loss (insufficient ion count), while too wide range may lead to too much background noise to be added to the component analysis. This issue is

exacerbated, with the existence of thermal tails that can complicate ranging further. However, in certain cases, comparing the concentrations measured by APT to the nominal value can provide some guidance as to whether the identification of some peaks of the relevant elements is reasonably or not.

Table 6. Overlapping peaks in the BG-Sr10 mass spectrum.

Mass-to-charge-state Ratio	Ion 1 and Charge	Ion 2 and Charge	Ion 3 and Charge
14	Si ⁺⁺	CH ⁺	
22	Ca ⁺⁺	SiO ⁺⁺	
23	Na ⁺	SiO ⁺⁺	
30	Si ⁺	SiO ₂ ⁺⁺	
31	SiO ₂ ⁺⁺	P ⁺	
43	Sr ⁺⁺	Ca ⁺	
44	Ca ⁺	Sr ⁺⁺	SiO ⁺
48	POH ⁺	Ca ⁺	
60	SiO ₂ ⁺	Si ₂ ⁺	

Table 7. Comparison of normal and measured bulk composition by APT of the BG-Sr10. APT compositions calculated with use of Atom Probe Lab v2.1.4 (A. J. London 2020)

Ion Type	BG-Sr10-09	BG-Sr10-10	BG-Sr10-11	BG-Sr10-12	BG-Sr10-13	BG-Sr10-14	Average	Nominal	EPMA
O	47.661	48.075	47.654	47.062	48.419	49.544	48.069	55.203	56.310
Si	15.781	17.096	16.637	16.440	18.463	18.264	17.114	16.216	17.450
Ca	15.702	14.142	13.787	14.113	14.129	12.637	14.085	8.54	8.360
Na	16.144	16.599	17.616	18.038	14.539	15.449	16.398	17.213	15.210
P	2.451	2.542	2.397	2.405	2.718	2.692	2.534	1.834	1.840
Sr	1.504	1.493	1.347	1.368	1.337	1.368	1.403	0.949	0.780
C	0.757	0.053	0.563	0.573	0.394	0.045	0.398	0	0

5.2.4. Comparison of BG-Sr10 with BG-Sr100

Compositionally, BG-Sr100 lacks the presence of Ca in composition and contains 10 times higher Sr than BG-Sr10. The morphology of BG-Sr100 particles is similar to BG-Sr10 (more details can be found in Section 3.1.1), and the needle preparation method and process are basically the same. The atom probe operating conditions for the two types of materials are listed in Table 8. A typical APT mass spectrum of BG-Sr100 is shown in Figure 48, the interpretation of which is basically the same as that of BG-Sr10, with key differences apparent in the increase in the proportion of the Sr^{2+} (42-44 Da) peaks and the decrease or absence of the Ca^{+2+} (20, 40 Da) peak. In theory, since BG-Sr100 does not contain Ca, there should be no peaks corresponding to Ca in the expected mass spectrum. Interestingly the peak of 40 Da is absent in the mass spectrum, however, the peak of 20 Da was still observed, but with a significant reduction in proportion (from 8.55% in BG-Sr10 to 0.044% in BG-Sr100). Combined with the overestimation of Ca in the previous BG-Sr10 component analysis, it is suspected that there is an, as yet, unidentified complex ion overlapping with Ca^{2+} at the peak of 20 Da. Figure 49 compares the 20 Da peak in the mass spectra of (a) BG-Sr10 and (b) BG-Sr100. After screening, the most likely additional element at 20 Da is NaOH^{2+} . However, since there is no corresponding single charge peak of NaOH at 40 Da or related neighboring isotopic peaks (e.g. 20.5 Da), its existence cannot be confirmed, and furthermore, the calculation of this overlapping peak cannot be solved. Another possible ion source for the 20 Da peak could be Ar^{2+} , which could be introduced during the initial sputtering of platinum on the specimen. In the sample of BG-Sr100, considering that the contribution of the peak of 20 Da to the overall concentration is only slight, the influence of the peak of 20 Da was not considered in the final calculation of its bulk concentration.

Table 9 shows the positions and corresponding elements of overlapping peaks in

the BG-Sr100 mass spectrum. Figure 50 compares the overlapping peak deconvolution calculation of Sr^{2+} and SiO^+ for BG-Sr10 and BG-Sr100 at the peak of 44 Da. It indicates that Sr^{2+} accounted for 27.57% of the overlapping peak in BG-Sr10 and 86.05% in BG-Sr100. The comparison of composition analysis of BG-Sr10 and BG-Sr100 is shown in Table 10. The measured contents of O, Si, Na, and P in BG-Sr10 and BG-Sr100 are very consistent. However the Sr content in BG-Sr100 is still nearly 1.5 times higher than the nominal composition. Compared with the Sr content in BG-Sr10, the Sr level in BG-Sr100 is indeed 10 times higher as expected. This adds confidence to compositional measurement in both materials. Furthermore, in future studies, comparisons between data are recommended to report measurements of "relative" compositional ratios such as Ca/Sr, rather than the composition of individual elements.

Table 8. List of experimental conditions for atom probe runs for BG-Sr10 and BG-Sr100.

Sample type	Specimen No.	Temperature (K)	Detection Rate (%)	Frequency (KHz)	Laser Pulse (pJ)	Spectrum Counts
BG-Sr10	R5083_08873	30	0.3	200	200	20.0 M
	R5083_08962				250	29.0 M
	R5083_09936				200	13.1 M
BG-Sr100	R5083_09949	30	0.3	200	225	9.7 M
	R5083_09942				250	27.9 M

5: Atom Probe Analyses of Synthetic Bone Substitutes

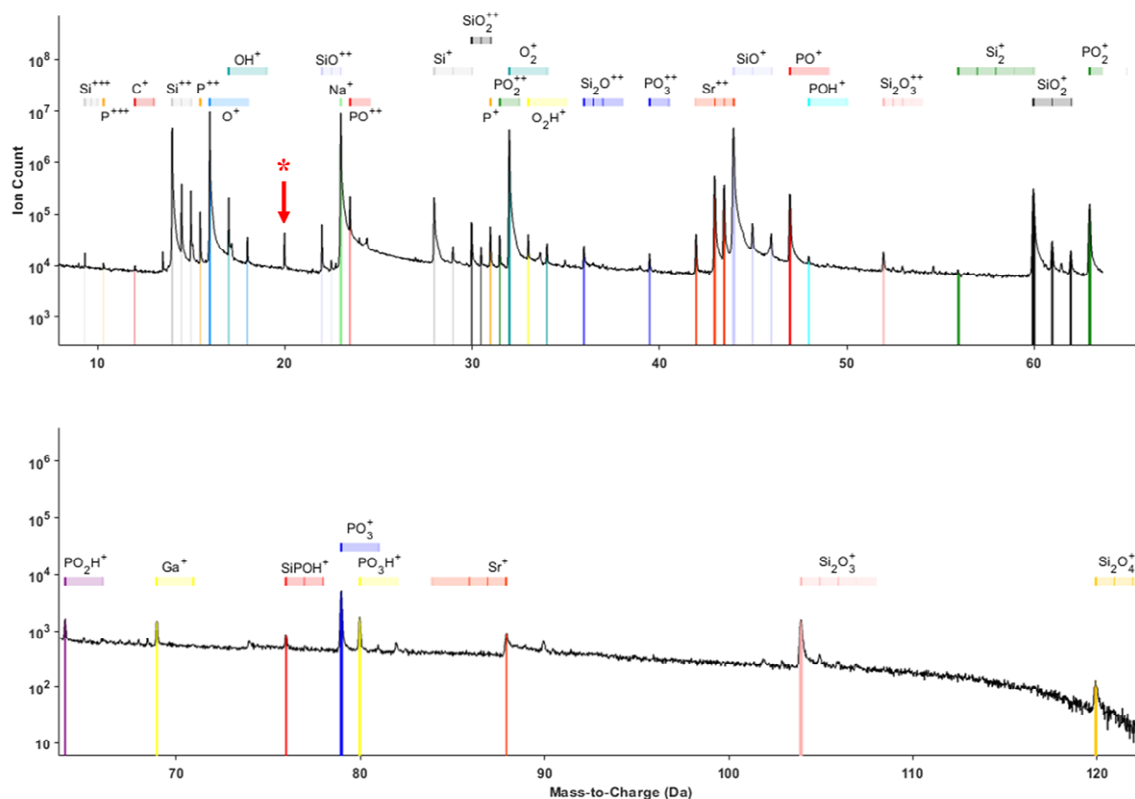


Figure 48. The mass spectrum of BG-Sr100 (5-120 Da), * represents the unidentified peak of 20 Da.

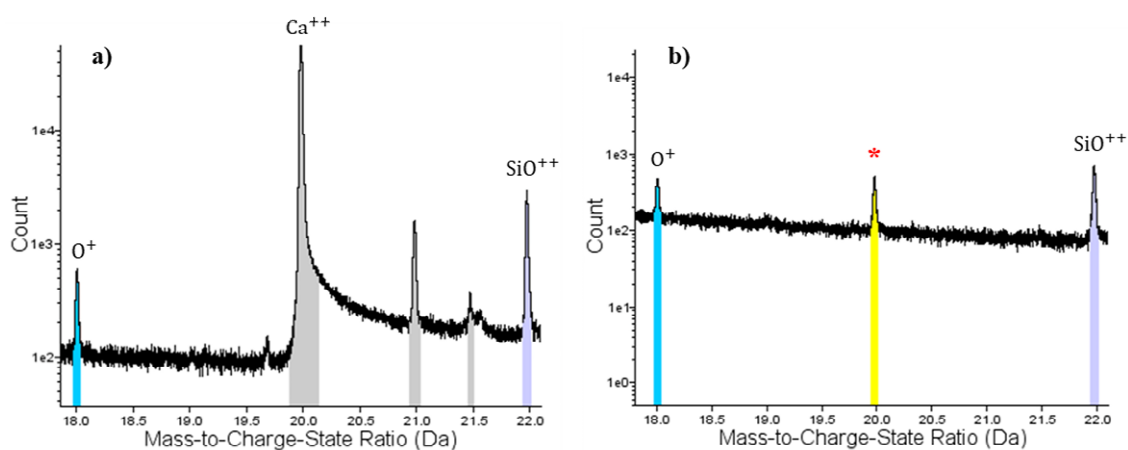


Figure 49. Comparison of 20 Da in (a) BG-Sr10 and (b) BG-Sr100 m/q spectra, ‘*’ represents the unidentified peak of 20 Da in the latter.

Table 9. Overlapping peaks in the BG-Sr100 mass spectrum.

5: Atom Probe Analyses of Synthetic Bone Substitutes

Mass-to-charge-state Ratio	Ion 1 and Charge	Ion 2 and Charge
23	Na^+	SiO^{++}
30	Si^+	SiO_2^{++}
31	SiO_2^{++}	P^+
44	Sr^{++}	SiO^+
60	SiO_2^+	Si_2^+

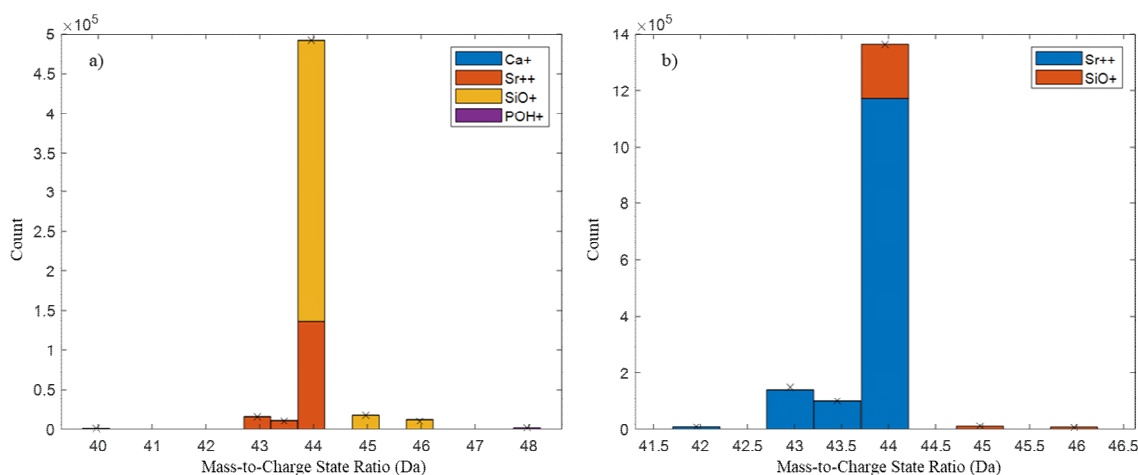


Figure 50. Comparison of overlapping of Sr^{2+} and SiO^+ in (a) BG-Sr10, the peak of 44 Da contains 27.57% Sr^{2+} and 72.41% SiO^+ . (b) BG-Sr100, the peak of 44 Da contains 86.05% Sr^{2+} and 14.03% SiO^+ .

Table 10. Comparison of composition analysis of BG-Sr10 and BG-Sr100. APT compositions were determined using Atom Probe Lab v2.1.4 (A. J. London 2020).

Ion Type	BG-Sr10				BG-Sr100				
	R5083_08873	R5083_08962	Average	Nominal	R5083_09936	R5083_09949	R5083_09942	Average	Nominal
O	48.419	49.544	48.069	55.203	48.221	48.662	49.192	48.692	55.203
Si	18.463	18.264	17.114	16.216	16.688	16.525	17.627	16.947	16.261
Ca	14.129	12.637	14.085	8.54	0.000	0.000	0.000	0.000	0
Na	14.539	15.449	16.398	17.213	18.228	17.703	15.134	17.022	17.213
P	2.718	2.692	2.534	1.834	2.529	2.569	2.611	2.570	1.834
Sr	1.337	1.368	1.403	0.949	14.332	14.538	15.435	14.768	9.49
C	0.394	0.045	0.398	0	0.002	0.002	0.002	0.002	0

5.3. Sr-Releasing Bioactive Glass-based (pSrBG) Scaffold

The composition (at %) of pSrBG scaffold can be found in Table 3. The scaffold is slightly different from bioactive glass in that K and Mg have been added to the material. Based on the discussed previous experience in parameter optimization of the bioactive glass particles, a more standardized comparison and optimization of APT experimental parameters is performed on the pSrBG scaffold with LEAP-5000XR. Parameters other than pulse energy, such as operating temperature (K), detection rate (%), and pulse frequency (kHz) are also compared and optimized.

5.3.1. APT Operating Conditions Optimization

A series of optimization experiments exploring temperature, detection rate, and pulse frequency were conducted on the pSrBG scaffold (Table 11). As the scaffold microstructure is also homogeneous, approximately 2,000,000 ions were collected under each unique condition which is can be assumed to be representative of direct comparative analysis, rather than running the entire tip to completion for each analysis condition, as was the case for the bioactive glass particle experiments.

Table 11: Experimental conditions were used to determine the optimal experimental conditions for analyzing pSrBG. (a) Detection rate and corresponding temperatures. (b) Pulse frequencies and corresponding temperatures

a)		b)	
Detection rate (%)	Temperature (K)	Pulse Frequency (kHz)	Temperature (K)
0.3, 0.4, 0.5	30, 40, 50	100, 125, 200	30, 40, 50

Firstly, the operating temperature and detection rate were systematically varied at a constant pulse frequency (200 kHz) to investigate effects of the operating temperature and detection rate (Table 11 (a)) on data quality in laser-pulsing mode of a LEAP-5000XR. The effect of pulse frequency was then investigated by systematically varying the pulse frequency and operating temperature at a constant detection rate (0.4%) (Table 11 (b)). It has been previously observed that increases in laser energy can reduce the occurrence of multiple events, so based on the results of the bioactive glass particles, a laser energy of 200 pJ was used for all experiments to minimize this effect to minimize data loss and improve overall quality of analysis.

5.3.1.1. Operating Temperature and Detection Rate.

It was found that changing the stage temperature of the instrument while maintaining the pulse frequency at 200 kHz affected the Sr levels detected in the analysis. Figure 51 shows that the measured strontium content increases with increasing temperature, and similar to the previous exploration of bioactive glass, the Sr concentration measured by APT was higher than the nominal concentration. This phenomena occurred in these experiments for all detection rates used. Figure 52 shows that Ca behaves similarly to Sr and was also affected by temperature. The higher the temperature, the higher the measured Ca concentration and the change is most drastically at the detection rate of 0.5%. The measured P composition was also found to depend on the stage temperature, with less P detected at high temperatures, but still overestimated than the nominal concentration (Figure 53). Oxygen concentration was found not to change significantly with temperature. The increase in the measured composition with increasing operating temperature may be the result of multiple events. As the temperature increases (holding other parameters constant), the required evaporation field for ions

evaporation to occur decreases, and multiple events decrease. Since the evaporation of Ca prefers to exist as single ions, the reduction of multiple events means more Ca is efficiently detected at the detector. The evaporation of P prefers to exist in the form of complex molecule ions such as P_xO_y ($x, y \geq 1$). At lower evaporation field the complex molecule ions are preferentially evaporated, while the detection loss of heavy complex ions (e.g. P_2O_5) within a limited time detection window may lead to the underestimation of P. The effect of varying pulse frequency at different temperature on P Composition in Figure 105 (Chapter 9) further support the idea of heavy complex ions loss at a higher temperature. Furthermore, less oxygen neutral species are expected to be lost at lower fields, it is possible that O experiences a combined effect of fewer multiple hits and greater molecular loss, both effects canceling each other out, resulting in no significant change in O concentration. This phenomenon can thus be minimized by using lower stage temperatures when analysing the pSrBG scaffold.

The detection rate is defined as the average number of atoms detected on a single pulse. In the laser mode, the sample is more likely to fracture with a higher detection rate. This is because in order to generate enough ions in each pulse, a higher electric field is required on the tip. It was found that the change in concentration was minimized at the 0.4% detection rate. In this series of experiments, background levels for each experiment were lower at a detection rate of 0.4% (Figure 54, left). Besides, the proportion of Sr^{2+} in the overlapping peak of 44 Da can be observed to be lower at the 0.4% detection rate (Figure 54, right). Combining effects of the background level, concentration changes, multiple events, and the charge state ratio of Sr, the optimal experimental temperature and detection rate of the pSrBG scaffold was assessed to be 30 K and 0.4%.

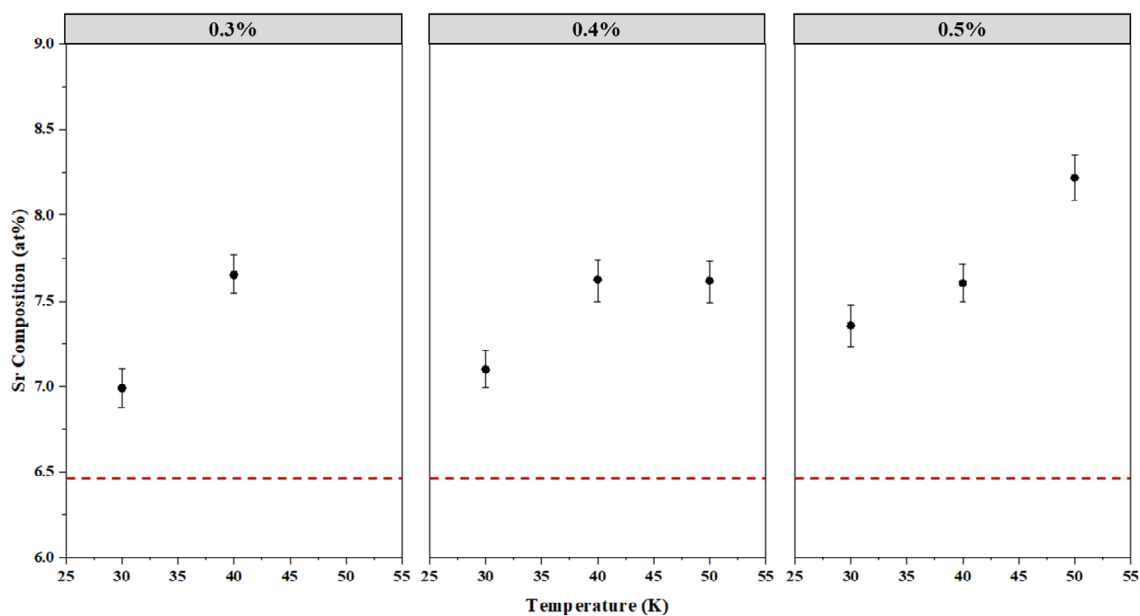


Figure 51. Graphs showing the effect of varying operating temperatures at different detection rates on Sr Composition, the dashed red line is representative of the nominal Sr composition of the pSrBG. Error bars represent 95 % confidence intervals based on deconvolution.

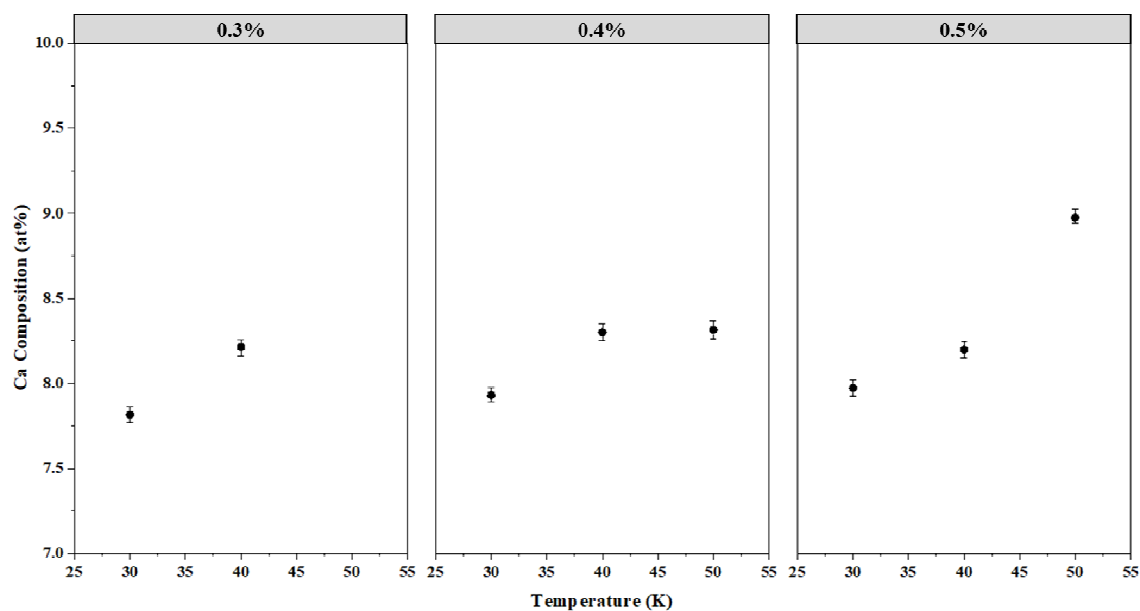


Figure 52. Graphs showing the effect of varying operating temperatures at different detection rates on Ca Composition, the nominal Ca composition of the pSrBG is 6.468%. Error bars represent 95 % confidence intervals based on deconvolution.

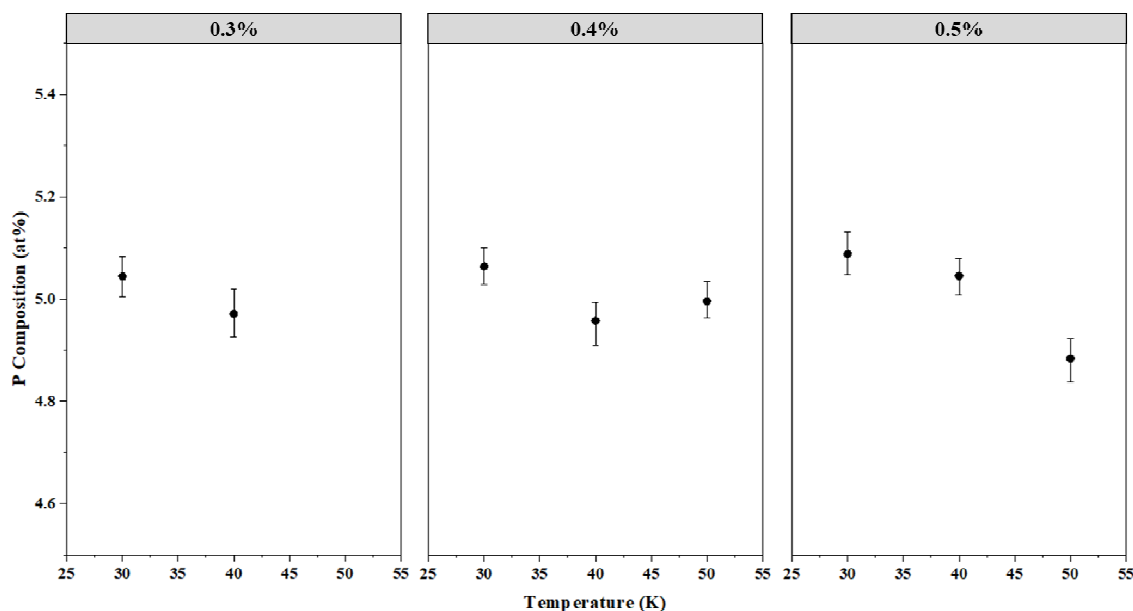


Figure 53. Graphs showing the effect of varying operating temperatures at different detection rates on P Composition, the nominal P composition of the pSrBG is 3.270%. Error bars represent 95 % confidence intervals based on deconvolution.

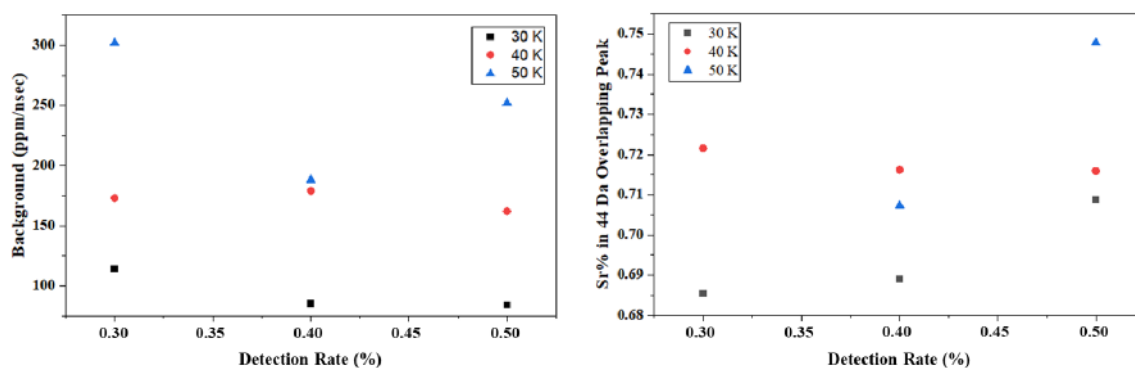


Figure 54. Graphs showing the effect of varying detection rates at the different temperatures on the background level (left graph) and the proportion of Sr^{2+} in the overlapping peak of 44 Da (right graph).

5.3.1.2. Pulse Frequency

In the laser pulsed mode, a lower pulse frequency is generally recommended. Firstly, because the laser mode is commonly applied to non-conductive samples, a higher pulse rate means a shorter time detection window. If the time between pulses is short of

that needed to conduct heat away from the sample surface, this can lead to an increase in the temperature of the specimen, a corresponding decrease in mass resolution, and result in an increase in the background level [106]. Secondly, for biological samples containing large amounts of macromolecular ions, the time-of-flight of heavy molecular ions may be too long to be detected within the shorter detection window, resulting in a specific loss of these ions [203], affecting composition measurements. In a series of experiments carried out in the current work, pulse frequency was however not found to have a significant effect on measured components of Sr, Ca and P (Figure 55). This may be the reason for the small range in the pulse frequencies tested of 125 kHz to 200 kHz. The left graph in Figure 56 shows the effect of different pulse frequencies on the background level. Similar to that of the concentration measurements, no conclusive results on the role of pulse frequency were obtained. Previous work by Gordon et al., established that increasing pulse frequencies (100-1000 kHz) resulted in a significant increase in background levels [21]. The proportion of Sr^{2+} in the overlapping peak of 44 Da increases with increasing pulse frequency (Figure 56, right). The author considers that a pulse frequency of 125 kHz is optimal for the pSrBG scaffold.

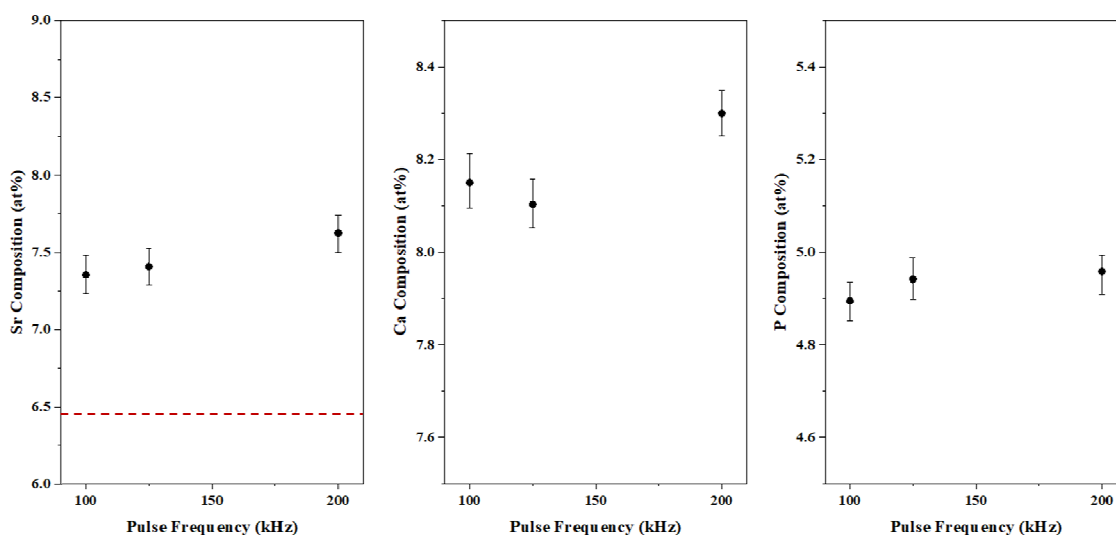


Figure 55. Graphs showing the effects of varying pulse frequency on Sr, Ca, and P compositions (at a constant detection rate of 0.4%, a temperature of 40K, and laser energy of 200pJ). The dashed red line in the left graph is representative of the nominal Sr composition, the nominal Ca and P composition is 6.468% and 3.270% respectively. Error bars represent 95 % confidence intervals based on deconvolution.

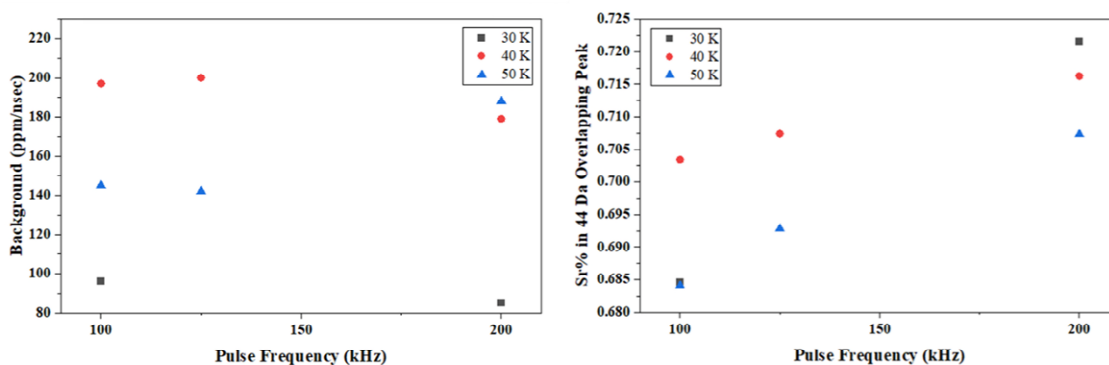


Figure 56. Graphs showing the effect of varying pulse frequency at the different temperatures on the background level (left graph) and the proportion of Sr^{2+} in the overlapping peak of 44 Da (right graph).

5.3.1.3. Pulse Energy

Previous analyses of bioactive glass particles have concluded that the optimal range of laser pulse energy for bioactive glass is approximately 200-250 pJ. Figure 57 explores the effect of different pulse energy on the composition of Sr, Ca, and P (left graph) and the ratio of Sr^{2+} in the 44 Da overlapping peak (right graph). The results of both concentration measurements and the Sr charge-state-ratio are similar to the previous conclusion from the analysis of the bioactive glass, more discussions of which can be found in Section 5.2.1. Moreover, with increasing laser power, both chemical resolution and background levels steadily improved, and the proportion of multiple hits decreased. The selected optimal pulse energy of the pSrBG scaffold in further experiments is therefore 200 pJ.

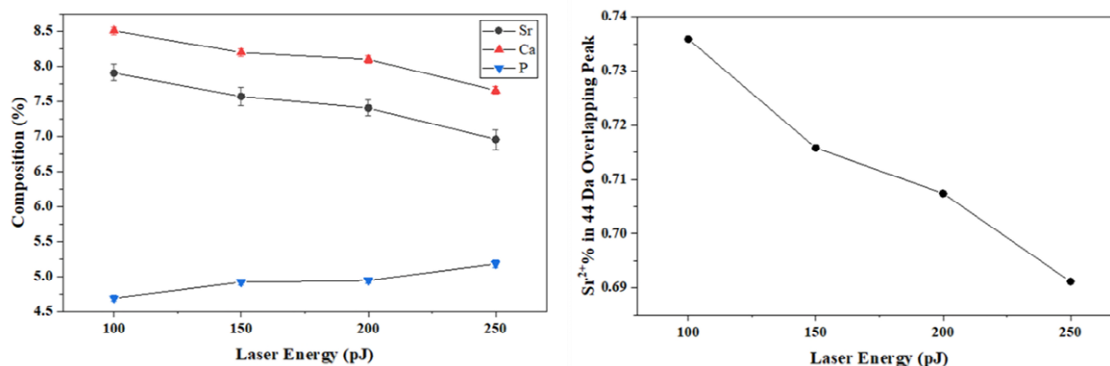


Figure 57. Graphs showing the effect of varying laser energy on Sr, Ca, and P composition (left graph) and the proportion of Sr²⁺ in overlapping peak of 44 Da (right graph). The nominal Sr, Ca and P composition are 6.468%, 6.468%, and 3.270% respectively.

5.3.2. Mass Spectra and Reconstruction Interpretation

In this study, multiple pSrBG specimens were successfully prepared using the tailored FIB-based preparation methods discussed in Chapter 4. Subsequent APT analysis on 6 of these specimens yielded a successful experiment rate of 90% (i.e. significant valid data acquired before tip fracture), incorporating between 12 - 25 million ions in the resulting respective datasets. Table 12 lists some key experimental conditions for atom probe analyses for the pSrBG. A mass spectrum of the pSrBG scaffold is presented in Figure 58, in which 7 million hits were detected using conditions of 30 K stage temperature, 0.4 % detection rate, 125 kHz pulse frequency, and a laser pulse energy of 200 pJ. Corresponding spatial reconstructions of the pSrBG scaffold are presented in Figure 59. All elements are expected to be homogeneously distributed in the sampled region of the microstructure, and this is what is observed in the reconstruction results with each isolated species evenly distributed.

5: Atom Probe Analyses of Synthetic Bone Substitutes

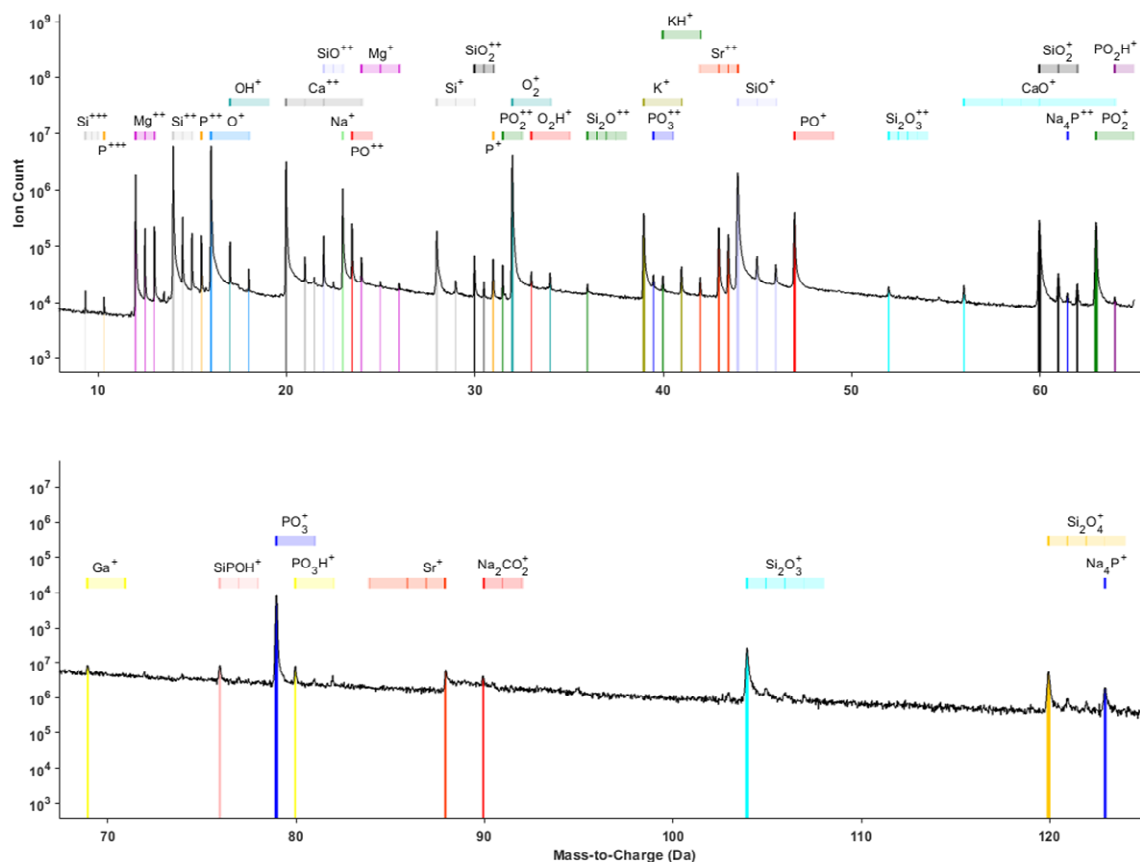


Figure 58. Representative mass spectrum of the pSrBG analysis (5-125 Da).

Table 12. Selected experimental conditions for atom probe runs for the pSrBG.

Specimen No.	Temperature (K)	Detection Rate (%)	Laser Pulse (pJ)	Pulse Frequency (KHz)	Spectrum Counts	Multiple Hits (%)	End State
R5083_10591	30	0.5	200	200	25.0 M	30.35	Good
R5083_10599	30	0.3	200	200	12.6 M	32.40	Fractured
R5083-10748	30	0.4	200	125	7.04 M	30.78	Good
R5083-11647	45	0.3	100	200	19.5 M	26.34	Fractured

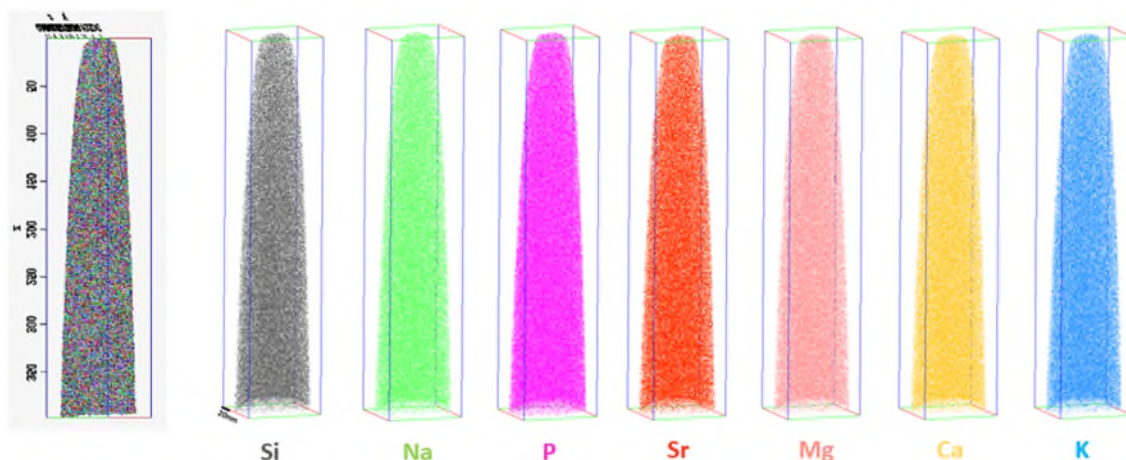


Figure 59. Atom maps for all ions and separately for silicon, sodium, phosphorous, strontium, magnesium, calcium, and potassium of the pSrBG specimen.

5.3.3. Composition Analysis

The scaffolds with added elements of K and Mg are more complex than bioactive glass. Table 13 shows the positions and corresponding elements of overlapping peaks in the mass spectrum. Peak overlap contributions of the pSrBG were again deconvoluted by using Atom Probe Lab v2.1.4 Overlap Group Tool. The measurement of the composition of the pSrBG scaffold by APT (Table 14) was similar to the previous situations for bioactive glass. There are many factors affecting the concentration measurements by APT, as discussed in depth previously in Sections 5.2.2 and 5.2.3. Upon inspection of the ion distribution maps and the corresponding 1D concentration profile through the major tip axis (z-direction) (Figure 60), it can be seen that the ions distributions of the pSrBG are all uniform within the extent of the APT analysis, which also indicates that the analysis process of the pSrBG is stable throughout the length of the experiment.

Table 13. Overlapping peaks in the pSrBG mass spectrum.

5: Atom Probe Analyses of Synthetic Bone Substitutes

Mass-to-charge-state Ratio	Ion 1 and Charge	Ion 2 and Charge	Ion 3 and Charge
22	SiO ⁺⁺	Ca ⁺⁺	
23	Na ⁺	SiO ⁺⁺	
24	Ca ⁺⁺	Mg ⁺	
30	Si ⁺	SiO ₂ ⁺⁺	
31	SiO ₂ ⁺⁺	P ⁺	
42	Sr ⁺⁺	KH ⁺	
44	SiO ⁺	Sr ⁺⁺	Ca ⁺
60	SiO ₂ ⁺	CaO ⁺	
64	CaO ⁺	PO ₂ H ⁺	
122.9	Si ₂ O ₄ ⁺	Na ₄ P ⁺	

Table 14. Comparison of normal and measured bulk composition by APT of the pSrBG. APT compositions determined using Atom Probe Lab v2.1.4 (A. J. London 2020)

Ion Type	R5083_10591	R5083_10599	R5083-10748	R5083-11647	Average	Nominal
O	53.216	53.549	52.023	54.117	53.226	59.084
Si	17.028	17.303	16.789	17.051	17.043	16.170
Na	2.555	2.457	2.687	2.430	2.532	2.907
Ca	9.088	8.677	9.461	8.631	8.964	6.468
P	4.506	4.593	4.435	4.574	4.527	3.270
Sr	7.867	7.685	8.664	7.770	7.996	6.468
K	1.591	1.578	1.631	1.474	1.568	2.907
Mg	4.140	4.153	4.302	3.944	4.135	2.725
C	0.009	0.007	0.008	0.009	0.008	0.000

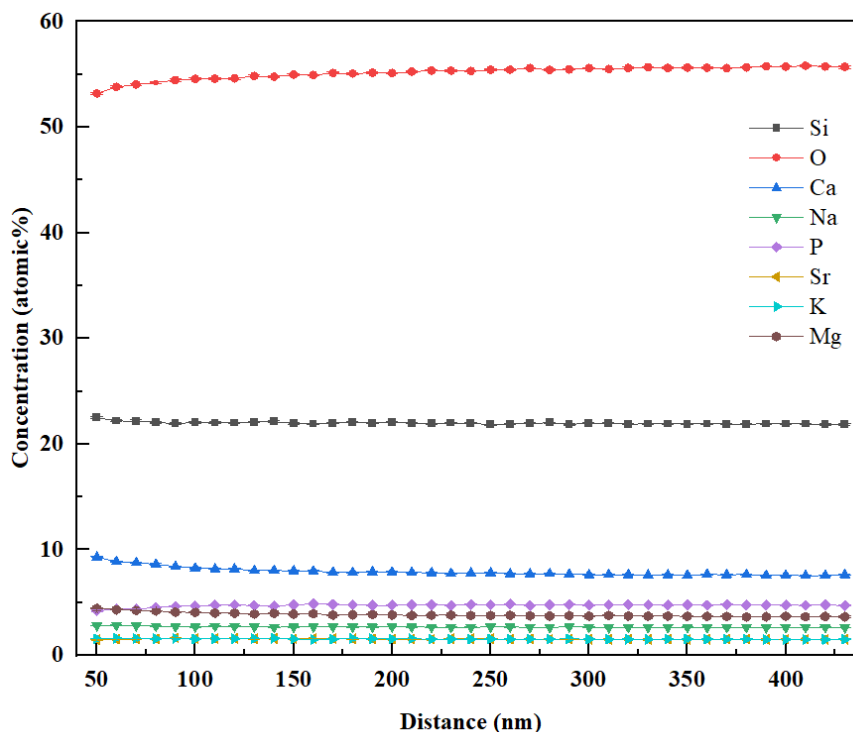


Figure 60. 1D concentration profile (through tip depth) of the pSrBG. The profile shown is background corrected, with molecular ions decomposed into their constituent elements.

5.4. Summary

This chapter explores the factors affecting the APT analysis of synthetic bone substitutes. Effects of experimental parameters such as temperature, detection rate, pulse frequency, and pulse energy on data quality such as mass spectrometry background level, multiple hits, mass-to-charge-state ratio, and reporting compositions were analyzed and discussed for two strontium-containing bioactive glass particles and the pSrBG scaffold. A balance needs to be sought among the various parameters. A short summary of each parameter is listed below.

- Temperature: overcooling leads to rapid fracture of the specimen before valid data can be obtained, while overheating causes increased background, increased irrelevant evaporation, and reduced mass spectral quality.
- Detection rate: in the laser mode, the needle is more likely to fracture with a higher

detection rate.

- Laser energy: increasing laser energy has the beneficial effect of decreasing multiple hits, but also worsens mass resolution through the formation of thermal tails in the spectra.
- Pulse frequency: for biological samples containing large amounts of macromolecular ions, lower pulse frequencies are generally recommended, which means a longer detection window to avoid the continuous increase of the temperature at the sample surface, and reduce the specific detection loss of macromolecular ions.

After comprehensive consideration, the optimal operating conditions for the analysis of various materials using the LEAP-5000XR were determined. For bioactive glass (BG-Sr10/BG-Sr100), it is recommended to use conditions of a stage temperature of 30 K, a detection rate of 0.3%, a pulse frequency of 200 kHz, and a laser pulse energy of 200-250 pJ. For the pSrBG scaffold, the best experimental conditions recommended are a temperature of 30 K, a detection rate of 0.4%, a pulse frequency of 125 kHz, and a laser pulse energy of 200 pJ. In addition to the optimization of experiment conditions, 3D reconstructions and compositional measurements were presented for each material in this chapter. APT can successfully and stably analyze synthetic bone substitute materials such as strontium-containing bioactive glass, and the pSrBG scaffold, guiding future research aimed at examining the APT exploration of animal bones and providing parameter support and data reference for future research on the interface between bioactive glass and animal bones. This chapter has a thorough research and discussion on the various parameters of APT on biomaterials, which may provide the researchers who are engaged in the APT research of any new materials in the future with the idea of parameter optimization or may provide some valuable references for researches of similar materials by APT.

Chapter 6

Atom Probe Analyses of Porcine Trabecular Bone

6.1. Introduction

Bone is a composite biomaterial the structure of which consists of organic phases, mineral phases and water. The organic phase is mainly composed of type I collagen, and the mineral phase is widely accepted to contain mineral crystals composed of nonstoichiometric calcium [204]. Structurally, bone can be distinguished between cortical and trabecular bone [205]. Trabecular bone is a spongy, porous bone found at the end of all long bones, and present in flat and irregular bones [206]. From the perspective of an engineering material, trabecular bone is a composite, anisotropic, three-dimensional, interconnected porous solid material, and its pores are filled with bone marrow and cells [206-208]. The tissue material of the trabecular is morphologically similar to cortical bone which consists of hydroxyapatite (HA), collagen, water, and trace amounts of other proteins [209]. However, trabecular bone has different material properties compared to cortical bone. Trabecular bone has lower calcium content and is lighter and less dense, whereas trabecular bone is highly vascularized with higher organic matter and water content than cortical bone making it more elastic [121, 210].

The nanoscale structure of collagen and mineral apatite in bone determines the physical properties of bone, including strength and toughness. The initially widely accepted model assumed that mineral apatite was mainly present in the interior of collagen fibrils, and that it resides and grows in "gap channels" between abutting collagen molecules and in "intermolecular spaces" between adjacent collagen molecules [211-214].

Subsequent investigators explored extrafibrillar mineral apatite between non-mineralized collagen fibrils, proposing that the initial mineral apatite nucleation and growth were not confined to the gap channels [215]. The study of collagen-mineral in bone is mainly limited to in vitro systems that only approximate the biological environment [216-218] or transmission electron microscopy studies with lower spatial and chemical resolution [120, 219-222]. Therefore, there is still extensive debate on nanostructures within the bone.

A few studies have reported the exploration of cortical bone using atom probe tomography [25, 112], but the more challenging trabecular bone has not been studied by APT. This chapter uses APT to perform a four-dimensional analysis of the spatial structure and chemical composition of porcine trabecular bone. Therein, the optimal operating conditions for the analysis of porcine trabecular bone using the LEAP-5000X are determined. Porcine trabecular bone is sampled in different directions, i.e. vertical/parallel to the trabecular rod, to obtain APT tips containing different orientations of collagen fibrils. The complex APT mass spectrum of porcine trabecular bone is ranged and carefully interpreted. 3D reconstructions of specimens containing different orientations of collagen fibrils are presented. Furthermore, the distribution of major elements in the bone between the organic and inorganic phases is also investigated. The components of different phases of porcine trabecular bone are studied and compared. Finally the limitations and challenges of APT for trabecular bone research are discussed.

6.2. APT Operating Conditions Optimization

The porcine trabecular bone sample investigated in this chapter is shown in Figure 24 (Section 3.1.3). Porcine trabecular bone APT needle-shaped specimens were prepared using the method discussed in Section 4.4. Table 15 presents a summary of total of 24 APT experiments that were performed on porcine trabecular bone tips, subdivided into seven groups. Initially, based on a systematic selection of parameters for synthetic bone substitutes, the parameters previously used for bioactive glass and pSrBG scaffold were used to conduct experiments on the porcine trabecular bone, as represented by the analyses in Group 1. Although experiments in Group 1 acquired sufficient spectrum counts to be considered viable experiments, the quality of the data acquired was extremely poor, incorporating: many specimen mini-fractured apparent in the experiments' voltage history, very large and messy background, and very low-resolution mass spectra (Figure 61). This further demonstrates the necessity for optimization of APT operating conditions for each different materials analyzed, even those ostensibly similar. In order to reduce the background level and occurrences of mini-fractures, the specimen temperature was increased and the operating laser energy was decreased in the experiments denoted as Group 2. These adjustments, significantly improved the specified problems observed in the Group 1 data, greatly improving the resolution of the mass spectrometry (Figure 62). However, under these conditions not enough ion counts were obtained for APT reconstructions to undertake significant spatial analysis in Group 2 samples. The limited data obtained from Group 2, was useful in that it demonstrated two distinct types of mass spectra when sampling porcine trabecular bone, one dominated by the detection of Ca ions and the other by the detection of C ions as shown in Figure 62. It is believed that different phases were detected at the very top of different specimens in Group 2 because of the non-homogeneous distribution of the two phases within the porcine trabecular bone,

but the specimens fractured in the experiment before more data was obtained sampling both phases in the same analysis. In order to obtain sufficient spectrum counts for larger spatial reconstruction, an attempt was made to use a metal i.e. gold, to circular coated on the tip to increase its electrical and thermal conductivity. However, all of experiments, denoted as Group 4, ended in rapid fracture of the specimen.

A series of optimization experiments, further investigating the effect of temperature, pulse frequency, and laser energy were then undertaken on the porcine trabecular bone. In Figure 63, the effect on the measured background level from changing laser energy at two respective pulse frequencies, is present in left graph. Similarly, the effect on the background level of varying laser energies, at two distinct specimen temperatures, is presented on the right. It is apparent that lower pulse frequency and temperature both tend to lower background levels, while varying the laser energy in the range of 60-100 pJ did not have much influence. Based on these results, the operating conditions of the temperature of 30-40 K, pulse frequency of 125 kHz, and laser energy around 60-100 pJ are recommended for further APT investigation on porcine trabecular bone. After obtained suitable operating conditions all experiments in Group 6 and 7 obtained sufficient spectral counts and good data quality, and the porcine trabecular bone was sampled in different directions, presented in Section 6.4.1 and Section 6.4.2.

6: Atom Probe Analyses of Porcine Trabecular Bone

Table 15. List of experiment conditions for different atom probe runs of porcine trabecular bone.

Group No.	Specimen No.	Temperature (K)	Detection Rate (%)	Frequency (KHz)	Laser Pulse (pJ)	Spectrum Counts
Group 1	R5083_11260	30	0.5	200	200	61 M
	R5083_11261				150	10 M
	R5083_11263				100	40 M
Group 2	R5083_12065	45	0.5	200	125	8.5 M
	R5083_12066		0.3		100	2.5 M
	R5083_12067		0.4		100	2.9 M
Group 3	R5083_12218	45	0.3	200	125	2.0 M
	R5083_12219		0.3		100	1.6 M
Group 4 (Gold coated)	R5083_12121	45	0.5	200	100	<1 M
	R5083_12122		0.3		125	<2 M
Group 5	R5083_12394	40	0.4	125	125	9.6 M
	R5083_12395				100	18 M
Group 6 (Horizontal sampling)	R5083_12600	40	0.3	125	100	11.1 M
	R5083_22613	30	0.4			15.1 M
	R5083_22623	40	0.3			75
	R5083_22723		0.4	60	32.7 M	
	R5083_22923		200	80	52.3 M	
	R5083_22924	125	60	31.8 M		
Group 7 (Vertical sampling)	R5083_23555	30	0.4	125	80	40.5 M
	R5083_23561					69.5 M
	R5083_23567				100	32.4 M
	R5083_23568					47.0 M
	R5083_23613					15.3 M
	R5083_23632					36.1 M

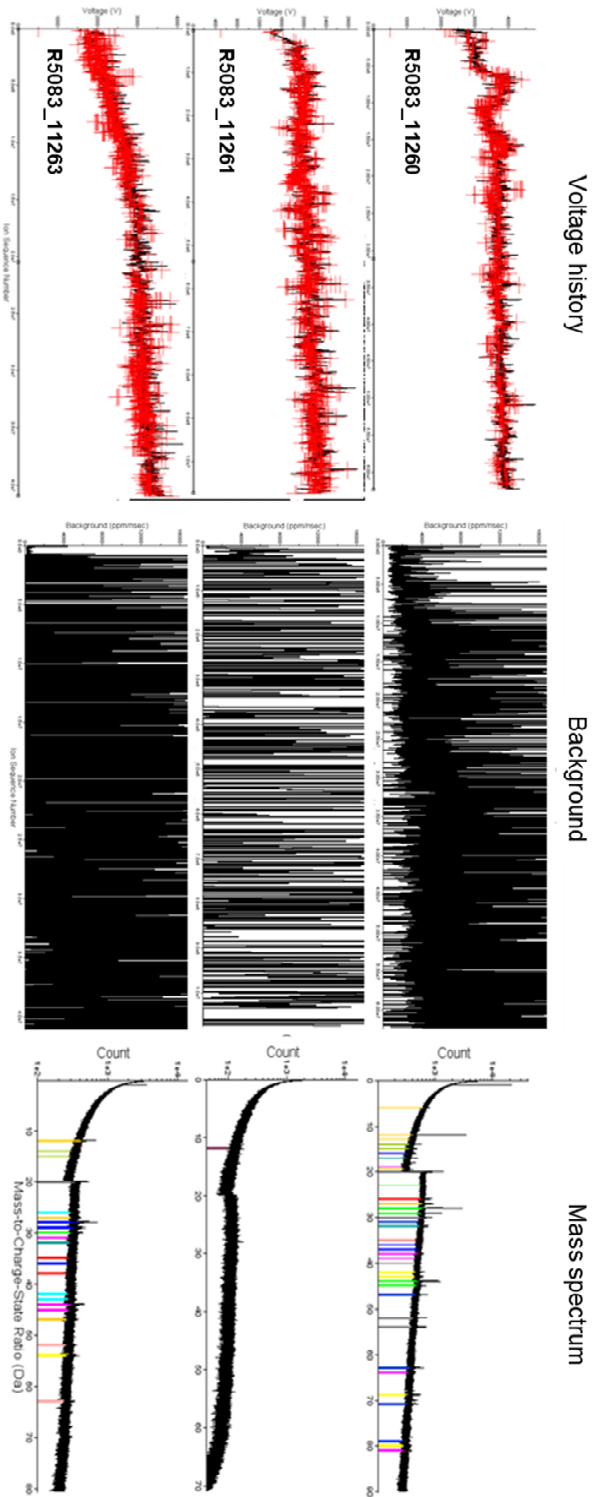


Figure 61. The running status and data quality of experiments in Group 1, the operating conditions for each analysis can be found in the Table 15. A large number of experiments as shown of many red crosses are detected in voltage histories (left), large and messy background (middle), and thus a very low mass resolution of mass spectra (right).

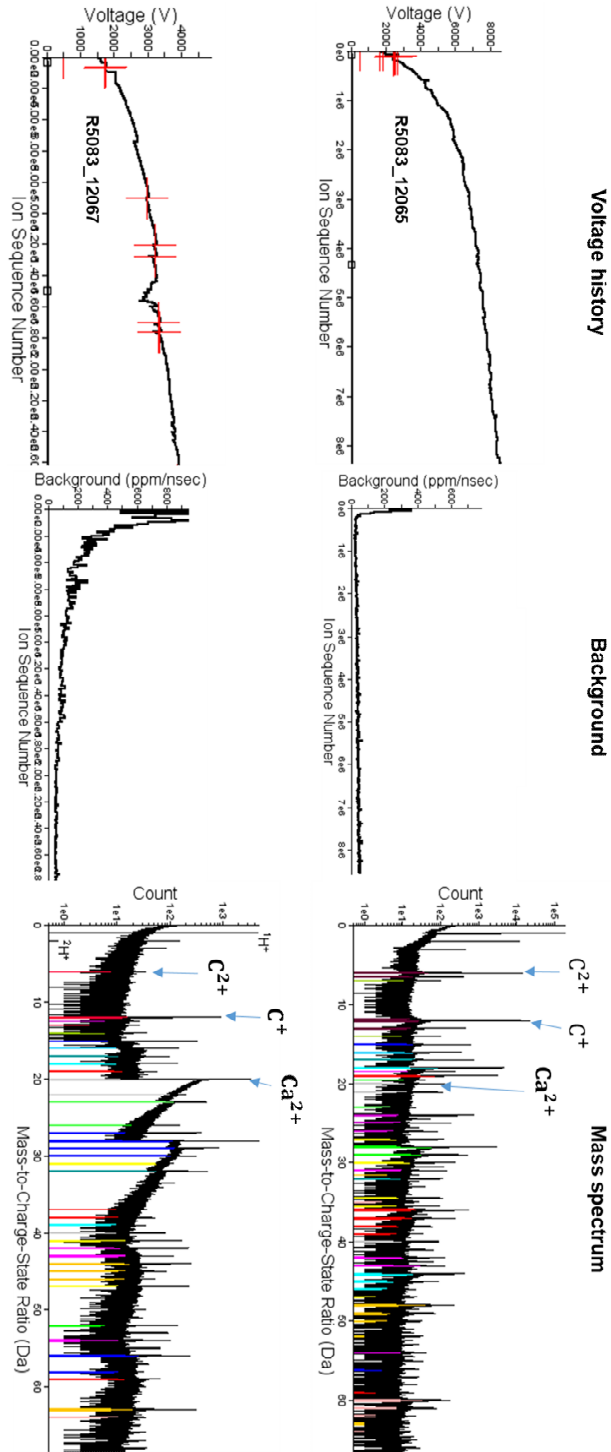


Figure 62. The running status and data quality of experiments in Group 2, the operating conditions for each analysis can be found in the Table 15. Few number of mini-fractures as shown of few red crosses are detected in voltage histories (left), improved background level (middle), and thus improved resolution of mass spectra (right). Two types of mass spectra are obtained, C rich (R5083_12065), and Ca-rich (R5083_12067).

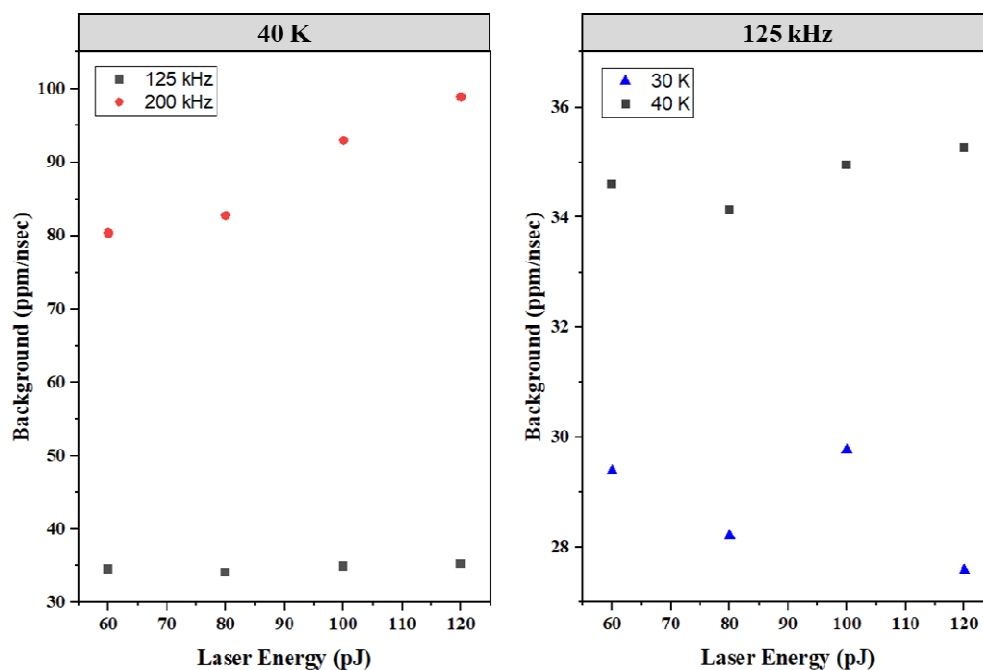


Figure 63. Effect on the background level of varying laser energy at different pulse frequency with a constant temperature of 40 K and detection rate of 0.4% (left). The effect of varying laser energy on the background level at different temperature with a constant pulse frequency of 125 kHz and detection rate of 0.4% (right).

6.3. Mass Spectra Interpretation

6.3.1. Main Structural Components of Bone

Bone composition is similar between living species, but there are differences in the proportions of the incorporated elements, a more detailed comparison between species can be found in the research by Jeroen et al. [223]. Here, important characteristics of the main components of bone will first be briefly summarized to aid in our interpretation of the complex mass spectrum of porcine trabecular bone obtained from APT analysis.

Bone tissue is composed of mineralized collagen fibrils, which are mainly composed of bioapatite (mineral phases) and type I collagen molecules (collagen phases). The main elements of bone can be classified as Ca, P, O, C, N, H, and other essential elements and trace elements contained in bone include Na, Mg, K, F, Cl, Sr, Br, Se, Zn,

Mn, Fe (refer to Table 16). The composition of collagen phase of bone is broadly described as being dominated by carbon and nitrogen, while the mineral phase are considered to be calcium and phosphorus based. The structure of biological apatite is unstable, allowing the chemical substitution of various minor elements to change its composition [224]. Various ionic substitutes for biological apatite can also be found in the bone, as presented in Figure 64. Therefore, in addition to considering basic elements of bone, molecular ions existing in biological ion substitutes, such as CO_3^{2-} and SeO_3^{2-} , should also be considered in APT mass spectrum interpretation.

Table 16. Comparative composition of hydroxyapatite obtained from cuttlefish bone (HAp_c), eggshells (HAp_e) and sea shells (HAp_s) [225].

	HAp_c	HAp_e	HAp_s
Sr (mol%) ^a	0.49	0.12	0.20
Na (mol%) ^a	0.74	0.13	0.34
Mg (mol%) ^a	0.60	1.40	0.26
Al (mol%) ^a	0.06	0.05	0.07
Fe (mol%) ^a	0.08	0.06	0.07
Ba (ppm) ^b		1318.02	24.23
Cr (ppm) ^b		1.80	1.59
K (ppm) ^b		524.72	149.00
Li (ppm) ^b		1.60	1.31
Mn (ppm) ^b		0.36	6.02
S (ppm) ^b	0.006 ^c	589.37	0.000
Si (ppm) ^b	0.02 ^c	0.52	10.26
Ca/P ^a	1.48	1.55	1.58

^aData from the rows are from Ref. [226]. ^b From Ref. [227]. ^c From Ref. [228].

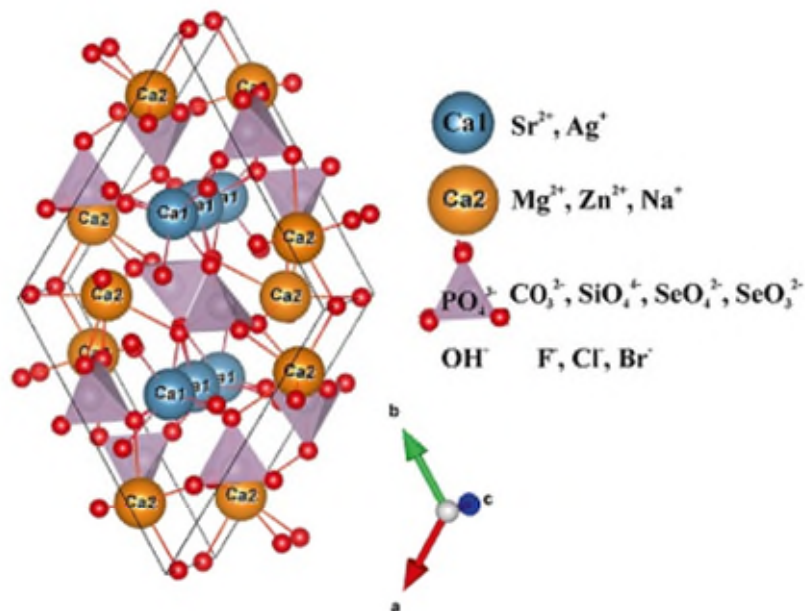


Figure 64. Hydroxyapatite crystal structure with Ca sites and substituting ions, generated by software VESTA 3 [224].

6.3.2. Mass Spectrum and Critical Overlaps

The interpretation of a typical APT mass spectrum from APT analysis of porcine trabecular bone can be seen in Figure 65. Corresponding peaks for the main elements expected in bone such as Ca, P, O, C, N, Na, Mg, and Sr, etc. can be observed. Similar to mass spectra obtained from the previous synthetic bone materials, Ca, Na, K, Mg, and Sr mainly exist as single-atom ion peaks, while P is mostly detected in the form of complex ions, such as PO , PO_2 , PO_3 , etc. However, the porcine trabecular bone mass spectrum is more complex than synthetic bone materials, in addition to the single atomic ion peaks of C and N, these analyses also incorporate detection of a large number of complex molecular ions of organic molecular fragments such as NH , CO , NO , CHO , CHN , CNO , etc. The situation is made further challenging by the fact that most of the molecular ions mass-to-charge-state ratio overlap with other components in the mass spectrum.

The relative contribution of each overlapping ion type to a single total peak can

be calculated based on the size of corresponding adjacent isotopic peaks. However, in order to correctly calculate a specific ion's contribution to each of the other peaks, at least one its isotopes must be detectable and non-overlapping. To undertake these calculations, and thus improve the overall accuracy of compositional measurements this study used either the "Decomposition of Peak" function in the AP Suite 6.1 software or the "Overlap Group Tool" in Atom Probe Lab v2.1.4. Some major overlapping peak combinations in the porcine bone trabecular are listed in Table 17, among them, the more noteworthy overlaps are C^+ and Mg^{2+} at 12-13 Da, CO^+ and CaO^{2+} at 28-30 Da, and CO_2^+ and CaO_3^{2+} at 44-46 Da.

The presence of C and Mg, respectively can be demonstrated by the single-atom ion peaks of $^{12}C^+$, and $^{24}Mg^+$. The detection of the $^{12}C^+$ peak is very obvious, while the detection of the $^{24}Mg^+$ peak is very limited as most of it is hidden in the thermal tail of the peak of 20 Da. In the overlapping peak of $^{12}C^+$ and $^{24}Mg^{2+}$, the adjacent isotope peak of $^{25}Mg^{2+}$ can be clearly observed at 12.5 Da in the mass spectrum, and the deconvolution calculation can be performed.

In the case of the overlapping ions of CO^+ and CaO^{2+} , and CO_2^+ and CaO_3^{2+} , at 28 Da and 44 Da respectively, none have resolvable adjacent isotopic peaks that do not overlap with others in the mass spectrum. Since there is a direct overlap between these species, an alternative method to distinguish these ions could incorporate using spatial associations with other ions such as organic phases (C and N-rich regions) or mineral phases (Ca and P-rich regions). For example, although the presence of peaks of 28 Da and 44 Da can be observed in both the mass spectra originating the organic phase and the mineral phase, carbon is considered to be the main contributor in the organic phase. Hence, the peaks of 28 Da and 44 Da are ranged as CO^+ and CO_2^+ , respectively, when interpreting the mass spectrum of specific organic phases. In contrast, when considering mass spectra

6: Atom Probe Analyses of Porcine Trabecular Bone

originating from regions associated with mineral phases, peaks of 28 Da and 44 Da are ranged as CaO^{2+} and CaO_3^{2+} , respectively. This method was used in all mass spectrum interpretation and thus composition calculations of different phases in porcine trabecular bone.

Table 17. Overlapping peaks in the porcine trabecular bone mass spectrum.

Mass-to-charge-state Ratio	Ion 1 and Charge	Ion 2 and Charge	Ion 3 and Charge
14	Si^{++}	CH^+	
22	Ca^{++}	SiO^{++}	
23	Na^+	SiO^{++}	
30	Si^+	SiO_2^{++}	
31	SiO_2^{++}	P^+	
43	Sr^{++}	Ca^+	
44	Ca^+	Sr^{++}	SiO^+
48	POH^+	Ca^+	
60	SiO_2^+	Si_2^+	

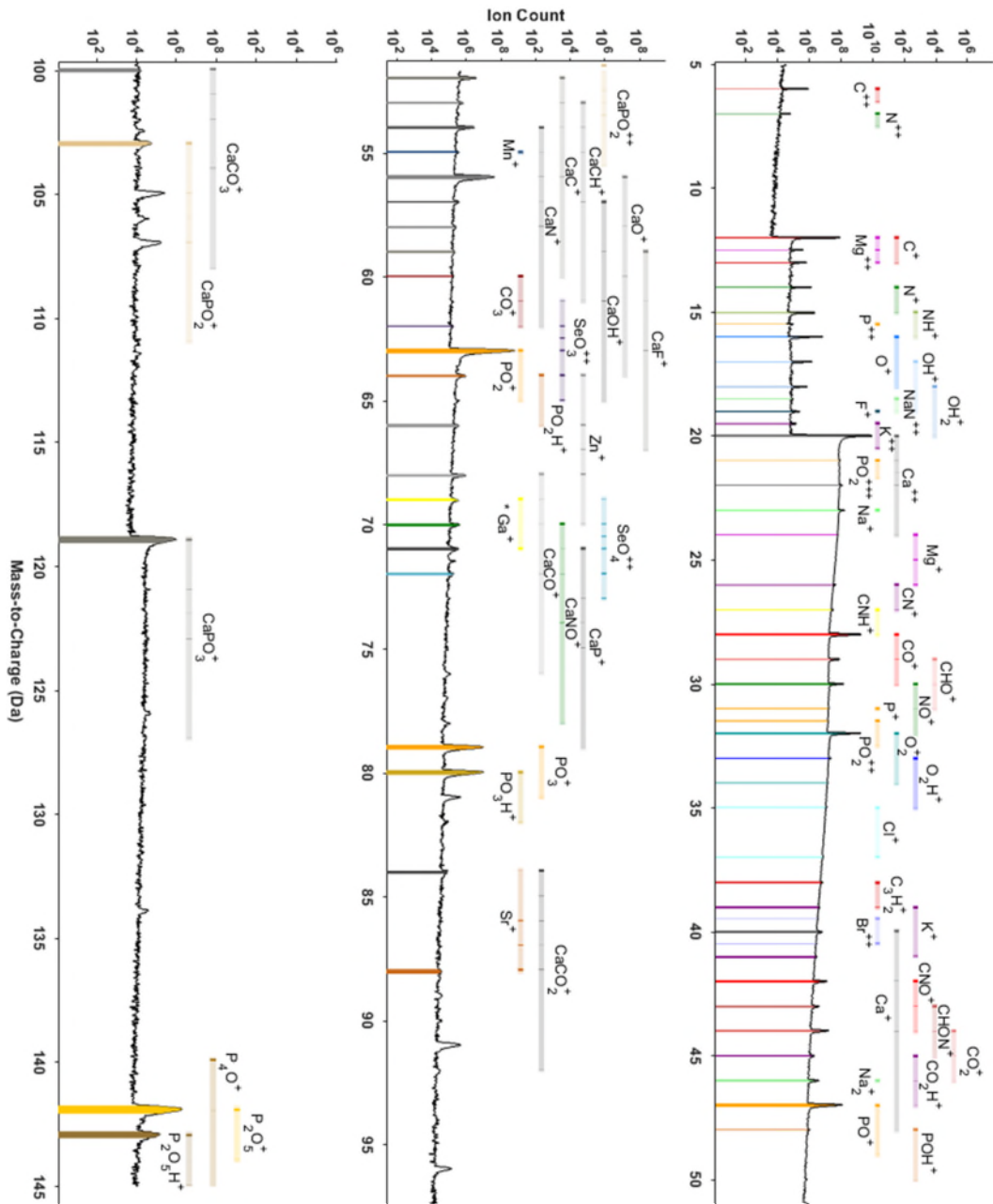


Figure 65. The typical mass spectrum of the porcine trabecular bone (5-145 Da).

6.4. Interpretation of the Spatial Reconstruction

Visualization analysis of all valid APT experiments on porcine trabecular bone is performed using IVAS 3.8.8 or AP Suite 6.1. This section presents five representative 3D reconstructions of porcine trabecular bones from different sampling directions (horizontal /vertical). Analysis such as iso-concentration surfaces of specific elements, volume renders of different elements concentration, ion distribution maps, and proxigram profiles are shown for each sample.

6.4.1. Horizontal Sampling

Horizontal sampling refers to sampling around the trabecular bone cavity, parallel to the trabecular rod. In theory, the arrangement of collagen fibrils should follow the same direction along the trabecular rod, around the trabecular bone cavity [229], as indicated by the gray lines in the schematic in the second panel in Figure 66. The specific location of the liftout of an example of cantilever and tips are shown in Figure 66. Theoretically, in the obtained APT specimen, the direction of collagen fibrils should be horizontal through the needle, i.e. running perpendicular across the long axis. The last two images in Figure 66 show an example of reconstructed collagen fibrils in the porcine trabecular tip by horizontal sampling, demonstrating that the collagen orientation in the reconstruction is consistent with the theoretical orientation in the horizontal sampling.

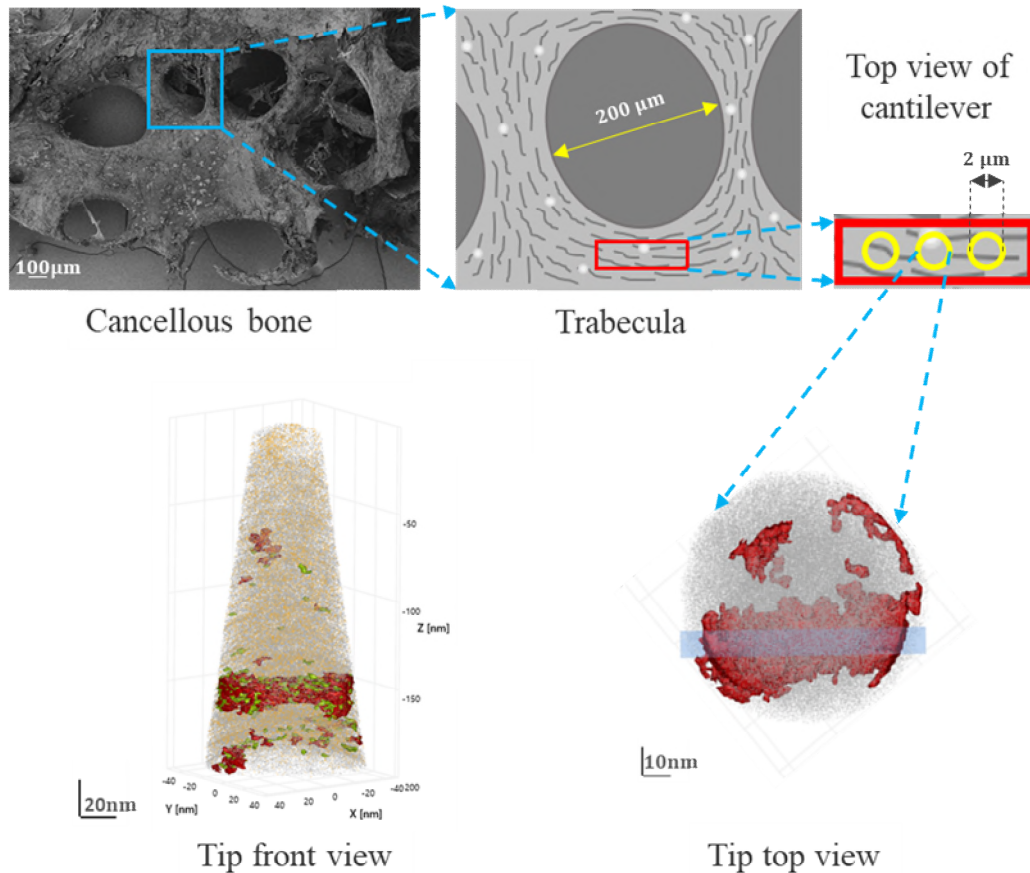


Figure 66. Schematic illustration of horizontal sampling of trabecular bone tissue in APT sample preparation. The second image on the left is a simple schematic representative of the region of bone microstructure highlighted by the blue box on the left. The short gray lines show the theoretical distribution direction of collagen fibrils around the trabecular bone cavity. The red box represents the position of the cantilever liftout for APT specimen preparation. The yellow circles represent APT needle positions. In the reconstructed tip, the collagen fibrils is horizontally across (perpendicular to the long axis of) the tip, the red volume represents the isosurface of C (10 at%), the green volume represents N isosurface (1.8 at%), and gray and yellow dots represent Ca and P ions respectively.

6.4.1.1. Specimen 1: R5083_12600

In bone tissue, almost all calcium present is contained in bioapatite, and most of the C is contained in the collagen even though both bioapatite and collagen fibrils contain C [230]. Therefore, the collagen phase of bone can be broadly described as carbon and nitrogen based, while the mineral phase is considered calcium and phosphorus based.

Figure 67 presents iso-concentration surfaces analyses of C (12 at%), N (1.6 at%),

and Ca (30 at%) respectively, applied to a reconstructed APT dataset containing more than 11.1 M ions. Several horizontal collagen fibrils can be observed in the upper half of the reconstruction. C and N were found to be highly co-located, and complementary to Ca. The contrast in the figures can observe the presence of collagen fibrils in the encapsulation of the mineralized matrix.

The position of collagen fibrils in the sample can be observed more intuitively from the concentration density map of isolated collagen fibrils (the black box in Figure 68). Specific plane selection (ROI thickness: 10 nm) was performed on isolated collagen fibrils in XYZ of three directions for better quantification of presence of collagen fibrils.

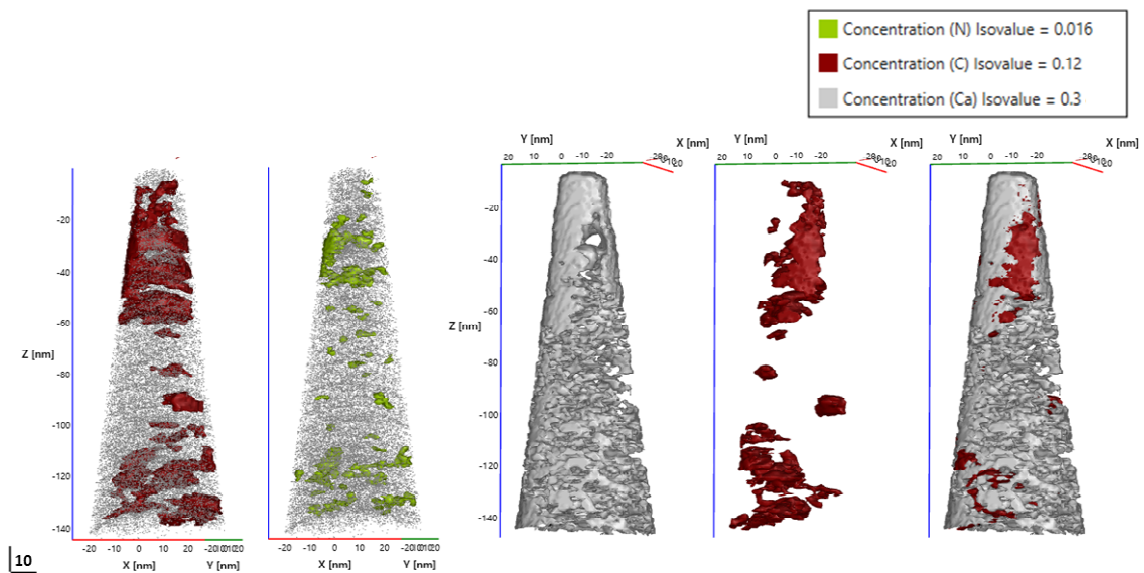


Figure 67. Lateral collagen fibrils present in the encapsulation of the mineralized matrix in the reconstruction of R5083_12600, iso-concentrations surface of C, N, and Ca represented in red (12 at%), green (1.6 at%) and gray (30 at%) respectively.

Figure 68 presents volume renders of respective element concentration in selected X-Z and Y-Z planes, i.e. 10nm thick slices of the reconstruction, highlighting isolated collagen fibrils. Concentration maps of different elements show more details of this

collagen fibril. The selected sections confirm that organic and inorganic are located in different positions. C and N are highly spatially correlated, to what can be readily distinguished as distinct collagen phases. The respective Ca and P distribution complement each other, but do not coincide with the organic phase, in what can be classified as the mineral phase. The distribution of O appears closely related to P and is mainly present in the mineral phase. Na is found to be distributed in a region between the organic and inorganic phases, more discussion will be done in Section 6.4.3.

Figure 69 correspond exactly to those planes in Figure 68, displays ion distribution maps of different elements concentration in selected planes in the X and Y-axis on isolated collagen fibrils. The ion map and its concentration map corroborate each other. In addition to the obvious observation of the complementarity of the collagen and mineral phases, the aggregation of C and N ions in the collagen fibrils can also be clearly observed at the atomic length scale (as marked by the pentagram in the figure).

Concentration maps and ion distribution maps on the selected plane of the Z-axis on the isolated collagen fibril show the atomic distribution in the cross-sectional of a collagen fibril (Figure 70). Ca and C are highly complementary in spatial distribution, and in ion distributions, C ions are aggregated significantly in the organic phase, while Ca and P ions are poorly distributed in the organic phase.

6: Atom Probe Analyses of Porcine Trabecular Bone

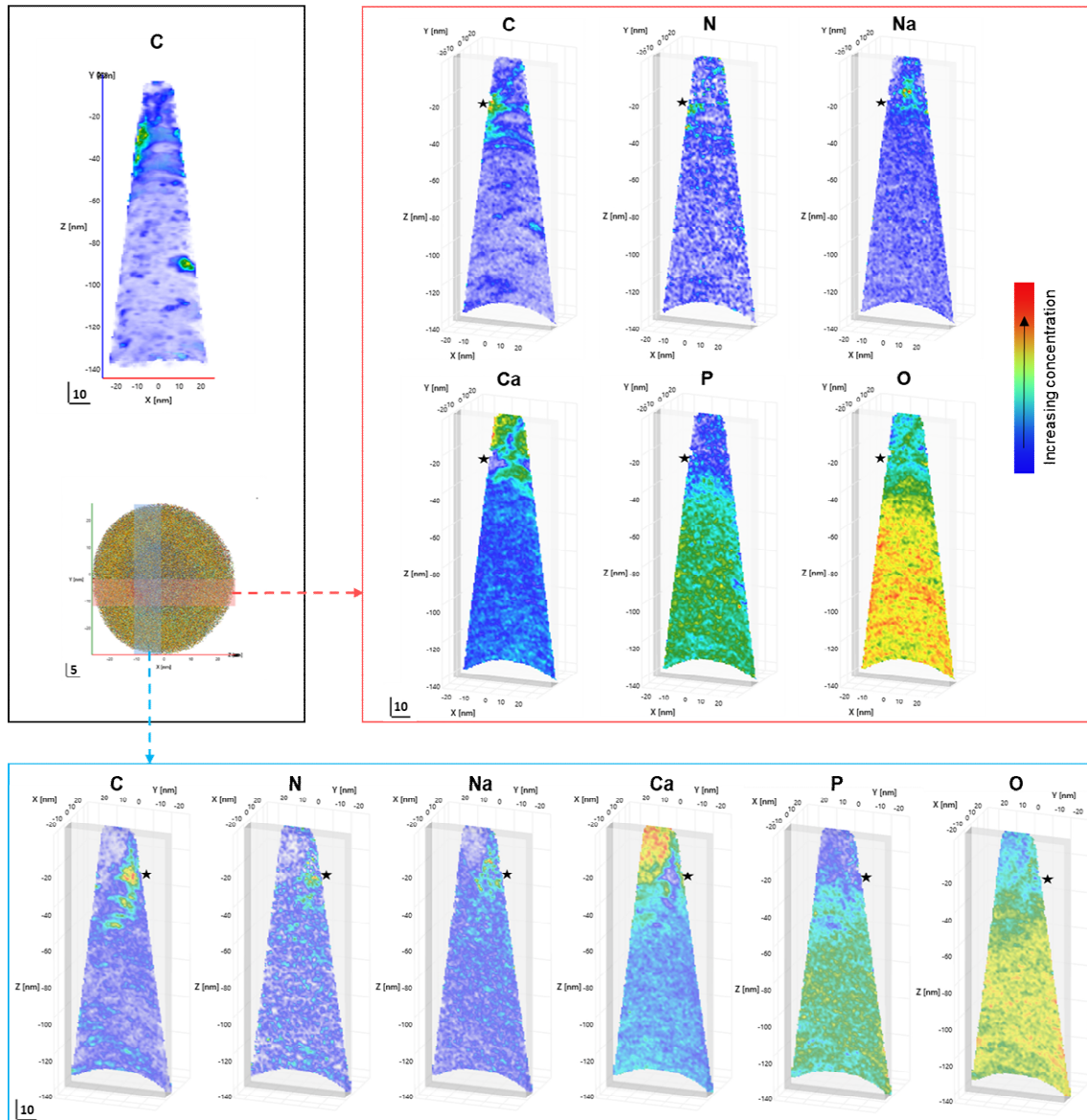


Figure 68. Volume renders of different elements concentration in different selected planes of R5083_12600. The black box includes the density map of isolated collagen fibrils and the schematic illustration of the selection of planes along the X and Y axes, respectively. The red box represents the selected X-Z planes (Y: -12 ~ -2 nm). The blue box represents the selected Y-Z planes (X: -11 ~ -1 nm). The star is marked next to the position of collagen fibrils and represents the same position in all figures.

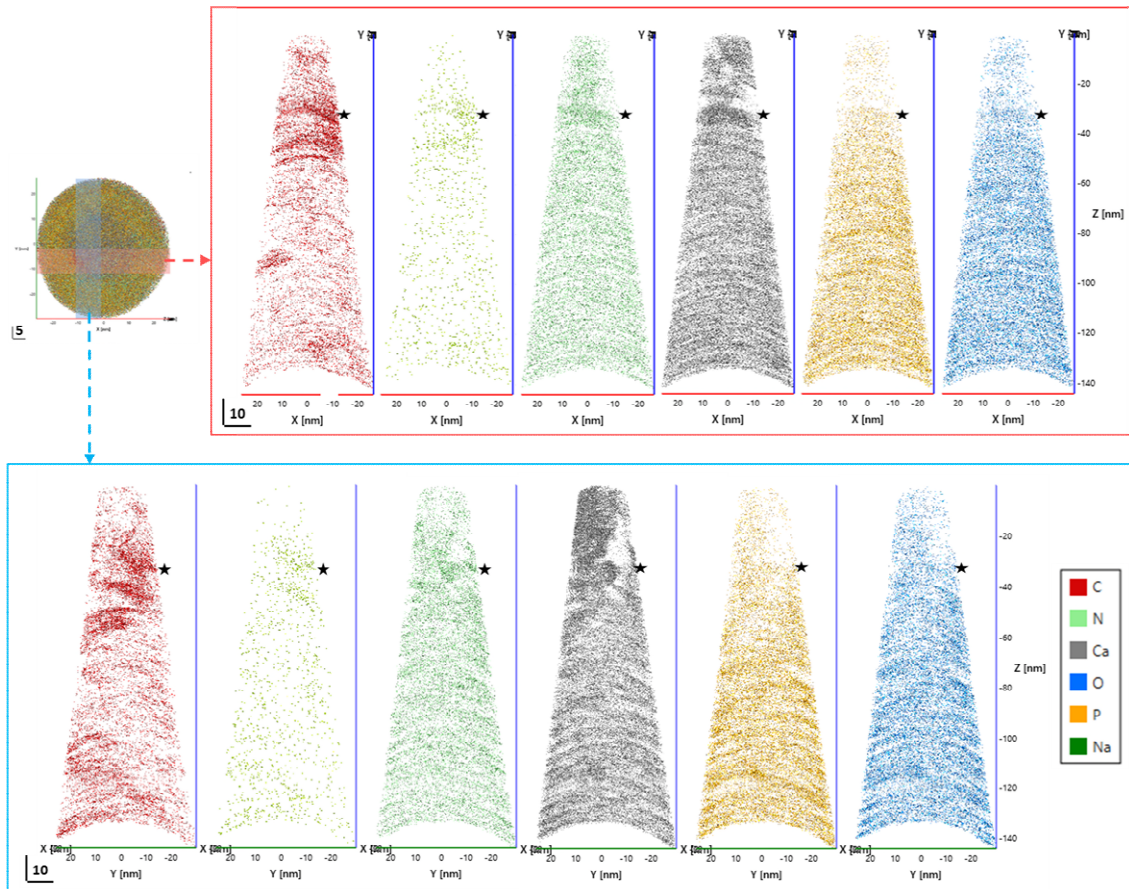


Figure 69. Ions distribution maps of different elements in selected sections of the X-Z planes (red box) and the Y-Z-planes (blue box) in R5083_12600. The star is marked next to the position of collagen fibrils and represents the same position in all figures.

Figure 71 shows proxigram analyses that measure elemental concentrations across the carbon iso-concentration surface defining the collagen phase interface. C and N concentrations were found greatly increased within the collagen fibrils, whereas Ca and P concentrations decreased. Conversely, away from the collagen fibrils, the concentrations of C and N decreased significantly, while the Ca and P increased. In the organic phase, the calcium concentration drops to around 10 at% and the carbon concentration rises to around 30 at%.

6: Atom Probe Analyses of Porcine Trabecular Bone

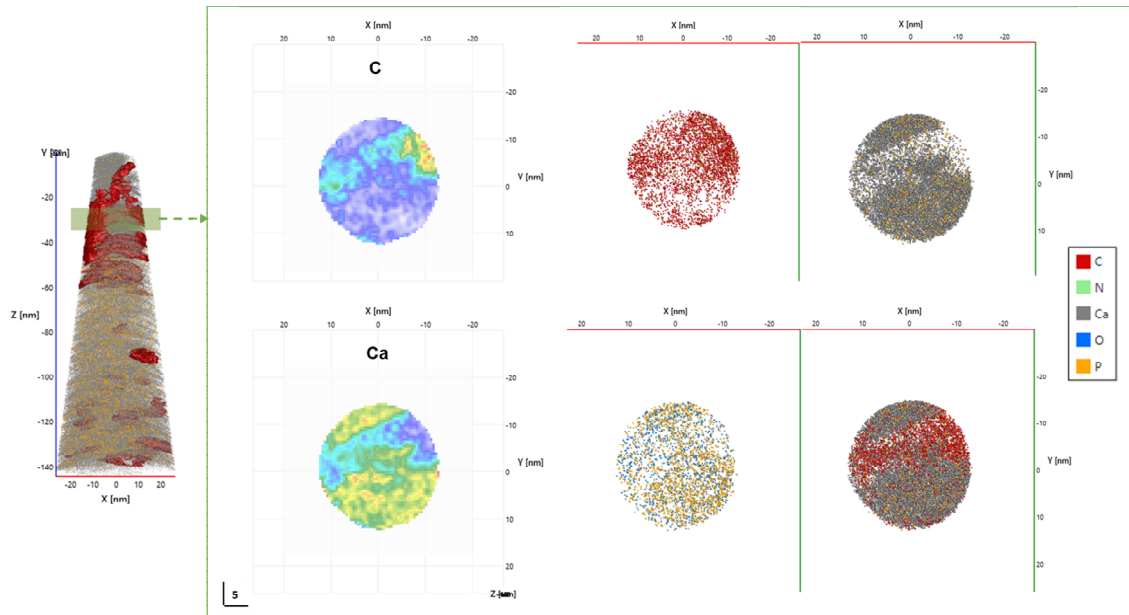


Figure 70. Volume renders of concentration of C and Ca, ions distribution maps of C and Ca in selected X-Y sections of the (Z: -25 ~ -35 nm) in R5083_12600. At the atomic scale, a horizontal collagen fibrils complementary to the mineral phase can be observed.

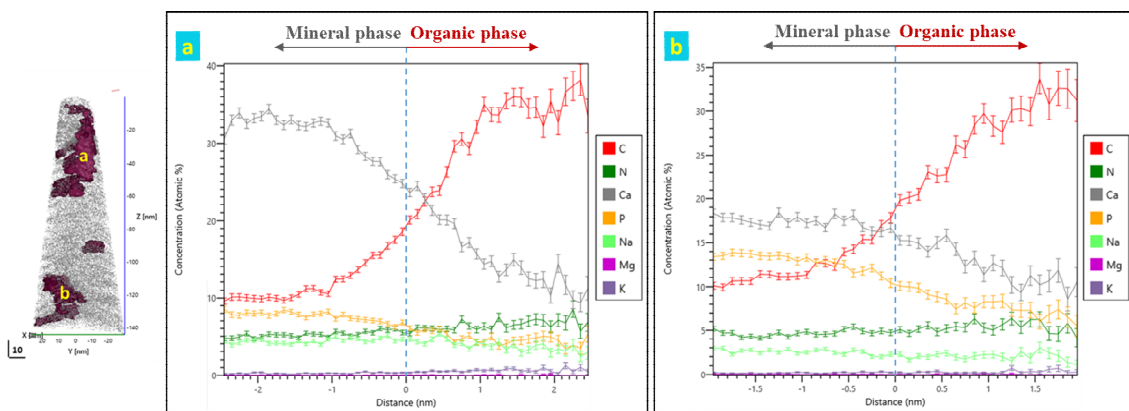


Figure 71. Proxigrams of top (a) and bottom (b) carbon iso-concentration surfaces, respectively in R5083_12600 dataset. From the mineral phase to the collagen phase, the concentration of Ca & P decreased, C & N increased, and the concentration of C gradually exceeded Ca.

6.4.1.2. Specimen 2: R5083_22723

Figure 72 shows iso-concentration surfaces of C (10 at%) and N (1.8 at%), in an APT reconstruction containing more than 32.7 M ions. A typical horizontal collagen fibril

can clearly be observed. The co-localization of carbon and nitrogen in the spatial distribution is also very significant.

The complete front and side view perspectives of the collagen fibril are shown in (a) and (b) of Figure 73, respectively. Volume renders of different elements concentration in selected vertical and horizontal (X-Y) plane incorporating this isolated collagen fibril are shown in (c) and (d) of Figure 73, respectively. On these figures, stars mark each end of collagen fibril, the measured width of which is approximately 25 nm. Similar to the results of R5083_12600 (Figure 68), C, N and Ca, P exist in different phases, and the collagen phases and mineral phases are spatially complementary.

Figure 74 presents ion distribution maps of different elements in within a vertical and horizontal plane, respectively, incorporating this isolated collagen fibril. The spatial distribution and segregation of elements in the organic and inorganic phases at the atomic scale can be observed in both the transverse cross-section and the longitudinal cross-section of the collagen fibril.

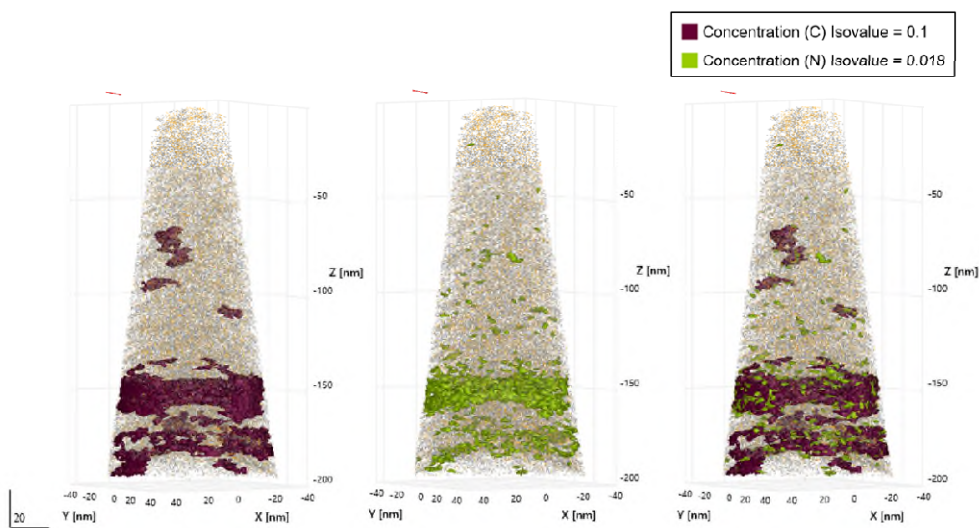


Figure 72. A typical horizontal collagen fibril through the reconstruction of R5083_22723. The iso-concentrations surfaces of C and N represent in red (10 at%), and green (1.8 at%). The gray and yellow dots represent Ca and P ions respectively.

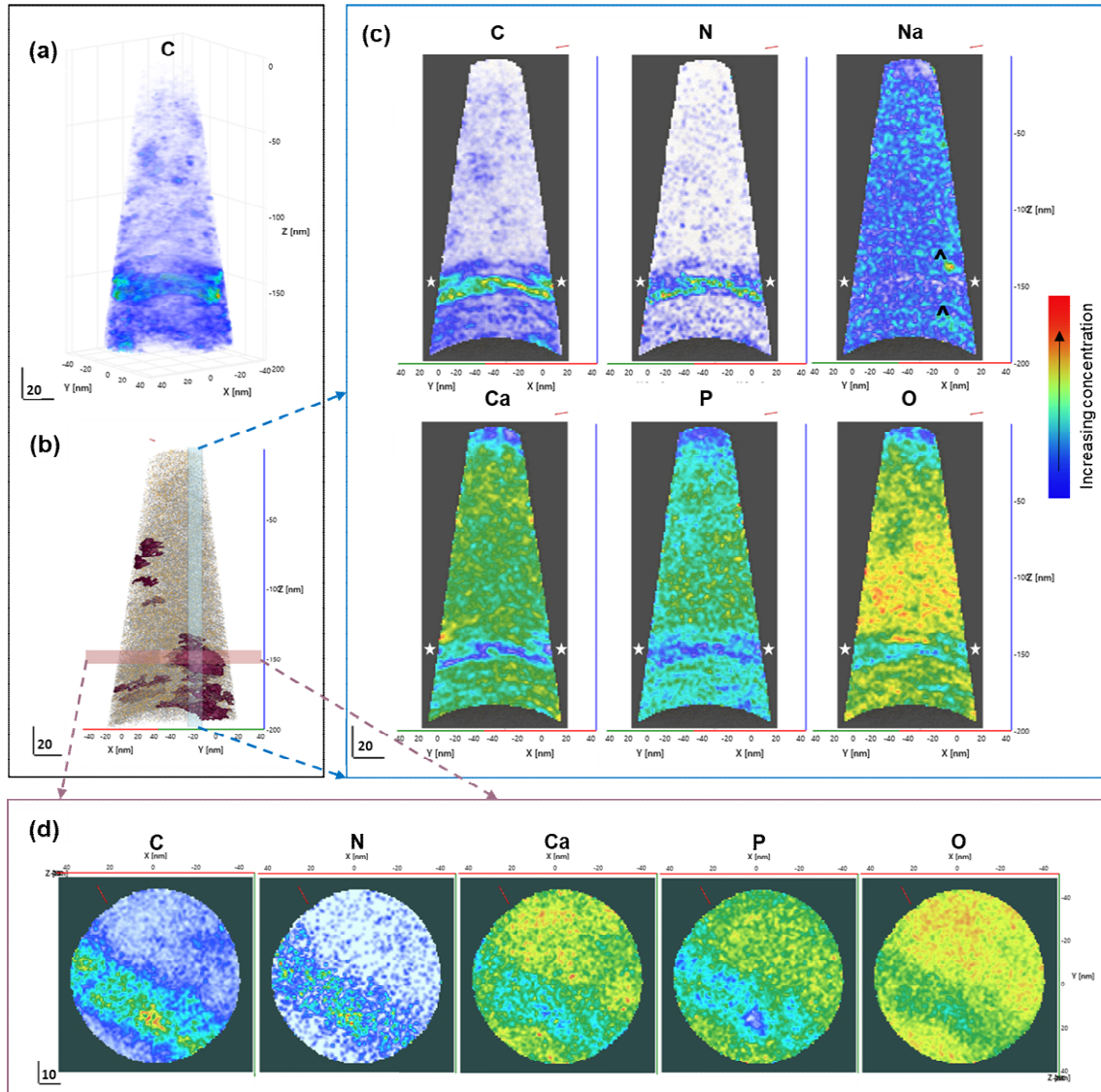


Figure 73. Volume renders of different elements concentration in different selected planes of R5083_22723. The black box includes the (a) density map of the isolated collagen fibril and the (b) schematic illustration of the selection of planes in different axes. (c) The blue box represents the selected vertical plane within the reconstruction. (d) The red box represents the selected X-Y plane (Z: -143 ~ -153 nm). The star marks both ends of the collagen fibril and represents the same position in all figures, and the position of the caret (^) indicates enriched regions of Na.

6: Atom Probe Analyses of Porcine Trabecular Bone

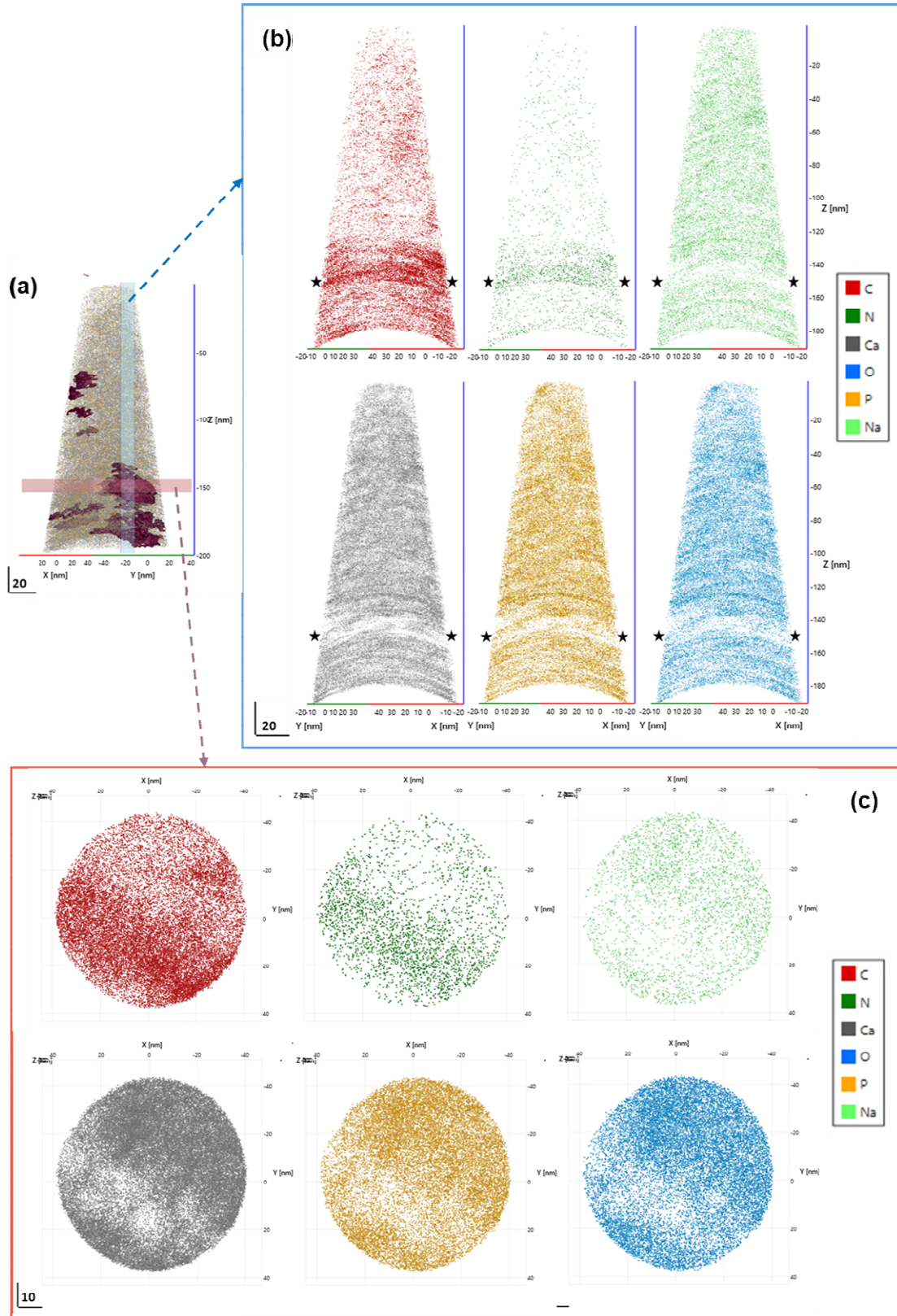


Figure 74. Ions distribution maps of different elements in selected vertical sections of the (blue box (b)) and the horizontal X-Y plane (red box (c)) in R5083_22723. The stars mark both ends of the collagen fibril and represents the same position in all figures.

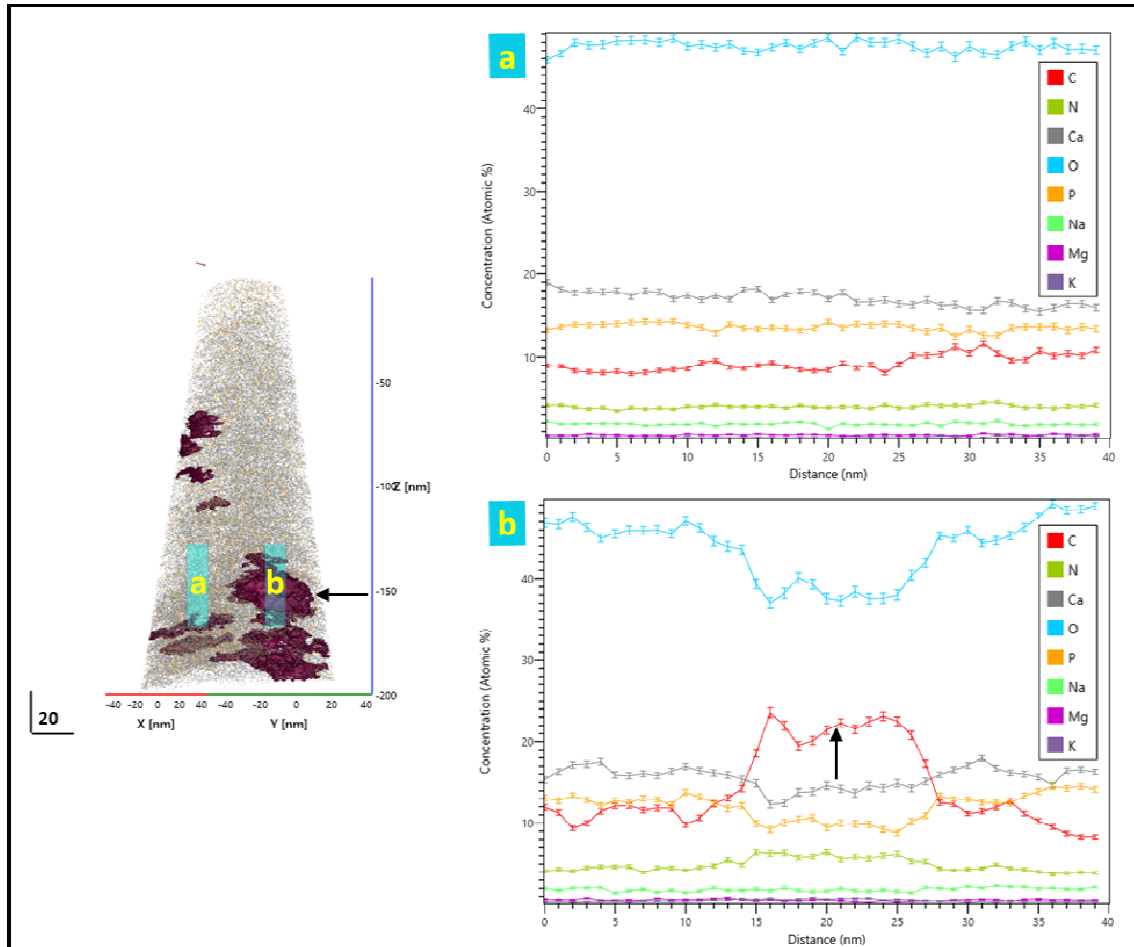


Figure 75. 1D concentration profiles along the Z axis, parallel to (a) and passing through (b) to the isolated collagen fibril, respectively, in R5083_22723. A significant increase (arrow pointed in b) in the C curve in the profile across the collagen fibrils, simultaneous increases in N and decreases in Ca, P, and O. ROIs: $85 \times 10 \times 40$ nm.

The 1D concentration profiles in Figure 75 that are parallel to, (a), and pass through, (b), the collagen fibril along the Z axis further confirm the presence of the collagen fibril and quantify its composition.

Figure 76 (a) shows the mineral matrix and the collagen fibril in more detail, a distinct channel is observed in the Ca iso-concentration surface (grey, 30 at%) and P iso-concentration surface (yellow, 15 at%), respectively, when not supplemented with the carbon iso-concentration surface which represent the position of the collagen threading through the mineral. The proxigram of the carbon iso-concentration surface is displayed

in Figure 76 (b), which measured the concentration changes of different elements across the mineral phase and organic phase. The result of concentration changes is similar to the previous specimen, from the mineral phase to the organic phase, the calcium concentration drops to about 15 at%, while the carbon concentration rises to about 30 at%.

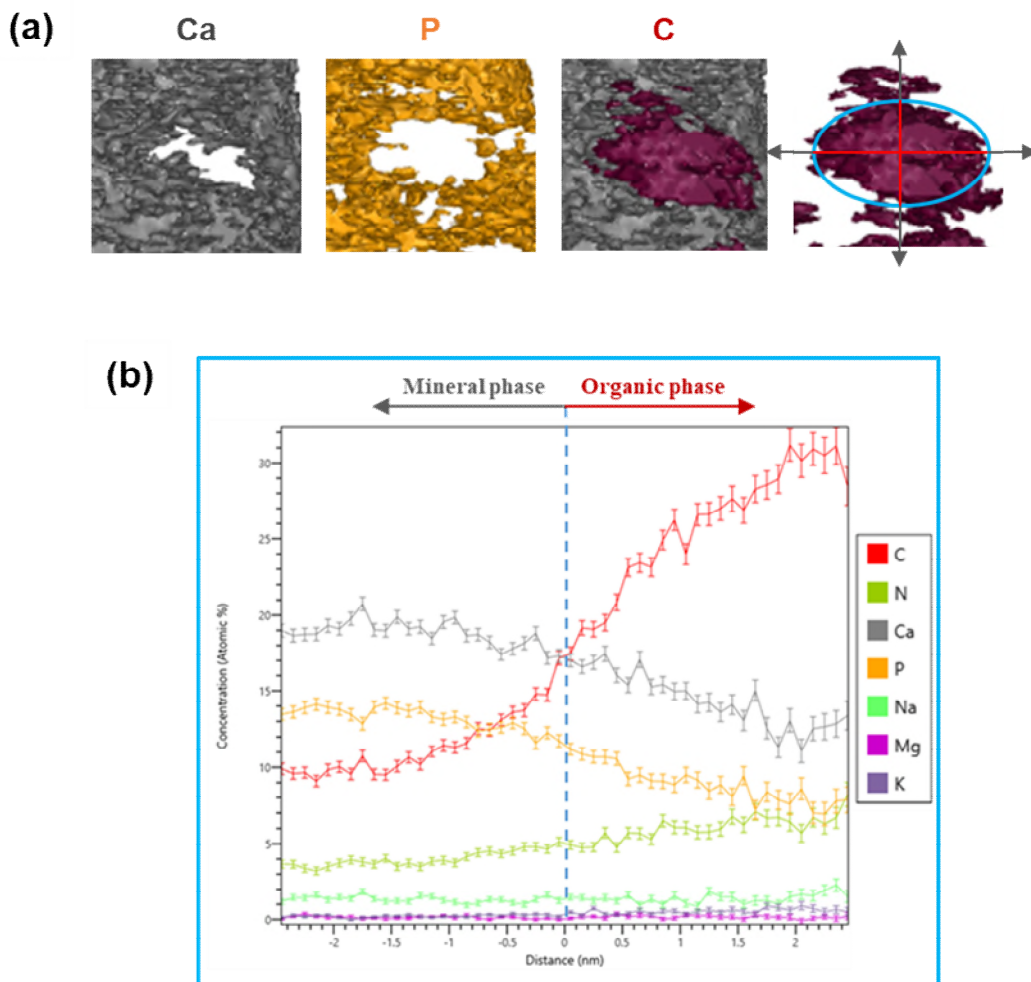


Figure 76. (a) Demonstration of the spatial relationship between the collagen fibril and the mineral phase in the reconstruction of R5083_22723. The iso-concentrations surfaces of Ca, P and C represented by gray (30 at%), yellow (15 at%), and red (10 at%), respectively. (b) the proxigram of the isolated collagen fibril, as measured from the C iso-concentration surface, from the mineral phase to the collagen phase, the concentration of Ca and P decreased, C and N increased, and the concentration of C gradually exceeded Ca.

6.4.1.3. Specimen 3: R5083_22923

Figure 77 displays the iso-concentration surfaces of C (10 at%), N (2.5 at%), and Ca (29 at%), and the volume renders of carbon concentration of specimen R5083_22923, an APT reconstruction containing more than 52.3 M ions. In the reconstruction of this specimen, a banded distribution of collagen fibrils that periodically intersect and spiral downward through the reconstruction can be observed, as shown by the blue and yellow dashed lines and aided by the application of iso-concentration surfaces.

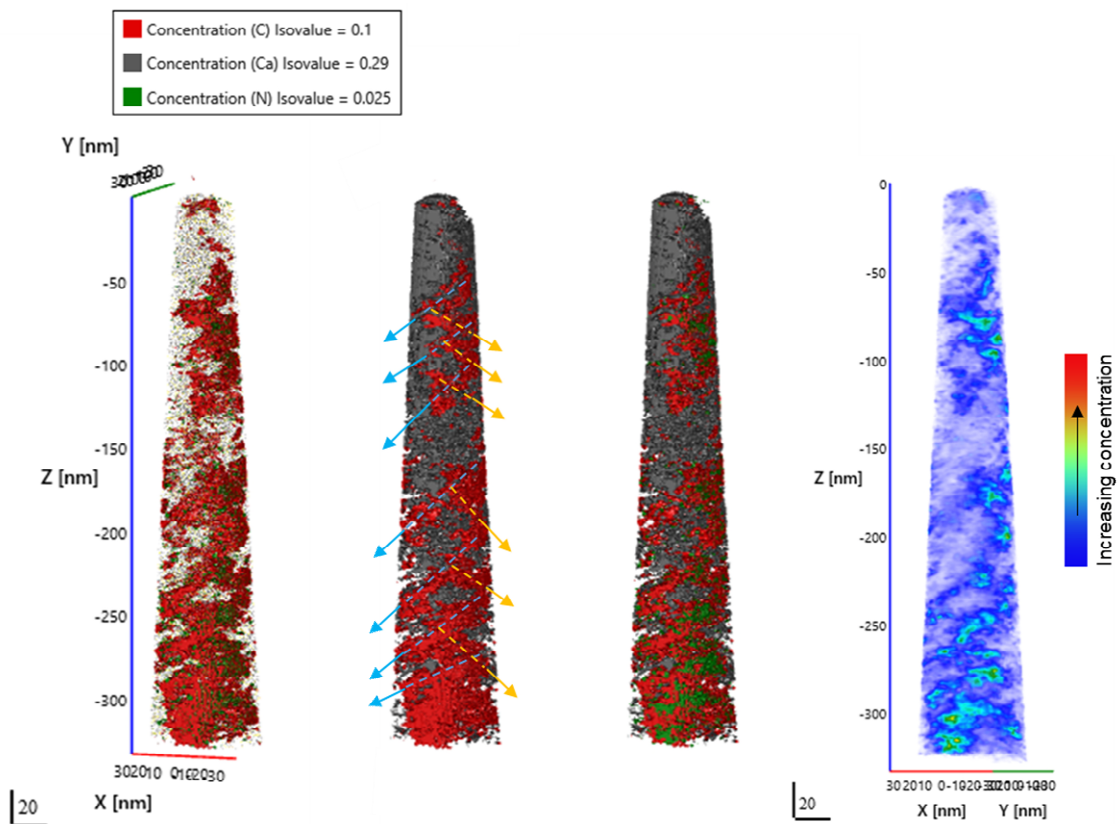


Figure 77. Collagen fibrils periodically intersect and spiral downward in the reconstruction of R5083_22923. The image on the right shows the concentration density map of isolated collagen fibrils (carbon). The iso-concentrations surfaces of C, N and Ca are represented in red (10 at%), green (2.5 at%), and gray (29 at%), respectively. The blue and yellow dashed lines indicate the crossed collagen fibrils in two directions respectively, and the respective arrows indicate the direction of the extending collagen fibrils.

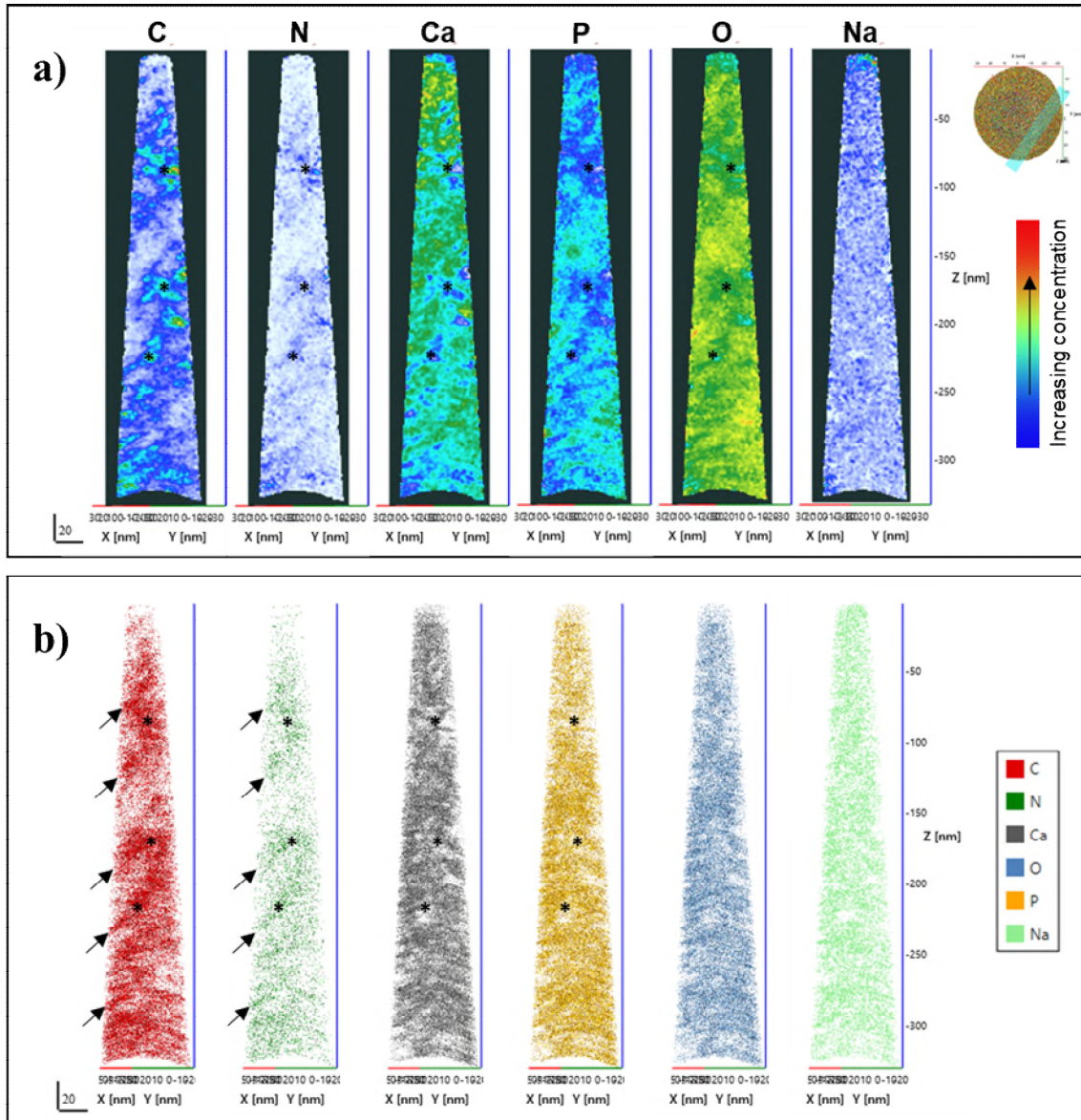


Figure 78. (a) Volume renders of different elements concentration in selected vertical sections in the reconstruction of R5083_22923. (b) Ions distribution maps of various elements in a selected plane. Organic collagen fibrils are marked with an asterisk (*) as examples. Periodic collagen fibril distribution can be observed in panel (b), as marked by arrows, and the spacing period is about 30 nm on average.

Figure 78 shows the concentration maps and ion distribution maps of various elements in selected vertical sections of the reconstructed tip. Collagen fibrils and minerals are mainly present in different areas of the specimen. The distribution of N is directly related to the location of carbon. The P is related to the distribution of Ca, but the atomic density is lower than that of Ca. At the atomic length scale, collagen fibrils

(marked as asterisk) can be observed to appear with an average period of 30 nm (Figure 78 (b)).

The proxigram of the carbon iso-concentration surface (the average value of the entire iso-concentration surface shown in red in Figure 77) is presented in Figure 79. Crossing through the interface of the mineral phase and organic phase, the calcium concentration drops to about 15 at%, while the carbon concentration rises to about 30 at% and nitrogen increases from 5 at% to around 7 at%.

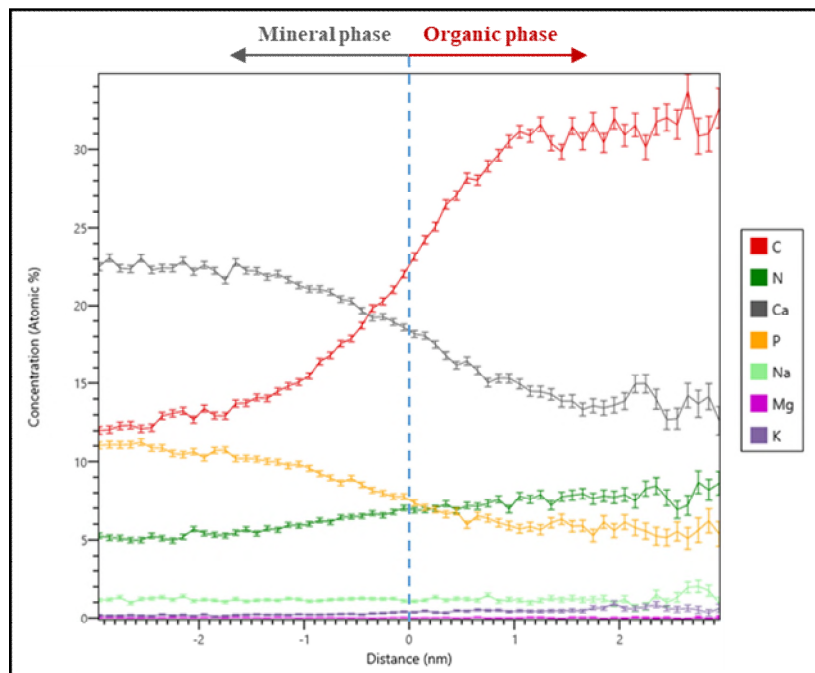


Figure 79. The proxigram of isolated collagen fibrils of R5083_22923. From the mineral phase to the collagen phase, the concentration of Ca and P decreased, C and N increased, and the concentration of C gradually exceeded Ca, confirming that the organic phase is dominated by C and N.

6.4.2. Vertical Sampling

Vertical sampling refers to sampling a cross-section of the trabecular rod. The theoretical arrangement of collagen fibrils in the trabecular rod is shown by the gray line in the simple schematic second panel in Figure 80. The specific orientation of the liftout in the simple schematic second panel in Figure 80. The specific orientation of the liftout of a typical cantilever and tips are illustrated in the second and third panels of Figure 80. Theoretically, in the obtained APT needle, the direction of collagen fibrils should be parallel along the long axis of the specimen. The last panel in Figure 80 shows an example of reconstructed collagen fibrils in the porcine trabecular tip by vertical sampling, demonstrating that the collagen orientation in the reconstruction is consistent with the theoretical orientation in the vertical sampling.

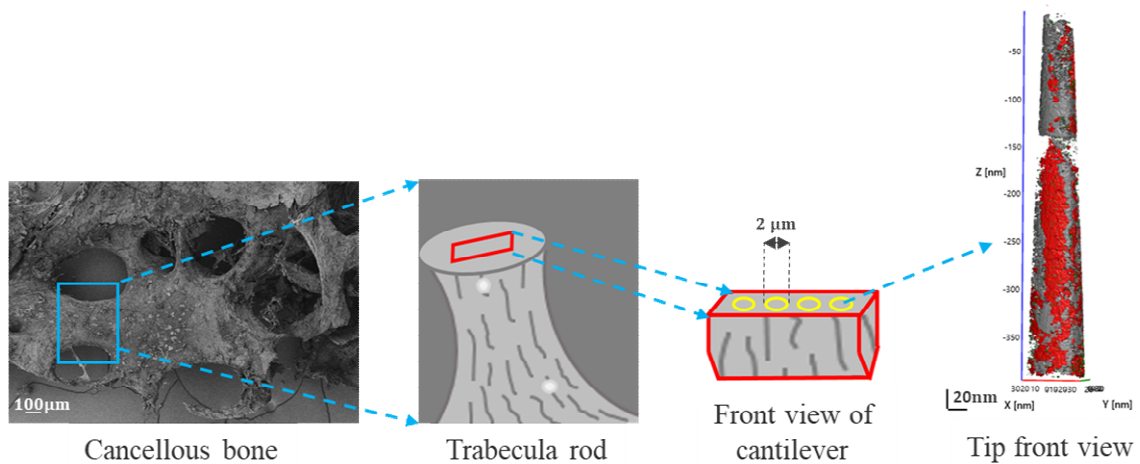


Figure 80. Schematic illustration of vertical sampling of trabecular bone tissue in APT sample preparation. The second image on the left is a simple schematic representative of the region of bone microstructure highlighted by the blue box on the left. The short gray lines show the theoretical distribution direction of collagen fibrils in the trabecular rod. The red box represents the position of the cantilever liftout for APT specimen preparation. The yellow circle represent APT needle positions. In the reconstructed tip, the collagen fibrils is parallel along the long axis of the tip, the red volume represents the isosurface of C (2 at%), and the gray volume represents the Ca isosurface (35 at%).

6.4.2.1. Specimen 4: R5083_23568

Figure 81 shows iso-concentration surfaces of C (12 at%), N (1.6 at%), Ca (30 at%), and P (15 at%) respectively, in reconstructed APT data containing more than 47 M ions. Unlike reconstructions of specimens prepared by horizontal sampling, the observed collagen fibrils in this tip are distributed vertically along the needle, three vertical collagen fibrils can be observed sandwiching the mineralized matrix.

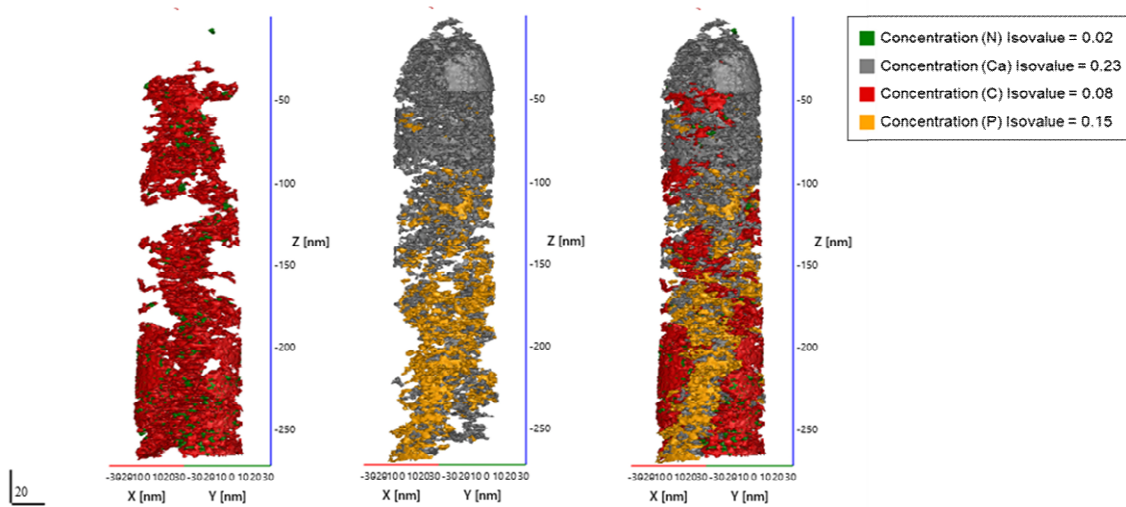


Figure 81. Collagen fibrils along the tip in the reconstruction of R5083_23568. The iso-concentrations surfaces of C, N, Ca and P are represented in red (8 at%), green (2 at%), gray (23 at%), and yellow (15 at%), respectively.

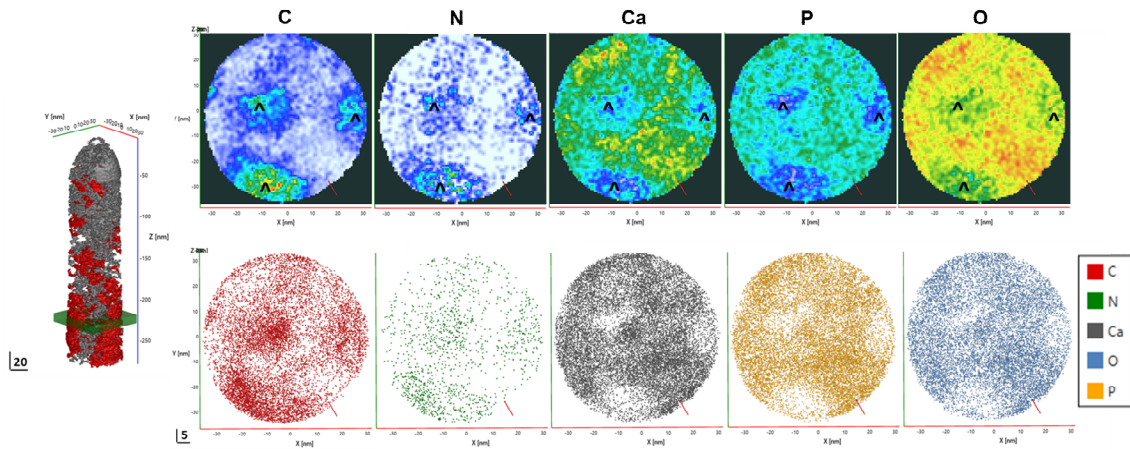


Figure 82. Concentration volume renders and corresponding ion distribution maps of different elements in the highlighted X-Y section (Z : -212 ~ -222 nm) in the reconstruction of R5083_23568. Organic collagen fibrils positions are marked with a caret (^). The cross-sections of three collagen fibrils can be observed.

Figure 82 shows the concentration maps and ion distribution maps of elements within the selected X-Y horizontal plane of the reconstructed specimen. This perspective helps observe the relative spatial locations of the three collagen fibrils in the reconstruction, in effect marking triangular distribution. Collagen fibrils are surrounded by a mineral matrix composed of co-located Ca and P. Three obvious channels are apparent in the mineral phase and the corresponding high-density aggregation of C and N atoms in the organic fibrils can be seen in the ion distribution map.

Figure 83 shows the concentration maps and ion distribution maps of elements within a selected vertical section of the reconstructed specimen. Within this section, two collagen phases are apparent, located on the left and right sides (marked with a hashtag) at the bottom of the sample, respectively, with a mineral phase region situated in between.

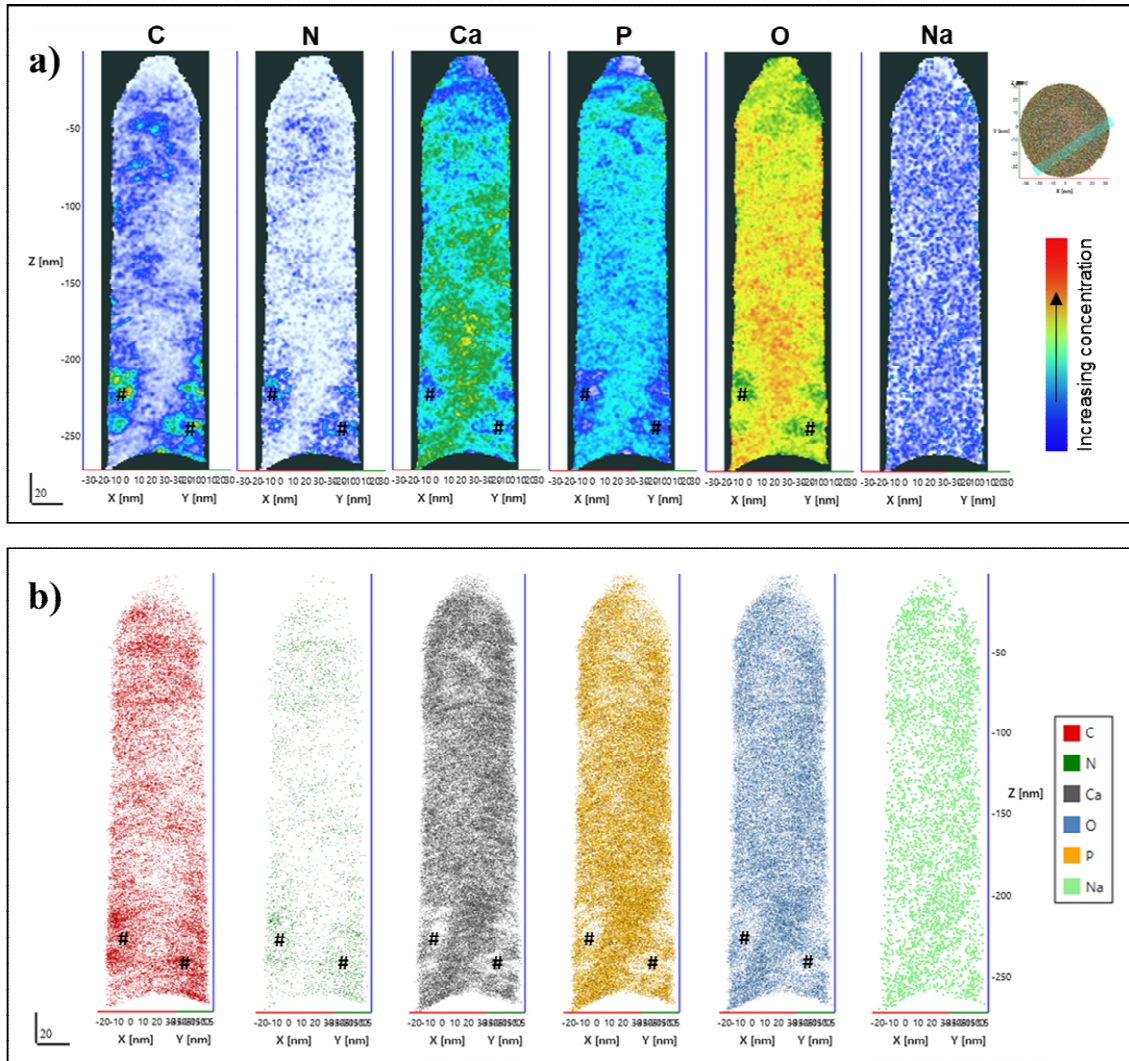


Figure 83. (a) Volume renders of elemental concentrations in selected sections of the indicated vertical section in the reconstruction of R5083_23568. (b) Ion distribution maps of various elements in the same vertical section. Organic collagen fibrils positions are marked with a hashtag (#) as examples.

6.4.2.2. Specimen 5: R5083_23632

Figure 84 shows iso-concentration surfaces of C (12 at%), N (1.6 at%), Ca (30 at%), and P (15 at%), respectively, in an APT dataset containing more than 36.1 M ions. Very long collagen fibrils can be observed vertically along the axis of the needle in this specimen. The previously observed segregation of elements to the organic and mineral phases are the same as the previously presented results. The volume rendering of carbon concentration at different rotations of the reconstruction around the Z-axis angles can be

obtained in Figure 85.

Figure 86 displays the composition maps and ion distribution maps of different elements within a selected vertical section within this reconstructed specimen. It can be observed that there are two long chains of organic fibrils composed of high levels of C and N atoms in the ion distribution map (b). Interestingly, there are also two high-density regions of Ca which about 70 nm apart (marked as hashtag). It should be pointed out there are limitation of spatial measurements as it dependent on reconstruction calibration.

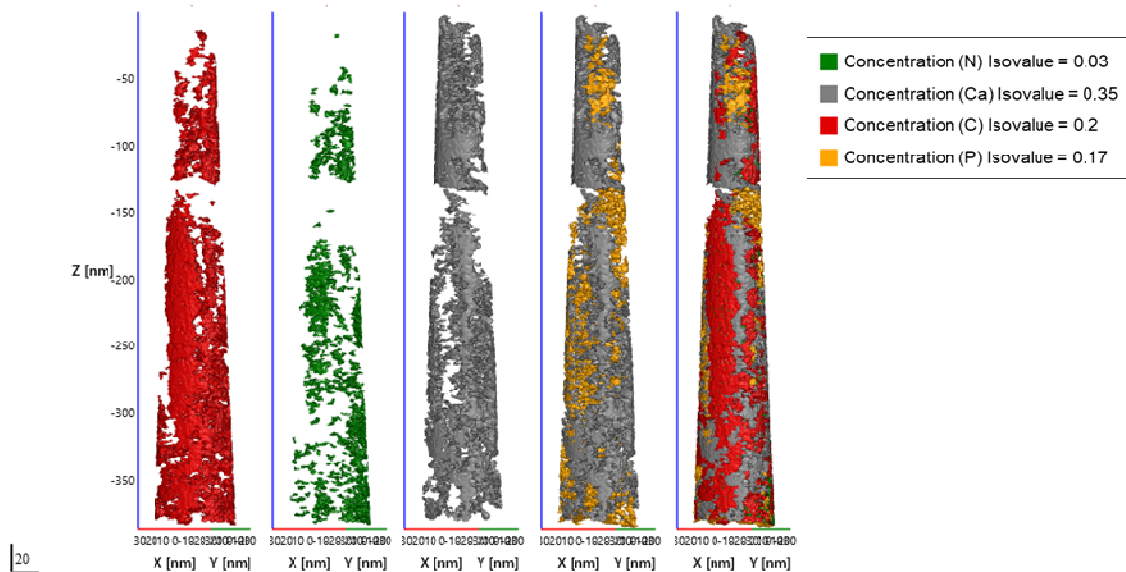


Figure 84. Collagen fibrils parallel along the tip in the reconstruction of R5083_23632. The iso-concentrations surfaces of C, N, Ca and P are represented in red (20 at%), green (3 at%), gray (35 at%), and yellow (17 at%), respectively.

Figure 87 displays the composition maps and ion distribution maps of different elements with two respective vertical sections in the reconstruction. The triangular spatial distribution of three collagen fibrils with respect to each other in the specimen can be observed in both planes selected in the needle, which agrees well with the results of the R5083_23568 (Figure 82). Again, it is observed that the spatial distributions of C and N

are highly consistent and represent the organic phase, which is surrounded by the mineral matrix. In the mineral phase, the distributions of Ca and P are co-located and complementary (existing in Ca-enriched regions and P-enriched regions), however neither of them is segregated to the organic phase.

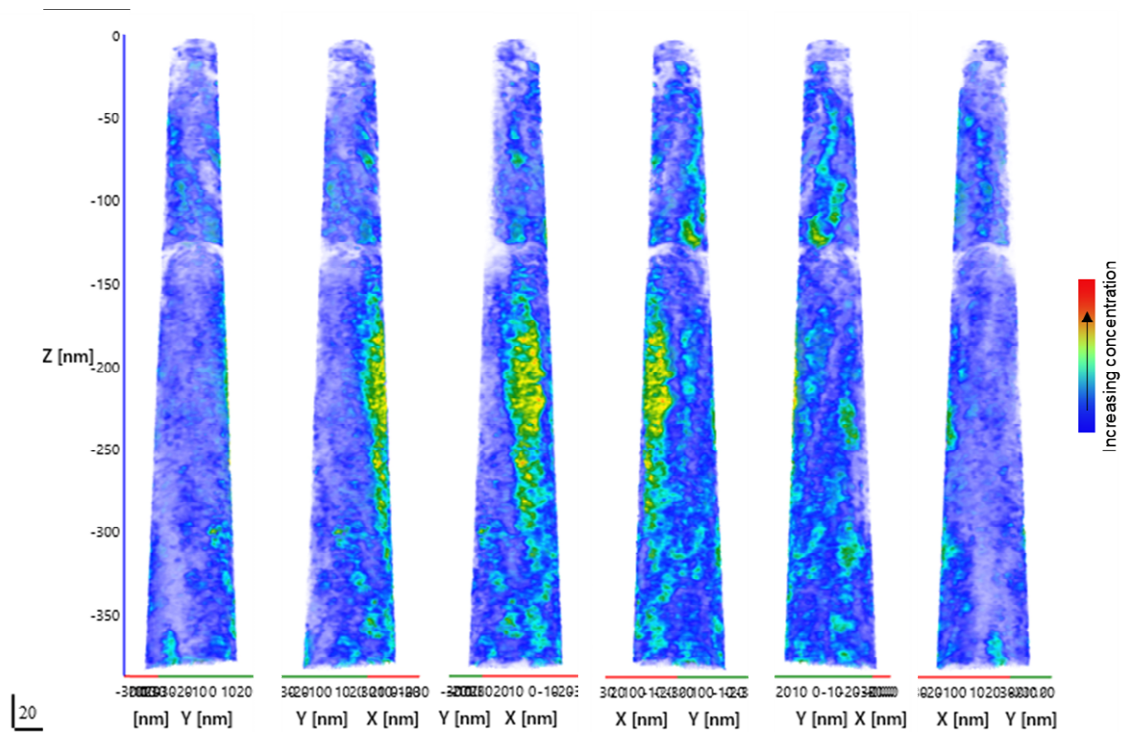


Figure 85. R5083_23632 Continuous volume rendering of carbon concentration, shown for different rotations of the reconstruction around the Z-axis.

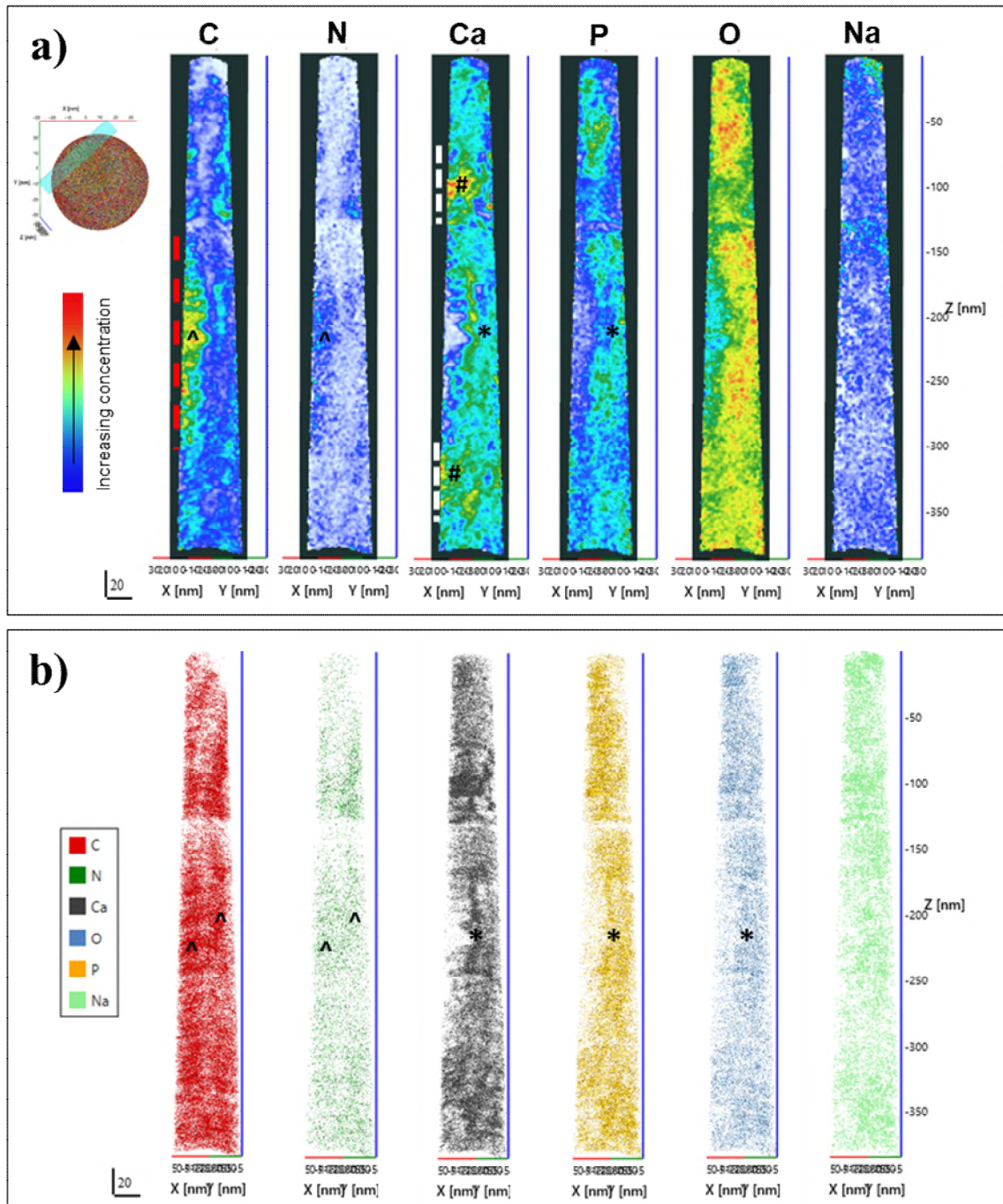


Figure 86. (a) Volume renders of elements concentration in the indicated vertical section of the reconstruction of R5083_23632. (b) Ion distribution maps of elements in the same selected section. Organic collagen fibril is marked with the caret (^), the mineral phase is marked with an asterisk (*), and the Ca-enriched region is marked with a hashtag (#). The red dotted line represents the measured length of the organic fibril. The white dotted line represents the measured length of mineral crystals, which is represented by Ca.

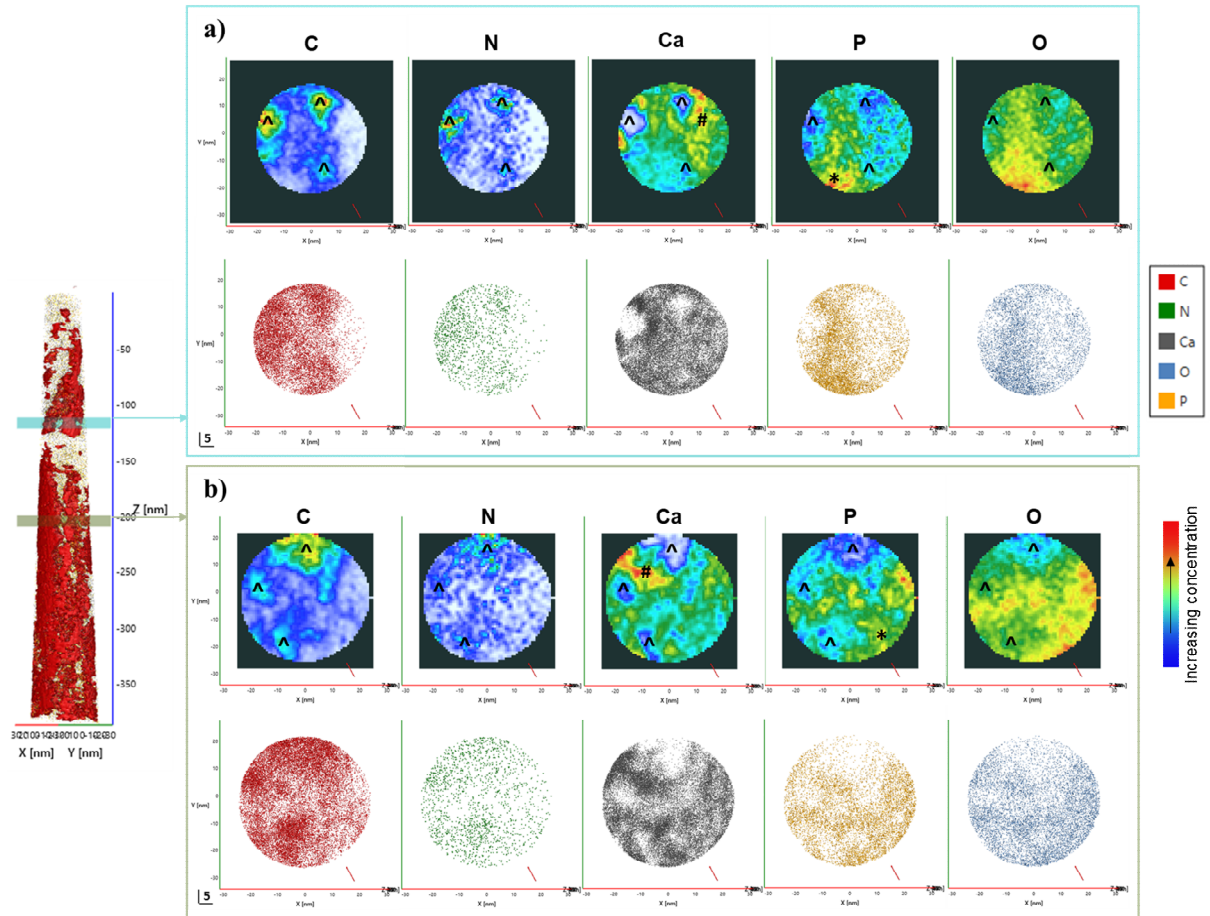


Figure 87. Concentration volume renders and corresponding ion distribution maps of elements in two selected X-Y horizontal sections in the reconstruction of R5083_23632. (a) region indicated by blue box Z: -112 ~-122 nm. (b) region indicated by green box Z: -200 ~-210 nm. The cross-sections of three collagen fibrils can be observed in both planes. Organic collagen fibril position is marked with a caret (^). The Ca enriched region is marked with a hashtag (#), the P an enriched region is marked with an asterisk (*).

The proxigram of the carbon iso-concentration surface is presented in Figure 88. Similar to all proxigrams of other specimens, the C and N concentrations increased significantly close to the interior of the collagen fibrils, while the Ca, P and O concentrations decreased significantly. Conversely, the concentrations of C and N decreased significantly away from collagen fibrils, whereas Ca, P and O increased. From the mineral phase to the organic phase, the Ca concentration drops to about 13 at%, the P concentration drops to around 5 at%, and the O concentration drops to about 30 at%, while the carbon and nitrogen concentration increased to about 30 at% and 7 at%

respectively.

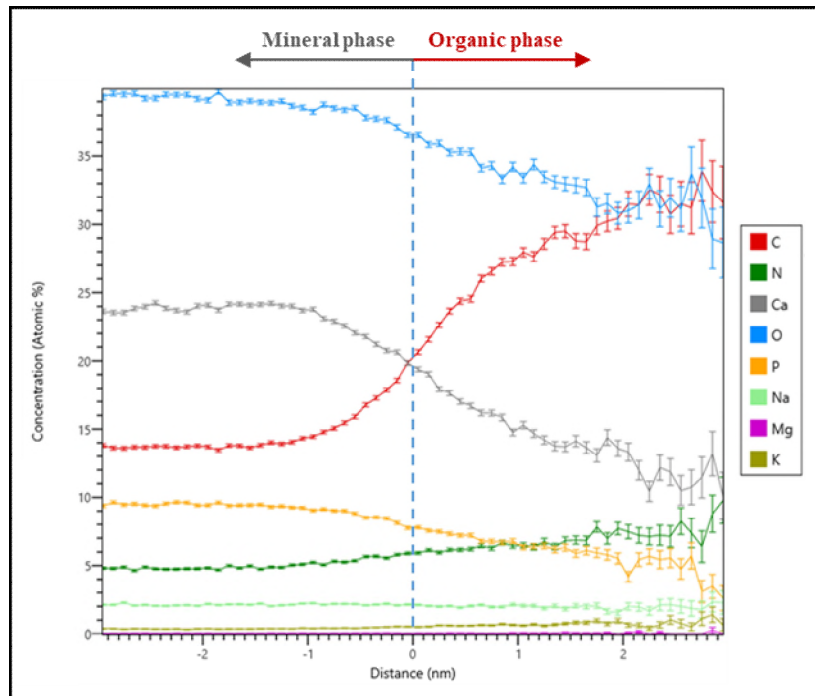


Figure 88. The proxigram of isolated collagen fibrils of R5083_23632. From the mineral phase to the collagen phase, the concentration of Ca, P, and O decreased, C, N, and K increased. The concentration of C gradually exceeded Ca, and the concentration of N gradually exceeded P.

6.4.3. Collagen Phase and Mineral Phase Exploration and Comparison

Needle-shaped APT specimen sampling porcine trabecular bone were prepared by different sampling orientations. In horizontal sampling, the collagen fibrils were kept transverse across the tip, and in vertical sampling, the collagen fibrils were parallel along the tip direction. Twelve high quality APT datasets were obtained, eight of which incorporated more than 30 M ion counts. High calcium and high carbon regions were observed in APT reconstructions of porcine trabecular bone, which correspond to the mineral and collagen phases, respectively. Collagen fibrils (organic phase) can be readily isolated for further imaging and analysis by creating C and N iso-concentration surfaces. Similarly, the iso-concentration surfaces corresponding to Ca and P can be used to

highlight and extract information from the bone mineral matrix (mineral phase). The spatial distribution tendencies of the main bone elements are consistent across all analyzed samples. It was observed that the distributions of C and N are highly correlated, i.e. located at the same regions of microstructure. The distributions of Ca and P are also co-located, but from region-to-region there are significant differences in their relative concentrations, i.e. distinct calcium-rich and phosphorus-rich regions are respectively observed in the mineral phase. The distribution of O was found to be most significantly correlated to P, which may also echo the performance of P on mass spectra that mainly exists in the form of oxide peaks. Figure 89 compares the mass spectra specific to the isolated mineral phase and collagen phase, respectively. The difference between the two phases can be most clearly demonstrated by comparing the relative proportions of Ca and C peaks in each case.

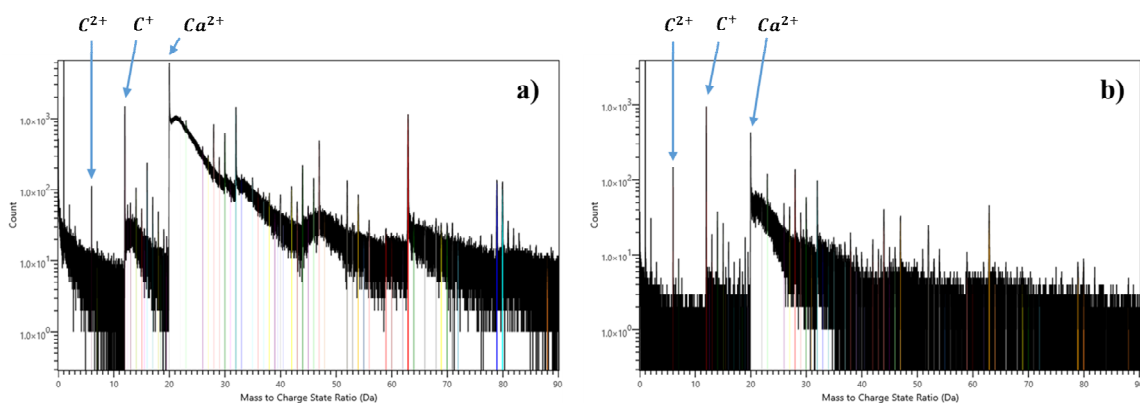


Figure 89. Region-specific mass spectra of (a) mineral phase and (b) collagen phase in the reconstruction of R5083_12600.

In bones, collagen molecules pack together to form collagen microfibrils. The spatial arrangement of collagen fibrils to most type of bone has a periodicity, which is 67 nm, and there are gap regions of 27 nm and overlap regions of 40 nm between collagen

molecules, as illustrated Figure 90 [231-233]. The reconstructed results obtained using different sampling directions during the FIB liftout stage of specimen preparation are consistent with the theoretical collagen directions in each sampling method (refer to Figure 66 and Figure 80). From the single collagen fibril observed in the specimen R5083_22723 by horizontal sampling, the width of this collagen fibril was measured to be around 25 nm (Figure 73), which is similar to the collagen fibril width measured in cortical bone by Langelier et al. [112]. In specimen of R5083_22932 by horizontal sampling, periodically spiral downward collagen fibrils are measured to have an average period of approximately 30 nm (Figure 78). It should be noticed that the spatial distance measurements be affected by calibration of the reconstruction and should be viewed as approximate. The structure of collagen fibrils observed is slightly curled and twisted, as apparent in Figure 77, and the direction is right-helical, which is agreed with the known rotation direction of collagen molecules [234, 235]. From the results of vertical sampling, the triangular arrangement of collagen fibrils extending through the specimen can be more readily observed by examining a horizontal cross-section of each reconstructions, in Figure 82 and Figure 87. In this image the respective positions of the collagen fibrils are highlighted by three distinct voids or channels through the mineral phase and also corresponding high-density aggregation of C and N atoms.

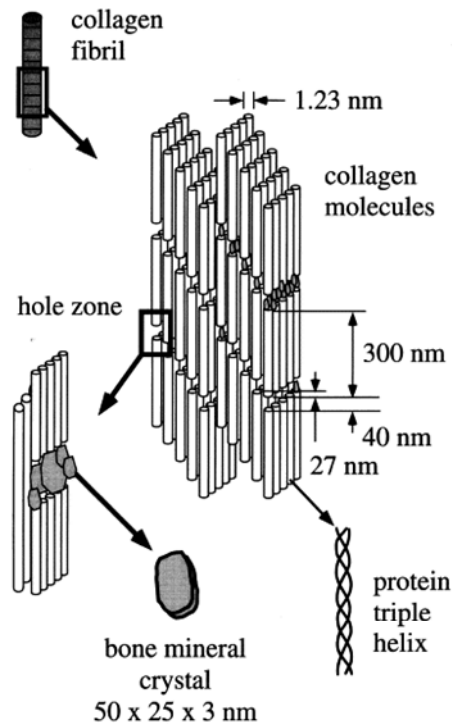


Figure 90. Schematic diagram of the arrangement of collagen and hydroxyapatite complexes [233].

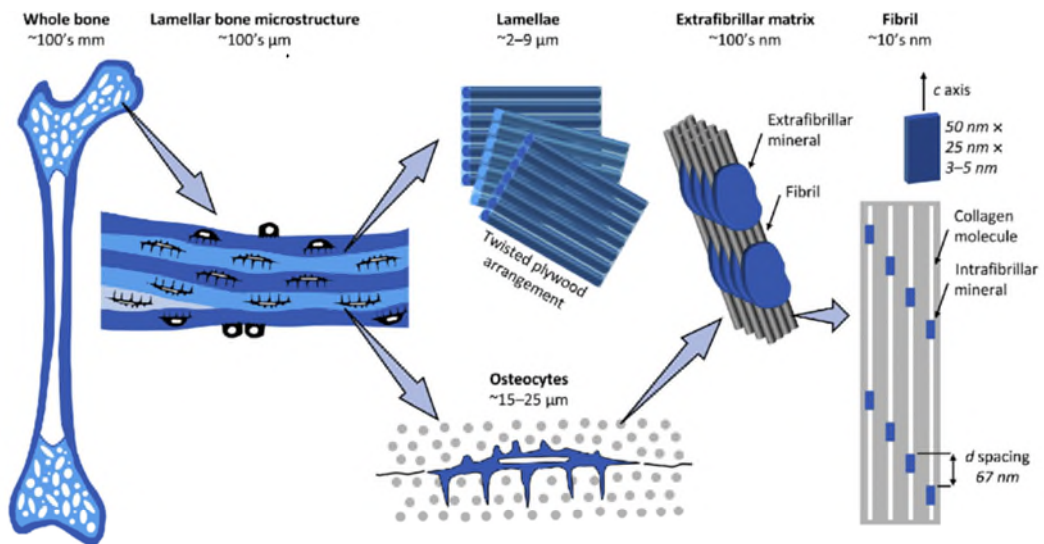


Figure 91. Bone consists of either a porous trabecular framework or a dense cortical structure – both are types of lamellar bone. Lamellae exhibit a twisted plywood arrangement, where neighboring lamellae have different fibril orientations. Osteocytes reside in lacunae interconnected through canaliculi. Lamellae are composed of collagen fibrils surrounded by extrafibrillar mineral platelets. Within the fibrils, type-I collagen molecules and carbonated apatite crystallites form a nanocomposite structure [236].

Mineralized collagen fibrils are the fundamental building block of bone. Models of bone mineralization can be classified as intrafibrillar mineralization, whereby bioapatite grows in the gap channel, and extrafibrillar mineralization, in which the bioapatite exists between collagen molecules [237]. Figure 91 shows a schematic overview diagram of bone composition, intrafibrillar mineralization, and extrafibrillar mineralization. Intrafibrillar mineralization was first proposed by Landis et al. [220, 238], and a large number of subsequent studies have proved that minerals do exist in the interstitial zone [239-242]. Extrafibrillar mineralization proposes that mineral growth in the bone cannot only exist in the gap regions of collagen fibrils, due to its limited space, and some must exist outside. That mineralization occurs as extrafibrillar [242-247].

In the APT reconstructions of the porcine trabecular bone presented in this study, extrafibrillar mineralization was mainly observed, i.e. collagen fibrils and minerals phases were present in different regions of the specimen. As previously discussed, the distribution of Ca and P is highly correlated to the mineral phase, but within this they occupy regions with different relative concentrations. For example, high calcium concentration regions in the mineral with low amounts of P, can be observed in such samples as R5083_12600.

A high concentration region of Ca be seen at the top of the tip of R5083_12600 in Figure 68, but no periodicity of Ca-rich regions occurrence was observed. In the reconstruction of R5083_23632, two high-concentration regions of Ca can be observed, marked with a hashtag in Figure 86 a), separated by the organic phase, marked with the caret. The measured length of the organic fibrils between the two Ca high-concentration regions is around 70 nm, shown as the red dotted line in Figure 86 a). The size of both Ca high-concentration regions is about 25 nm~50 nm, as highlighted shown as the white dotted line in Figure 86 a), which is similar to the commonly accepted size of the

biological apatite platelets in fibrils. Hence, the author proposes that the observation in this case may indicate the presence of intrafibrillar mineralization in the porcine trabecular bone.

Figure 92 compares the mass spectra of specific selected regions of interest within the mineral and organic phases, respectively in specimen of R5083 _12600. Once again, it is confirmed that the dominant element is different between the organic phase and the mineral phase. Similar variations in concentrations of different elements between the organic and mineral phases were observed in all proxigrams obtained in porcine trabecular bone specimens. Compared with the mineral phase, there was a decrease of nearly 20 at% of Ca in the organic phase. Despite the apparent decrease, the concentration of Ca in the organic phase still remained at 10-15 at%, which may also indicate that most of the mineralization occurred in extrafibrils, but the existence of intrafibrillar mineralization is undeniable in the observation of APT reconstruction of porcine trabecular bone.

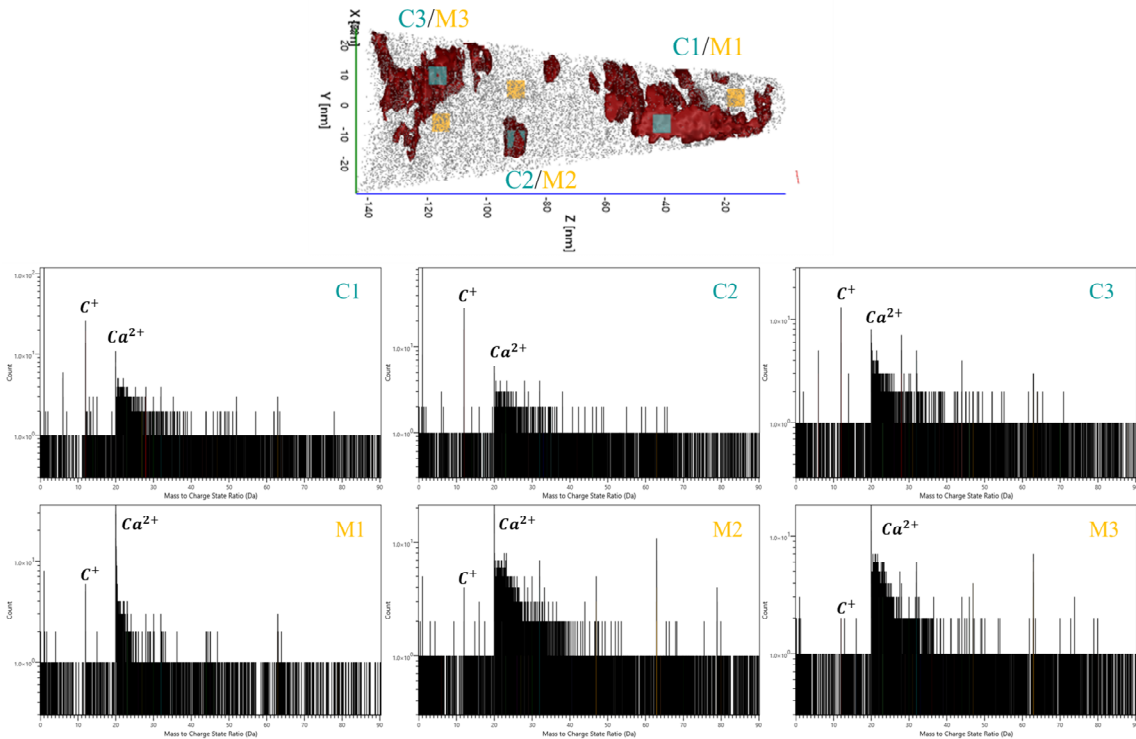


Figure 92. Comparison of mass spectra of selected specific regions of interest within mineral and organic phases in the reconstruction of R5083_12600. Regions C1-3 are selected from the organic phase and M1-3 are selected from entirely within the mineral phase. The dimensions of each selected volume is 6*6*6 nm.

6.4.4. Distribution of Other Essential and Trace Elements

Bone contains many trace elements such as Na, Mg, Sr, K, F, Cl, Br, Se, Zn, Mn, etc [248]. Trace elements present in bone tissue are closely related to the normal function of each type of cell, playing a vital role in bone metabolism and the bone regeneration process [249, 250]. The author observes and summarizes the distribution of some trace elements of the porcine trabecular bone in APT reconstructions.

Sodium. The physiology of sodium effects on calcium metabolism, Sodium increases calcium excretion and low calcium is associated with low bone mineral density [251]. The ionic radius of Na^+ (0.102 nm) is similar to that of Ca^{2+} (0.099 nm) ions, which in the natural bone mineral can replace Ca^{2+} in the lattice of hydroxyapatite to form an

ion substitute of apatite [252]. Existing APT studies of chitons [26], apatites [21], nacre [149], and dentin [114] suggest that the distribution of Na is predominantly within the organic phase rather than crystallographic domains. In this research, Na is present throughout the regions of the bone sampled in the APT analysis but is mainly located at the organic-mineral interface.

Figure 93 displays two detailed distribution maps of Na in two specimens of porcine trabecular bone. By overlaying the volume rendering of the Ca and P concentration map with Na, it can be observed that Na tends to localize at the organic–mineral interfaces rather than simply co-localizing with the C-rich regions, i.e. the organic phase. As shown in 1D concentration diagrams of the organic-mineral interface of the specimen of R5083_12600 in Figure 94, the red and gray lines represent the concentration changes of Ca and C, respectively, leading up to, and across, the organic-inorganic interface. Comparing the concentration change of Na in the concentration profile, it can be found that Na has a small increase at interfaces of organic and mineral, as indicated by the black arrows in Figure 94.

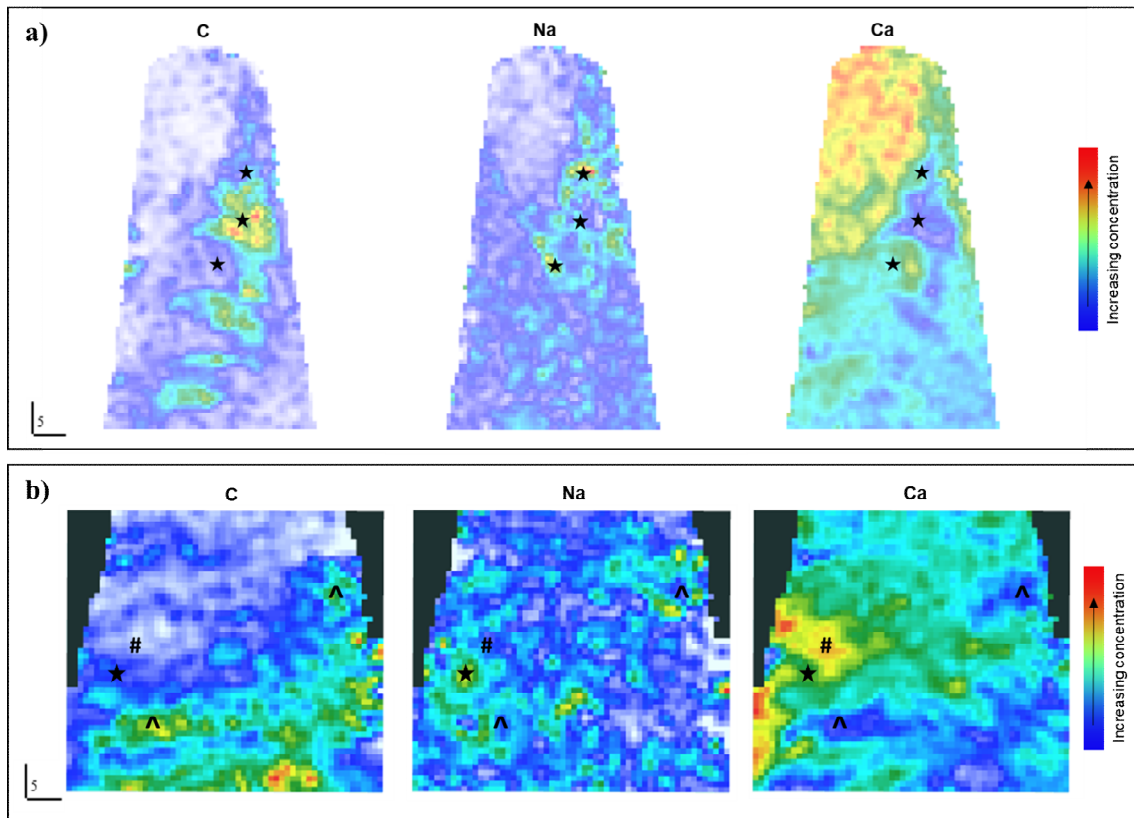


Figure 93. The volume rendering of Na concentration map compared to the volume rendering of Ca and P concentration maps suggest Na tends to be localized at the organic-inorganic interface in both (a) reconstruction of R5083_12600 and (b) reconstruction of R5083_22613. The pentagram is marked as the Na enrichment area, and the caret (^) is marked as the C enrichment area, the hashtag (#) is marked as the Ca enrichment area.

Magnesium. Mg ions can positively affect bone metabolism, adjust osteoblast/osteoclast activity, cell adhesion and proliferation, and differentiation of stem cells to an osteoblastic phenotype [253]. Mg has been shown to affect the mineralization process by regulating the crystallization of hydroxyapatite by stabilizing its precursor amorphous calcium phosphate (ACP), whose deficiency leads to the arrest of bone growth, osteopenia, and bone fragility [254, 255]. Previous APT studies on both enamel have confirmed that Mg is mainly present in the mineral phase [27, 98, 148]. Research of human enamel by Licata et al. [114] suggested that the Ca/P ratio is directly related to Mg segregation, a similar interdependence exists between Ca and Mg contents, i.e., Ca

concentration increases with Mg concentration. Herein, Mg was observed to be more abundant in the mineral phase than in the organic phase in the porcine trabecular bone as observed in Figure 95. In contrast, in the organic phase, neither the iso-concentration analysis in reconstruction nor corresponding peaks identification in specific mass spectra analysis only identified very trace amount of Mg.

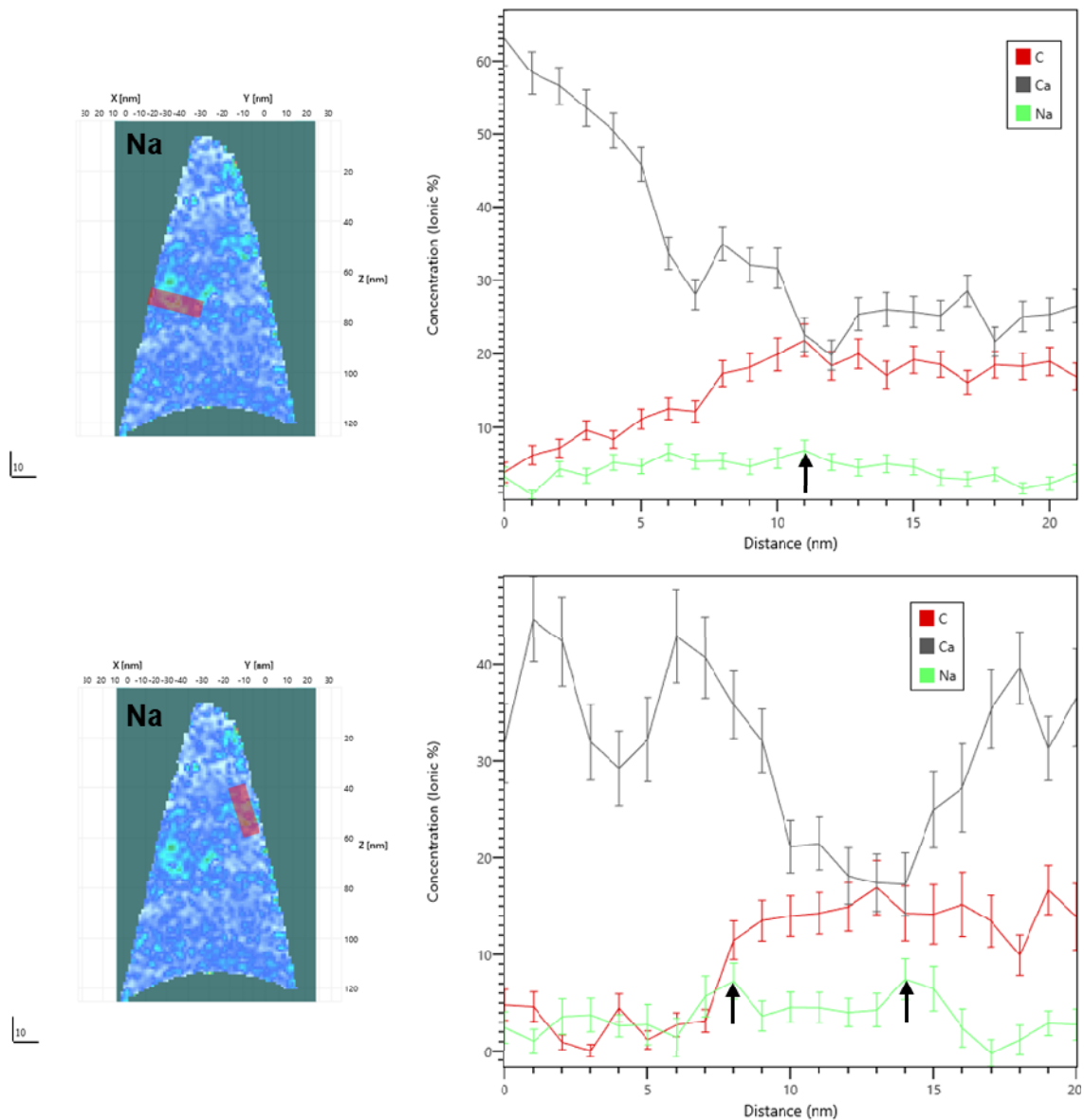


Figure 94. An increase in the concentration of Na (as black arrows marked) at the organic-inorganic interface can be observed in 1D concentration maps of the selected regions of interest in the reconstruction of R5083_22613.

Strontium. The concentration of Sr in bone tissue is low, typically between 0.008 and 0.010 at%, but Sr plays an important role in the bone remodelling process, in which the concentration of Sr in actively metabolizing bone can be increased to a total of 3 to 7 at% [256]. Studies have shown that Sr can stimulate the differentiation and regeneration of stem cells, and promote the activity of osteoblasts and bone formation [257]. In the mass spectrum of porcine trabecular bone, a small single peak at 88 Da of Sr^+ can be found. Furthermore, Sr^{2+} in the 44 Da peak of the mass spectrum overlaps with CaO^{3+} and/or CO^{2+} . Considering the content of Sr is very small relative to C and Ca, the overlap of Sr^{2+} at 44 Da is not considered for the identification and quantification of Sr in this study. From the volume rendering of the concentration of Sr, it can be observed that it is more concentrated in the organic phase of porcine trabecular bone as is apparent in Figure 95. The author proposes that this may be related to the initial aggregation and growth of bioapatite in collagen fibrils, and the biological metabolism close to the organic phase could be more active.

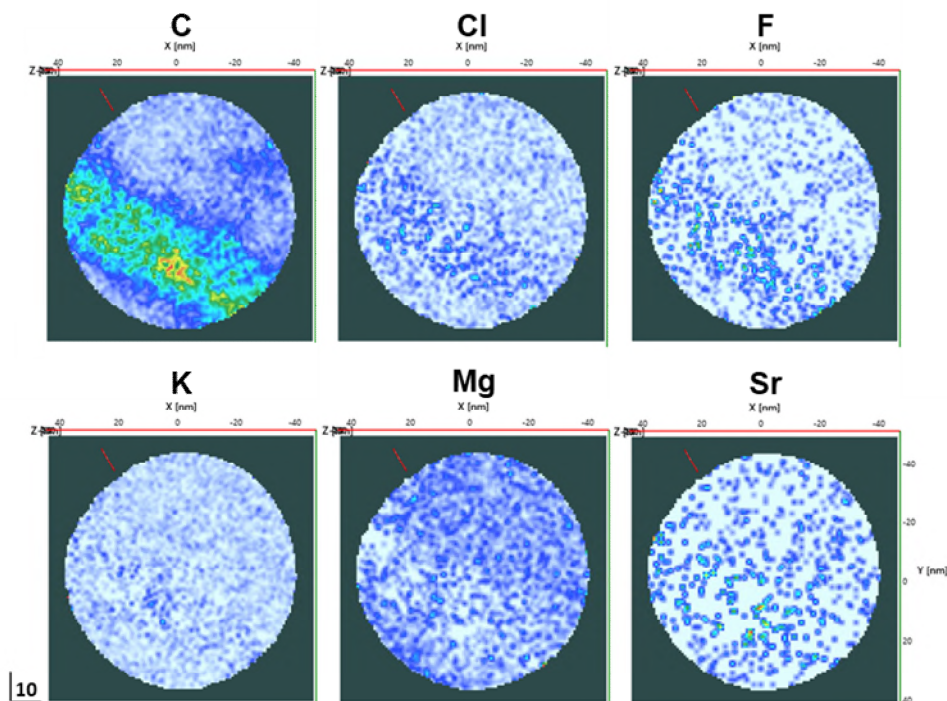


Figure 95. In the X-Y horizontal plane, volume renders of concentration maps of various elements compared with the distribution of C indicating the location of the organic phase in the reconstruction of R5083_22723.

Other trace elements. There are some challenges and need for caution when analyzing trace elements such as K, F, Cl, Br, Se, Zn, and Mn in the APT data. Most of the corresponding peaks of these trace elements or associated complex ions can be found in the mass spectrum of the porcine trabecular bone. However, these peaks are typically not obvious, and contributions may be buried in the background of the mass spectrum, due to their small amounts, or occurring peak overlaps with other elements or complex molecular ions. These issues introduce noise and uncertainty into interpretation of elemental distributions and concentration measurements. Keeping such limitations in mind, information on the positional distribution of these trace elements as initially observed is summarized as follows:

- Zn: main peaks of Zn^+ and Zn^{2+} were found to be overlapped with $^{64}\text{PO}_2\text{H}^+$ and $^{32}\text{O}_2^+$. Hence, the detection of Zn has not included for consideration since

the content of Zn is very small compared with P and O making peak deconvolution not feasible.

- K: obvious independent peaks of K^+ and K^{2+} were observed at 39 Da and 19.5 Da in the mass spectrum respectively. The distribution of K was observed mainly in the organic phase.
- Mn: independent peaks of Mn^+ and Mn^{2+} were observed at 55 Da and 27.5 Da in the mass spectrum respectively. Similar to Na, Mn tends to be located around organic components, at the organic-mineral interfaces.
- Se: the locality of Se in bone is hard to observe. Peaks associated to single ion forms of Se were not found. Detection of small of SeO_3^{2+} was found at 63/64 Da in the mass spectrum. Similarly, very small of SeO_4^{2+} was found in 71 and 72 Da.
- F: An independent peak of F^+ at 19 Da was found in the mass spectrum, also noting 19 Da could also be $C_3H_2^{++}$ or H_3O^+ , and it was observed co-located in the organic phase.
- Cl: peaks of Cl^+ were found at 35 and 37 Da without overlap in the mass spectrum. The distribution of Cl^+ was observed mainly located in the organic phase.
- Br: very small peaks of Br^{2+} at 39.5 and 40.5 Da were found in the mass spectrum, and it was observed mostly located in the mineral phase.

6.5. Composition Investigation

The chemical sensitivity of APT and the wealth of information provided by its mass spectrum allow the quantification of elements. Compositions of seven porcine trabecular bone tips were analyzed using the AtomProbeLab-v0.2.4 in MATLAB. In this thesis, the author suggests that the comparative value of the overall bulk composition measured for the entire reconstructed different tip is low due to the small volumes of microstructure incorporated by each APT experiment, combined with the random sampling of different relative amounts of the organic and mineral phase in analysis of the trabecular bone. Therefore, compositional comparisons between different phases contained within each tip or specific selected sites within the same specimen were carried out as demonstrated in the example in Figure 96. The compositional analysis of collagen phases only considered the organic phases which were isolated using carbon iso-concentration surfaces applied to the reconstruction. In contrast, the compositional analysis of mineral phases were measured by analyzing the remaining component of the reconstruction after the removal of the collagen phase. Specific sites compositional calculation refer to the more precise analysis of different regions of interest (of the same dimensions) selected from different phases within the same specimen.

Examples of compositional analysis of the collagen phase, mineral phase, and specific sites of R5083_22723, respectively, are summarized in Table 18. Significant compositional differences can be observed between the collagen and mineral phases. The content of C in the collagen phase is more than 6 times that of the mineral phase, and the content of N in the collagen phase is more than 2 times that of the mineral phase. Ca and P in the mineral phase are around 1.5 times more than those in the collagen phase. For trace elements, it can be observed that the proportion of Na, K, F, Cl, Sr, and Se in organic phases is relatively higher than in mineral phases. Similar results can also be observed in

the concentration analysis of the collagen phase, mineral phase, and specific sites of R5083_12600 (Table 19). The calculated composition of the different phases of each specimen is shown in Table 20.

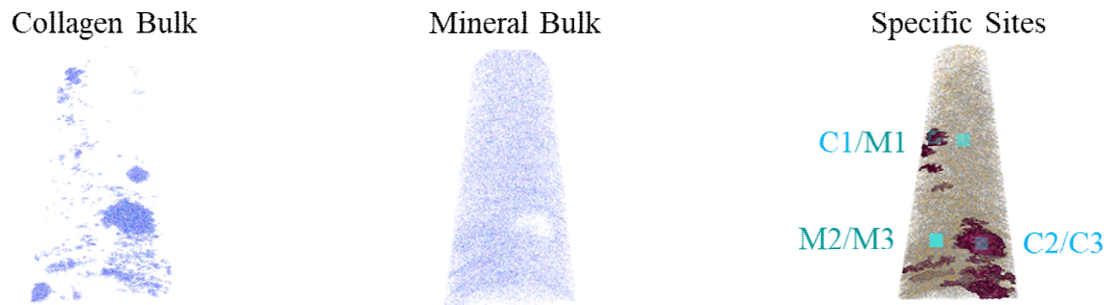
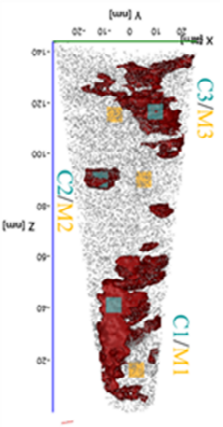


Figure 96. Schematic representations of the collagen phase, mineral phase and specific sites in R5083_22723. The C1-3 are selected from the organic phase and M1-3 are selected from the mineral phase, size of each specific sites is $10 \times 10 \times 10$ nm.

Table 18. Concentration analysis of organic, mineral, and specific sites of R5083_22723. Results are reported using the MATLAB package of AtomProbelab-v0.2.4.

Phase	Site	C (atom%)	N	Ca	P	O	Na	Mg	K	F	Cl	Sr	Br	Se	Mn	Ca/P
	No.															
Collagen Bulk	-	25.119	5.902	15.985	9.777	39.790	1.341	0.743	0.413	0.271	0.303	0.038	0.017	0.251	0.050	1.635
Mineral Bulk	-	3.901	2.803	24.779	15.451	51.116	1.084	0.454	0.087	0.047	0.109	0.013	0.012	0.122	0.022	1.604
Collagen	C1	26.249	4.948	13.520	8.077	44.357	1.319	0.486	0.445	0.180	0.158	0.025	0.018	0.139	0.080	1.674
	C2	27.035	6.656	15.909	9.579	36.889	1.382	0.717	0.602	0.482	0.611	0.028	0.023	0.087	0.000	1.661
	C3	23.262	6.179	16.677	10.806	38.637	1.612	1.245	0.454	0.360	0.342	0.090	0.021	0.293	0.022	1.543
Mineral	M1	2.510	1.644	21.751	17.954	54.178	0.874	0.483	0.330	0.072	0.069	0.015	0.089	0.006	0.024	1.212
	M2	3.583	2.671	22.357	16.482	53.185	0.987	0.300	0.000	0.061	0.043	0.011	0.036	0.252	0.032	1.356
	M3	4.984	3.049	23.747	16.447	50.246	0.537	0.470	0.023	0.094	0.149	0.040	0.064	0.122	0.027	1.444

Table 19. Concentration analysis of organic, mineral, and specific sites of R5083_12600. Results are reported using the MATLAB package of AtomProbeLab-v0.2.4.



Phase	Site	C (atom%)	N	Ca	P	O	Na	Mg	K	F	Cl	Sr	Br	Se	Mn	Ca/P	
	No.																
Collagen Bulk	-	30.620	5.786	18.631	6.226	33.872	2.912	0.331	0.279	0.603	0.466	0.028	0.036	0.161	0.047	2.992	
	Mineral Bulk	-	4.582	3.200	25.380	15.507	48.855	1.487	0.447	0.055	0.110	0.217	0.014	0.017	0.104	0.023	1.637
		Collagen	C1	36.959	7.490	18.835	3.506	26.547	2.562	0.406	0.666	0.702	1.219	0.013	0.089	0.857	0.148
C2			31.958	4.087	14.339	8.373	36.560	2.285	0.323	0.161	0.890	0.465	0.032	0.088	0.157	0.282	1.713
C3	28.177		4.914	15.068	8.695	40.887	0.963	0.287	0.099	0.292	0.379	0.013	0.050	0.130	0.046	1.733	
Mineral	M1	7.736	2.895	51.153	6.557	28.028	2.437	0.977	0.000	0.000	0.199	0.000	0.000	0.018	0.000	7.801	
	M2	5.625	2.831	18.271	18.933	52.755	1.265	0.184	0.020	0.093	0.000	0.000	0.001	0.000	0.023	0.965	
	M3	3.468	2.920	19.620	17.896	52.761	1.635	1.137	0.038	0.152	0.000	0.138	0.044	0.190	0.001	1.096	

6: Atom Probe Analyses of Porcine Trabecular Bone

Table 20. Concentration analysis (atom %) of organic and mineral of 7 specimens of porcine trabecular bone. Results are reported using the MATLAB package of AtomProbeLab-v0.2.4.

Sample No.	Phase	C	N	Ca	P	O	Na	Mg	K	F	Cl	Sr	Br	Se	Mn	Ca/P
R5083_12600	Collagen Bulk	30.620	5.786	18.631	6.226	33.872	2.912	0.331	0.279	0.603	0.466	0.028	0.036	0.161	0.047	2.992
	Mineral Bulk	4.582	3.200	25.380	15.507	48.855	1.487	0.447	0.055	0.110	0.217	0.014	0.017	0.104	0.023	1.637
R5083_22613	Collagen Bulk	28.795	5.994	18.638	7.281	35.567	1.948	0.301	0.350	0.271	0.379	0.068	0.019	0.342	0.048	2.560
	Mineral Bulk	6.325	3.517	23.790	15.235	49.053	1.178	0.334	0.112	0.051	0.185	0.028	0.000	0.149	0.045	1.562
R5083_22723	Collagen Bulk	25.119	5.902	15.985	9.777	39.790	1.341	0.743	0.413	0.271	0.303	0.038	0.017	0.251	0.050	1.635
	Mineral Bulk	3.901	2.803	24.779	15.451	51.116	1.084	0.454	0.087	0.047	0.109	0.013	0.012	0.122	0.022	1.604
R5083_22923	Collagen Bulk	27.359	7.016	15.482	8.000	39.272	1.103	0.409	0.434	0.219	0.434	0.032	0.001	0.216	0.023	1.935
	Mineral Bulk	5.878	4.236	25.491	13.120	49.674	1.049	0.131	0.074	0.000	0.232	0.017	0.009	0.079	0.009	1.943
R5083_23567	Collagen Bulk	20.312	4.393	19.758	10.819	42.265	1.330	0.423	0.204	0.129	0.274	0.024	0.016	0.013	0.040	1.826
	Mineral Bulk	4.421	2.940	25.685	15.491	49.676	1.049	0.421	0.076	0.038	0.139	0.018	0.006	0.019	0.021	1.658
R5083_23568	Collagen Bulk	25.763	6.775	13.849	9.745	41.898	0.691	0.362	0.320	0.175	0.334	0.040	0.008	0.000	0.040	1.421
	Mineral Bulk	5.791	4.406	22.994	14.340	51.047	0.713	0.253	0.115	0.046	0.208	0.021	0.008	0.024	0.036	1.604
R5083_23632	Collagen Bulk	38.656	6.234	15.912	5.751	30.674	0.851	0.353	0.367	0.395	0.307	0.034	0.004	0.423	0.040	2.767
	Mineral Bulk	11.380	4.218	26.572	10.911	45.141	0.737	0.260	0.152	0.120	0.155	0.030	0.006	0.291	0.027	2.435
Average	Collagen Bulk	28.047	5.908	17.154	8.326	37.515	1.314	0.446	0.354	0.257	0.339	0.039	0.011	0.249	0.040	2.145
	Mineral Bulk	4.915	3.517	24.866	14.781	50.073	1.076	0.341	0.082	0.048	0.181	0.017	0.010	0.070	0.022	1.689

The Ca/P ratio in each phase was calculated and compared. The averaged Ca/P ratio of the APT reconstructed whole sample of the porcine trabecular bone was around 1.616 (calculations were done for the entire specimen of each tip without phase separation). The average Ca/P in the mineral phase of the porcine trabecular bone as measured by APT is about 1.69, and the average Ca/P in the intrafibrillar of collagen is around 2.15, as assessed from the measurements summarised in Table 20. The Ca/P ratio of selected mineral regions of interest near collagen fibrils are all less than 1.45 (see Table 18 and Table 19).

The theoretical value of Ca/P of hydroxyapatite is 1.67 [258], and in biological systems, the range of Ca/P is 1-2.1, which is affected by various factors such as gender and age [259]. The Ca/P ratio, microcrystal size and apatite stability all increase with the increase of calcification [260-262]. The biological apatite is always carbonate substituted, for example, the location of CO_3^{2-} groups on the phosphate site in the apatite lattice can explain why the value of the Ca/P ratio is higher than 1.67 in cortical bone [263]. However, the Ca/P ratio of trabecular bone is lower than cortical bone as the trabecular bone is rich in collagen, bone marrow, and blood, which is less mature and contains fewer carbonate ions relative to cortical bone [262]. This supports the validity of the smaller mean Ca/P value of 1.62 that was measured across the entire summed volume of all of the APT reconstructions of the porcine trabecular bone. It also explains that when only the mineral phase is considered in the concentration analysis of the porcine trabecular bone, the obtained Ca/P ratio of 1.69 was found very close to the theoretical value of 1.67.

As previously discussed, there are channels between the collagen arrangements, and during the early mineralization process, bioapatite grows in these channels. It has been proposed that collagen mineralization proceeds through an amorphous calcium phosphate (ACP) which is subsequently converted to crystalline hydroxyapatite, and the

initiation and permeation of minerals in the form of ACP begins at channel sites [237]. Herein, from the calculation of the Ca/P ratio of minerals near collagen fibrils, e.g. specific sites in Figure 96, in porcine trabecular bone, it was measured that the ratios are below that of the bulk mineral, less than 1.45, which is close to the theoretical ACP Ca/P ratio of 1.5. This suggests that hydroxyapatite closer to the collagen fibrils is less crystalline, i.e. less mature than the mineral matrix further away from the fibrils.

To explain the higher Ca/P ratio detected inside collagen fibril, the author has two hypotheses. The first is that the growth of bioapatite in the channel is initiated by the accumulation of Ca in a bio-alkaline environment, but this opinion needs to be further confirmed. The other proposed explanation is based on the description of the bone mineralization mechanism as in Antiope et al. [264]. Assuming that the gap channel is the nucleation point where mineral growth occurs, the minerals grow preferentially in the direction of their crystallographic c-axis (due to little space between collagen chains, thus the little ability to extend in the direction perpendicular to the fibrils), fill the entire gap channel and extend beyond gaps. Thus at a given point in time, the regions away from these gap channels are ACPs, and the cores are more inclined to become HA, which means Ca/P is higher in inner regions than in distant regions. Crucial to this view is whether tested samples are mature bone or not, and the bone undergoes constant remodeling, hence it is hard to confidently know, in a study such as this, if the extracted regions sampled by APT are mature, or a metastable situation during early mineralization stages or phase transformation was captured. Since multiple tips were analyzed in APT, and the Ca/P ratios observed were higher intrafibrillar than the outside of fibrils in all tips, the author believes that it can be assumed that the porcine trabecular measured in this study were mature bone and in line with the second hypothetical situations mentioned.

Composition measurements by APT also have certain limitations. As discussed

previously in synthetic bone samples, there are many factors that affect the measurement of concentrations by APT, such as high levels of background noise in non-conductive samples, misidentification of mass spectra peaks, selection of peak ranges, peak overlap, multiple events, etc. In particular for bio-mineralized materials with heterogeneous phases and various interatomic bonds, many types of complex molecular ions are evaporated during the experiment, and in large numbers, which increases the occurrence of multiple events and the inaccuracies of spectrometry interpretation, which has also been mentioned in previous other research of bone-type materials by APT [21, 25, 112]. In addition, non-conductive biological samples usually result in peaks in the spectra with large thermal tails in the mass spectrum which can result in the loss of significant information regarding other types of ions that should be detected in the adjacent proceeding region. The author suggests that, in addition to optimizing experimental parameters for each material, major contributing peaks in mass spectrum and peaks that can be interpreted with confidence should be primarily considered in the compositional analysis.

6.6. Further Features of APT Analysis of Porcine Trabecular Bone

In the APT investigation of the porcine trabecular bone, some unexpected phenomena and problems were encountered and could not be fully explained. This section discusses the observation of such, as yet, unexplained phenomenon during reconstruction and how to distinguish the extracted organic phase as collagen fibrils or non-collagenous proteins.

6.6.1. Reconstruction Observed to Incorporate A “Hole” Area?

In numerous reconstructions of porcine trabecular bone tips, it was observed that there was a porosity region in the reconstructed results of some samples, as shown in Figure 97 e). The pore volume is composed of blocky or discontinuous strip-shaped groups of ions, as the example displayed in the ion density map in Figure 98. The content of Ca and P in the pore area is very small, while the content of C and N increases obviously, but they all were detected in the form of macromolecular ions. As shown in the volume rendering of the concentration maps of undecomposed C (ionic of carbon), decomposed C (carbon-containing compound ions are broken down into their constituent atoms), decomposed Ca, and decomposed P of the specimen of R5083_23561 in Figure 99, the single carbon ion and the C-containing macromolecular ions were distributed in different regions, but all complementary to the mineral phase. This chapter mainly presents the reconstruction analyses of the hole area within the R5083_22924, however, further similar results from another experiment, R5083_23561, can be found in the Appendix.

What causes the hole area in the reconstruction? To investigate, the voltage history map, detection rate history map, target flux history map, and detector hits map of R5083_22924, have all been re-analyzed trying to better understand the behavior of the sample during the evaporation process. When the evaporation of the tip reaches the hole area, shown as the red box in Figure 97 a), it is apparent that there is a phase change and preferential evaporation has now occurred. In this area, some substance on the surface evaporates more easily than the rest of the tip, or the tip surface consists of many small protrusions, effectively acting as mini-tips that more readily emit ions. This faster evaporation leads to the many hot spots seen in panel d) of Figure 97. Under the original applied voltage, upon reaching this region of the specimen, a large number of ions were evaporated suddenly, shown as an increase in the detection rate which can be seen in panel

b) of Figure 97, the observed detection rate was higher than the object detection rate in the hole region. Since a certain target detection rate was set, the voltage will be reduced to re-achieve the target detection rate, as shown by the voltage drop observed in panel a) of Figure 97. Interestingly, the specimen has not fractured while subject to these events.

This naturally leads to the question: from what materials is the hole region composed? Field evaporation of molecular ions has long been documented and has been attributed to a lower critical electric field to induce field evaporation associated with molecules, rather than individual atoms [265, 266]. In this void region, these molecular ions are preferentially evaporated due to their low evaporation field, so they do not form single ions of C, N. Furthermore, during the evaporation process, as the voltage further decreases, the macromolecules are evaporated more steadily. Therefore, in the mass spectrum specific of this hole region in Figure 100, peaks of large molecular ions such as 15, 28, and 56 Da can be observed, rather than the single ion C or N at 12 and 14 Da. According to the interpretation of this mass spectrum, the signal can be explained by the detection of amino acid fragments, hence components in the holes are most likely to be amino acids, which make up proteins or collagen chains [120]. Table 21 summarizes the compositional analysis of species in selected specific regions of the hole in two tips, the resulting C/N ratio is about 2:1. No research on amino acids specifically in porcine bones was found in the literature, but research on human bones suggests that the C/N ratio of amino acids in collagen is about 3:1 [265]. If so, it is a possible explanation that the hole in the reconstruction is representative of the gap channel that has not yet been mineralized. However, once again, the critical question is how to confirm the bone stage of this specimen.

Is this hole real? First of all, it can be confirmed that the needle has undergone an obvious phase change in this region. There are limitations that the APT reconstruction has

inaccuracies. The APT model assumes that the sample is a hemispherical shape and relies on the continuous evaporation of atoms across the apex surface, atom-by-atom and layer-by-layer. However, for complex multiphase samples, this assumption is often a source of significant error, there may be obvious differences in the 3D reconstruction such as artifacts or spatial positioning errors, as have been mentioned in several studies [266-268]. It is difficult to assess the actual shape taken by the evaporating surface. In the reconstruction of the porcine trabecular bone, due to the beam sensitivity of the specimen, TEM was not performed on the tip prior to APT analysis, and the diameter selected for the reconstruction was only based on the measurement of the tip diameter by SEM/FIB after the tip production, and the field of view measurement during the APT experiment. Therefore, the reconstruction of porcine trabecular bone may be some inaccuracies. Although the exact pore size could not be determined, but its presence and the substance detected in this area were amino acid-based collagen molecules can be confidently proposed.

6: Atom Probe Analyses of Porcine Trabecular Bone

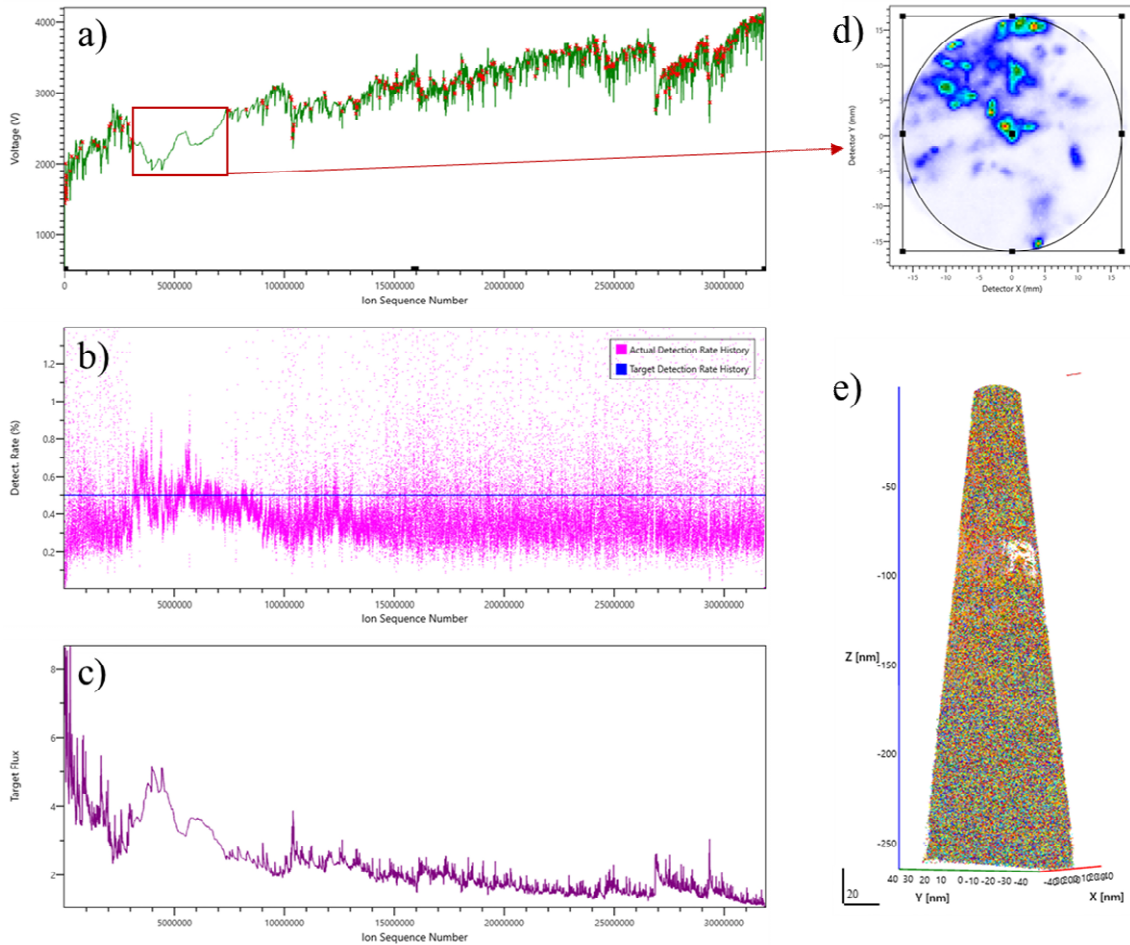


Figure 97. Instantaneous experimental conditions, specimen evaporation response and corresponding reconstruction of R5083_22924. (a) applied voltage history, (b) detection rate history, (c) target flux history, (d) detector map of ion hits corresponding the section of the experiment defined by the selected red box area in (a), and (e) 3D reconstruction of the specimen.

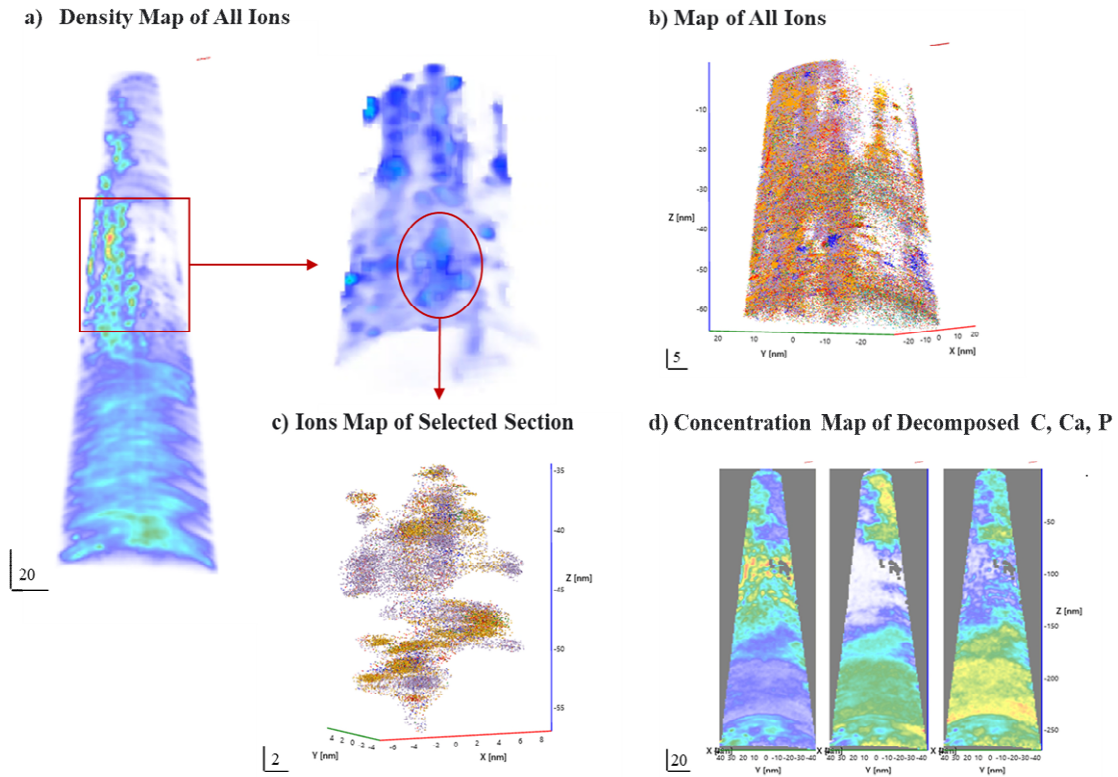


Figure 98. More detailed analysis of the pore region in the R5083_22924. (a) Density map of all ions of the specimen, a higher ion concentration can be observed in the pore region (the red box). (b) and (c) Ions distribution maps of the pore region and selected specific area (the red circle). (d) Volume renders of concentration map of decomposed C, Ca, and P in the tip.

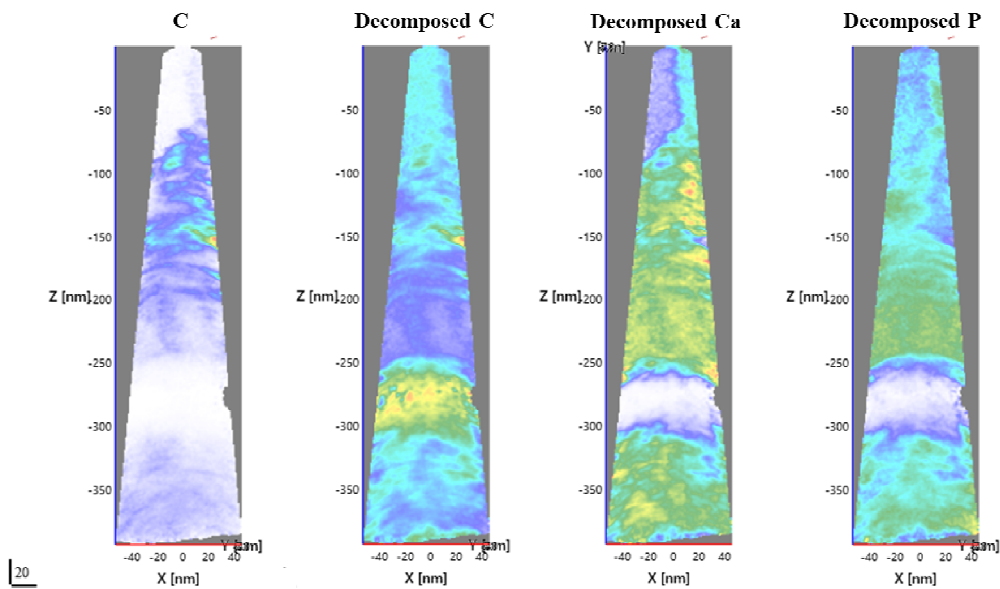


Figure 99. Volume renders of concentration map of undecomposed C, decomposed C, decomposed Ca, and decomposed P in the R5083_23561 APT experiment.

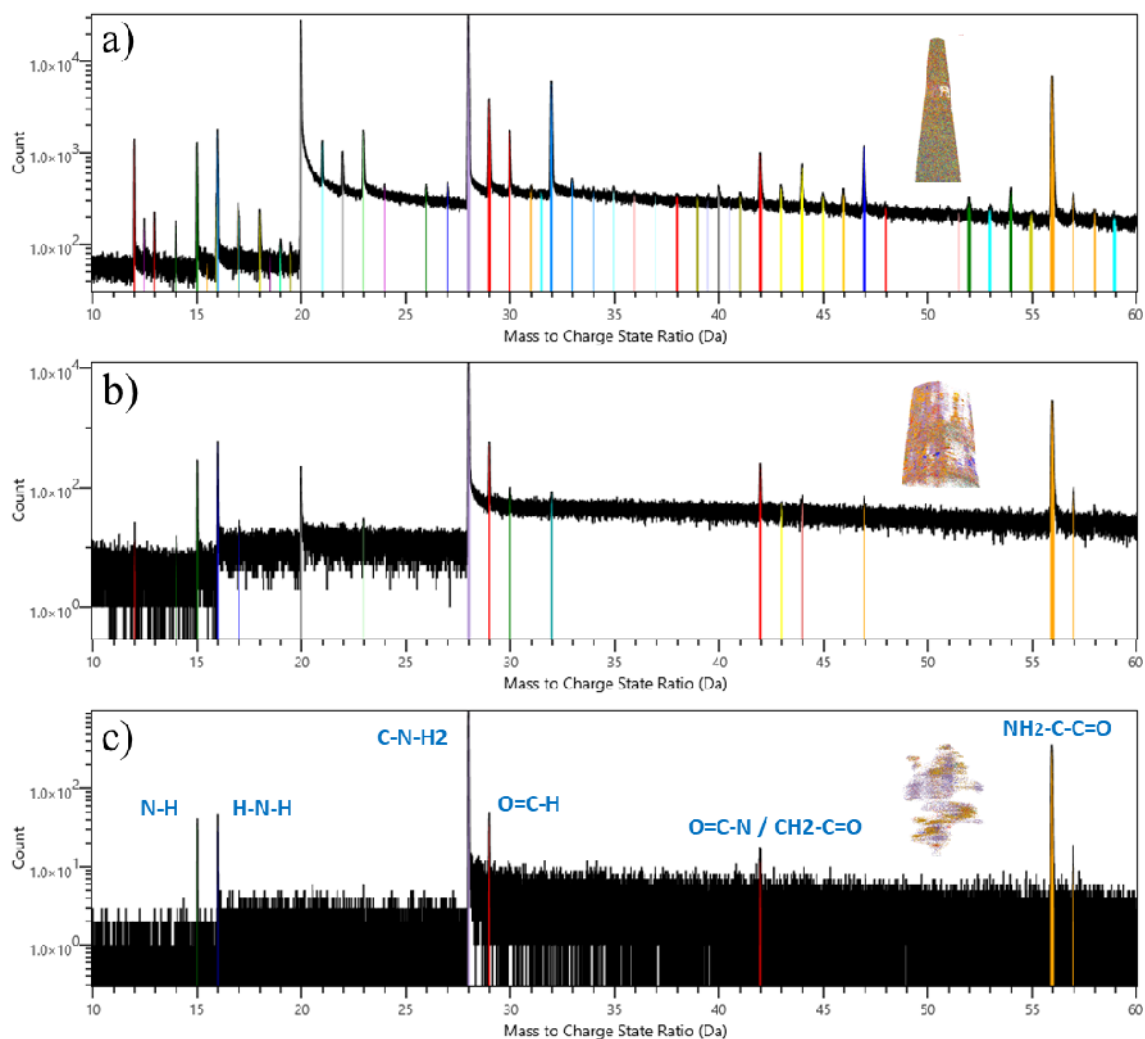


Figure 100. Comparison of mass spectra isolated to different regions in the sample of R5083_22924. (a) The mass spectrum of all ions. (b) The specific mass spectrum of the pore region. (c) The mass spectrum of the selected specific region within the pore.

Table 21. Compositional analysis (at%) of protein-like for selected specific regions in R5083_22924 and R5083_23561 reconstructions.

Specimen No.	C	N	O	H	Ca
R5083_22924	29.084	20.565	9.042	41.309	0
R5083_23561	27.249	22.540	5.580	44.602	0.0268

6.6.2. Are the Observed Organic Regions Collagenous Fibrils or Non-Collagenous Proteins?

The study of bones from various species by Jeroen et al. [223] showed that, in general, much less variation in the composition of trabecular bone was found among the species compared to samples of cortical bone. Ash concentrations in dogs, pigs and sheep were very similar to human samples, however, trabecular bones from pigs and sheep showed lower than expected collagen concentrations but greater amounts of extractable non-collagenous proteins compared to other species as shown in Figure 101 from Reference [223]. In turn, this poses a question to this study: are the organic phases that have been observed and characterized by APT in this work definitely collagen or could they in fact be a different non-collagen protein?

What is the difference between collagen fibril and non-collagen fibril? The main structure of collagen is Gly-X-Y, with X usually Pro (proline) or Lys (lysine), and Y usually Hyp (hydroxyl-proline, hydroxylysine) [269]. Representatives of non-collagenous include osteonectin and osteocalcin (Table 22) [270]. Both osteonectin and osteocalcin (calcium-binding glycoprotein) contain Cys (cysteine), osteonectin has a Cys-rich domain, and osteocalcin contains less Cys [269]. The key is that among all amino acids, only Cys and Met (methionine) contain S as an additional element. Therefore, S can be used as a tracking signal to detect whether extracted organic phases are non-collagenous proteins or not.

Traces of S were attempted to be found in the mass spectrum of the porcine trabecular bone, but there exists a direct overlap between S^+ and O^{2+} among 32-36 Da peaks, and the mass-to-charge-state ratios of their isotopes were also similar. Hence, upon initial analysis there is no method to confidently confirm the existence of S in the specimen from the APT data collected in this study. However, a possibility exists that

detection of the $^{33}\text{S}^+$ isotope, if non-overlapping, could provide a reference for deconvolution of the other shared oxygen and sulphur peaks. Hence, the authors assumed that the peak at 33 Da in the mass spectrum was $^{33}\text{S}^+$, and deconvoluted the overlap of S^+ and O^{2+} among 32-36 Da, as shown in Figure 102, to estimate how much S might be contained in the bulk sample, the organic phase, and mineral phase, respectively, the results are summarized in Table 23. From the hypothesis, if the extracted organic phase is a non-collagenous protein, then the S measured in the organic phase should be higher than that in the bulk as well as in the mineral phase. However, the measurements for both specimens of R5038_12600 and R5038_22723 indicated that there was no S enrichment in organic phases. This would indicate that collagen-like organic fibrils in these two tips should not be non-collagenous proteins. Similarly, this method can be used to search for non-collagen proteins in other tips of porcine trabecular bone.

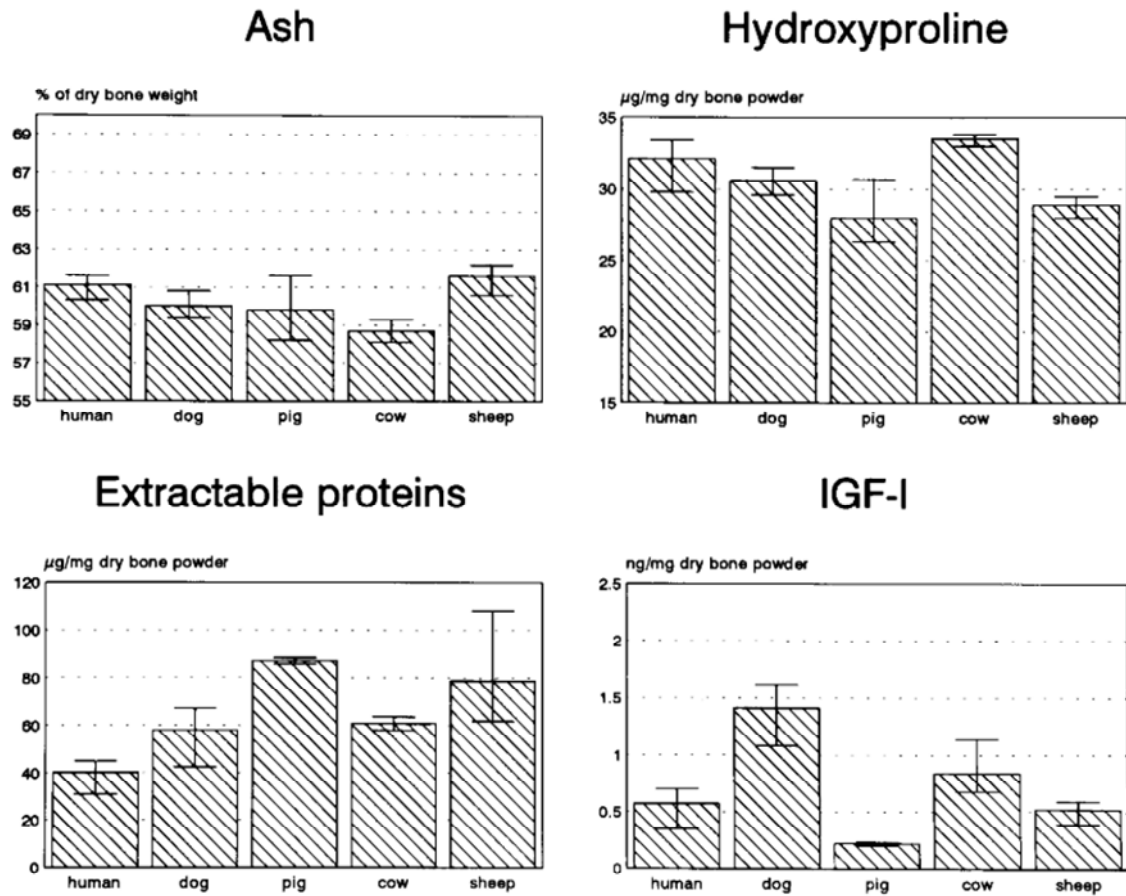


Figure 101. Bone composition of trabecular samples from the lumbar spine of five different species: human, dog, pig, cow, and sheep. Bars indicate the mean value of three examined cases per species; error bars indicate the range [223].

Table 22. Protein constituents of the organic matrix of bone [270].

	% organic	Molecules ² per hydroxy- apatite crystal
Structural proteins		
Collagen type I	85	2.7
Minor collagens (types V, III)	5	0.2
Noncollagenous matrix proteins		
Osteocalcin	1.5	2.2
Osteonectin	2.0	0.6
Matrix gla protein	0.4	0.3
Osteopontin	1.0	0.2
Other phosphoproteins	0.5	0.2
Other sialo- and glycoproteins	1.0	0.1
Proteoglycans and glycosaminoglycans	0.2	0.02
Serum proteins	2.0	0.01
Other proteins and peptides	1.4	–
Biologically active factors	<0.1	<0.001
Mitogens and growth factors		
Differentiation and induction factors		

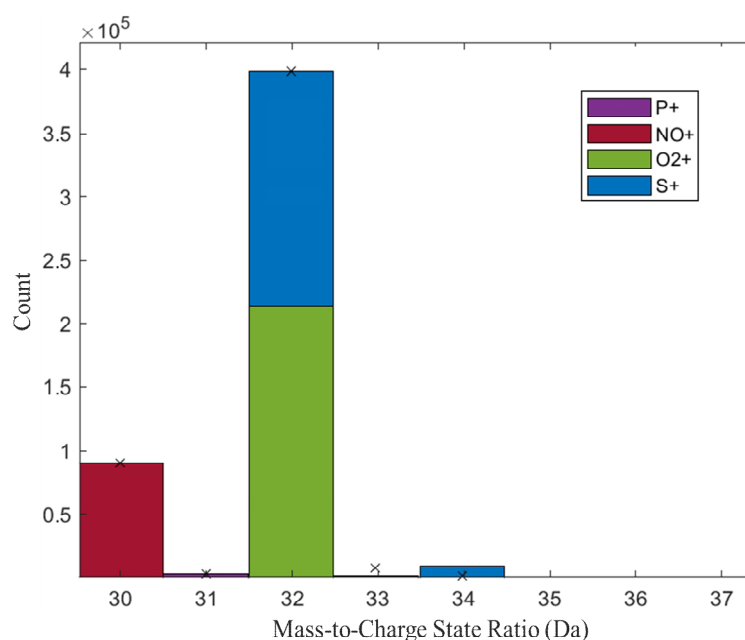


Figure 102. Ion count histogram showing the approximate contribution of each ion type to the different m/z peaks, where 32 Da contains 53.58% O_2^+ and 46.42% S^+ . Plot created using AtomProbeLab-v0.2.4.

Table 23. Comparison of sulfur content in bulk, organic and mineral phases respectively (atom %).

Phase	R5083_12600	R5083_22723
Bulk	4.82	3.12
Organic	3.13	2.71
Mineral	4.93	3.31

6.7. Summary

In this chapter, the APT analysis of porcine trabecular bone was explored. The main findings of this work are outlined as follows:

Optimizing APT Analysis

- FIB lift-out specimen preparation was successfully undertaken in two different orientations with respect to the trabecular bone, and thus to the different orientations of the collagen fibrils with respect to the long axis of the manufactured needle-shaped specimen, as shown in Figure 66 and Figure 80.
- Building on the findings of Chapter 5, undertook a systematic study of how APT experimental operating conditions influence resulting mass spectra and compositional analyses.
- Based on balancing effects such as minimizing background, preventing specimen mini-fractures, etc., the following experimental conditions were recommended for routinely generating viable high quality APT datasets for porcine trabecular bone: the temperature of 30-40 K, a pulse frequency of 125 kHz, a detection rate of 0.4%, and laser energy around 60-100 pJ.

Mass Spectra Interpretation

- Bone analysis resulted in the complex mass spectrum incorporating an array of peaks due to the evaporation of complex ions. Nearly all peaks were successfully labelled as exemplified in Figure 65.
- Further complicating the interpretation of mass spectra was a significant number of peak overlaps, which have been identified and are presented in Table 17. Some main overlaps such as $^{12}\text{C}^+ / ^{12}\text{Mg}^{2+}$, $^{28}\text{CO}^+ / ^{28}\text{CaO}^{2+}$, and $^{44}\text{CO}^{2+} / ^{44}\text{CaO}_3^{2+}$ were discussed and solved. As the discussion of the overlapping peak at 28 Da, it was demonstrated that deconvolution of the relative ionic contributions should be addressed on a phase-by-phase basis (i.e. mass spectrum originating from mineral and organic regions, respectively, should be deconvolved in isolation)
- Signals from trace elements in the mass spectra were identified, and limitations in quantification (e.g. due to challenging peak overlap problems)

Bone Phase Analysis

Mineral Phase

- Mineral phase was delineated from the collagen phase by its high Ca, P content and low C, N concentration.
- Within the mineral phase, distinct regions significantly differing in composition were identified, specifically high Ca, low P regions and vice versa, as exemplified in Figure 68 and Figure 86.
- Increased P concentrations also correlated with increased levels of O.
- Measurement of mineral composition specific to individual samples were presented in Table 20.
- APT analysis enabled measurements of Ca/P values, specific to the mineral phase

and also with smaller nanoscale volumes to investigate variation within these regions

- Results of Ca/P analyses supported existing bone mineralization mechanisms: mineralization proceeds through ACP, whose nucleation point is in the gap channel, ACP gradually grows and fills the entire gap channel, and gradually extends beyond the channel.

Collagen Phase

- Collagen phase was delineated from the mineral phase by high C, N, and low Ca, P. Individual measurements including Ca/P values are presented, for example, in Table 18 and Table 19.
- Specimen preparation along two distinct orientations with respect to the trabecular bones enabled a more holistic characterization of the collagen fibrils.
- In spatial distribution, the complementation of the collagen phase and mineral phase was clearly observed in each specimen, and the aggregation of C and N ions and the absence of Ca and P ions in the collagen fibril phase could also be clearly seen at the atomic length scale. For example, cross sections in Figure 73 clearly show the collagen fibril threading through the mineral phase
- Figure 77 highlights a banded, winding arrangement of periodically spaced fibrils which appears in agreement with the theoretically expected right-helical morphology.
- Specimens made in the vertical orientation such as Figure 82 and Figure 87, also showed a triangular, approximately equidistant separation between fibrils.
- APT enabled spatial measurements of aspects of collagen fibril morphology and distribution. Although some caution should be applied with the interpretation of these measurements as APT reconstruction calibration limitations will contribute

to some imprecision.

- As highlighted in Figure 93 and Figure 94 Na was found to segregate at mineral/collagen boundaries
- Although S is difficult to quantify due to the overlap with the much more intense O signal, however, mapping its distribution appears to confirm that the organic phase sampled in this study was in fact collagen and not some other non-collagen protein.

Observation of “Hole” Artefacts in the Reconstruction

- A recurring hole/void artifact was observed across multiple reconstructions (e.g. Figure 97).
- Isolating the limited mass spectra data originating from this region, identified what could be interpreted as amino acid ionic fragments (e.g. Figure 100).
- It was proposed that this artifact originated from the presence of amino-acid-based collagen.

This chapter makes an in-depth APT exploration of porcine trabecular bone, which not only shows that apt can be used to analyze non-conductive animal bones, but also reveals the interesting microstructure of porcine trabecular bone under the unique atomic-level perspective of APT. The author hopes to inspire future interest and confidence in generations in APT research in the biological field. The results of this chapter combined with the bioactive glass analysis results in chapter 5, lay a solid foundation for further research on APT at the interface of the two materials in the future.

Chapter 7

Conclusions

The work presented in this thesis focuses on developing Atom Probe Tomography specimen preparation, experimental protocols, 3D reconstruction, and data interpretation for biomaterials characterization. The atom probe analysis of two strontium-containing bioactive glass particles, the pSrBG scaffold, and porcine trabecular bone were investigated. In general, the various biomaterials performed well in APT. Although the success rate in the early stage of the project is low (about 10%), with the improvement of the sample preparation method and the optimization of APT parameters, the success rate of later experiments (nice needle with ion counts of more than 5 million) can reach around 90%. Among those specimens used, animal bones were much more difficult in sample preparation, APT experiments, and data interpretation than two strontium-containing bioactive glass particles and the pSrBG scaffold. For example, in sample preparation, the beam damage of animal bone is more severely compared to bioactive glass, as a countermeasure, even lower ion accelerating voltage and current are used. Compared with bioactive glass, animal bones are more unstable in APT experiments due to their unique pore structure, and the complex mass spectrum and multiphase structure of animal bones increase the difficulty of their data interpretation. The main conclusions of this work are outlined as follows, it is hoped that the author's work can provide useful strategies and parameter references for researchers who study similar materials in the future.

Overcoming Sample Preparation Challenges for Hard Biological Specimens

APT analysis of biological-related materials remains challenging with difficulties in sample preparation. Challenges encountered in the preparation of hard biological samples for APT have been highlighted and addressed in this thesis. In particular, significant recurring issues included:

- Cracking, and subsequent loss of lift-out cantilevers, due to contact with FIB micromanipulator.
- Severe bending of the needle-shaped specimen during FIB annular milling.
- Inclusion of micropores in the final specimen critically limiting viability in the APT experiment.

Some insights and strategies for researchers studying similar materials using APT were provided.

It was shown that during sample preparation, for brittle or beam-sensitive samples like biological materials, compared to using the conventional liftout method, placing the micromanipulator close to one side of the cantilever to avoid direct contact between the micromanipulator and the cantilever (leaving a gap for tungsten deposition) can effectively avoid the occurrence of cracks and cantilever loss. This liftout method is also suitable for materials that are surface sensitive or those where a region of interest targeted for analysis is on the surface of the sample. Furthermore, creating enough space around the cantilever (milling a square area at the cutoff region in advance) is an effective way to prevent re-sticking during milling.

Tip bending of beam-sensitive samples can be avoided by balancing the influence of the conditions during annular milling, such as reducing the voltage and current of the imaging electron beam. Herein, the combination of low imaging voltage (≤ 3 kV) and

beam current (≤ 500 pA) can eliminate sample bending for bioactive glass particles and the pSrBG scaffolds. The recipe of electron beam voltages ≤ 2 kV and currents ≤ 200 pA for imaging was found to be important to avoid tip damage for porcine trabecular bone which is even more sensitive. Furthermore, low ion accelerating voltage (≤ 2 kV) and current (≤ 200 pA) were both critical factors for the successful preparation of a suitable APT tip in the final stage of tip sharpening. Strategies of avoiding excessive magnification ($\leq 3.5K$ X) and prolonged imaging were also used to minimize specimen damage and maximize viability.

For samples containing pores or cracks, tip loss was often unavoidable during sample preparation. For such samples, it is recommended that longer cantilevers should be retained during trench milling of the liftout process. Furthermore, by properly adjusting the position of the milling pattern during annular milling, unpredictable voids or cracks on the needle can be removed as much as possible to preserve the tip and maintain viability.

Optimal APT Analysis Conditions

The effects of APT experimental parameters such as temperature, detection rate, laser pulse frequency, and laser pulse energy on the nature and quality of the resulting mass spectrum have been systematically investigated. In particular features of the data such as background levels, multiple hit frequency, mass-to-charge-state ratios, and measured composition of synthetic bone materials and porcine trabecular bone have all been analyzed and discussed.

For non-thermally conductive samples, the choice of specimen stage temperature is found to be of particular importance, due to the relatively slow cooling rate after the application of each laser pulse. Too high or too low temperatures all easily lead to a quick

fracture of the tip. High temperature also causes delayed evaporation, which manifests as large thermal tails after peaks in the mass spectrum. This can be extremely detrimental to the analysis due to associated increases in the background level and the action of overwhelming smaller adjacent peaks, thereby reducing the mass spectrum resolution and limiting the sensitivity of compositional measurements.

Carefully increasing laser pulse energy was found to reduce the background level, improve spectral resolution, reduce the proportion of multiple hit detector events, and increase the proportion of evaporated single-charge-state ions. However, setting laser energies too high can also lead to evaporation being uncorrelated to pulses, resulting in an increase in thermal tails present. Setting a high detection rate for the experiment caused the sample to break more easily due to the higher electric field required to generate sufficient ion evaporation per pulse. Meanwhile, a lower pulse frequency was recommended for this class of non-conductive samples since higher pulse rates mean shorter time detection windows. Too short time intervals between pulses are insufficient to transfer heat away from the sample surface, which can lead to an increase in the sample temperature. Moreover, large complex ions routinely evaporated by biological materials have long time-of-flight, and thus a short detection window may easily lead to specific loss of these ions and inaccuracy in composition measurements.

A balance was found among various parameters for each specimen material respectively, and the optimal operating conditions for the analysis of various materials using the LEAP-5000XR were determined. For bioactive glass (BG-Sr10/BG-Sr100), it was recommended to use the conditions of a stage temperature of 30K, a detection rate of 0.3%, a pulse frequency of 200 kHz, and a pulse energy of 200-250pJ. For the pSrBG scaffolds, the optimal experimental conditions recommended were a temperature of 30 K, a detection rate of 0.4%, a pulse frequency of 125 kHz, and a pulse energy of 200 pJ. In

addition, based on balancing effects such as minimizing background, preventing specimen mini-fractures, etc., the following experimental conditions were recommended for routinely generating viable high quality APT datasets for porcine trabecular bone: the temperature of 30-40 K, a pulse frequency of 125 kHz, a detection rate of 0.4%, and a laser energy of 60-100 pJ.

APT Analysis of Synthetic Bone Substitutes

This research demonstrates that APT can successfully analyze synthetic bone substitute materials, such as strontium-containing bioactive glass particles and the pSrBG scaffold. The synthetic bone substitute used in this chapter are designed to be homogeneous, the accurate APT characterization can refine their composition, ensure uniform distribution of elements at the nanoscale for each materials, and provide the analytical basis for future interfacial analysis of related material (e.g. post-implantation analysis to see whether material changes/degradation). This work also highlights the importance of careful interpretation of the mass spectrum, including overlapping peak deconvolution, when undertaking compositional analysis for each material. The APT analysis of BG-Sr10 and BG-Sr100 was stable, and the distribution of ions in the material was uniform, which was consistent with expectations. Comparisons of BG-Sr10 with BG-Sr100 were undertaken, and although the Sr content in both materials was nearly 1.5 times higher than the nominal composition, the Sr content in BG-Sr100 was 10 times higher than that in BG-Sr10 as expected.

Based on experiences of BG-Sr10 and BG-Sr100, the APT analysis of pSrBG was stable. 6 tips of the pSrBG scaffold were analyzed by APT with a 90% success rate (valid data without tip breakage), which contained 12-25 million ions in the resulting datasets.

APT measurements of the composition of the pSrBG scaffold were similar to previous observations of strontium-containing bioactive glass particles. The reconstruction results for ions were confirmed to be distributed homogeneously.

APT Analysis of Porcine Trabecular Bone

APT can successfully analyze porcine trabecular bone. The bone analysis resulted in the complex mass spectrum incorporating an array of peaks due to the evaporation of complex ions. Nearly all peaks in the complex mass spectra of porcine trabecular bone were successfully labelled based on the main components and trace elements of bones. Some major overlaps occurred in the bone mass spectra such as $^{12}\text{C}^+ / ^{12}\text{Mg}^{2+}$, $^{28}\text{CO}^+ / ^{28}\text{CaO}^{2+}$, and $^{44}\text{CO}_2^+ / ^{44}\text{CaO}_3^{2+}$ were discussed and solved. For example, as the discussion of the overlapping peak at 28 Da, it was demonstrated that deconvolution of the relative ionic contributions should be addressed on a phase-by-phase basis.

The collagen phases and mineral phases were successfully identified in the reconstructions of porcine trabecular bone tips. The mineral phase was delineated from the collagen phase by its high Ca, P content and low C, N concentration. The collagen phase was delineated from the mineral phase by high C, N, and low Ca, P. The reconstructed spatial distributions more fully characterize the collagen fibrils by orientating the extracted tip in different directions (perpendicular/parallel to the trabecular rods), and confirmed the orientation of the collagen fibrils in line with theoretical expectations. In spatial distribution, the complementation of the collagen phase and mineral phase was clearly observed in each specimen. The specimen made in the parallel orientation, as shown in Figure 77, showed a winding arrangement of periodically spaced fibrils, consistent with the theoretically expected right-helical morphology. Specimens

made in the vertical orientation, as shown in Figure 82 and Figure 87, also showed triangular, approximately equidistant separations between fibrils. APT enabled spatial measurements of aspects of collagen fibril morphology and distribution. Although some caution should be applied with the interpretation of these measurements as APT reconstruction calibration limitations will contribute to some imprecision.

Detailed comparisons of the collagen phase and mineral phase were carried out. The co-location of the C and N distributions which represent the collagen phase was observed. The distribution of Ca and P which represent the mineral phase was similarly correlated, and the distribution of O is closely related to P. Furthermore, the aggregation of C and N ions in the collagen phase and the encapsulation of collagen fibrils by the mineral matrix can also be clearly seen at the atomic length scale. Distributions of other trace elements such as Na, Mg, and Sr in porcine trabecular bone were also discussed. For example, the physiology of sodium affects calcium metabolism, and Na in the porcine trabecular bone was observed to distribute mainly around the collagen-mineral interface, rather than simply co-localizing with the organic phase.

Compositional analyses were performed at the collagen phase and mineral phase of different tips or selected specific regions within a specimen. Significant compositional differences between collagen and mineral phases were observed. The APT analysis enabled measurements of Ca/P values, specific to mineral phases and can also with smaller nanoscale volumes to study variation within these regions. In this work, the average Ca/P ratio of APT-reconstructed porcine trabecular bone whole specimen (without phase separation) was 1.616, which is consistent with the general phenomenon that the Ca/P value of trabecular bone is smaller than the hydroxyapatite theoretical value of 1.67, due to the trabecular bone is less mature, and rich in collagen, bone marrow and blood. The Ca/P ratios in the mineral phases, within collagen fibrils (intrafibrillar), and

around collagen fibrils were measured and compared by APT. The mean Ca/P in the mineral phase was 1.69, which is close to the theoretical Ca/P value of hydroxyapatite. The calculation of the Ca/P ratio of minerals near collagen fibrils was measured below that of the bulk mineral, less than 1.45, which is close to the theoretical ACP Ca/P ratio of 1.5. Suggesting that hydroxyapatite closer to the collagen fibrils is less crystalline, i.e. less mature than the mineral matrix further away from the fibrils. The mean Ca/P of intrafibrillar was higher than that of these regions near the collagen, results supported the existing bone mineralization mechanisms: mineralization proceeds through ACP, whose nucleation point is in the gap channel, ACP gradually grows and fills the entire gap channel, and gradually extends beyond the channel.

In addition, further features of APT analysis of porcine trabecular bone were discussed. Reasonable conjectures and explanations were given for the recurring hole/void artifact across multiple reconstructions, and proposed that amino acid ionic fragments were captured in the hole region. Besides, a question was raised about the identity of the captured organic in porcine trabecular bone, and a method of distinguishing whether the extracted organic phase is collagenous or non-collagenous was provided, and confirmed that the organic phase sampled in this study was collagen instead of some other non-collagen protein.

In this thesis, Atom Probe Tomography was developed for unique nanoscale insight into biological materials. Although the APT exploration of biological materials in this work is full of challenges, such as involving relatively small sampling volumes, some trace overlaps are too challenging to deconvolve, and the current accuracy of composition is hard to currently quantify due to influences such as systematic changing of experimental conditions. This work successfully demonstrates the ability of APT to probe biological materials such as bone with sufficient chemical and spatial resolution. For

example, APT has the capacity to isolate small phases for compositional analysis and mapping trace elements within the specimen. Furthermore, APT has the strength to demonstrate compositional variations in nanovolumes within different phases, e.g. mineral phases and collagen phases. APT has shown the ability to provide unique discoveries in the structure and chemistry of organic and inorganic materials.

Chapter 8

Future Work

In addition to the work carried out in this thesis, there are still several issues that should be improved or investigated in the future.

Comparison of APT Analysis of Trabeculae Bone between Species

Building on the APT exploration of porcine trabecular bone in this thesis, trabecular bone from different species can be studied using APT, hopefully providing information on chemical and structural differences within and between species, such as comparisons of bones from animals of different ages, comparison of trabecular bones between different animal. It aims to explore the subtle differences in the bone between species and provide data support for the advancement of biomaterials-research. Provide unique insights further to reveal the structure of bone at the atomic level.

Simulations for Molecular Ion Stability

The development and application of Density Functional Theory (DFT) simulations can be investigated to study the stability of specific molecular ions exposed to an intense electric field. A large number of molecular ions are generated during the evaporation of APT analysis of biological materials. Unstable ions decompose into two/more smaller particles on the way to atom probe detector. Therefore, if the molecule is determined to be unstable, one would not expect to detect this form experimentally.

This is extremely valuable information when trying to identify all possible ion types that could be attributed to a particular mass-to-charge-state ratio of the peak. Using simulations to preclude specific molecules as physical possibilities for detection reduces the number of ions that must be considered when identifying each peak, reducing the complexity of fully characterizing the mass spectra. Preliminary calculations have been successfully developed, demonstrating the feasibility of this method for interpreting steel and alloy analyses [202, 271]. Furthermore, this simulation can be combined with standard materials such as pure hydroxyapatite to further probe effects of APT operating conditions on composition to refine experiments, and to gain a better understand accuracy of composition quantitative measurements.

APT study of Sr Bone Uptake from the pSrBG Scaffold

Strontium-containing bioactive glass, pSrBG scaffold, and animal bone have been fully characterized by APT as references. Further development and optimization of the APT to characterize the bone-strontium biomaterial interface will be developed in the future. Chiara et al. report the nanoscale characterization of the interface between newly formed bone and bioactive glass [272], but the atomic-scale analysis of the interface between bone and bioactive glass-based biomaterial has not yet been reported. Studies of the bone-implant interface of dental titanium-based implants by APT by Johan et al. [115] and Gustav et al. [89] proved the possibility of APT for interface characterization. The application of APT to the study of the tissue-implant interface can provide unprecedented resolution of the implant interface and provide important insights into the mechanisms behind osseointegration.

Previously in vivo bone repair assessment was performed using non-pregnant

skeletally mature female sheep, using 8 mm diameter cylindrical defects in the left medial femoral condyle per animal, using an electric drill with a stop to limit defect depth to 15 mm, as published in the paper by Helen et al. [15]. Samples can be taken at 6 and 12 weeks after implantation and will be characterized by APT. Sr uptake will be characterized using a mapping scheme at intervals of 100 μm from the interface and across the interface. Results can be compared with complementary characterization techniques such as histology and histomorphometry. Sampling and analysis after implantation can also be performed on the two types of Sr containing bioactive glasses characterized in the Chapter 5 to compare the amount of elements' diffusion in bioactive glasses with different Sr content after different amounts of times. Although, it is foreseeable that the analysis of this organic-inorganic interface by APT will face further challenges (e.g. orientation selection of the interface in specimen, potential brittleness at interface affecting viability, potential overlaps with small amounts of Sr diffusing into bone, experimental conditions to balance viability and quantifying Sr on the bone side of interface), the potential for unique insight of APT into the interface is very exciting.

Combination of Correlative Techniques

Increasingly researchers are embracing the power of combining complementary characterization tools for a more holistic perspective. While the APT has the potential for unique insights, it only contains a small part of a larger picture, so complementary microscopes could also be utilized to obtain richer research in the future. For example, electron microscopy (EM) could generate density-dependent images to distinguish mineralized tissue from organic tissue. EM was previously implemented by the Stevens Group to identify highly crystalline nanoparticles embedded in human aorta tissues [273]. High resolution-optical microscopy and Raman spectroscopy can be used to determine

bone crystallinity [274]. TEM can be combined with APT to further improve the accuracy of reconstruction. By combining APT with other microscopy techniques, there is the potential to better understand the complex processes that occur at the smallest-scale implant interfaces, leading to the development of improved biomaterials.

Chapter 9

Bibliography

1. Wang, W. and K.W.K. Yeung, *Bone grafts and biomaterials substitutes for bone defect repair: A review*. *Bioact Mater*, 2017. **2**(4): p. 224-247.
2. Jones, J.R., *Review of bioactive glass: from Hench to hybrids*. *Acta biomaterialia*, 2013. **9**(1): p. 4457-4486.
3. Xynos, I.D., et al., *Gene - expression profiling of human osteoblasts following treatment with the ionic products of Bioglass® 45S5 dissolution*. *Journal of Biomedical Materials Research: An Official Journal of The Society for Biomaterials, The Japanese Society for Biomaterials, and The Australian Society for Biomaterials and the Korean Society for Biomaterials*, 2001. **55**(2): p. 151-157.
4. Vogel, M., et al., *Development of multinuclear giant cells during the degradation of Bioglass® particles in rabbits*. *Journal of Biomedical Materials Research Part A: An Official Journal of The Society for Biomaterials, The Japanese Society for Biomaterials, and The Australian Society for Biomaterials and the Korean Society for Biomaterials*, 2004. **70**(3): p. 370-379.
5. Leu, A. and J.K. Leach, *Proangiogenic potential of a collagen/bioactive glass substrate*. *Pharmaceutical research*, 2008. **25**(5): p. 1222-1229.
6. Meunier, P.J., et al., *The effects of strontium ranelate on the risk of vertebral fracture in women with postmenopausal osteoporosis*. *New England Journal of Medicine*, 2004. **350**(5): p. 459-468.
7. Reginster, J.-Y., et al., *Strontium ranelate reduces the risk of nonvertebral fractures in postmenopausal women with osteoporosis: Treatment of Peripheral Osteoporosis (TROPOS) study*. *The journal of clinical endocrinology & metabolism*, 2005. **90**(5): p. 2816-2822.
8. Querido, W., A.L. Rossi, and M.J.M. Farina, *The effects of strontium on bone mineral: A review on current knowledge and microanalytical approaches*. 2016. **80**: p. 122-134.
9. Gentleman, E., et al., *The effects of strontium-substituted bioactive glasses on osteoblasts and osteoclasts in vitro*. *Biomaterials*, 2010. **31**(14): p. 3949-3956.
10. Fredholm, Y.C., et al., *Influence of strontium for calcium substitution in bioactive glasses on degradation, ion release and apatite formation*. 2011. **9**(70): p. 880-889.
11. Arepalli, S.K., et al., *Enhanced bioactivity, biocompatibility and mechanical behavior of strontium substituted bioactive glasses*. *Materials Science and Engineering: C*, 2016. **69**: p. 108-116.
12. Chandran, S., et al., *Strontium Hydroxyapatite scaffolds engineered with stem cells aid osteointegration and osteogenesis in osteoporotic sheep model*. *Colloids and Surfaces B: Biointerfaces*, 2018. **163**: p. 346-354.
13. Reitmaier, S., et al., *Strontium (II) and mechanical loading additively augment bone*

- formation in calcium phosphate scaffolds*. Journal of Orthopaedic Research®, 2018. **36**(1): p. 106-117.
14. Neves, N., et al., *In vivo and clinical application of strontium-enriched biomaterials for bone regeneration: A systematic review*. Bone & joint research, 2017. **6**(6): p. 366-375.
 15. Autefage, H., et al., *Multiscale analyses reveal native-like lamellar bone repair and near perfect bone-contact with porous strontium-loaded bioactive glass*. Biomaterials, 2019.
 16. Rahaman, M.N., et al., *Bioactive glass in tissue engineering*. 2011. **7**(6): p. 2355-2373.
 17. Thavornnyutikarn, B., et al., *Porous 45S5 Bioglass®-based scaffolds using stereolithography: effect of partial pre-sintering on structural and mechanical properties of scaffolds*. Materials Science and Engineering: C, 2017. **75**: p. 1281-1288.
 18. Liu, J., et al., *Fabrication and characterization of porous 45S5 glass scaffolds via direct selective laser sintering*. Materials and Manufacturing Processes, 2013. **28**(6): p. 610-615.
 19. Fabert, M., et al., *Crystallization and sintering of borosilicate bioactive glasses for application in tissue engineering*. Journal of materials chemistry B, 2017. **5**(23): p. 4514-4525.
 20. El-Ghannam, A. and P. Ducheyne, *1.9 Bioactive Ceramics*. Comprehensive Biomaterials II; Ducheyne, P., Ed.; Elsevier: Oxford, UK, 2017: p. 204-234.
 21. Gordon, L.M., L. Tran, and D.J.A.n. Joester, *Atom probe tomography of apatites and bone-type mineralized tissues*. 2012. **6**(12): p. 10667-10675.
 22. Schrof, S., et al., *3D Raman mapping of the collagen fibril orientation in human osteonal lamellae*. Journal of structural biology, 2014. **187**(3): p. 266-275.
 23. Hyde, J. and C. English, *Microstructural characterisation techniques for the study of reactor pressure vessel (RPV) embrittlement*, in *Irradiation Embrittlement of Reactor Pressure Vessels (RPVs) in Nuclear Power Plants*. 2015, Elsevier. p. 211-294.
 24. Geiser, B.P., et al. *Spatial distribution maps for atom probe tomography*. in *2006 19th International Vacuum Nanoelectronics Conference*. 2006. IEEE.
 25. Brian Langelier¹, X.W.K.G., ², *Atomic scale chemical tomography of human bone*. 2017.
 26. Gordon, L.M. and D. Joester, *Nanoscale chemical tomography of buried organic–inorganic interfaces in the chiton tooth*. Nature, 2011. **469**(7329): p. 194.
 27. Gordon, L.M., et al., *Dental materials. Amorphous intergranular phases control the properties of rodent tooth enamel*. Science, 2015. **347**(6223): p. 746-50.
 28. DerkJoester, L.M.G.a., *Mapping residual organics and carbonate at grain boundaries and the amorphous interphase in mouse incisor enamel*. 2015.
 29. Integration, A.R.T., *Atomically Resolved Tissue Integration*. 2014.
 30. Agarwal, R. and A.J.J.A.d.d.r. Garcia, *Biomaterial strategies for engineering implants for enhanced osseointegration and bone repair*. 2015. **94**: p. 53-62.
 31. Lieberman, J.R. and G.E. Friedlaender, *Bone regeneration and repair: biology and clinical applications*. 2005: Springer.
 32. Lee, K. and S.B. Goodman, *Current state and future of joint replacements in the hip and knee*. Expert review of medical devices, 2008. **5**(3): p. 383-393.
 33. Boskey, A.L., *Mineralization of bones and teeth*. Elements, 2007. **3**(6): p. 385-391.
 34. Witmer, D.K., S.T. Marshall, and B.D. Browner, *Emergency Care of Musculoskeletal*

- Injuries*. Townsend, Courtney M.; Beauchamp, R. Daniel; Evers, B. Mark, 2016: p. 462-504.
35. Marsell, R. and T.A. Einhorn, *The biology of fracture healing*. Injury, 2011. **42**(6): p. 551-555.
36. Cruess, R. and J. Dumont, *Fracture healing*. Canadian journal of surgery. Journal canadien de chirurgie, 1975. **18**(5): p. 403-413.
37. Bolander, M.E., *Regulation of fracture repair by growth factors*. Proceedings of the Society for Experimental Biology and Medicine, 1992. **200**(2): p. 165-170.
38. Ortega, N., D.J. Behonick, and Z. Werb, *Matrix remodeling during endochondral ossification*. Trends in cell biology, 2004. **14**(2): p. 86-93.
39. Mackie, E., et al., *Endochondral ossification: how cartilage is converted into bone in the developing skeleton*. The international journal of biochemistry & cell biology, 2008. **40**(1): p. 46-62.
40. Dimitriou, R., et al., *Bone regeneration: current concepts and future directions*. BMC medicine, 2011. **9**(1): p. 66.
41. Campana, V., et al., *Bone substitutes in orthopaedic surgery: from basic science to clinical practice*. Journal of Materials Science: Materials in Medicine, 2014. **25**(10): p. 2445-2461.
42. van Meekeren, J., *Heel-en Geneeskunstige Aanmerkingen*. Commelijjn. Google Scholar, 1668.
43. Albrektsson, T. and C. Johansson, *Osteoinduction, osteoconduction and osseointegration*. European spine journal, 2001. **10**(2): p. S96-S101.
44. Heiple, K.G., S.W. CHASE, and C.H. HERNDON, *A comparative study of the healing process following different types of bone transplantation*. JBJS, 1963. **45**(8): p. 1593-1616.
45. Khan, S.N., et al., *The biology of bone grafting*. JAAOS-Journal of the American Academy of Orthopaedic Surgeons, 2005. **13**(1): p. 77-86.
46. Boskey, A.L., *Bone composition: relationship to bone fragility and antiosteoporotic drug effects*. Bonekey Rep, 2013. **2**: p. 447.
47. Roberts, T.T. and A.J. Rosenbaum, *Bone grafts, bone substitutes and orthobiologics: the bridge between basic science and clinical advancements in fracture healing*. Organogenesis, 2012. **8**(4): p. 114-124.
48. Jones, J.R., *Review of bioactive glass: from Hench to hybrids*. Acta Biomater, 2013. **9**(1): p. 4457-86.
49. De Long, W., et al., *Bone grafts and bone graft substitutes in orthopaedic trauma surgery*. The Journal of Bone & Joint Surgery, 2007. **89**(3): p. 649-658.
50. GlobalData, *MediPoint: Bone Grafts and Substitutes - Global Analysis and Market Forecasts*. 2014.
51. Zwingenberger, S., et al., *Recommendations and considerations for the use of biologics in orthopedic surgery*. BioDrugs, 2012. **26**(4): p. 245-256.
52. Dreesmann, H., *Ueber Knochenplombirung*. DMW-Deutsche Medizinische Wochenschrift, 1893. **19**(19): p. 445-446.
53. Carson, J.S. and M.P. Bostrom, *Synthetic bone scaffolds and fracture repair*. Injury, 2007. **38**(1): p. S33-S37.
54. Niu, C.-C., et al., *A comparison of posterolateral lumbar fusion comparing autograft,*

- autogenous laminectomy bone with bone marrow aspirate, and calcium sulphate with bone marrow aspirate: a prospective randomized study.* Spine, 2009. **34**(25): p. 2715-2719.
55. Egli, P., W. Müller, and R. Schenk, *Porous hydroxyapatite and tricalcium phosphate cylinders with two different pore size ranges implanted in the cancellous bone of rabbits. A comparative histomorphometric and histologic study of bony ingrowth and implant substitution.* Clinical orthopaedics and related research, 1988(232): p. 127-138.
 56. Le Huec, J., et al., *Influence of porosity on the mechanical resistance of hydroxyapatite ceramics under compressive stress.* Biomaterials, 1995. **16**(2): p. 113-118.
 57. Dorozhkin, S.V., *Calcium orthophosphates: applications in nature, biology, and medicine.* 2012: Pan Stanford.
 58. Kattimani, V.S., S. Kondaka, and K.P. Lingamaneni, *Hydroxyapatite—Past, present, and future in bone regeneration.* Bone and Tissue Regeneration Insights, 2016. **7**: p. BTRI. S36138.
 59. Habibovic, P., et al., *Osteoconduction and osteoinduction of low-temperature 3D printed bioceramic implants.* Biomaterials, 2008. **29**(7): p. 944-953.
 60. Ripamonti, U., et al., *The induction of bone formation by smart biphasic hydroxyapatite tricalcium phosphate biomimetic matrices in the non - human primate Papio ursinus.* Journal of cellular and molecular medicine, 2008. **12**(6b): p. 2609-2621.
 61. Ripamonti, U., et al., *The induction of bone formation by coral-derived calcium carbonate/hydroxyapatite constructs.* Biomaterials, 2009. **30**(7): p. 1428-1439.
 62. Wenisch, S., et al., *In vivo mechanisms of hydroxyapatite ceramic degradation by osteoclasts: fine structural microscopy.* Journal of Biomedical Materials Research Part A: An Official Journal of The Society for Biomaterials, The Japanese Society for Biomaterials, and The Australian Society for Biomaterials and the Korean Society for Biomaterials, 2003. **67**(3): p. 713-718.
 63. Ambard, A.J. and L. Mueninghoff, *Calcium phosphate cement: review of mechanical and biological properties.* Journal of Prosthodontics, 2006. **15**(5): p. 321-328.
 64. Brown, W., *A new calcium phosphate setting cement.* J Dent Res, 1983. **63**: p. 672.
 65. Zhang, J., et al., *Calcium phosphate cements for bone substitution: chemistry, handling and mechanical properties.* Acta biomaterialia, 2014. **10**(3): p. 1035-1049.
 66. Hench, L.L., et al., *Bonding mechanisms at the interface of ceramic prosthetic materials.* Journal of biomedical materials research, 1971. **5**(6): p. 117-141.
 67. Hench, L.L., *The story of Bioglass®.* Journal of Materials Science: Materials in Medicine, 2006. **17**(11): p. 967-978.
 68. Moimas, L., et al., *Rabbit pilot study on the resorbability of three-dimensional bioactive glass fibre scaffolds.* Acta biomaterialia, 2006. **2**(2): p. 191-199.
 69. Williams, D.F., *Definitions in biomaterials: proceedings of a consensus conference of the European Society for Biomaterials, Chester, England, March 3-5, 1986.* Vol. 4. 1987: Elsevier Science Limited.
 70. Kokubo, T. and H. Takadama, *How useful is SBF in predicting in vivo bone bioactivity?* Biomaterials, 2006. **27**(15): p. 2907-2915.
 71. Schoen, F. and L. Hench, *Toxicology and biocompatibility of Bioglass.* J. Biomed. Mater Res, 1981. **15**.

9: Bibliography

72. Gentleman, E., et al., *Comparative materials differences revealed in engineered bone as a function of cell-specific differentiation*. Nature materials, 2009. **8**(9): p. 763.
73. Hench, L.L. and J.M. Polak, *Third-generation biomedical materials*. Science, 2002. **295**(5557): p. 1014-1017.
74. Ducheyne, P. and Q. Qiu, *Bioactive ceramics: the effect of surface reactivity on bone formation and bone cell function*. Biomaterials, 1999. **20**(23-24): p. 2287-2303.
75. Azenha, M.R., et al., *Evaluation of crystallized biosilicate in the reconstruction of calvarial defects*. Journal of maxillofacial and oral surgery, 2015. **14**(3): p. 659-665.
76. Thompson, K.H. and C. Orvig, *Boon and bane of metal ions in medicine*. Science, 2003. **300**(5621): p. 936-939.
77. Bi, L., et al., *Evaluation of bone regeneration, angiogenesis, and hydroxyapatite conversion in critical - sized rat calvarial defects implanted with bioactive glass scaffolds*. Journal of Biomedical Materials Research Part A, 2012. **100**(12): p. 3267-3275.
78. Querido, W., A.L. Rossi, and M. Farina, *The effects of strontium on bone mineral: A review on current knowledge and microanalytical approaches*. Micron, 2016. **80**: p. 122-134.
79. Gentleman, E., et al., *The effects of strontium-substituted bioactive glasses on osteoblasts and osteoclasts in vitro*. 2010. **31**(14): p. 3949-3956.
80. O'Donnell, M., et al., *Structural analysis of a series of strontium-substituted apatites*. Acta Biomaterialia, 2008. **4**(5): p. 1455-1464.
81. Stanley, H.R., et al., *Using 45S5 bioglass cones as endosseous ridge maintenance implants to prevent alveolar ridge resorption: a 5-year evaluation*. International journal of oral & maxillofacial implants, 1997. **12**(1).
82. Agna, J.W., H.C. Knowles, and G. Alverson, *The mineral content of normal human bone*. The Journal of clinical investigation, 1958. **37**(10): p. 1357-1361.
83. Klenke, F.M., et al., *Impact of pore size on the vascularization and osseointegration of ceramic bone substitutes in vivo*. Journal of Biomedical Materials Research Part A: An Official Journal of The Society for Biomaterials, The Japanese Society for Biomaterials, and The Australian Society for Biomaterials and the Korean Society for Biomaterials, 2008. **85**(3): p. 777-786.
84. Wu, Z.Y., et al., *Melt-derived bioactive glass scaffolds produced by a gel-cast foaming technique*. Acta Biomaterialia, 2011. **7**(4): p. 1807-1816.
85. Fu, Q., et al., *Mechanical and in vitro performance of 13–93 bioactive glass scaffolds prepared by a polymer foam replication technique*. Acta biomaterialia, 2008. **4**(6): p. 1854-1864.
86. Merrett, K., et al., *Surface analysis methods for characterizing polymeric biomaterials*. Journal of Biomaterials Science, Polymer Edition, 2002. **13**(6): p. 593-621.
87. Lausmaa, J., et al., *Surface characterization of biomaterials*. Amsterdam: Elsevier, 1988.
88. Anders Palmquist¹, Kathryn Grandfield², and T.M. Birgitta Norlindh¹, Rickard Brañemark⁴ and Peter Thomsen¹, *Bone–titanium oxide interface in humans revealed by transmission electron microscopy and electron tomography*. 2011.
89. Gustav Sundell a, Christer Dahlin b,c, Martin Andersson d, Mattias Thuvander a, *The bone-implant interface of dental implants in humans on the atomic scale*. 2016.
90. Cunningham, T., et al., *Atomic force profilometry and long scan atomic force microscopy*:

- new techniques for characterisation of surfaces*. Surface engineering, 2000. **16**(4): p. 295-298.
91. Missirlis, E. and W. Lemm, *Modern aspects of protein adsorption on biomaterials*. 2012: Springer Science & Business Media.
 92. Ross, M.H. and W. Pawlina, *Histology*. 2006: Lippincott Williams & Wilkins.
 93. Parfitt, A.M., et al., *Bone histomorphometry: standardization of nomenclature, symbols, and units: report of the ASBMR Histomorphometry Nomenclature Committee*. Journal of bone and mineral research, 1987. **2**(6): p. 595-610.
 94. Sodhi, R.N., *Application of surface analytical and modification techniques to biomaterial research*. Journal of electron spectroscopy and related phenomena, 1996. **81**(3): p. 269-284.
 95. Battistoni, C., et al., *Surface characterization of biocompatible hydroxyapatite coatings*. Surface and Interface Analysis: An International Journal devoted to the development and application of techniques for the analysis of surfaces, interfaces and thin films, 2000. **29**(11): p. 773-781.
 96. Lyman, C.E., et al., *Scanning electron microscopy, X-ray microanalysis, and analytical electron microscopy: a laboratory workbook*. 2012: Springer Science & Business Media.
 97. Leng, Y., J. Chen, and S.J.B. Qu, *TEM study of calcium phosphate precipitation on HA/TCP ceramics*. 2003. **24**(13): p. 2125-2131.
 98. Gordon, L.M. and D.J.F.i.p. Joester, *Mapping residual organics and carbonate at grain boundaries and the amorphous interphase in mouse incisor enamel*. 2015. **6**: p. 57.
 99. Penel, G., et al., *Composition of bone and apatitic biomaterials as revealed by intravital Raman microspectroscopy*. Bone, 2005. **36**(5): p. 893-901.
 100. Carden, A. and M.D. Morris, *Application of vibrational spectroscopy to the study of mineralized tissues*. Journal of biomedical optics, 2000. **5**(3): p. 259-269.
 101. Aparicio, S., et al., *Optimal methods for processing mineralized tissues for Fourier transform infrared microspectroscopy*. 2002. **70**(5): p. 422-429.
 102. Karlsson, J., et al., *Atomically resolved tissue integration*. 2014. **14**(8): p. 4220-4223.
 103. Schrof, S., et al., *3D Raman mapping of the collagen fibril orientation in human osteonal lamellae*. 2014. **187**(3): p. 266-275.
 104. Gupta, H.S., et al., *Cooperative deformation of mineral and collagen in bone at the nanoscale*. 2006. **103**(47): p. 17741-17746.
 105. Ro, C.-U., J. Osán, and R. Van Grieken, *Determination of low-Z elements in individual environmental particles using windowless EPMA*. Analytical Chemistry, 1999. **71**(8): p. 1521-1528.
 106. Gault, B., et al., *Atom probe microscopy*. Vol. 160. 2012: Springer Science & Business Media.
 107. Geiser, B.P., et al., *Spatial distribution maps for atom probe tomography*. 2007. **13**(6): p. 437-447.
 108. Joester, D., et al., *Organic materials and organic/inorganic heterostructures in atom probe tomography*. 2012. **20**(3): p. 26-31.
 109. Miller, M. and A.-P. Tomography, *Analysis at the Atomic Level*. 2000, Kluwer Academic/Plenum Press, New York.

110. Kelly, T.F. and M.K.J.R.o.S.I. Miller, *Atom probe tomography*. 2007. **78**(3): p. 031101.
111. Reddy, S.M., et al., *Atom probe tomography: development and application to the geosciences*. Geostandards and Geoanalytical Research, 2020. **44**(1): p. 5-50.
112. Lee, B.E., B. Langelier, and K. Grandfield, *Visualization of Collagen–Mineral Arrangement using Atom Probe Tomography*. bioRxiv, 2020.
113. Mosiman, D.S., et al., *Atom Probe Tomography of Encapsulated Hydroxyapatite Nanoparticles*. Small Methods, 2020: p. 2000692.
114. Licata, O., et al., *Probing Heterogeneity in Bovine Enamel Composition through Nanoscale Chemical Imaging using Atom Probe Tomography*. Archives of Oral Biology, 2020. **112**: p. 104682.
115. Karlsson, J., et al., *Atomically resolved tissue integration*. Nano letters, 2014. **14**(8): p. 4220-4223.
116. Sundell, G., et al., *Atom Probe Tomography for 3D Structural and Chemical Analysis of Individual Proteins*. Small, 2019. **15**(24): p. 1900316.
117. Gault, B., et al., *Origin of the spatial resolution in atom probe microscopy*. 2009. **95**(3): p. 034103.
118. Gault, B., et al., *Advances in the reconstruction of atom probe tomography data*. 2011. **111**(6): p. 448-457.
119. Huang, J., et al., *FIB Preparation of Bone-Implant Interfaces for Correlative On-Axis Rotation Electron Tomography and Atom Probe Tomography*. 2014. **20**(S3): p. 352-353.
120. Reznikov, N., et al., *Fractal-like hierarchical organization of bone begins at the nanoscale*. 2018. **360**(6388): p. eaao2189.
121. Gong, J., J. Arnold, and S. Cohn, *Composition of trabecular and cortical bone*. The Anatomical Record, 1964. **149**(3): p. 325-331.
122. Caeiro, J., P. González, and D. Guede, *Biomechanics and bone (& II): Trials in different hierarchical levels of bone and alternative tools for the determination of bone strength*. Rev Osteoporos Metab Miner, 2013. **5**(2): p. 99-108.
123. Schwartz, C.L., et al., *Cryo - fluorescence microscopy facilitates correlations between light and cryo - electron microscopy and reduces the rate of photobleaching*. Journal of microscopy, 2007. **227**(2): p. 98-109.
124. Zhou, W., et al., *Fundamentals of scanning electron microscopy (SEM)*, in *Scanning microscopy for nanotechnology*. 2006, Springer. p. 1-40.
125. Goodhew, P.J., J. Humphreys, and R. Beanland, *Electron microscopy and analysis*. 2000: CRC press.
126. Kulkarni, K.N., et al., *Electron Probe Micro-Analyzer: An Equipment for Accurate and Precise Micro-Composition Analysis*, in *Electron Microscopy in Science and Engineering*. 2022, Springer. p. 71-93.
127. Newbury, D.E., *Barriers to quantitative electron probe X-ray microanalysis for low voltage scanning electron microscopy*. Journal of research of the National Institute of Standards and Technology, 2002. **107**(6): p. 605.
128. Herbig, M., P. Choi, and D. Raabe, *Combining structural and chemical information at the nanometer scale by correlative transmission electron microscopy and atom probe tomography*. Ultramicroscopy, 2015. **153**: p. 32-39.

9: Bibliography

129. Moody, M.P., et al., *Qualification of the tomographic reconstruction in atom probe by advanced spatial distribution map techniques*. Ultramicroscopy, 2009. **109**(7): p. 815-824.
130. Gault, B., et al., *Atom probe tomography*. Nature Reviews Methods Primers, 2021. **1**(1): p. 1-30.
131. Bas, P., et al., *A general protocol for the reconstruction of 3D atom probe data*. Applied Surface Science, 1995. **87**: p. 298-304.
132. Gault, B., et al., *Impact of directional walk on atom probe microanalysis*. Ultramicroscopy, 2012. **113**: p. 182-191.
133. Cerezo, A., T. Godfrey, and G. Smith, *Application of a position - sensitive detector to atom probe microanalysis*. Review of Scientific Instruments, 1988. **59**(6): p. 862-866.
134. Gault, B., et al., *Estimation of the reconstruction parameters for atom probe tomography*. Microscopy and Microanalysis, 2008. **14**(4): p. 296-305.
135. Larson, D.J., et al., *Atom probe tomography spatial reconstruction: Status and directions*. Current Opinion in Solid State and Materials Science, 2013. **17**(5): p. 236-247.
136. Saxey, D., *Correlated ion analysis and the interpretation of atom probe mass spectra*. Ultramicroscopy, 2011. **111**(6): p. 473-479.
137. Miller, M., K. Russell, and G.J.U. Thompson, *Strategies for fabricating atom probe specimens with a dual beam FIB*. 2005. **102**(4): p. 287-298.
138. Thompson, K., et al., *In situ site-specific specimen preparation for atom probe tomography*. 2007. **107**(2-3): p. 131-139.
139. Vurpillot, F., A. Bostel, and D. Blavette, *Trajectory overlaps and local magnification in three-dimensional atom probe*. Applied Physics Letters, 2000. **76**(21): p. 3127-3129.
140. Larson, D.J., et al., *Improvements in planar feature reconstructions in atom probe tomography*. Journal of Microscopy, 2011. **243**(1): p. 15-30.
141. Larson, D.J., et al., *On the use of simulated field-evaporated specimen apex shapes in atom probe tomography data reconstruction*. Microscopy and Microanalysis, 2012. **18**(5): p. 953-963.
142. Vurpillot, F., D. Larson, and A. Cerezo, *Improvement of multilayer analyses with a three - dimensional atom probe*. Surface and Interface Analysis: An International Journal devoted to the development and application of techniques for the analysis of surfaces, interfaces and thin films, 2004. **36**(5 - 6): p. 552-558.
143. De Geuser, F., et al., *An improved reconstruction procedure for the correction of local magnification effects in three - dimensional atom - probe*. Surface and Interface Analysis: An International Journal devoted to the development and application of techniques for the analysis of surfaces, interfaces and thin films, 2007. **39**(2 - 3): p. 268-272.
144. Ehrlich, G. and K. Stolt, *Surface diffusion*. Annual Review of Physical Chemistry, 1980. **31**(1): p. 603-637.
145. Antczak, G. and G. Ehrlich, *Jump processes in surface diffusion*. Surface science reports, 2007. **62**(2): p. 39-61.
146. Yao, L., et al., *On the multiplicity of field evaporation events in atom probe: A new dimension to the analysis of mass spectra*. Philosophical Magazine Letters, 2010. **90**(2): p. 121-129.

147. Thuvander, M., et al., *Quantitative atom probe analysis of carbides*. Ultramicroscopy, 2011. **111**(6): p. 604-608.
148. La Fontaine, A., et al., *Atomic-scale compositional mapping reveals Mg-rich amorphous calcium phosphate in human dental enamel*. Science advances, 2016. **2**(9): p. e1601145.
149. Eder, K., et al., *Overcoming challenges associated with the analysis of nacre in the atom probe*. 2019.
150. Kelly, T.F., et al., *First data from a commercial local electrode atom probe (LEAP)*. Microscopy and Microanalysis, 2004. **10**(3): p. 373-383.
151. Miller, M. and M. Burke, *An APFIM survey of grain boundary segregation and precipitation in irradiated pressure vessel steels*. 1992, Oak Ridge National Lab.
152. Kölling, S. and W. Vandervorst, *Failure mechanisms of silicon-based atom-probe tips*. Ultramicroscopy, 2009. **109**(5): p. 486-491.
153. Vurpillot, F., et al., *Thermal response of a field emitter subjected to ultra-fast laser illumination*. Journal of Physics D: Applied Physics, 2009. **42**(12): p. 125502.
154. Martin, T.L., et al., *Comparing the consistency of atom probe tomography measurements of small-scale segregation and clustering between the LEAP 3000 and LEAP 5000 instruments*. Microscopy and Microanalysis, 2017. **23**(2): p. 227-237.
155. Hyde, J., et al., *Atom probe tomography of reactor pressure vessel steels: An analysis of data integrity*. Ultramicroscopy, 2011. **111**(6): p. 676-682.
156. Sadygov, R.G., D. Cociorva, and J.R. Yates, *Large-scale database searching using tandem mass spectra: looking up the answer in the back of the book*. Nature methods, 2004. **1**(3): p. 195-202.
157. Horai, H., et al., *MassBank: a public repository for sharing mass spectral data for life sciences*. Journal of mass spectrometry, 2010. **45**(7): p. 703-714.
158. Haley, D., P. Choi, and D. Raabe, *Guided mass spectrum labelling in atom probe tomography*. Ultramicroscopy, 2015. **159**: p. 338-345.
159. Haley, D., *"Weights", an Atom Probe Helper Program*. 2013, Atom Probe Lab: <https://sourceforge.net/projects/apptools/files/extras/>.
160. Hudson, D., G. Smith, and B. Gault, *Optimisation of mass ranging for atom probe microanalysis and application to the corrosion processes in Zr alloys*. Ultramicroscopy, 2011. **111**(6): p. 480-486.
161. Vella, A., et al., *Field evaporation mechanism of bulk oxides under ultra fast laser illumination*. Journal of Applied Physics, 2011. **110**(4): p. 044321.
162. London, A.J., D. Haley, and M.P. Moody, *Single-ion deconvolution of mass peak overlaps for atom probe microscopy*. Microscopy and Microanalysis, 2017. **23**(2): p. 300-306.
163. London, A.J., *Quantifying uncertainty from mass-peak overlaps in atom probe microscopy*. Microscopy and Microanalysis, 2019. **25**(2): p. 378-388.
164. Hellman, O.C., J.B. Du Rivage, and D.N. Seidman, *Efficient sampling for three-dimensional atom probe microscopy data*. Ultramicroscopy, 2003. **95**: p. 199-205.
165. Hellman, O.C., et al., *Analysis of three-dimensional atom-probe data by the proximity histogram*. Microscopy and Microanalysis, 2000. **6**(5): p. 437-444.
166. Hellman, O.C. and D.N. Seidman, *Measurement of the Gibbsian interfacial excess of solute at an interface of arbitrary geometry using three-dimensional atom probe*

- microscopy*. Materials Science and Engineering: A, 2002. **327**(1): p. 24-28.
167. Ishitani, T. and H. Kaga, *Calculation of local temperature rise in focused-ion-beam sample preparation*. Microscopy, 1995. **44**(5): p. 331-336.
168. Zhang, W., *Characterization and simulation of electron/ion beam damage on soft materials in FIB-SEM microscopes*. 2019.
169. Schmied, R., et al., *A combined approach to predict spatial temperature evolution and its consequences during FIB processing of soft matter*. Physical Chemistry Chemical Physics, 2014. **16**(13): p. 6153-6158.
170. Thach, R.E. and S.S. Thach, *Damage to biological samples caused by the electron beam during electron microscopy*. Biophysical journal, 1971. **11**(2): p. 204-210.
171. Talmon, Y., *Electron beam radiation damage to organic and biological cryospecimens, in Cryotechniques in biological electron microscopy*. 1987, Springer. p. 64-84.
172. Bassim, N.D., et al., *Minimizing damage during FIB sample preparation of soft materials*. Journal of Microscopy, 2012. **245**(3): p. 288-301.
173. Wolff, A., et al., *Modelling of focused ion beam induced increases in sample temperature: a case study of heat damage in biological samples*. Journal of Microscopy, 2018. **272**(1): p. 47-59.
174. Fager, C., et al., *Optimization of FIB-SEM tomography and reconstruction for soft, porous, and poorly conducting materials*. Microscopy and Microanalysis, 2020. **26**(4): p. 837-845.
175. Glaeser, R.M. and K.A. Taylor, *Radiation damage relative to transmission electron microscopy of biological specimens at low temperature: a review*. Journal of microscopy, 1978. **112**(1): p. 127-138.
176. Drobne, D., et al., *Surface damage induced by FIB milling and imaging of biological samples is controllable*. Microscopy research and technique, 2007. **70**(10): p. 895-903.
177. Bailey, R.J., et al., *Evaluating focused ion beam induced damage in soft materials*. Micron, 2013. **50**: p. 51-56.
178. Heymann, J.A., et al., *Site-specific 3D imaging of cells and tissues with a dual beam microscope*. Journal of structural biology, 2006. **155**(1): p. 63-73.
179. Schroeder-Reiter, E., et al., *Focused ion beam (FIB) combined with high resolution scanning electron microscopy: a promising tool for 3D analysis of chromosome architecture*. Journal of structural biology, 2009. **165**(2): p. 97-106.
180. Schneider, P., et al., *Serial FIB/SEM imaging for quantitative 3D assessment of the osteocyte lacuno-canalicular network*. Bone, 2011. **49**(2): p. 304-311.
181. Grandfield, K. and H. Engqvist, *Focused ion beam in the study of biomaterials and biological matter*. Advances in Materials Science and Engineering, 2012. **2012**.
182. Kizilyaprak, C., et al., *Investigation of resins suitable for the preparation of biological sample for 3-D electron microscopy*. Journal of structural biology, 2015. **189**(2): p. 135-146.
183. Diez-Escudero, A., et al., *Focus ion beam/scanning electron microscopy characterization of osteoclastic resorption of calcium phosphate substrates*. Tissue Engineering Part C: Methods, 2017. **23**(2): p. 118-124.
184. Kim, S., et al., *Minimization of focused ion beam damage in nanostructured polymer thin films*. Ultramicroscopy, 2011. **111**(3): p. 191-199.

9: Bibliography

185. Giannuzzi, L.A., B.I. Prenitzer, and B.W. Kempshall, *Ion-solid interactions*, in *Introduction to focused ion beams*. 2005, Springer. p. 13-52.
186. Miller, M., K. Russell, and G. Thompson, *Strategies for fabricating atom probe specimens with a dual beam FIB*. *Ultramicroscopy*, 2005. **102**(4): p. 287-298.
187. Miller, M.K., et al., *Review of atom probe FIB-based specimen preparation methods*. 2007. **13**(6): p. 428-436.
188. Bunton, J., et al., *Optimized laser thermal pulsing of atom probe tomography: LEAP 4000X™*. *Microscopy and Microanalysis*, 2010. **16**(S2): p. 10-11.
189. Liu, H., H. Liu, and T. Tsong, *Numerical calculation of the temperature distribution and evolution of the field - ion emitter under pulsed and continuous - wave laser irradiation*. *Journal of applied physics*, 1986. **59**(4): p. 1334-1340.
190. Bunton, J.H., et al., *Advances in pulsed-laser atom probe: Instrument and specimen design for optimum performance*. *Microscopy and Microanalysis*, 2007. **13**(6): p. 418-427.
191. Kingham, D.R., *The post-ionization of field evaporated ions: A theoretical explanation of multiple charge states*. *Surface Science*, 1982. **116**(2): p. 273-301.
192. Marquis, E.A. and B. Gault, *Determination of the tip temperature in laser assisted atom-probe tomography using charge state distributions*. *Journal of Applied Physics*, 2008. **104**(8): p. 084914.
193. Kellogg, G., *Determining the field emitter temperature during laser irradiation in the pulsed laser atom probe*. *Journal of Applied Physics*, 1981. **52**(8): p. 5320-5328.
194. A. J. London, *AtomProbeLab*. <https://sourceforge.net/projects/atomprobelab/>, 2020.
195. Santhanagopalan, D., et al., *Effects of laser energy and wavelength on the analysis of LiFePO₄ using laser assisted atom probe tomography*. *Ultramicroscopy*, 2015. **148**: p. 57-66.
196. Bachhav, M., et al., *Investigation of O-18 enriched hematite (α -Fe₂O₃) by laser assisted atom probe tomography*. *International Journal of Mass Spectrometry*, 2013. **335**: p. 57-60.
197. Kinno, T., et al., *Laser-assisted atom probe tomography of ¹⁸O-enriched oxide thin film for quantitative analysis of oxygen*. *Applied surface science*, 2014. **290**: p. 194-198.
198. Karahka, M., Y. Xia, and H. Kreuzer, *The mystery of missing species in atom probe tomography of composite materials*. *Applied Physics Letters*, 2015. **107**(6): p. 062105.
199. Kirchhofer, R., et al., *Quantifying compositional homogeneity in pb (zr, ti) o 3 using atom probe tomography*. *Journal of the American Ceramic Society*, 2014. **97**(9): p. 2677-2697.
200. Devaraj, A., et al., *Role of photoexcitation and field ionization in the measurement of accurate oxide stoichiometry by laser-assisted atom probe tomography*. *The journal of physical chemistry letters*, 2013. **4**(6): p. 993-998.
201. Fehsenfeld, F., et al., *Translational energy spectrum of O₂-ions formed by 4 keV O₂⁺ ions impacting on argon*. *Journal of Physics B: Atomic and Molecular Physics (1968-1987)*, 1973. **6**(9): p. L268.
202. Gault, B., et al., *Behavior of molecules and molecular ions near a field emitter*. *New Journal of Physics*, 2016. **18**(3): p. 033031.
203. Müller, M., et al., *Compositional nonuniformities in pulsed laser atom probe tomography*

- analysis of compound semiconductors*. Journal of Applied Physics, 2012. **111**(6): p. 064908.
204. Kini, U. and B. Nandeesh, *Physiology of bone formation, remodeling, and metabolism, in Radionuclide and hybrid bone imaging*. 2012, Springer. p. 29-57.
205. Wehrli, F.W., *Structural and functional assessment of trabecular and cortical bone by micro magnetic resonance imaging*. Journal of Magnetic Resonance Imaging: An Official Journal of the International Society for Magnetic Resonance in Medicine, 2007. **25**(2): p. 390-409.
206. Keaveny, T.M., et al., *Biomechanics of trabecular bone*. Annual review of biomedical engineering, 2001. **3**(1): p. 307-333.
207. Chappard, D., et al., *Trabecular bone microarchitecture: a review*. Morphologie, 2008. **92**(299): p. 162-170.
208. Parkinson, I.H. and N.L. Fazzalari, *Characterisation of trabecular bone structure, in Skeletal aging and osteoporosis*. 2013, Springer. p. 31-51.
209. Choi, K. and S.A. Goldstein, *A comparison of the fatigue behavior of human trabecular and cortical bone tissue*. Journal of biomechanics, 1992. **25**(12): p. 1371-1381.
210. Ott, S.M., *Cortical or trabecular bone: what's the difference?* American journal of nephrology, 2018. **47**(6): p. 373-376.
211. Hodge, A., J. Petruska, and G. Ramachandran, *Aspects of protein structure*. Academic, 1963: p. 289-300.
212. Hodge, A.J., *Structure at the electron microscopic level*. Treatise on collagen, 1967. **1**: p. 185-205.
213. Katz, E.P. and S.-T. Li, *Structure and function of bone collagen fibrils*. Journal of molecular biology, 1973. **80**(1): p. 1-15.
214. Hodge, A.J., *Molecular models illustrating the possible distributions of 'holes' in simple systematically staggered arrays of type I collagen molecules in native-type fibrils*. Connective tissue research, 1989. **21**(1-4): p. 137-147.
215. Alexander, B., et al., *The nanometre-scale physiology of bone: steric modelling and scanning transmission electron microscopy of collagen–mineral structure*. Journal of the Royal Society Interface, 2012. **9**(73): p. 1774-1786.
216. Zhang, W., et al., *Nucleation sites of calcium phosphate crystals during collagen mineralization*. Journal of the American Ceramic Society, 2003. **86**(6): p. 1052-1054.
217. Zhang, W., S. Liao, and F. Cui, *Hierarchical self-assembly of nano-fibrils in mineralized collagen*. Chemistry of Materials, 2003. **15**(16): p. 3221-3226.
218. Tao, J., et al., *Energetic basis for the molecular-scale organization of bone*. Proceedings of the National Academy of Sciences, 2015. **112**(2): p. 326-331.
219. Landis, W.J. and M.J. Song, *Early mineral deposition in calcifying tendon characterized by high voltage electron microscopy and three-dimensional graphic imaging*. Journal of structural biology, 1991. **107**(2): p. 116-127.
220. Landis, W., et al., *Mineral and organic matrix interaction in normally calcifying tendon visualized in three dimensions by high-voltage electron microscopic tomography and graphic image reconstruction*. Journal of structural biology, 1993. **110**(1): p. 39-54.
221. McNally, E., et al., *Scanning transmission electron microscopic tomography of cortical*

- bone using Z-contrast imaging*. Micron, 2013. **49**: p. 46-53.
222. Schwarcz, H.P., E.A. McNally, and G.A. Botton, *Dark-field transmission electron microscopy of cortical bone reveals details of extrafibrillar crystals*. Journal of Structural Biology, 2014. **188**(3): p. 240-248.
223. Aerssens, J., et al., *Interspecies differences in bone composition, density, and quality: potential implications for in vivo bone research*. Endocrinology, 1998. **139**(2): p. 663-670.
224. Momma, K. and F. Izumi, *VESTA 3 for three-dimensional visualization of crystal, volumetric and morphology data*. Journal of applied crystallography, 2011. **44**(6): p. 1272-1276.
225. Ressler, A., et al., *Ionic substituted hydroxyapatite for bone regeneration applications: A review*. Open Ceramics, 2021. **6**: p. 100122.
226. Ressler, A., et al., *From bio-waste to bone substitute: Synthesis of biomimetic hydroxyapatite and its use in chitosan-based composite scaffold preparation*. Chemical and Biochemical Engineering Quarterly, 2020. **34**(2): p. 59-71.
227. Lee, S.-W., et al., *Comparative Study of hydroxyapatite prepared from seashells and eggshells as a bone graft material*. Tissue Engineering and Regenerative Medicine, 2014. **11**(2): p. 113-120.
228. Palaveniene, A., et al., *Osteoconductive 3D porous composite scaffold from regenerated cellulose and cuttlebone-derived hydroxyapatite*. Journal of Biomaterials Applications, 2019. **33**(6): p. 876-890.
229. Gao, C., et al., *Bone biomaterials and interactions with stem cells*. Bone research, 2017. **5**(1): p. 1-33.
230. Glimcher, M.J., *Bone: nature of the calcium phosphate crystals and cellular, structural, and physical chemical mechanisms in their formation*. Reviews in mineralogy and geochemistry, 2006. **64**(1): p. 223-282.
231. Hodge, A. and J. Petruska, *Aspect of Protein Structure; Ramachandran GN, editor*. 1963, New York: Academic Press.
232. Petruska, J.A. and A.J. Hodge, *A subunit model for the tropocollagen macromolecule*. Proceedings of the National Academy of Sciences, 1964. **51**(5): p. 871-876.
233. Rho, J.-Y., L. Kuhn-Spearing, and P. Zioupos, *Mechanical properties and the hierarchical structure of bone*. Medical engineering & physics, 1998. **20**(2): p. 92-102.
234. Orgel, J.P., et al., *The in situ supermolecular structure of type I collagen*. Structure, 2001. **9**(11): p. 1061-1069.
235. Orgel, J.P., et al., *Microfibrillar structure of type I collagen in situ*. Proceedings of the National Academy of Sciences, 2006. **103**(24): p. 9001-9005.
236. Shah, F.A., P. Thomsen, and A. Palmquist, *Osseointegration and current interpretations of the bone-implant interface*. Acta biomaterialia, 2019. **84**: p. 1-15.
237. Xu, Y., et al., *Intermolecular channels direct crystal orientation in mineralized collagen*. Nature communications, 2020. **11**(1): p. 1-12.
238. Landis, W.J., et al., *Electron microscopic observations of bone tissue prepared by ultracryomicrotomy*. Journal of ultrastructure research, 1977. **59**(2): p. 185-206.
239. Weiner, S. and W. Traub, *Bone structure: from ångstroms to microns*. The FASEB journal, 1992. **6**(3): p. 879-885.

240. Landis, W.J., et al., *Structural relations between collagen and mineral in bone as determined by high voltage electron microscopic tomography*. Microscopy research and technique, 1996. **33**(2): p. 192-202.
241. Reznikov, N., R. Shahar, and S. Weiner, *Bone hierarchical structure in three dimensions*. Acta biomaterialia, 2014. **10**(9): p. 3815-3826.
242. Alexander, B.E., et al. *The nano-physiology of mineralized tissues*. in *Summer Bioengineering Conference*. 2009. American Society of Mechanical Engineers.
243. Lees, S. and K. Probst, *The locus of mineral crystallites in bone*. Connective tissue research, 1988. **18**(1): p. 41-54.
244. Chyou, P.-H., A.M. Nomura, and G.N. Stemmermann, *A prospective study of diet, smoking, and lower urinary tract cancer*. Annals of epidemiology, 1993. **3**(3): p. 211-216.
245. Sasaki, N., et al., *Atomic force microscopic studies on the structure of bovine femoral cortical bone at the collagen fibril-mineral level*. Journal of Materials Science: Materials in Medicine, 2002. **13**(3): p. 333-337.
246. Hassenkam, T., et al., *High-resolution AFM imaging of intact and fractured trabecular bone*. Bone, 2004. **35**(1): p. 4-10.
247. Jantou-Morris, V., M.A. Horton, and D.W. McComb, *The nano-morphological relationships between apatite crystals and collagen fibrils in ivory dentine*. Biomaterials, 2010. **31**(19): p. 5275-5286.
248. Wopenka, B. and J.D. Pasteris, *A mineralogical perspective on the apatite in bone*. Materials Science and Engineering: C, 2005. **25**(2): p. 131-143.
249. Mavrogenis, A., et al., *Biology of implant osseointegration*. J Musculoskelet Neuronal Interact, 2009. **9**(2): p. 61-71.
250. Bose, S., et al., *Understanding of dopant-induced osteogenesis and angiogenesis in calcium phosphate ceramics*. Trends in biotechnology, 2013. **31**(10): p. 594-605.
251. Šarić, M. and M. Piasek, *Effects of sodium chloride on bone health*. Arhiv za higijenu rada i toksikologiju, 2005. **56**(1): p. 39-44.
252. Matsunaga, K. and H. Murata, *Formation energies of substitutional sodium and potassium in hydroxyapatite*. Materials transactions, 2009: p. 0902090667-0902090667.
253. Chen, S., et al., *Biomimetic synthesis of Mg - substituted hydroxyapatite nanocomposites and three - dimensional printing of composite scaffolds for bone regeneration*. Journal of Biomedical Materials Research Part A, 2019. **107**(11): p. 2512-2521.
254. Cacciotti, I., et al., *Mg-substituted hydroxyapatite nanopowders: synthesis, thermal stability and sintering behaviour*. Journal of the European Ceramic Society, 2009. **29**(14): p. 2969-2978.
255. Farzadi, A., et al., *Magnesium incorporated hydroxyapatite: Synthesis and structural properties characterization*. Ceramics International, 2014. **40**(4): p. 6021-6029.
256. Stipniece, L., et al., *Strontium substituted hydroxyapatite promotes direct primary human osteoblast maturation*. Ceramics International, 2021. **47**(3): p. 3368-3379.
257. Pilmane, M., et al., *Strontium and strontium ranelate: Historical review of some of their functions*. Materials Science and Engineering: C, 2017. **78**: p. 1222-1230.
258. Jeong, J., et al., *Bioactive calcium phosphate materials and applications in bone*

- regeneration*. Biomaterials research, 2019. **23**(1): p. 1-11.
259. Loughrill, E., et al., *Calcium to phosphorus ratio, essential elements and vitamin D content of infant foods in the UK: Possible implications for bone health*. Maternal & child nutrition, 2017. **13**(3): p. e12368.
260. Grynepas, M.D., L.C. Bonar, and M.J. Glimcher, *Failure to detect an amorphous calcium-phosphate solid phase in bone mineral: a radial distribution function study*. Calcified tissue international, 1984. **36**(1): p. 291-301.
261. Bigi, A., et al., *The role of magnesium on the structure of biological apatites*. Calcified tissue international, 1992. **50**(5): p. 439-444.
262. Bigi, A., et al., *Chemical and structural characterization of the mineral phase from cortical and trabecular bone*. Journal of inorganic biochemistry, 1997. **68**(1): p. 45-51.
263. Xiao-Yan, W., et al., *Comparative study on inorganic composition and crystallographic properties of cortical and cancellous bone*. Biomedical and Environmental Sciences, 2010. **23**(6): p. 473-480.
264. Lotsari, A., et al., *Transformation of amorphous calcium phosphate to bone-like apatite*. Nature communications, 2018. **9**(1): p. 1-11.
265. Schwarcz, H.P. and H. Nahal, *Theoretical and observed C/N ratios in human bone collagen*. Journal of Archaeological Science, 2021. **131**: p. 105396.
266. Marquis, E., et al., *Evolution of tip shape during field evaporation of complex multilayer structures*. Journal of microscopy, 2011. **241**(3): p. 225-233.
267. Melkonyan, D., et al., *Atom probe tomography analysis of SiGe fins embedded in SiO₂: Facts and artefacts*. Ultramicroscopy, 2017. **179**: p. 100-107.
268. Fletcher, C., M.P. Moody, and D. Haley, *Towards model-driven reconstruction in atom probe tomography*. Journal of Physics D: Applied Physics, 2020. **53**(47): p. 475303.
269. Hoang, Q.Q., et al., *Bone recognition mechanism of porcine osteocalcin from crystal structure*. Nature, 2003. **425**(6961): p. 977-980.
270. Hauschka, P.V. and F.H. Wians Jr, *Osteocalcin - hydroxyapatite interaction in the extracellular organic matrix of bone*. The Anatomical Record, 1989. **224**(2): p. 180-188.
271. Moody, M.P., et al., *Atomically resolved tomography to directly inform simulations for structure–property relationships*. Nature communications, 2014. **5**(1): p. 1-10.
272. Micheletti, C., et al., *From tissue retrieval to electron tomography: nanoscale characterization of the interface between bone and bioactive glass*. Journal of the Royal Society Interface, 2021. **18**(182): p. 20210181.
273. Bertazzo, S., et al., *Nano-analytical electron microscopy reveals fundamental insights into human cardiovascular tissue calcification*. 2013. **12**(6): p. 576.
274. Gentleman, E., et al., *Comparative materials differences revealed in engineered bone as a function of cell-specific differentiation*. 2009. **8**(9): p. 763.
275. Dorozhkin, S.V. and M. Epple, *Biological and medical significance of calcium phosphates*. Angewandte Chemie International Edition, 2002. **41**(17): p. 3130-3146.

Chapter 10

Appendix

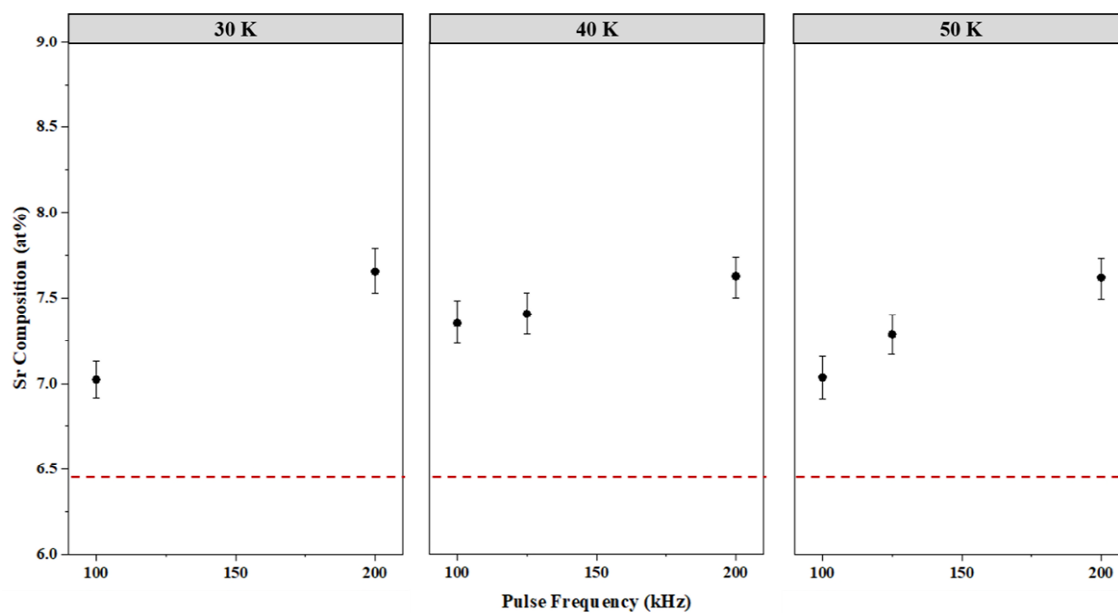


Figure 103. Graphs showing the effect of varying pulse frequency at different temperatures on Sr Composition, the dashed red line is representative of the nominal Sr composition of the pSrBG. Error bars represent 95 % confidence intervals based on deconvolution.

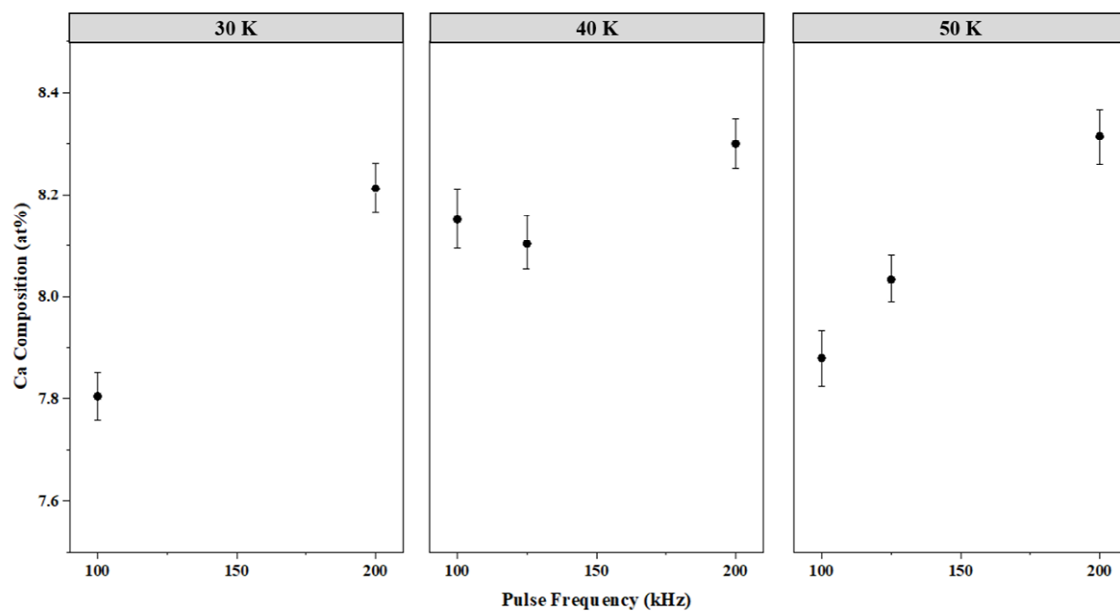


Figure 104. Graphs showing the effect of varying pulse frequency at different temperatures on Ca Composition, the nominal Ca composition of the pSrBG is 6.468%. Error bars represent 95 % confidence intervals based on deconvolution.

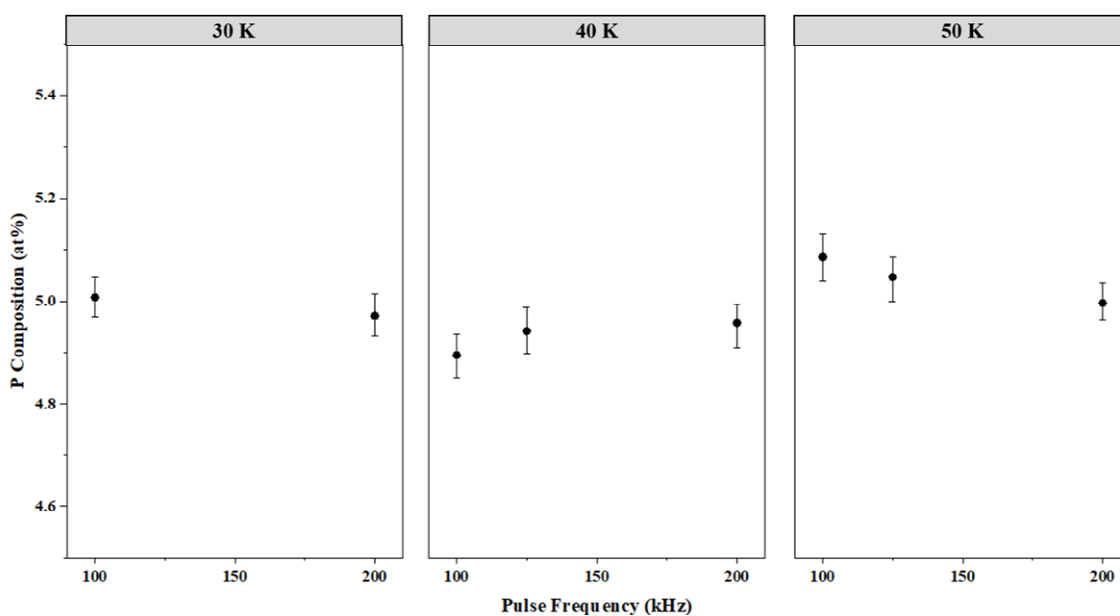


Figure 105. Graphs showing the effect of varying pulse frequency at different temperatures on P Composition, the nominal P composition of the pSrBG is 3.270%. Error bars represent 95 % confidence intervals based on deconvolution.

Table 24. Comparison in the composition of human enamel, dentin, bone and synthetic hydroxyapatite [275].

Composition (wt%)	Enamel	Dentin	Bone	Synthetic HAp
Ca ²⁺	36.5	35.1	34.8	39.6
PO ₄ ³⁻	17.7	16.9	15.2	18.5
Na ⁺	0.5	0.6	0.9	—
Mg ²⁺	0.44	1.23	0.72	—
K ⁺	0.08	0.05	0.03	—
CO ₃ ²⁻	3.5	5.6	7.4	—
F ⁻	0.01	0.06	0.03	—
Cl ⁻	0.30	0.01	0.13	—

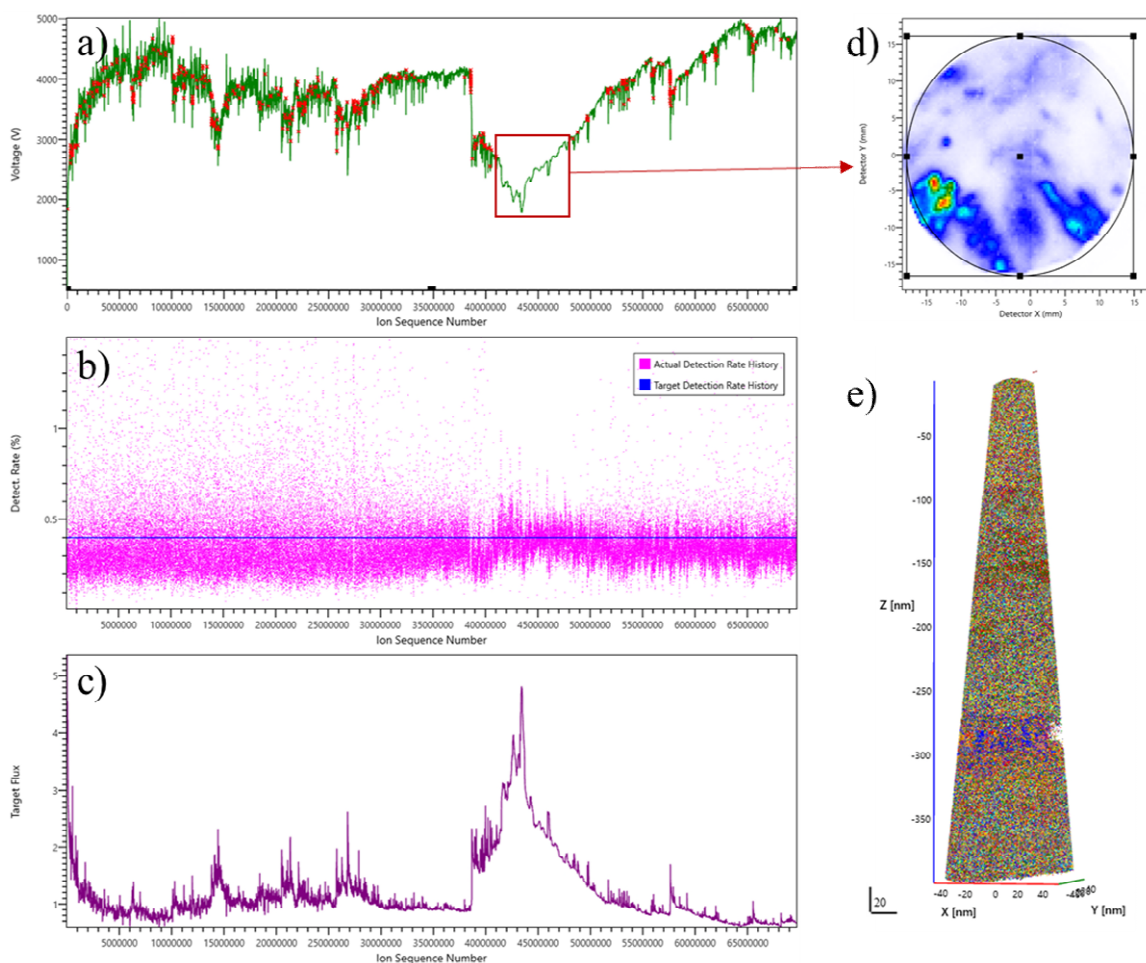


Figure 106. Instantaneous experimental conditions, specimen evaporation response and corresponding reconstruction of R5083_23561. (a) applied voltage history, (b) detection rate history, (c) target flux history, (d) detector map of ion hits corresponding the section of the experiment defined by the selected red box area in (a), and (e) 3D reconstruction of the specimen.

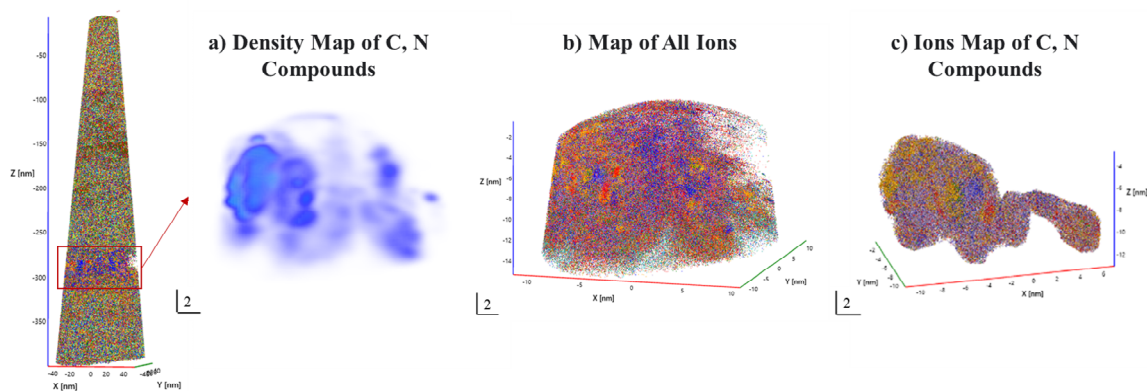


Figure 107. More detailed analysis of the pore region in the R5083_23561. (a) Density map of C and N compounds in the pore region (the red box). (b) & (c) Ions distribution maps of the pore region and the selected specific area.

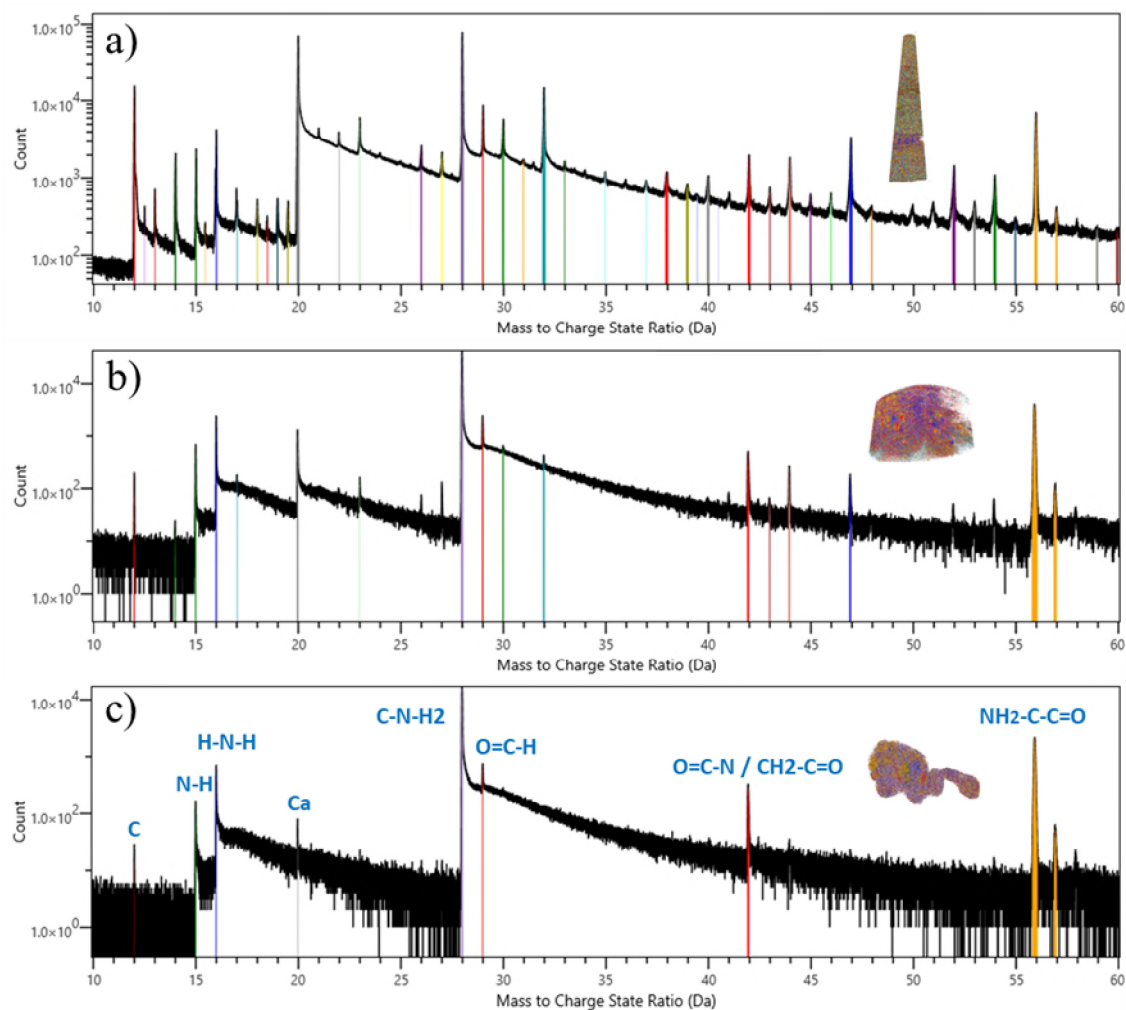


Figure 108. Comparison of mass spectra isolated to different regions in the sample of R5083_23561. (a) The mass spectrum of all ions. (b) The specific mass spectrum of the pore region. (c) The mass spectrum of the selected specific region within the pore.